Long- and short-lived radiogenic isotope constraints on the history of the early Earth and the Moon

Inaugural-Dissertation

zur

Erlangung des Doktorgrades

der Mathematisch-Naturwissenschaftlichen Fakultät

der Universität zu Köln

vorgelegt von

Eric Hasenstab

Aus Aschaffenburg

Köln, 2022

Berichterstatter: Prof. Dr. Carsten Münker

PD Dr. Daniel Herwartz

Tag der mündlichen Prüfung: 29.04.2022

A scientist in his laboratory is not a mere technician: he is also a child confronting natural phenomena that impress him as though they were fairy tales.

Marie Curie

Table of contents

I. Abstract

The only known habitable planet is the Earth. As geological processes are what led to Earth's habitability, understanding Earth's geodynamic evolution is of crucial importance. However, the geodynamic processes of the early Earth, during the Hadean (>4.0Ga), remain enigmatic. This is a consequence of Earth's accessible rock record beginning as late as in the Eoarchean, more than 500 Ma after Earth has accreted. Unraveling Earth's earliest processes therefore requires indirect methods such as isotope systematics. Variations in the isotope composition of short-lived decay systems such as ^{129}I-^{129}Xe, ^{146}Sm-^{142}Nd, or ^{182}Hf-^{182}W have provided strong evidence that substantial geodynamic processes on Earth (e.g. silicate differentiation) already operated during the Hadean. Constraints on Hadean geodynamics are further corroborated by long-lived ^{176}Lu-^{176}Hf and ^{147}Sm-^{143}Nd isotope systematics that support a complex and active history for the infant Earth. Evidence for such a vigorous early planetary evolution is found not only on Earth but also on our closest neighbor, the Moon. Although lunar research has shown that Earth and Moon must be closely related in terms of the material from which it accreted, it remains highly debated if these planetary bodies are chondritic or not.

This study investigates the differentiation history of the Earth-Moon system. In three chapters, we report the isotope compositions of various long- and short-lived decay series for 3.53 to 2.63 Ga Archean rocks from the Pilbara Craton (^{138}La-^{138}Ce, ^{147}-^{143}Nd and ^{176}Lu-^{176}Hf, **Chapter I**), ~3.8 to 2.0 Ga rocks from SW Greenland (^{147,146}Sm-^{143,142}Nd and ^{176}Lu-^{176}Hf, **Chapter II**) and 4.4 to 3.1 Ga lunar rocks (^{138}La-^{138}Ce and ^{147}Sm-^{143}Nd, **Chapter III**). In rocks from the Pilbara Craton, Ce-Nd-Hf isotope compositions are strongly coupled and yield correlations that are similar to those observed in modern mantle-derived rocks. However, a few ultramafic rocks reveal decoupled Hf-Nd isotope compositions, where extremely high $\varepsilon Hf_{(i)}$ values but only moderately elevated $\varepsilon^{143}Nd_{(i)}$ values are observed. This decoupling stands in contrast to the previously observed decoupling of Hf-Nd isotopes in Isua rocks from SW Greenland, where $\varepsilon^{143}Nd_{(i)}$ scatters variable and $\varepsilon Hf_{(i)}$ being moderately elevated. In order to better constrain the origin of this decoupling we have conducted trace element and Hf-Nd-(Ce) isotope modelling. For both studied Archean localities, we were able to exclude a perovskite-related origin within a magma ocean, since sequestered perovskite cumulates would severely fractionate incompatible trace element compositions (REE, HFSE Th and Ti) (**Chapter I** and **Chapter II**). Rather, the decoupling of Hf-Nd isotopes in the Pilbara Craton is formed by the admixture of garnet-depleted melt residues into the ascending mantle plume that have a high potential to fractionate the ^{176}Lu-^{176}Hf from ^{147}Sm-^{143}Nd systematics. In contrast, in the Isua region enriched slab melts were likely responsible for the observed decoupling of Hf-Nd isotopes. Further, we have developed a new analytical tool to separate and measure mass independent and radiogenic isotopes at ultra-high precision on a Thermo Finnigan Neptune Plus® MC ICP-MS device (**Chapter II**). We applied our new analytical protocol to well-characterized ~3.8 to ~3.4 Ga rocks from the Isua supracrustal belt. Our observed ^{142}Nd/^{144}Nd compositions of Isua rocks yield excellent agreement with previously reported literature data, validating our analytical protocol. Notably, our study is the first to resolve small ^{142}Nd/^{144}Nd differences between

~3.8 and ~3.7 Ga rocks from the Isua greenstone belt. Generally, we see a decrease of μ^{142}Nd anomalies between ~3.8 to ~3.4 Ga that can be interpreted to reflect replenishing lower mantle (i.e., bulk silicate Earth material) that carried no μ^{142}Nd anomalies. To better characterize the composition of the Earth-Moon system, we investigated ^{147}Sm-^{143}Nd and ^{138}La-^{138}Ce isotope systematics as well as trace element characteristics of lunar rocks (**Chapter III**). Generally, all uncertainty-propagated Ce-Nd isotope best fit arrays do not intersect the chondritic value, arguing for a non-chondritic composition of the Moon. Combined trace element and Hf-Nd-Ce isotope modelling, including coupled ^{176}Lu-^{176}Hf-^{147}Sm-^{143}Nd systematics from existing literature data, reveals that the Moon must be depleted in its incompatible trace element composition. However, the degree of depletion must be significantly smaller than inferred in previous models. In a next step, we compare Ce-Nd isotope compositions of near-contemporaneous 3.3±0.25 Ga lunar and terrestrial rocks from the Pilbara (**Chapter I**) and Kaapvaal Craton. Our study reveals that the Archean terrestrial rock record also does not intersect the chondritic value. Instead, the lunar and terrestrial array share a common intersection that is indistinguishable from our modelled one. We take this as evidence that not only the Moon but also Earth must be slightly depleted. These findings have far-reaching consequences and require a revaluation of depleted and primitive mantle domains and their mass balances in terrestrial crustal and mantle reservoirs.

II. Kurzzusammenfassung

Die Erde ist der einzige uns bekannt Planet auf dem es Leben gibt. Da es die geologischen Prozesse waren, die die Erde zu einem bewohnbaren Planeten geformt haben, ist das Verständnis der frühen geodynamischen Erdgeschichte von zentraler Bedeutung. Gerade jedoch die frühen geodynamischen Prozesse des Hadaikums bleiben noch immer rätselhaft, da selbst die ältesten Gesteine der Erde das Eoarchaikum nicht überschreiten und somit mehr als 500 Ma hadaischer Erdgeschichte nicht länger erhalten sind. Um diese frühen Prozesse dennoch zu entschlüsseln haben sich indirekte Methoden bewährt. Variationen in der Isotopenzusammensetzung von kurzlebigen Zerfallssystemen wie ^{129}I-^{129}Xe, ^{146}Sm-^{142}Nd, oder ^{182}Hf-^{182}W haben starke Belege geliefert, dass bereits im Hadaikum geodynamische Prozesse (z.B. Silikat Differenzierung) abliefen. Nachweise für geodynamische Prozesse im Hadaikum sind auch durch die beiden langlebigen Zerfallsreihen ^{176}Lu-^{176}Hf und ^{147}Sm-^{143}Nd gesichert, die eine aktive und komplexe Geschichte der jungen Erde belegen. Die Belege für eine so lebhafte frühe planetare Entwicklung finden sich jedoch nicht nur auf der Erde, sondern auch auf unserem nächsten Nachbarn, dem Mond. Obwohl die Mondforschung der letzten Jahrzehnte zeigen konnte, dass Erde und Mond von sehr ähnlichem Material akkretierten, bleibt die Frage nach einer chondritischen Zusammensetzung für diese beiden planetaren Körper noch immer hochumstritten.

Diese Studie untersucht die Differenzierungsgeschichte des frühen Erde-Mond Systems. In drei Kapiteln werden Isotopenzusammensetzungen für verschiedene kurz- und langlebige Zerfallsreihen für 3.53 bis 2.63 Ga archaische Gesteine vom Pilbara Kraton in NW Australien (^{138}La-^{138}Ce, ^{147}-^{143}Nd und ^{176}Lu-^{176}Hf, **Kapitel I)**, ~3.8 bis 2.0 Ga Gesteine aus SW Grönland (^{147,146}Sm-^{143,142}Nd und ^{176}Lu-^{176}Hf, **Kapitel II**) und 4.4 bis 3.1 Ga Mondgesteine (^{138}La-^{138}Ce und ^{147}Sm-^{143}Nd, **Kapitel III**) berichtet. In den Gesteinen des Pilbara Kratons sind Ce-Nd-Hf Isotope stark gekoppelt und ähneln in ihrer Zusammensetzung denen aus rezenten Mantelgesteinen. Allerdings zeigen ein paar ultramafische Gesteine entkoppelte Hf-Nd Isotopenzusammensetzungen in denen stark erhöhte $\varepsilon Hf_{(i)}$ aber nur moderate erhöhte $\varepsilon^{143}Nd_{(i)}$ Werte beobachtet werden. Diese Arte der Entkopplung ist gegensätzlich zu der die in Isua Gesteinen aus SW Grönland beobachtet wird, wo $\varepsilon^{143}Nd_{(i)}$ Werte stark streuen, $\varepsilon Hf_{(i)}$ Werte jedoch konstant sind. Um den Ursprung dieser Entkopplung besser zu verstehen, werden Spurenelement und Hf-Nd-(Ce) Isotopenmodellierungen durchgeführt. Für beide Archaische Lokalitäten kann ein Perovskit-bezogener Ursprung innerhalb eines Magma Ozeans ausgeschlossen werden, da solche Perovskit Kumulate die Zusammensetzung an inkompatiblen Spurenelementen (REE, HFSE, Th und Ti) zu stark fraktionieren würden. (**Kapitel I** und **Kapitel II**). Im Pilbara Kraton wird die Entkopplung von Hf-Nd Isotopen eher durch das Beimischen von Granat-verarmte Schmelzresiduen in den aufsteigenden Mantelplume hervorgerufen, die hohes Potential haben, das ^{176}Lu-^{176}Hf vom ^{147}Sm-^{143}Nd Zerfallssystem zu fraktionieren. Im Gegensatz dazu waren in der Isua Region wahrscheinlich *Slab*-Schmelzen für die Entkopplung von Hf-Nd Isotopen verantwortlich. Darüber hinaus wird eine neue analytische Methodik beschrieben, die die Abtrennung und Messung von massenunabhängigen und radiogenen Nd Isotope in ultra-hoher Präzision an einer Thermo Finnigan Neptune Plus® MC ICP-MS ermöglicht (**Kapitel II**). Diese neue analytische Methodik wird and gut charakterisierten ~3.8 bis ~3.4 Ga Gesteinen des Isua

suprakrustalen Grünsteingürtels angewendet. Die hier beobachteten $^{142}Nd/^{144}Nd$ Isotopen Zusammensetzungen zeigen eine hervorragende Übereinstimmung mit bereits publizierten Literaturdaten und validieren unsere neue analytische Methodik. Darüber hinaus ist diese Studie die erste die es schafft kleine $^{142}Nd/^{144}Nd$ Isotopenunterschiede zwischen den ~3.8 und ~3.7 Ga Gesteinen auflösen zu können. Ein generelles Abnehmen an $\mu^{142}Nd$ Anomalien zwischen ~3.8 bis 3.4 Ga wird als Homogenisierung durch den darunter liegenden Mantel interpretiert, der keine $\mu^{142}Nd$ Anomalien aufweist und vermutlich die Durchschnittszusammensetzung der Erde hatte. Um die Zusammensetzung des Erde-Mond Systems besser zu bestimmen werden ^{147}Sm-^{143}Nd und ^{138}La-^{138}Ce Isotopensystematiken sowie Spurenelementzusammensetzungen von Mondgesteinen untersucht (**Kapitel III**). Generell schneidet keiner der fehlerfortgepflanzten Ce-Nd Isotopen Arrays die chondritische Zusammensetzung, was für eine nicht-chondritische Zusammensetzung des Mondes spricht. Kombinierte Hf-Nd-Ce Isotopen- sowie Spurenelement-Modellierungen, die auch ^{176}Lu-^{176}Hf und ^{147}Sm-^{143}Nd Systematiken aus Literaturdaten miteinbeziehen, zeigen, dass der Mond in seiner inkompatiblen Spurenelementzusammensetzung verarmt sein muss. Allerdings muss der Grad der Verarmung deutlich geringer sein als in bisherigen Modellen postuliert. In einem nächsten Schritt werden die Ce-Nd Isotopenzusammensetzungen von nahezu gleichaltrigen 3.3±0.25 Ga Gesteinen der Pilbara (**Kapitel I**) und Kaapvaal Kratons verglichen. Diese Studie enthüllt, dass auch terrestrische fehlerfortgepflanzte Arrays nicht die chondritische Zusammensetzung schneiden. Dafür zeigen der lunare und terrestrische Array einen gemeinsamen Schnittpunkt der von der hier modellierten Zusammensetzung des Mondes ununterscheidbar ist. Das wird als Beleg interpretiert, dass nicht nur der Mond, sondern auch die Erde leicht verarmt sein muss. Diese Erkenntnis hat weitreichende Konsequenzen und erfordern eine Neubewertung von verarmten und primitiven Reservoiren und deren Massenbilanzen in terrestrischen krustalen und Mantelreservoiren.

III. Introduction

III.1. The early solar system

Investigating the solar system's oldest materials provides insights into its initial stages, and the subsequent formation processes of planetary bodies. A profound knowledge of these primordial processes can account for Earth's unique characteristics and how it became a habitable planet. Insights into the initial stages of our solar system come from astronomical investigations of other young solar systems combined with modelling constraints based on isotope systematics and the composition of early solar system materials. In combination, these methods have helped us to understand how planets formed from a primordial molecular cloud. The oldest dated matter from our solar system are 4.568 Ga Calcium-Aluminum-rich inclusions (CAIs). This age is interpreted to represent the solar system initial (SSI), the moment where the first solid material has condensed (Lugmair and Shukolyukov, 1998; Scott and Krot, 2005; Jacobsen et al., 2008; Bouvier and Wadhwa, 2010; Krot, 2019).

Chondrites formed in the first few Ma of the solar system (Trieloff et al., 2003; Bizzarro et al., 2005; Bouvier et al., 2007; Kleine et al., 2008), representing the most primitive meteorite class. Chondrites acquired their name from the broad presence of chondrules, that are round objects typically varying in size between µm to mm. Many chondrules show chemical zoning that resulted from subsequent gas-melt reactions with the remaining solar nebular (Friend et al., 2016; Barosch et al., 2019). Interstitial matrix is another major component of chondrites. It has been shown previously that the chemical composition of matrix and chondrules show complementary Mg/Si ratios, strongly arguing that both components originated from the same region of the solar nebular (Hezel and Palme, 2010; Palme et al., 2015). In addition, chondrites also contain minor amounts of Fe-Ni metal alloys, amoeboid olivine aggregates, and refractory phases such as CAIs (Krot et al., 2004; Scott and Krot, 2005; Krot, 2019). Chondrites are broadly subdivided into three groups

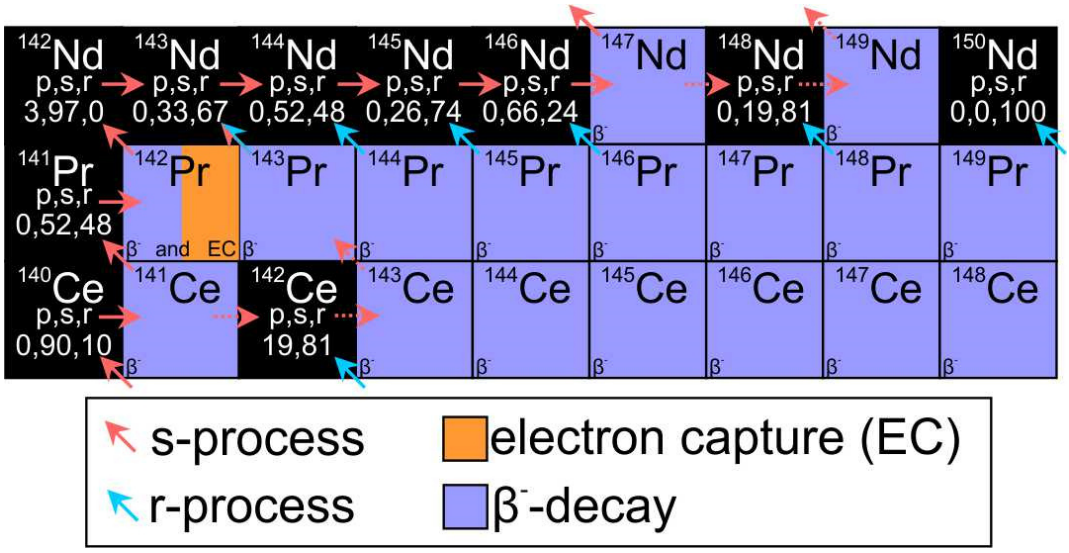

Fig. III.1: Proportions of the s-, r-, and p-process on the formation of Nd isotopes. Abbreviations p, s, and r rand their denoted numbers refer to the proportions of the respective process. Dashed s-process lines represent minor s-process branches. Data for the proportions of s, r, and p-process contributions to different isotopes were taken from Bisterzo et al., (2014).

comprising (i) enstatite, (ii) ordinary, and (iii) carbonaceous chondrites. Chondrites are generally regarded as the most unprocessed and primitive material of our solar system that resisted and/or escaped early solar system processes (e.g., Mezger et al., 2020). However, some chondrules record evidence of a complex history including several heating and remelting events, arguing against the pristineness of some chondrites (Rubin, 2010). Refractory lithophile trace elements bear near-constant ratios in chondrites, making them suitable as a reference reservoir for normalizing selected trace elements (e.g., rare earth elements; hereinafter REE or most high field strength elements; hereinafter denoted as HFSE) and long-lived isotope systematics (^{138}La-^{136}Ce, ^{146,147}Sm-^{142,143}Nd, or ^{176}Lu-^{176}Hf) (Bouvier et al., 2008; Palme and O'Neill, 2013; Israel et al., 2019; Willig and Stracke, 2019), an assumption that is challenged in **Chapter III**.

Despite the widespread view that chondrites represent the bulk Earth composition for a variety of elemental compositions, many elements (e.g., Ti, Cr, Zr, Mo, Ru, or Nd isotopes) reveal an isotopic zonation with respect to the heliocentric distance of their formation (Trinquier et al., 2009; Burkhardt et al., 2016; Fischer-Gödde and Kleine, 2017; Render et al., 2017; Boyet et al., 2018; Mezger et al., 2020). Generally, isotopic differences originate from neutron/proton capture reactions during nucleosynthesis. At least three different processes are needed to explain the isotopic inventory of our solar system (Fig. III.1 and III.2): (1) The s-process (slow neutron capture process) operates in asymptotic giant branch

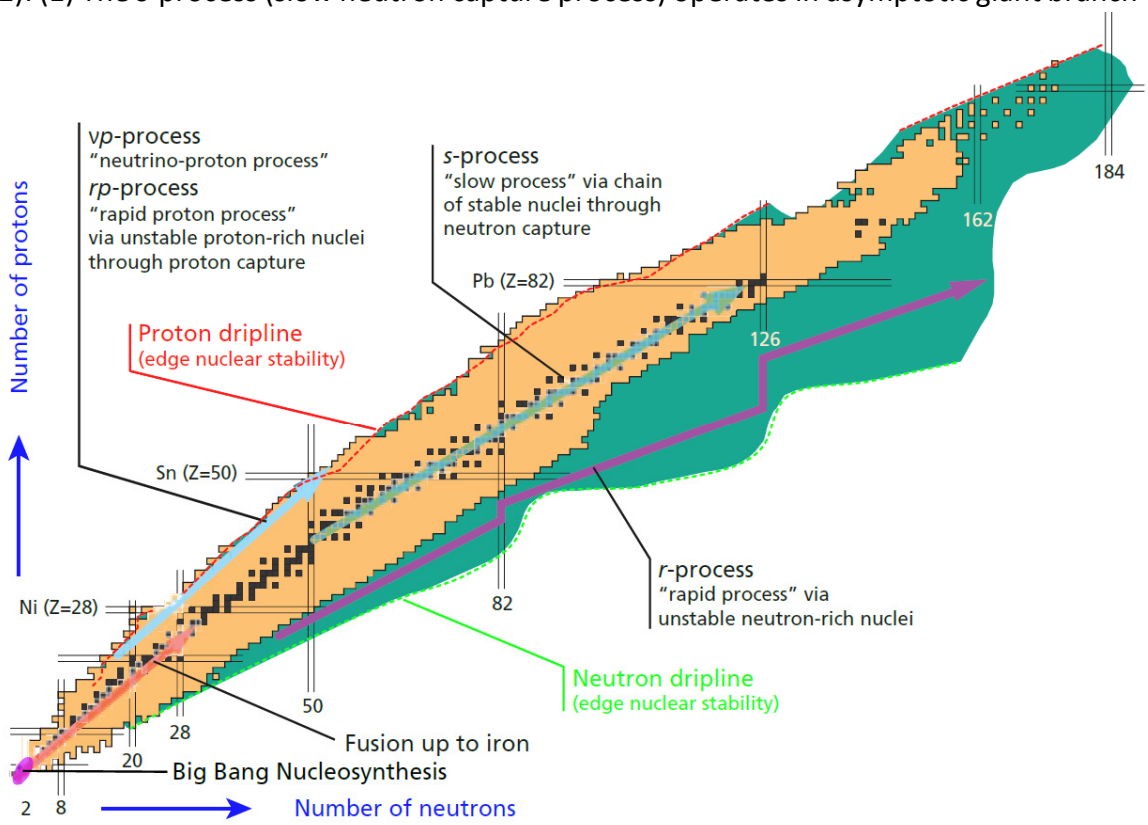

Fig. III.2: Chart of the nuclides showing the formation of the elements and isotopes. Shown are various nucleosynthetic processes responsible for the formation of nuclides. "Magic numbers" for atomic nuclei are emphasized with black lines, representing particularly stable nuclides. Among those magical numbers are some isotopes of particular interest in this study, such as ^{139}La, ^{140}Ce, ^{141}Pr and ^{142}Nd, all built up by 82 neutrons in their nucleus. While the s-process is predominantly responsible for the formation of stable nuclides (black squares) within the valley of stability, the r-process and the p-process are predominantly responsible for the formation of neutron or proton-rich nuclides, respectively. Taken from Rodriguez, (2014).

stars and is mainly responsible for forming stable nuclides along the "valley of nuclear stability", where the neutron capture rate is higher than the decay rate (i.e., up to ^{209}Bi) (cf. Bisterzo et al., 2014; Rodriguez, 2014) (see also Fig. III.1). (2) The r-process (rapid neutron capture process) occurs during the collapse of neutron star merger or supernovae where the neutron fluxes are significantly higher when compared to the s-process. This process is responsible for the formation of high-mass neutron-rich isotopes, even beyond the valley of nuclear stability. (3) Proton-rich p-process nuclides depict nuclides that have formed by proton-capture, photodisintegration, electron capture, or neutrino processes, although more complex decay chains of s- and r-process nuclides or spallation reactions are also possible (Arnould and Goriely, 2003; Bisterzo et al., 2014; Hidaka and Yoneda, 2014).

III.2. Planetary Growth and the formation of the Moon

After the first solid material condensed in the solar system, larger bodies began to accrete. Further accretion led to the formation of 10-100 km-sized planetesimals (Weidenschilling, 2011). Remnants of this early stage of accretion are still preserved today as asteroids or meteorites and are a unique opportunity to investigate such early accretion processes. Within several 10^5 years, runaway growth of some of the early planetesimals formed the first planetary embryos (Kortenkamp et al., 2000), weighing up to 10% of Earth's mass (Yu and Jacobsen, 2011) (Fig. III.3). The further progression of accretion was highly chaotic, where fewer but high-energy collisions characterized this latest stage of accretion. The energy released during such collisions had the potential to create magma oceans that also lead to silicate-metal segregation, forming planetary cores (Rubie et al., 2011). The short lived ^{182}Hf-^{182}W system ($T_{1/2}$=8.9×10^6 years) (Vockenhuber et al., 2004) has proven to be particular useful to unravel these early processes. Since Hf behaves strongly lithophile and W behaves moderately lithophile but is also strongly sequestered into Fe-alloys, the ^{182}Hf-^{182}W system has become particular important to trace early silicate differentiation, core

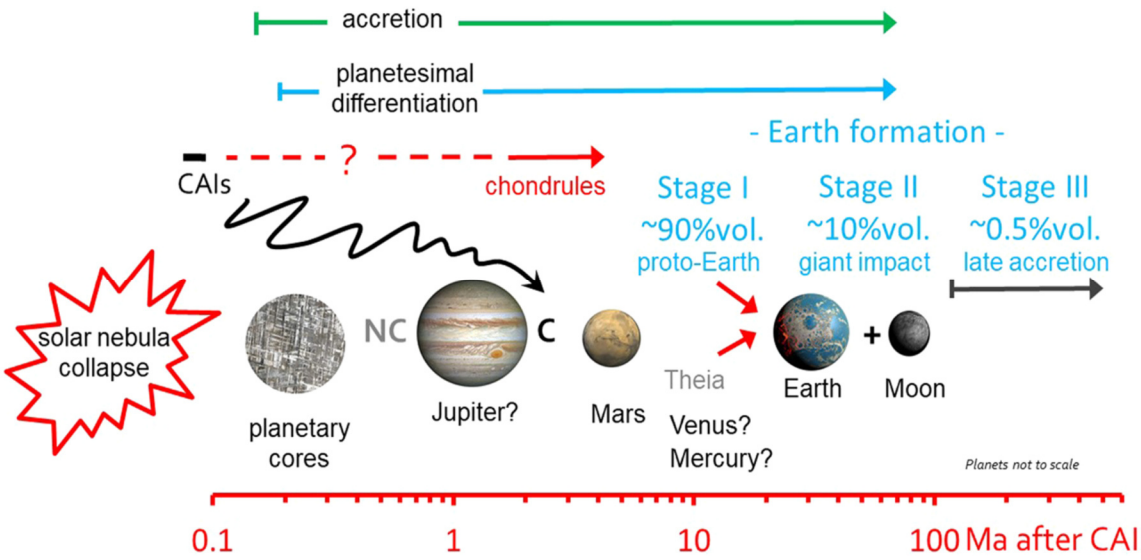

Fig. III.3: Chronological evolution of the accretion and formation of planetary bodies. Taken from Mezger et al. (2020).

formation of planetary bodies and early geochronology in general (e.g., Yin et al., 2002; Kleine et al., 2004; Yu and Jacobsen, 2011; Kruijer et al., 2017; Thiemens et al., 2019).

Presumably the most spectacular outcome of the late collision-style accretion was the formation of the Earth-Moon system that likely formed after a Mars-sized impactor collided with the proto-Earth (Canup and Asphaug, 2001). Formation as the consequence of planetary impacts can provide enough energy to homogenize both planetary bodies, possibly leading to a synestia-like structure from which Earth and Moon were able to re-accrete in the aftermath of the impact (Pahlevan and Stevenson, 2007; Stewart et al., 2018). Although the giant impact model is widely accepted, the Moon's origin has been debated in the past, and alternative models for its formation have been proposed. These include the loss of terrestrial material due to a fast spinning Earth (Cuk and Stewart, 2012) or the formation after multiple smaller impacts (Rufu et al., 2017).

The timing of the Moon's formation is constrained by short-lived ^{182}Hf-^{182}W isotope systematics. Based on ^{182}W/^{184}W constraints, studies have calculated minimum ages for

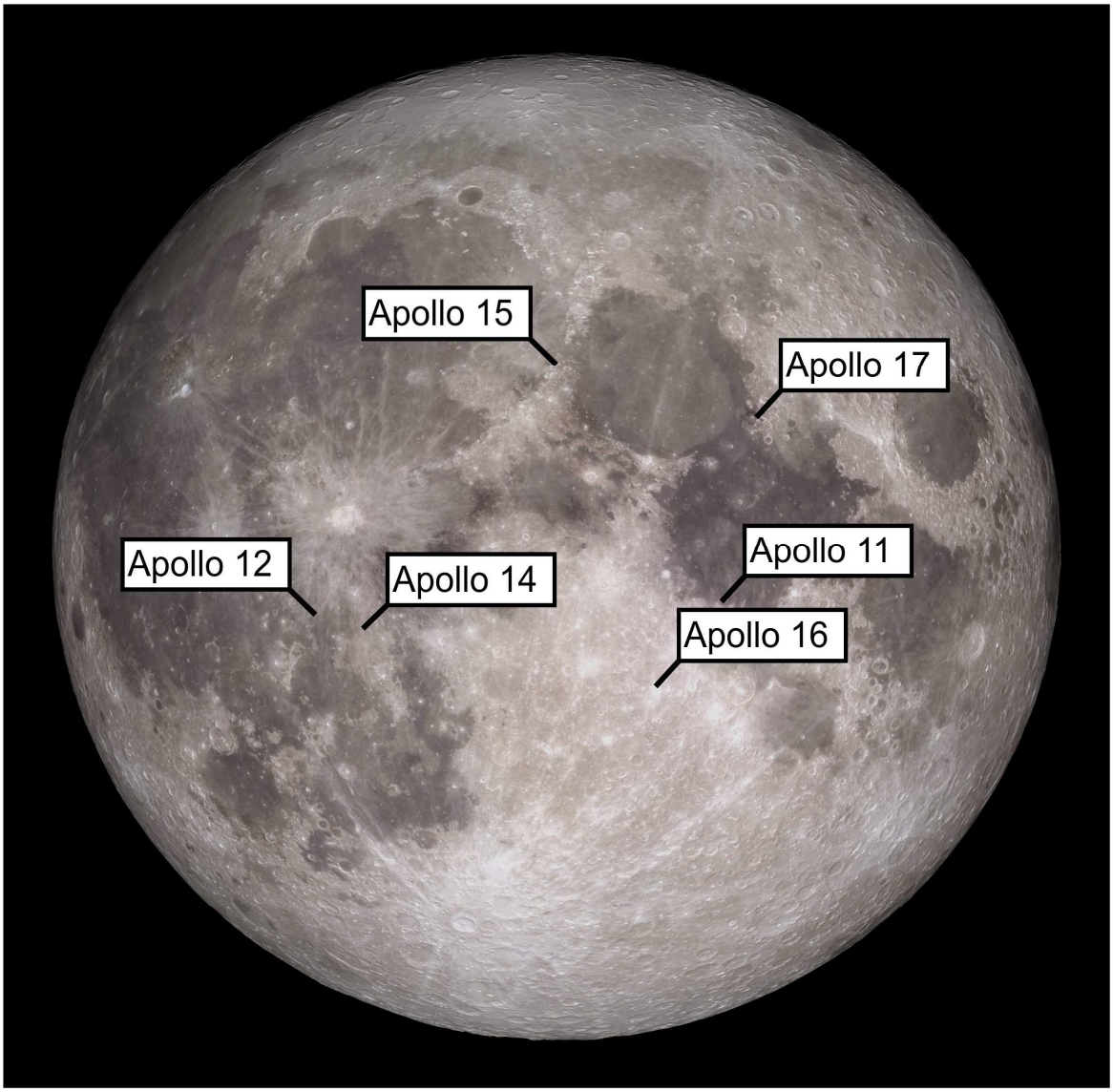

Fig. III.4: Shown are all Apollo landing sites that delivered most of the available returned lunar sample material. Picture modified from NASA (image source: nasa.gov).

the formation of the Moon between 30 and 70 Ma, with maximum ages ranging between 52 and 110 Ma (Halliday, 2008; Kleine et al., 2009; Yu and Jacobsen, 2011). However, these ages rely on accurate Hf/W ratios for bulk Earth and bulk Moon. In a recent study, Thiemens et al. (2019) demonstrated that the bulk Moon has a higher Hf/W ratio than bulk silicate Earth. Taking this into consideration, the authors calculated an age for lunar formation of approximately 50 Ma.

Strong chemical similarities have been observed between lunar and terrestrial rocks ever since the Apollo missions delivered the first material from the Moon, allowing direct comparisons (Fig. III.4). Although some studies have suggested small differences in $\Delta^{17}O$ compositions between the Earth and Moon (Herwartz et al., 2014; Greenwood et al., 2018; Cano et al., 2020), Young et al. (2016) have argued for an identical composition of both planetary bodies. Even if these small differences can be statistically resolved, they are almost two orders of magnitude smaller than the $\Delta^{17}O$ differences between other planetary bodies such as Mars or Vesta (Mohapatra and Murty, 2003; Zhang et al., 2019). The close similarities in the oxygen isotope composition between lunar and terrestrial rocks is also in good agreement with findings from other mass independent isotope systematics (e.g., Cr or Ti) that are indistinguishable on both planetary bodies, further arguing for the close relationship of both planetary bodies (Zhang et al., 2012; Mougel et al., 2018).

Although lunar and terrestrial rocks show close similarities of mass independent isotope compositions, major and trace element characteristics of lunar rocks are markedly different from terrestrial compositions. The first analysis of KREEP-rich (K-Rare Earth Element-P-rich composition) rocks (Meyer et al., 1971), revealed a lunar rock type that showed an extraordinary chemical composition, markedly different from any known terrestrial composition. The major driving force for the geochemical variability in lunar rocks was ascribed lunar magma ocean (LMO) crystallization (Warren and Wasson, 1979; Snyder et al., 1992; Elardo et al., 2011; Elkins-Tanton et al., 2011; Neal, 2017; Charlier et al., 2018; Borg et al., 2019) that formed several distinct lunar mantle cumulates. This includes the sequestration of ilmenite-bearing cumulates, interpreted as the source for lunar high Ti basalts (Snyder et al., 1992). After 99.5% of the lunar mantle has been crystallized (Snyder et al., 1992), a residual KREEP melt remained that is expected to have geochemical properties in good agreement with those observed in KREEP-rich rocks (Warren and Wasson, 1979; Snyder et al., 1992; Elardo et al., 2011; Elkins-Tanton et al., 2011). While LMO cumulate-related volcanism is erupted into mare, a substantial amount of the lunar crust is built up by Ferroan Anorthosites that are interpreted to represent floating plagioclase cumulates (e.g., Ryder, 1991; Snyder et al., 1992).

III.3. Trace element partitioning and rare earth decay series

To unravel geochemical characteristics of differentiated mantle and crustal reservoirs, trace element compositions and radiogenic isotopes have become analytical key tools in the past. Different elements show different compatibilities in mantle minerals, defined as the partition coefficient D which gives the enrichment factor of a particular element in a given mineral relative to the melt composition (Fig. III.5). Trace elements usually do not

form their own minerals but substitute for other elements causing stress in the crystal lattice and their (in-) compatibility strongly depends on their ionic charge and radius. Generally, substituting trace elements with ionic charges differing from the substituted

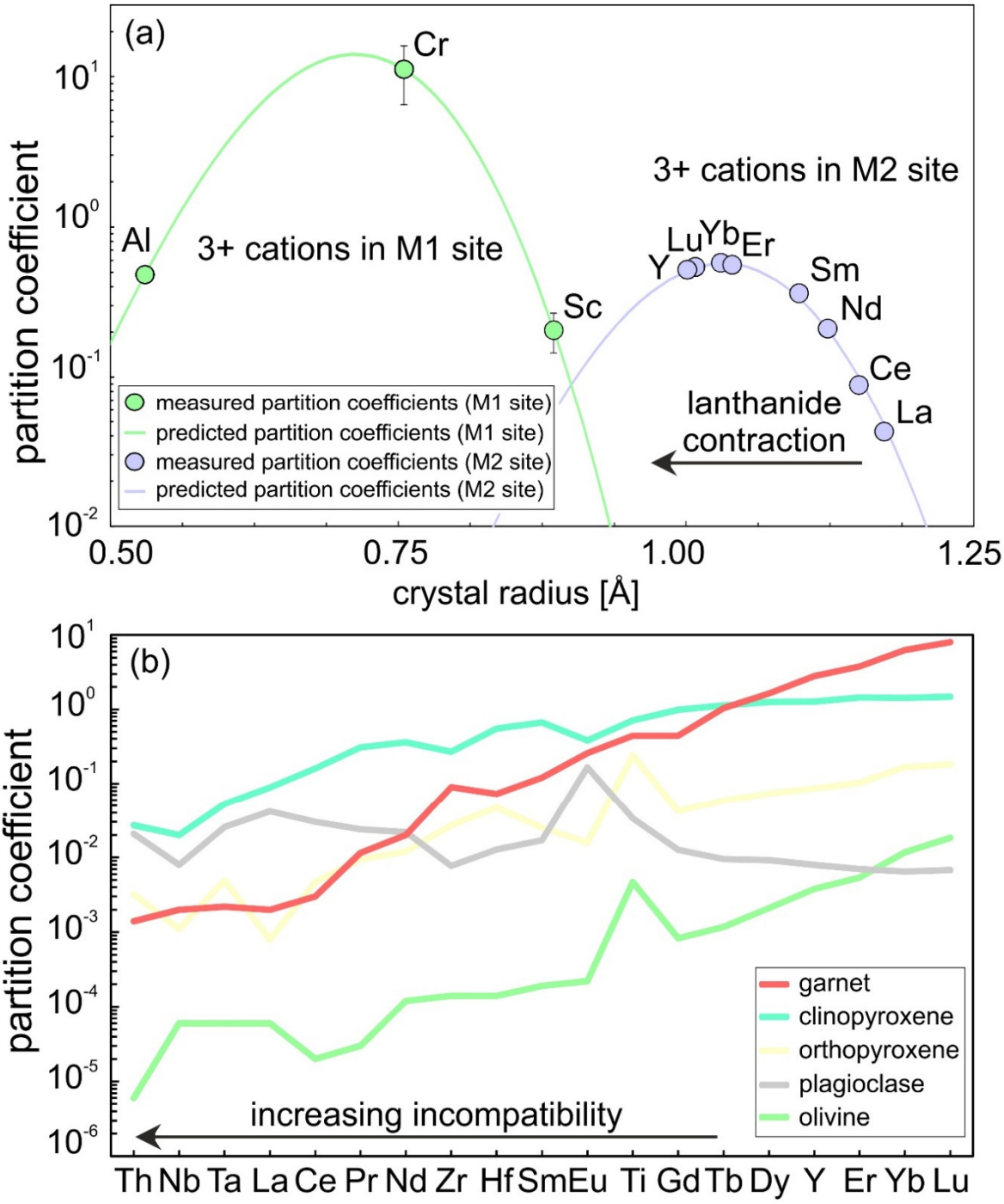

Fig. III.5: Partition coefficients in various minerals. a) Calculated and predicted partition coefficient hyperboles for 3+ cations occupying the M1 and M2 crystal site. b) Typical partition coefficients in Earth's most common mantle minerals. Lattice strain model calculated after Blundy and Wood (1994) with partition coefficients for clinopyroxene from McDade et al. (2004). HFSE and REE partitioning coefficients from previous studies (Phinney and Morrision, 1990; Westrenen et al., 2000; McDade et al., 2003; Dygert et al., 2020).

element will cause more stress than substituents with similar properties. Mineral proportions, chemical composition, temperature, pressure, presence of fluids, or oxygen fugacity can have additional effects on the partitioning behavior (e.g., Candela and Bouton, 1990; Blundy and Wood, 1994; McDade et al., 2003; Caro et al., 2005). The substitution of elements into different crystal sites strongly affects partitioning behavior. This is exemplified in Figure 3a, where partition coefficients for various 3+ cations are shown. Despite their identical ionic charge, these elements fall on two individual hyperboles, depending on the crystal site into which they are incorporated (Blundy and Wood, 1994). Since sets of partition coefficients are usually far from complete, partition coefficients are often extrapolated. As exemplified in Figure III.5a, extrapolating partition coefficients requires a profound knowledge of the elemental behavior within the crystal structure.

The different compatibility of various elements causes them to fractionate during geological processes. The fractionation patterns of the REE have been extensively studied since they can yield valuable information on the source from which the rocks were derived (cf. Pearce, 2008). The REE comprise a group of lithophile trace elements that are moderately to highly incompatible in Earth's most common upper mantle minerals. The different compatibility among the REE is due to their variable ionic radii (caused by the lanthanide contraction), making REE fractionate during silicate differentiation (such as partial melting or fractional crystallization) (Fig. III.5).

In addition, REE include several decay systems that can be used to obtain time-integrated information of rocks. This feature gives REE decay series the potential to obtain geochronological constraints and information about parental sources of investigated rock suites. There are four REE decay systems that are currently applied to geochemical issues (^{176}Lu-^{176}Hf, ^{147,146}Sm-^{143,142}Nd and ^{138}La-^{138}Ce). The two long-lived decay systematics ^{147}Sm-^{143}Nd ($T_{1/2}$=106 Ga) (Lugmair and Marti, 1978) and ^{176}Lu-^{176}Hf ($T_{1/2}$=37 Ga) (Söderlund et al., 2004) have become key analytical tools used to characterize modern to ancient mantle depletion (e.g., Chauvel et al., 2008; Hoffmann et al., 2011b; Rizo et al., 2011; Schneider et

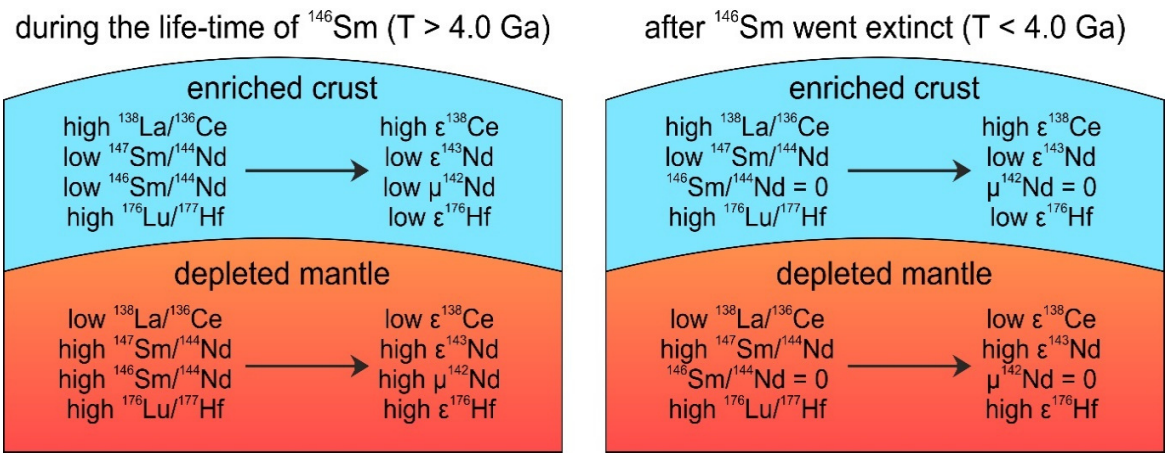

Fig. III.6: Mantle differentiation and its effects on parent/daughter fractionation. During mantle differentiation, complementary depleted and enriched reservoirs are produced. Depending on the parent/daughter fractionation, excesses or deficits of the radiogenic daughter nuclides will be produced over time (relative to unfractionated, primitive mantle). If such differentiation events occurred within the lifetime of ^{146}Sm (i.e., >4.0 Ga), this will also cause an imprint on ^{142}Nd/^{144}Nd compositions.

al., 2019, **Chapter I**, **Chapter II**) (Fig. III.6) and to draw conclusions on the bulk composition of planetary bodies (e.g., Caro and Bourdon, 2010; Sprung et al., 2013, **Chapter III**). In geochronology, ^{176}Lu-^{176}Hf systematics have gained particular importance due to its high closing temperature and a generally high potential to fractionate Lu from Hf in various minerals, notably garnet (e.g., Scherer et al., 2000). In addition, the ^{147}Sm-^{143}Nd and ^{176}Lu-^{176}Hf systems have become an indispensable tool to characterize mantle reservoirs and trace ancient mantle depletion. During crustal extraction, escaping melts form the enriched crust (low Lu/Hf and Sm/Nd) leave behind a depleted mantle (high Lu/Hf and Sm/Nd) (Fig. III.5). Consequently, the enriched crust will evolve towards a time-integrated deficit in its ^{143}Nd/^{144}Nd and ^{176}Hf/^{177}Hf composition relative to unfractionated bulk silicate Earth material (usually referred to as primitive mantle that is equivalent to chondrites) whereas depleted domains will evolve towards excesses. These radiogenic fingerprints help constrain the timing of events such as ancient melt depletion, crustal residence times, and the onset of plate tectonics (e.g., Vervoort et al., 2000; Hoffmann et al., 2010; Hoffmann et al., 2011; van de Löcht et al., 2020; **Chapter I**).

The short-lived decay from ^{146}Sm to ^{142}Nd ($T_{1/2}$=68 or 103 Ma) (Friedman et al., 1966; Meissner et al., 1987; Kinoshita et al., 2012) has been applied to many Archean rocks to investigate if ^{142}Nd/^{144}Nd isotope composition might hint at early (Hadean) silicate differentiation on Earth (e.g., Harper and Jacobsen, 1992; Caro et al., 2003; Boyet and Carlson, 2005; Bennett et al., 2007). By combining short- and long-lived Sm-Nd decay systems, it is possible to obtain precise model ages for previous silicate differentiation events (Caro et al., 2003; Bennett et al., 2007; Rizo et al., 2011; Caro et al., 2017; Morino et al., 2017; Saji et al., 2018, **Chapter II**). Although the short lived ^{146}Sm decay was functionally extinct by the end of the Hadean, anomalous ^{142}Nd/^{144}Nd compositions can still be preserved in Neoarchean or even modern rocks (Debaille et al., 2013; Horan et al., 2018; Peters et al., 2018). Therefore, ^{142}Nd/^{144}Nd isotope studies can also be used as a tool to infer mantle homogenization rates and the preservation potential of primordial mantle domains (Saji et al., 2018; Schneider et al., 2018; Hyung and Jacobsen, 2020).

Although the ^{138}La-^{138}Ce decay system can be applied to similar geochemical issues as ^{147}Sm-^{143}Nd or ^{176}Lu-^{176}Hf, the slow isotopic ingrowth from ^{138}La to ^{138}Ce ($\lambda_\beta = 2.37\times10^{-12}$ a^{-1}) (Tanimizu, 2000) has prevented this isotope system from broader applications. Nevertheless, recent studies showed excellent correlations between radiogenic ^{138}Ce and ^{143}Nd isotopes (Israel et al., 2019; Willig and Stracke, 2019; **Chapter I**, **Chapter III**). Since the light rare earth elements (LREE) (e.g., La, Ce, Nd and Sm) are all similarly (in-) compatible in mantle minerals, they show a strong coupling. This feature gives coupled Ce-Nd isotope studies a unique potential to investigate the refractory incompatible trace element composition of planetary bodies, such as Earth or Moon (**Chapter III**).

III.4. Present, Archean and Hadean geodynamic processes on Earth

Earth's convecting mantle, active plate tectonics, and the continuous creation and obliteration of its crust is responsible for the limited preservation of Archean crust (e.g., Lee et al., 2011) (Fig. III.7). The involved processes create distinct geochemical features,

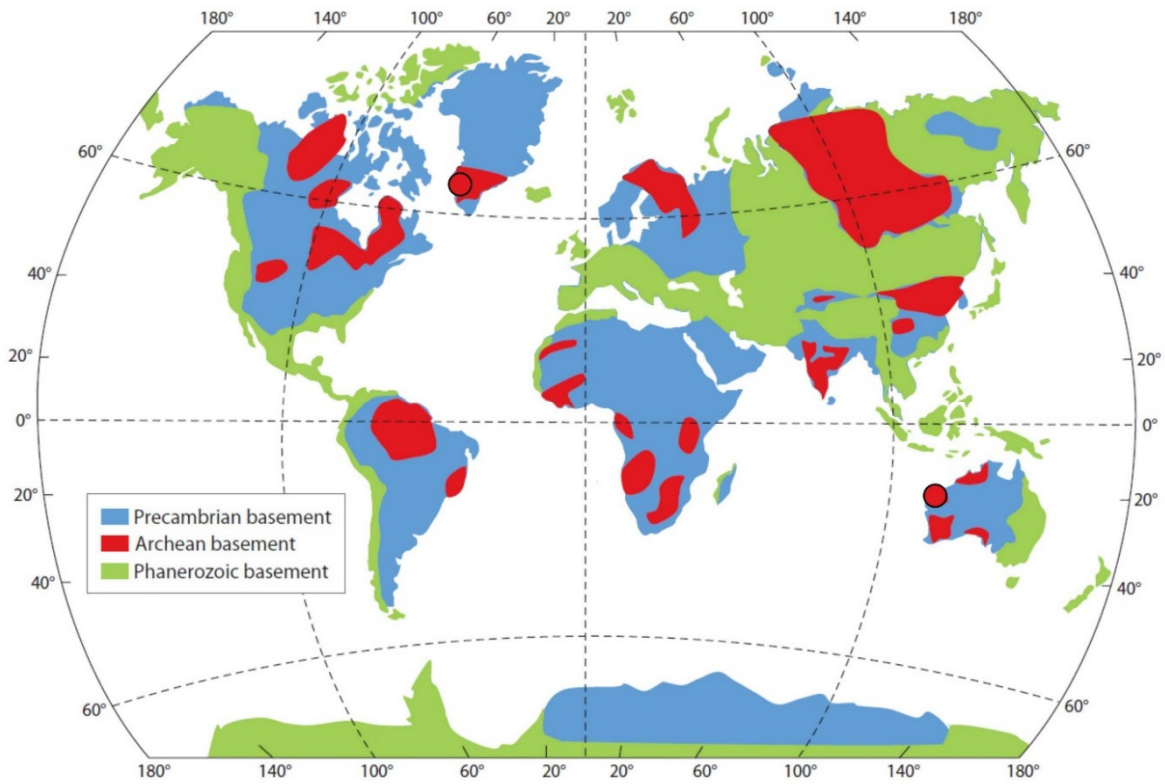

Fig. III.7: Geological map showing the preservation of Archean crust. Red circles mark the studied areas. Modified after Lee et al., (2011).

and therefore, Earth's geochemical properties are highly diverse. Generally, Earth's upper mantle is depleted in incompatible trace elements (such as REE or HFSE) as a consequence of partial melting, whereas a complementary enriched reservoir exists in the overlying crust (Fig. III.6). Such planetary differentiation events are well-described for the Earth, Moon, and Mars (e.g., Nyquist et al., 1995; Caro et al., 2003; Foley et al., 2005; Bennett et al., 2007; Gaffney and Borg, 2014; Caro et al., 2017; Kruijer et al., 2017; Saji et al., 2018). The fundamental difference between Earth and our closest neighbors, however, is that on Earth plate tectonics have operated globally and continuously since at least the Phanerozoic, with periodic episodes in the Archean (e.g., Polat et al., 2002; Polat and Hofmann, 2003; Van Kranendonk, 2007; O'Neill et al., 2007; Smithies et al., 2007c; Hoffmann et al., 2011b; Szilas, 2018; van de Löcht et al., 2020, **Chapter I**, **Chapter II**). One of the most exceptional outcomes of plate tectonics is subduction, wherein denser oceanic crust is transported back into the mantle to participate in mantle convection. This process can refertilize and alter the mantle geochemistry. By means of radiogenic Sr-Nd-Pb isotopes, four endmembers have been identified that are able to explain the observed geochemical range: EM-1 (enriched mantle 1), EM-2 (enriched mantle 2), DMM (depleted mantle MORB) and HIMU (also "high μ", with $\mu=^{238}U/^{204}Pb$) (e.g., Hofmann, 1997; Stracke et al., 2005). In addition, BSE can be considered as another mantle endmember composition, although its chemical composition is highly debated (Caro et al., 2008; O'Neill and Palme, 2008; Caro and Bourdon, 2010; Campbell et al., 2012; Bouvier and Boyet, 2016; Burkhardt et al., 2016; Boyet et al., 2018; Saji et al., 2020).

In contrast to the well-characterized modern mantle endmembers, unraveling Archean and Hadean geodynamic processes on Earth is more ambiguous. The characterization of the

different modern mantle reservoirs (that were affected by deep mantle recycling processes) mainly rely on combined radiogenic Sr-Nd-Pb isotope constraints (e.g., Hofmann, 1997; Stracke et al., 2005). However, ^{87}Rb-^{87}Sr as well as $^{235,238}U$-$^{207,206}Pb/^{204}Pb$ systematics are often overprinted during post-magmatic alteration, a process that is very common in Archean rocks. Without reliable ^{87}Rb-^{87}Sr or $^{235,238}U$-$^{207,206}Pb/^{204}Pb$ data, mantle characterization of Archean rocks is mainly reduced to radiogenic Hf-Nd isotope and trace element data, providing less constraints and leading to more ambiguous interpretations. Although still debated, there is evidence that plate tectonics operated already at 3.2 Ga locally within the Pilbara Craton, NW Australia, as witnessed by a fully preserved Wilson cycle (Van Kranendonk et al., 2010). Even older evidence for (at least local) Eoarchean plate tectonics comes from ~3.7-3.8 Ga rocks from the Isua region, SW-Greenland, that show strongly boninitic affinities as well as island arc-like trace element characteristics, strongly arguing for source enrichment within a subduction-like setting (Polat et al., 2002; Polat and Hofmann, 2003; Hoffmann et al., 2011, **Chapter II**). In addition, Archean cratons usually comprise high volumes of tonalite-trondhjemite-granodiorite intrusions (TTG) that carry arc-like trace element signatures (e.g., Moyen and Martin, 2012). However, geochemical evidence for early Phanerozoic-style plate tectonics has been challenged by modeling constraints that largely preclude such tectonic settings in the early Archean due to higher mantle temperatures (Herzberg et al., 2010). Instead, it has been hypothesized that Hadean-Archean plate tectonics operated more sluggish (Korenaga, 2008; Herzberg et al., 2010). Alternatively, it has been proposed that Hadean-Archean plate tectonics operated more vertically compared to modern tectonics, by building thick piles of (mafic) crust that might have lead to gravitational overturn events (Van Kranendonk et al., 2004; Wiemer et al., 2018). During such overturn events, the thickened mafic crust would have sunken down, initiating the rise of felsic domes in between the destabilized mafic crust (Fig. III.8). Such a unique tectonic regime is observed in the Pilbara Craton, where felsic domes are separated from each other by greenstone synclines (Van Kranendonk et al., 2004; Wiemer et al., 2018). Escaping partial melts of such hydrated mafic crust can also explain the major and trace element geochemistry of Archean TTGs without the need of early subduction-like settings (Johnson et al., 2017).

Many Archean cratons preserve uncontaminated mantle-derived rocks that show positive $\varepsilon Nd_{(i)}$ and $\varepsilon Hf_{(i)}$ values, including the ~3.6 to 3.2 Ga Kaapvaal Craton, ~3.6 to 2.6 Ga Pilbara Craton and the ~3.85 to 3.6 Ga Itsaq Gneiss Complex and associated greenstone belts (e.g., Hoffmann et al., 2010; Hoffmann et al., 2011b; Puchtel et al., 2016; Schneider et al., 2019; van de Löcht et al., 2020; Murphy et al., 2021, **Chapter I**). These features have been interpreted to reflect depleted parental sources for these mantle-derived rocks. However, this was likely not the result of one global differentiation event, since different cratons show different $^{142}Nd/^{144}Nd$ compositions (Bennett et al., 2007). While the Isua greenstone belt, the Pilbara Craton or the Kaapvaal Craton all have positive $\varepsilon Nd_{(i)}$ and $\varepsilon Hf_{(i)}$ values, the Pilbara Craton shows no $\mu^{142}Nd$ anomalies (Archer et al., 2019; Murphy et al., 2021), the Isua Craton shows positive $\mu^{142}Nd$ anomalies (e.g., Boyet and Carlson, 2006; Rizo et al., 2011; Saji et al., 2018, **Chapter II**) whereas the Kaapvaal Craton is characterized by negative

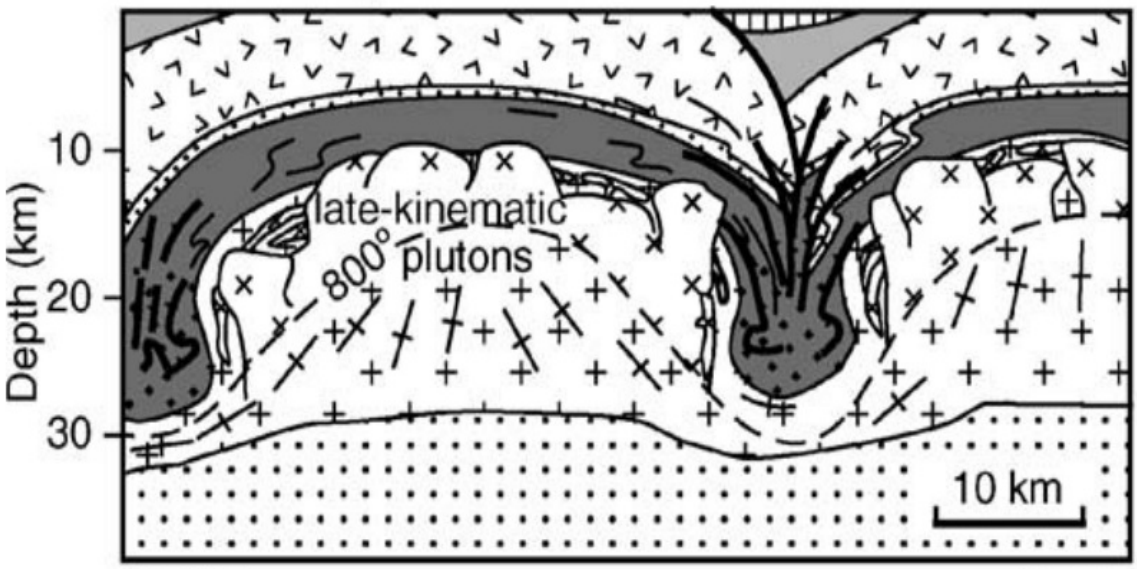

Fig. III.8: Shown is the typical dome and keel structure found in the Pilbara Craton. This is a consequence of overturn events that lead to the rise of felsic intrusion as a consequence of gravitational instabilities. In between the felsic intrusion, the denser mafic crust will sink down. Today, the mafic greenstones are exposed as synclines in between the felsic batholiths. Taken from van Kranendonk et al., (2004).

μ^{142}Nd values (Puchtel et al., 2016; Schneider et al., 2018). The individual μ^{142}Nd composition of different cratons is rather linked to different local differentiation events (Bennett et al., 2007). In addition, the observed isotope evidence are often inconsistent with the geodynamic settings. For instance, continuous pulses of ultramafic volcanism in the Pilbara Craton was recently interpreted to result from plume-style volcanism (Smithies et al., 2005b). It is assumed that volcanic rocks from the Pilbara Craton tap deep primitive mantle sources, in accordance with the observation of chondritic ^{187}Re-^{187}Os systematics (Puchtel et al., 2021). However, this observation conflicts with the observation of positive $\varepsilon Nd_{(i)}$ or $\varepsilon Hf_{(i)}$ values that argue for a depleted origin (Gruau et al., 1987; Murphy et al., 2021; Puchtel et al., 2021). The link between these observations are still poorly understood and hard to reconcile. Reasons for this finding could involve mantle mixing, early depletion, or a non-chondritic Earth (Caro et al., 2008; O'Neill and Palme, 2008; Caro and Bourdon, 2010; Campbell et al., 2012; Puchtel et al., 2021; Hofmann et al., 2022) and will be discussed in more detail in **Chapter I** and **Chapter III.**

III.5. Alteration

It is critical that the Archean rocks investigated to understand the early magmatic history of Earth have not been overprinted by secondary processes. Archean rocks are commonly exposed to weathering, hydrothermal fluid alteration, or subsequent metamorphic events that can severely overprint pristine magmatic features. Depending on different (fluid-) mobilities, certain elements can become highly mobile (such as large ion lithophile elements), whereas others remain (largely) immobile (such as REE or HFSE) (Polat and Hofmann, 2003). This is especially relevant for long-lived isotope systems, since radiogenic isotope compositions at the time of crystallization are back-calculated by using present day parent/daughter ratios. If the parent/daughter ratios were overprinted during post-

magmatic alteration, the decay corrections might become over- or underestimated, creating geologically meaningless isotope compositions that will lead to wrong models. As discussed above, ^{87}Rb-^{87}Sr and $^{235,238}U$-$^{207,206}Pb$ isotope systematics often experienced open system behavior during post-magmatic alteration, whereas ^{147}Sm-^{143}Nd and ^{176}Lu-^{176}Hf isotope systematics often remained unaffected. This is also crucial (although not yet well-documented) for ^{138}La-^{138}Ce isotope systematics, where the oxidation of Ce^{3+} to Ce^{4+} during terrestrial weathering makes this isotope system particularly vulnerable for post magmatic alteration (**Chapter I**).

Although Hf and Nd isotopes have been regarded as unaltered in many studies, the isotope compositions of mantle-derived rocks often stand in conflict with in-situ Hf isotopes from zircons, especially in the Pilbara Craton (Nebel et al., 2014; Petersson et al., 2019; Petersson et al., 2020; Murphy et al., 2021; Puchtel et al., 2021; Salerno et al., 2021; **Chapter I**). Since zircons are one of Earth's most durable and robust minerals, many studies investigating in-situ Hf isotopes from zircons have argued that the discrepancy between whole rocks and zircons is a consequence of altered whole rocks. However, due to the low Zr concentrations in mantle rocks (Palme and O'Neill, 2013), zircon crystals form in Zr enriched, felsic environments such as TTG melts. Such TTG melts are no primary mantle melts, but rather secondary melts from older precursor rocks (Hoffmann et al., 2011a; Hoffmann et al., 2014). Therefore, it remains ambiguous whether the inconsistencies between whole rocks and zircon isotope data reflect alteration processes or might be linked to petrological reasons (Liou et al., 2021).

In modern rocks, Hf-Nd isotopes show a strong coupling among different petrological rock types (clastic and chemical sediments, MORBs or OIBs) (Chauvel et al., 2008). Notably, rocks from some Archean cratons show Hf-Nd isotope characteristics that significantly deviate from this modern array. There are some Archean lithostratigraphic successions (such as the Weltevreden Formation of the Barberton Greenstone Belt or volcanic rocks from the Pilbara Craton) that are characterized by extremely positive $\varepsilon Hf_{(i)}$ values (at only slightly elevated $\varepsilon Nd_{(i)}$ values) (Blichert-Toft et al., 2015; Puchtel et al., 2016, **Chapter I**). In contrast, ~3.7 rocks from the Isua region show a different style of decoupled Hf-Nd isotopes, where most rocks have slightly positive and uniform $\varepsilon Hf_{(i)}$ values at strongly variable $\varepsilon Nd_{(i)}$ values (Hoffmann et al., 2010; Hoffmann et al., 2011; Rizo et al., 2011, **Chapter II**). The origin of decoupled Hf-Nd isotope patterns in many Archean rock successions remains ambiguous, but in many cases, alteration cannot be clearly ruled out. It is challenging to assess whether decoupled Hf-Nd isotope compositions represent the pristine Archean mantle or post-magmatic open system behavior. Clarifying this issue is of particular importance, since many geodynamic conclusions and models rely on long-lived isotope systematics (**Chapter II**).

III.6. A chondritic Earth?

The refractory, incompatible trace element composition of planetary bodies of the inner solar system still remains poorly understood. For many refractory lithophile elements, chondrites were regarded to best represent the bulk silicate Earth. Therefore, the

chondritic/primitive mantle composition is often used to normalize terrestrial rocks (Bouvier et al., 2008; Palme and O'Neill, 2013; Israel et al., 2019; Willig and Stracke, 2019). Although most refractory trace elements ratios are near-constant in various chondrite classes, some elemental-isotopic constraints have provided evidence for a non-chondritic Earth. For example, the strongly coupled terrestrial Hf-Nd isotope array does not intersect the chondritic value. Although some interpreted this to result from the admixture of recycled oceanic sediments (Chauvel et al., 2008), other studies have interpreted this feature to provide evidence for a non-chondritic Earth (e.g., O'Neill and Palme, 2008; Caro and Bourdon, 2010).

In addition to the ambiguity of long-lived Hf-Nd isotope systematics, increasing analytical precision revealed a ~10 to 20 ppm excess for short-lived $^{142}Nd/^{144}Nd$ variations between Earth and enstatite and ordinary chondrites, respectively (Boyet and Carlson, 2005; Carlson et al., 2007; Gannoun et al., 2011; Burkhardt et al., 2016; Fukai and Yokoyama, 2017; Boyet et al., 2018; Fukai and Yokoyama, 2019; Saji et al., 2020). However, the origin of Earth's elevated $^{142}Nd/^{144}Nd$ compositions remains highly debated and two explanations have been held responsible for these observations, either advocating nucleosynthetic variations or a non-chondritic Earth.

The first explanation suggests that different chondrite classes (enstatite, ordinary and carbonaceous chondrites) all inherited different amounts of s-process material, with enstatite chondrites being most enriched in s-process material whereas carbonaceous chondrites are most depleted in that component (Gannoun et al., 2011; Boyet and Gannoun, 2013; Burkhardt et al., 2016; Fukai and Yokoyama, 2017; Boyet et al., 2018; Fukai and Yokoyama, 2019) (Fig. III.1). Although enstatite chondrites were found to show the closest similarities with Earth for many isotope systematics (such as Ti or Cr) (Trinquier et al., 2007; Trinquier et al., 2009), this most Earth-like chondrite class displays a $^{142}Nd/^{144}Nd$ composition that is still ~10 ppm lower than that of Earth (e.g., Boyet and Gannoun, 2013; Boyet et al., 2018). Accordingly, it was suggested that Earth was accreted from material with an s-process excess (Burkhardt et al., 2016). Since such s-process excess material has not been found so far, it is assumed that it was fully consumed during accretion and therefore no longer exists. However, the difference between Earth and a modelled s-process mixing line defined by chondrites remains ambiguous since none of the aforementioned studies have calculated statistically robust best fits that could provide numerical estimations for minimum or maximum differences between Earth and chondrites (**Chapter III**). More recently, Saji et al. (2020) have reported Nd isotope data for chondrites and concluded that Earth does not fall on the predicted s-process mixing line. The findings by Saji et al. (2020) contradict a pure s-process mixing model and rather suggest that the difference between Earth and chondrites reflects a p-process excess for material proto-Earth accreted from.

Alternatively, the superchondritic model suggests that Earth experienced a loss of enriched silicate material that formed within an earlier differentiation event (Boyet and Carlson, 2006; Caro et al., 2008; O'Neill and Palme, 2008; Brandon et al., 2009a; Brandon et al., 2009b; Caro and Bourdon, 2010; Gannoun et al., 2011; Qin et al., 2011). In the so-called depleted or superchondritic Earth model (superchondritic refers to its elevated $^{147}Sm/^{144}Nd$

ratios), Earth experienced an early (≥4.5 Ga) differentiation that created enriched and depleted reservoirs (Boyet and Carlson, 2005; Bennett et al., 2007; O'Neill and Palme, 2008; Caro and Bourdon, 2010). Subsequently, the early enriched reservoir was partly removed, either stored away in a hidden reservoir (Boyet and Carlson, 2006; Bennett et al., 2007) or ultimately lost by collisional erosion during accretion (O'Neill and Palme, 2008). In either way, the early enriched reservoir was no longer able to interact with the remaining part of Earth's mantle and is no longer accessible. Given that there is evidence for early silicate differentiation on Mars (as early as 20-30 Ma after solar system formation, (Foley et al., 2005; Kruijer et al., 2017), it seems reasonable to assume that differentiation processes on other terrestrial planets like Earth have started similarly early (**Chapter III**). Notably, the p-process excess model as well as the superchondritic Earth model would only create elevated $^{142}Nd/^{144}Nd$ compositions, without affecting other mass independent Nd isotopes. This means that these two processes are not distinguishable by mass independent Nd isotopes alone and other isotope systems must be involved. In **Chapter III**, the incompatible trace element composition of the Earth-Moon system is deduced from an independent long-lived ^{138}La-^{138}Ce and ^{147}Sm-^{143}Nd isotope approach to finally clarify whether or not the Earth and Moon are chondritic.

IV. Chapter overview

This thesis provides new insights into long- and short-lived REE-related decay series currently applied to geochemical issues, namely ^{138}La-^{138}Ce, ^{147}Sm-^{143}Nd, ^{176}Lu-^{176}Hf, and ^{146}Sm-^{142}Nd. In **Chapter I**, we present the first study that reports coupled ^{138}La-^{138}Ce, ^{147}Sm-^{143}Nd, and ^{176}Lu-^{176}Hf isotope compositions of Archean rocks. The analyzed samples display a wide range of predominantly (ultra-) mafic mantle-derived but also some crustal rocks from the Pilbara Craton, NW Australia. These rocks span crystallization ages of almost 1000 Ma of near-continuous mafic volcanism. Our reported isotope composition of (ultra-) mafic rocks provide new constraints on the temporal evolution of the Archean mantle and the involved mantle reservoirs.

In **Chapter II**, a new analytical protocol for separating and measuring high precision Nd isotope compositions was developed. This new method allows us to determine ^{142}Nd/^{144}Nd anomalies accurately and precisely, even in the lower ppm level. In a next step, we combine this method with long-lived ^{147}Sm-^{143}Nd isotope systematics and apply it to Archean rocks from the Isua supracrustal belt, SW Greenland. By combining these two isotope systems, we are able to calculate differentiation model ages for the Isua mantle source. Further, we infer mantle homogenization times that can explain the disappearance of ^{142}Nd/^{144}Nd anomalies by the end of the Archean.

In **Chapter III**, we report the first coupled ^{138}La-^{138}Ce, ^{147}Sm-^{143}Nd isotope data and trace element data for lunar rocks. This chapter places new constraints on whether the Earth-Moon system is chondritic or not. After carefully investigating whether our data was significantly affected by neutron capture processes on the lunar surface, we incorporate our data into the existing framework of literature Hf-Nd isotope data. In order to reconcile the observational Hf-Nd-Ce isotope constraints, we conduct refractory lithophile trace element and Hf-Nd-Ce isotope modelling. In our model, we calculate a hypothetical lunar composition that is required to explain the existing Hf-Nd-Nd isotope and trace element constraints. In a next step, we examine whether this composition also represents the terrestrial lithophile refractory trace element composition.

Chapter I

1. Evolution of the early to late Archean mantle from Hf-Nd-Ce isotope systematics in basalts and komatiites from the Pilbara Craton

1.1. Abstract

Inferences on the early evolution of the Earth's mantle can be deduced from long-lived radiogenic isotope systems such as ^{176}Lu-^{176}Hf and ^{147}Sm-^{143}Nd, for which both parent and daughter elements largely remain immobile at low metamorphic grades. However, it remains ambiguous when and to what extent mantle-crust differentiation processes had started in the Archean. For a better understanding of Archean mantle-crust evolution, we determined the initial ^{176}Lu-^{176}Hf, ^{147}Sm-^{143}Nd, and, in a new approach, the ^{138}La-^{138}Ce isotope compositions of a suite of Archean mafic-ultramafic rock samples from the 3.53-2.83 Ga old Pilbara Craton and 2.78-2.63 Ga old Fortescue Group in NW Australia. These rocks represent one of the best-preserved Archean successions worldwide and contain mafic-ultramafic rocks that were erupted during repeated and long-lived pulses of volcanism throughout much of the Archean. Mantle-derived mafic-ultramafic rock samples were collected from six major stratigraphic groups of the Pilbara Craton and the overlying Fortescue Group in order to characterize the parental mantle source regions of the lavas and to reconstruct the temporal evolution of the ambient mantle beneath this piece of cratonic lithosphere. In addition, we analyzed contemporaneous TTG-like igneous suites and interbedded sediments in order to reconstruct the lithospheric evolution of the Pilbara Craton.

The Hf-Nd-Ce isotope data imply the onset of mantle-crust differentiation in the Pilbara Craton as early as ~4.2 Ga, well prior to any of the preserved stratigraphy. Within error, coupled Ce-Nd-Hf isotope arrays all intersect chondritic values, implying that the Earth is of broadly chondritic composition, also for the ^{138}La-^{138}Ce isotope system. Mafic rocks usually yield strongly coupled $\varepsilon Hf_{(i)}$, $\varepsilon Nd_{(i)}$ and $\varepsilon Ce_{(i)}$ values that form a mixing line between an evolving depleted upper mantle composition and the primitive mantle value ($\varepsilon Hf_{(i)}$ ca. 0.0 to + 3.2, $\varepsilon Nd_{(i)}$ ca. +0.2 to +1.7 and $\varepsilon Ce_{(i)}$ ca. +0.3 to -0.1). As all Paleoarchean samples lack co-variations between Nb/Th with $\varepsilon Hf_{(i)}$ or $\varepsilon Nd_{(i)}$, contamination with an enriched crust is unlikely to explain this mixing trend. The most primitive mantle-like mafic samples show elevated Gd_N/Yb_N ratios (2.2-1.4), implying the involvement of a deep-rooted, near-primitive, upwelling mantle that was progressively mixed into the depleted upper mantle.

In contrast to the mafic rocks, most, but not all komatiites are decoupled in their initial Hf-Nd-Ce isotope compositions, by having extremely radiogenic $\varepsilon Hf_{(i)}$ values at only moderately high $\varepsilon Nd_{(i)}$ and low $\varepsilon Ce_{(i)}$ values. This decoupling is best explained by the assimilation of mantle domains that underwent early melt depletion in the garnet stability field and evolved at high $^{176}Lu/^{177}Hf$ ratios but at moderate $^{147}Sm/^{144}Nd$ and $^{138}La/^{136}Ce$ ratios over time. The disappearance of rocks with decoupled Hf-Nd isotope compositions after ~3.2 Ga is likely linked to decreasing mantle temperatures that were no longer able to melt such refractory mantle domains. Collectively, our new data for mafic rocks from the Pilbara Craton confirm the presence of long-term depleted mantle domains in the early Archean that are not sampled by the zircon Hf isotope record in the Pilbara Craton.

1.2. Introduction

The ^{176}Lu-^{176}Hf and ^{147}Sm-^{143}Nd decay systems have become key analytical tools for reconstructing the early depletion history of the terrestrial mantle due to their robustness (e.g., Bennett et al., 1993; Vervoort and Blichert-Toft, 1999; Hoffmann et al., 2011b). In contrast, the ^{138}La-^{138}Ce system has only rarely been applied to the early terrestrial rock record, because the slow radiogenic decay of ^{138}La to ^{138}Ce ($\lambda=2.37\times10^{-12}$ a^{-1}) and limited fractionation of La/Ce in igneous systems result in small Ce isotope variations that are analytically difficult to resolve. During mantle-crust differentiation, Lu and Sm are more compatible in the mantle compared to Nd and Hf, whereas La is more incompatible in the mantle compared to Ce. Thus, depleted mantle domains will evolve towards positive initial $\varepsilon Hf_{(i)}$ and $\varepsilon Nd_{(i)}$, but towards negative $\varepsilon Ce_{(i)}$ values. Hence, ^{138}La-^{138}Ce systematics could, in principle, be applied to similar geochemical issues as the ^{176}Lu-^{177}Hf or ^{147}Sm-^{144}Nd systems. As a consequence, combined Ce-Nd-Hf isotope studies can place further constraints on early Earth differentiation processes such as the observed decoupling of Hf-Nd isotopes in Archean rocks (e.g. Hoffmann et al., 2011b; Rizo et al., 2011).

The Pilbara Craton is an excellent example to study the evolution of mantle-crust differentiation processes on early Earth, due to long-lived volcanic pulses of mafic-ultramafic volcanism (Van Kranendonk et al., 2002). For other cratons, such as the North Atlantic Craton, mantle evolution processes have been complicated by secondary metamorphic events, which can disturb the Hf-Nd isotope signatures of such highly metamorphosed rocks (e.g. Gruau et al., 1996; Hoffmann et al., 2011b). In contrast, the majority of rocks from the Pilbara Craton have only been affected by low-grade metamorphism, largely at lower greenschist facies and only locally at amphibolite facies conditions (Collins and Van Kranendonk, 1999; Van Kranendonk et al., 2002). Although there exist other cratons that contain older rocks, the well-preserved and low metamorphic grade lithostratigraphic successions in the Pilbara Craton provide a near-continuous record of igneous evolution for almost a billion years of Earth history, from 3.59-2.63 Ga (e.g., Van Kranendonk et al., 2002; Smithies et al., 2007a; Petersson et al., 2019).

Based on predominantly positive $\varepsilon Nd_{(i)}$ values, many studies on Pilbara mafic-ultramafic rock samples suggest a moderately depleted mantle reservoir as a source for the dominantly mafic-ultramafic greenstone belt stratigraphy (e.g., Gruau et al., 1987; Arndt et

al., 2001; Smithies et al., 2007b). However, previously reported Hf isotope data challenged these interpretations (Nebel et al., 2014; Kemp et al., 2015; Petersson et al., 2019; Petersson et al., 2020). For example, studies on zircons by Kemp et al. (2015) and Petersson et al., (2019, 2020) argued that the mantle beneath the Pilbara Craton did not start to differentiate until ~3.6 Ga. In contrast Nebel et al. (2014) reported extremely radiogenic $\varepsilon Hf_{(i)}$ values in ~3.5-3.2 Ga komatiites, which requires a highly depleted mantle reservoir to have been present already in the Hadean, a conclusion previously also reached by Tessalina et al. (2010).

In this study, we present high-precision isotope dilution (ID) and isotope composition data for ^{176}Lu-^{176}Hf, ^{147}Sm-^{143}Nd and ^{138}La-^{138}Ce on a variety of rock samples from the Pilbara Craton in order to better understand the long-term depletion history of the ambient mantle beneath the evolving Pilbara Craton and the early Archean mantle in general. We analyzed 39 basalts and komatiites, five granitoids, and three sedimentary rocks that were previously studied by Tusch et al., (2021)for their major and trace element data, as well as for their ^{182}W isotope systematics. Furthermore, we analyzed six basalts from the Jeerinah Formation that were provided by the Geological Survey of Western Australia, as well as ten komatiites that were previously studied by Maier et al. (2009) for platinum group element (PGE) concentrations. In total, we present combined ^{176}Lu-^{176}Hf and ^{147}Sm-^{143}Nd systematics on 63 mantle-derived rocks, granitoids, and sediments. For a better understanding of the ^{138}La-^{138}Ce system in the Archean, we also report ^{138}La-^{138}Ce data for a subset of 40 of these samples. The data are evaluated with an emphasis on the temporal evolution of the Archean mantle and source domain characteristics.

1.3. Geological setting

The Pilbara Craton is located in the northwestern part of Western Australia and is composed of several distinct litho-tectonic terranes that contain thick successions of mafic-ultramafic and felsic volcanic rocks (Van Kranendonk et al., 2007). The volcanic rocks erupted in several episodes lasting from at least 3.59-2.63 Ga, accompanied by pulses of granitic magmatism over the range of 3.49-2.83 Ga. Typical dome-and-keel structures are preserved in the Paleoarchean nucleus of the East Pilbara Terrane (EPT) (Fig. 1.1) (Van Kranendonk et al., 2004). The oldest unambiguous evidence for magmatic activity in the Pilbara Craton is provided by 3.7-3.8 Ga inherited zircons (Van Kranendonk et al., 2002; Kemp et al., 2015) and recently Petersson et al. (2019) have identified gabbroic enclaves (3.59-3.58 Ga Mount Webber Gabbro) that may be remnants of a mafic proto-crust.

Between ca. 3.53 and 3.23 Ga, cycles of mafic-ultramafic volcanism dominated the evolution of the EPT, deposited in three unconformity-bound groups: the ca. 3.53-3.43 Ga Warrawoona Group, the ca. 3.35-3.32 Ga Kelly Group and the 3.27-3.235 Ga Sulphur Springs Group (Van Kranendonk et al., 2007; Hickman, 2012). From the increasingly thickened mafic crust, partial melts escaped and formed repeated generations of felsic intrusions (Smithies et al., 2007a; Van Kranendonk, 2010; Wiemer et al., 2018). The thickened mafic crust also acted as a thermal incubator, thus softening the middle crust

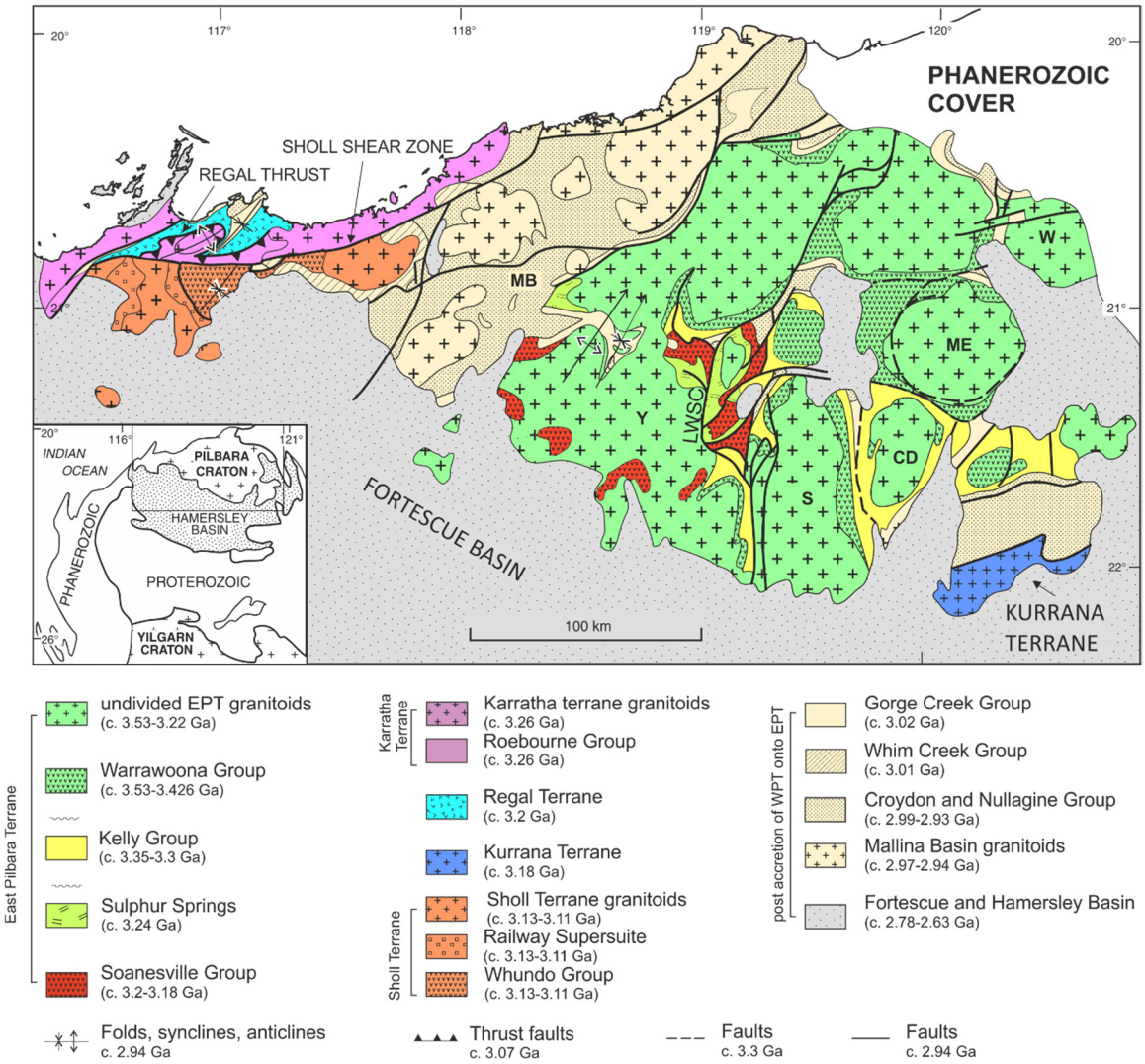

Fig. 1.1: Simplified geological map of the northern Pilbara Craton. Shown are greenstones and granitoids of the East Pilbara Terrane, Kurrana Terrane, Karratha Terrane, Regal Terrane, Sholl Terrane and the late volcano-sedimentary Mallina Basin and De Grey Supergroup (MB=Mallina Basin; MCB=Mosquito Creek basin) and Fortescue Basin. Abbreviations for different granitoids that were sampled in this study: CD=Corunna Downs; ME=Mount Edgar; S=Shaw; W=Warrawagine; Y=Yule. Modified after Van Kranendonk et al., (2007a), (2010).

and causing gravitational instabilities (e.g., Collins and Van Kranendonk, 1999; Wiemer et al., 2018). During gravitational collapse, the negatively buoyant overlaying mafic crust sank into the middle crust, which, in turn, caused the rise of felsic domes and the typical dome-and-keel geometry (Collins and Van Kranendonk, 1999; Van Kranendonk et al., 2004; Wiemer et al., 2018).

At ~3.2 Ga, plume-initiated rifting separated the Kurrana and Karratha terranes from the EPT, which led to the eruption of the 3.18 Ga Soanesville Group and the contemporaneous Dalton Suite of intrusive layered mafic-ultramafic rocks in the EPT (Van Kranendonk et al., 2007a, 2010). This rifting event was recently interpreted in favor of the onset of Phanerozoic-style late tectonics, and the tectono-magmatic history of the craton between 2.9 and 3.2 Ga was interpreted to represent a full Wilson cycle (Van Kranendonk et al., 2010). This also includes the ~3.12 Ga Whundo Group volcanics that provide evidence for subduction-related volcanism in the Pilbara Craton (Smithies et al., 2007c). Between 3.07 to 2.91 Ga, the West Pilbara Superterrane (WPS), the EPT, and the southeastern Kurrana Terrane accreted during three orogenic events (Van Kranendonk et al., 2007), followed by

deposition of the 3.02-2.92 Ga De Grey Supergroup in an extensional basin (Van Kranendonk et al., 2007; Hickman, 2012) that was coeval with 2.935 Ga granitoid intrusions of the Yule Granitic Complex. Volcanic rocks from the De Grey Supergroup show strongly enriched geochemical characteristics indicating enriched, metasomatized mantle sources of possible lithospheric mantle origin (Smithies et al., 2004).

Deposition of the 2.78-2.63 Ga Fortescue Group followed cratonization of the Pilbara Craton, which was completed by the emplacement of ca. 2.83 granitoid rocks (Van Kranendonk et al., 2007). The dominantly continental flood basaltic lavas of the Fortescue Group were fed by a series of large feeder dikes, including the 2.78 Ga Black Range dolerite suite that erupted lavas of the lowermost Mount Roe basalt (Arndt et al., 2001; Thorne and Trendall, 2001). The Fortescue Group lavas originated from plume-generated komatiite volcanism that was contaminated by older crustal basement, in a similar way to Phanerozoic large igneous provinces (Mole et al., 2018).

1.4. Methods

Analyses were performed on powder aliquots from 2-3 kg of rock sample grounded in an agate mill. For Ce, Nd, and Hf measurements, 120-1200 mg of sample powder were digested in Parr© bombs. For Sm/Nd and Lu/Hf measurements, mixed ^{149}Sm-^{150}Nd and ^{176}Lu-^{180}Hf isotope tracers were added prior to digestion following previously described protocols (Münker et al., 2001; Hoffmann et al., 2011a). For La-Ce (ID) measurements, a 20% aliquot was spiked with a ^{138}La-^{142}Ce isotope tracer after sample digestion. For isotope analysis we additionally added 1 ml of 65% $HClO_4$ to some replicates after Parr© bomb digestions to prevent the formation of insoluble rare-earth elements (REE) and high field strength (HFSE)-fluorides although addition of $HClO_4$ did not have an effect on the results of concentration or isotope measurements (Appendix A1). Lutetium-Hf separation was performed following the analytical protocol of Münker et al. (2001). The light rare-earth element (LREE)-bearing matrix from Lu-Hf separation as well as the 20% La-Ce ID aliquot were processed after Schnabel et al. (2017). The leftover REE cut was then processed through Ln Spec resin after Pin and Zalduegui (1997) to obtain pure Sm and Nd fractions. Total procedural blanks were always <150 pg for Ce, <100 pg for La, <39 pg for Nd, <19 pg for Sm, and <140 pg for Hf and Lu, respectively, and were all negligible.

All ID and isotope composition measurements were performed on a Thermo Fischer Neptune© or a Thermo Fischer Neptune Plus© MC-ICP MS at Cologne. Lanthanum-Ce measurements were performed following the protocol of Schnabel et al. (2017), but for Ce isotope composition measurements, $10^{12}\Omega$ amplifiers were replaced by $10^{13}\Omega$ amplifiers. Mass bias correction was performed by using the exponential law and a ^{136}Ce/^{140}Ce=0.002124072 (Makishima and Nakamura, 1991). All Ce data are reported relative to the Mainz-AMES standard solution (^{138}Ce/^{136}Ce=1.33738) (Willbold, 2007). The tailing effect of ^{140}Ce on ^{136}Ce and ^{138}Ce was recorded by measuring the ratios of half-masses relative to the peak mass (Willbold, 2007), but tail contributions on ^{138}Ce were always in the sub-ppm range (e.g., Schnabel et al., 2017). For Ce ID measurements, Ba was used for mass bias correction assuming a ^{137}Ba/^{135}Ba ratio of 1.70383, whereas for La ID measurements, Nd was used for mass bias correction (^{146}Nd/^{144}Nd=0.7219). The external

reproducibility for $^{138}Ce/^{136}Ce$ ratios is given as relative standard deviation (RSD) and amounts to ±21 ppm (2 RSD), based on multiple measurements (n=13) of six digestions of the reference material BHVO-2.

Neodymium isotope compositions are reported relative to a $^{143}Nd/^{144}Nd$ value of 0.511859 for La Jolla standard. Mass bias correction followed the exponential law using a $^{146}Nd/^{144}Nd$ of 0.7219. The external long-term reproducibility of Nd isotope measurements amounts to ±40 ppm (2 RSD) (cf. Marien et al., 2019). Hafnium isotope compositions are given relative to the Münster AMES standard, having a $^{176}Hf/^{177}Hf$ ratio of 0.282160 (Münker et al., 2001). All measured $^{176}Hf/^{177}Hf$ isotope data were mass bias corrected by using the exponential law and a $^{179}Hf/^{177}Hf$ of 0.7325. Mass bias correction for Lu measurements was performed by using a $^{173}Yb/^{171}Yb$ ratio of 1.29197. The external long-term reproducibility of $^{176}Hf/^{177}Hf$ analysis amounts to ±40 ppm (cf. Marien et al., 2019). The external reproducibilities on $^{138}La/^{136}Ce$ $^{147}Sm/^{144}Nd$ and $^{176}Lu/^{177}Hf$ amount to ≤0.2% (2 RSD). Calculated errors on our reported initial Hf-Nd-Ce isotope compositions represent the propagated errors of the parent/daughter ratio, the age uncertainty and the external reproducibility given by multiple digestions of reference materials.

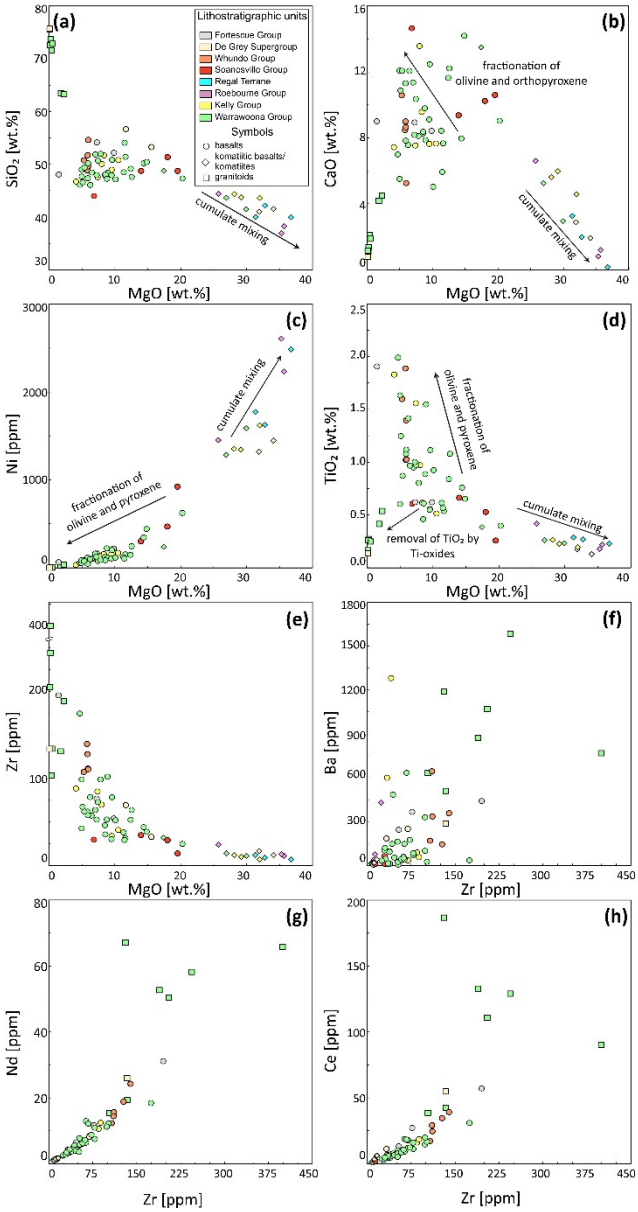

Fig. 1.2: Co-variation diagrams for selected major and trace elements in mafic-ultramafic to felsic Pilbara Craton samples. a) - e) Selected major and trace elements plotted against MgO demonstrate the preservation of pristine igneous fractionation trends. f) Barium vs. Zr plot illustrating post-magmatic disturbances of large ion lithophile elements. g) and h) show preserved igneous trends for Ce, Nd and Hf (not shown) with Zr, implying that the elements relevant for radiogenic isotope measurements have preserved their pristine igneous composition. Shown symbols also include data from Maier et al., (2009) and Tusch et al., (2021) for samples that were also analyzed in this study.

1.5. Results

1.5.1. Major and trace element compositions

Major and trace element data for mafic-ultramafic samples of the ~3.53-3.31 Ga Warrawoona and Kelly groups are broadly consistent with previously reported data for

rocks from the EPT (Smithies et al., 2007a; Smithies et al., 2018). For mafic-ultramafic samples, MgO contents generally vary between 4.11-29.2 wt.% (Fig. 1.2) (see for further information on major and trace element data). The concentrations of SiO_2 (43.7-54.1 wt.%), TiO_2 (0.218-2.00), and Al_2O_3 (4.88-14.9 wt.%) also vary significantly (Fig. 1.2). Primitive mantle normalized trace element patterns of these samples are predominantly flat, as indicated by moderate La/Yb_{CN} (0.546-3.32) and Gd/Yb_{PM} ratios (0.851-1.93) (Fig. 1.3). Some mafic samples show minor depletions of Nb and Ta compared to La (Nb/La=0.568-1.14) (Fig. 1.3). Ratios of Th/Yb are often lower (0.0535-0.697) when compared to previously published data for EPT samples (Smithies et al., 2018). In most samples, Ce anomalies are absent (Ce/Ce*=0.917-1.17), whereas Eu anomalies occur more frequently and range from 0.754-1.59.

The younger (c. 3.2 Ga) samples of the Soanesville Group, Dalton Suite, and Roebourne Group show similar MgO (6.84-25.7 wt.%), Al_2O_3 (2.44-10.2 wt.%) and SiO_2 contents (40.0-51.4 wt.%) compared to the older Warrawoona and Kelly Group samples, but exhibit significantly lower TiO_2 contents (0.170-0.656 wt.%) (Fig. 1.2). Furthermore, these samples show depletions of LREE over heavy rare-earth elements (HREE), as indicated by lower La/Yb_{CN} (0.761-4.27), and predominantly superchondritic Sm/Nd ratios (0.229-0.372) as previously described (Smithies et al., 2007a, 2018). Compared to the older Warrawoona and Kelly Group samples, Th/Yb (0.0834-0.229) are lower, Nb/La ratios define a narrower range (0.464-0.738), and Eu and Ce anomalies are largely absent (Ce/Ce*=0.962-0.990; Eu/Eu*=0.963-1.27).

Samples of the ~3.12-2.63 Ga Whundo Group, De Grey Supergroup, and the Fortescue Group show generally the highest SiO_2 (48.8-56.7 wt.%) and Al_2O_3 (9.29-15.6 wt.%) contents and the lowest MgO (5.29-15.6 wt.%), excluding two ultramafic rocks from the De Grey Supergroup (MgO>30 wt.%) (Fig. 1.2). Samples of the De Grey Supergroup have the

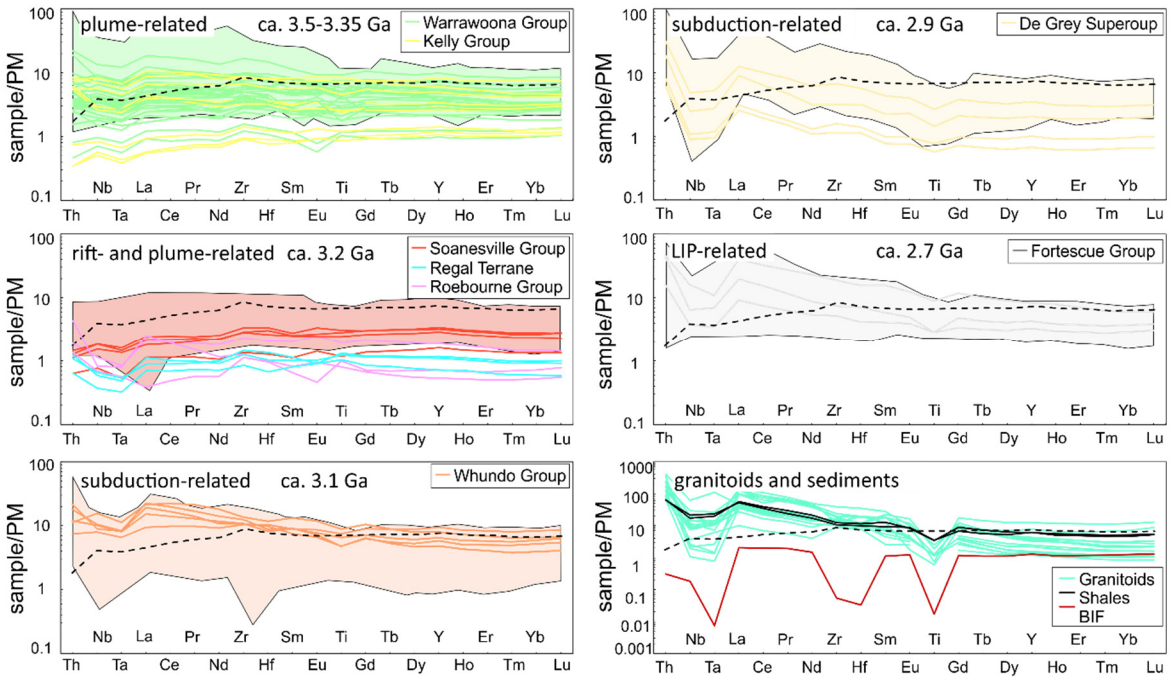

Fig. 1.3: Primitive mantle (PM) normalized incompatible trace element patterns for selected stratigraphic units, rock types, and geological settings. Additional data from Tusch et al., (2021) for samples that were also analyzed in this study. Colored fields represent compiled literature data. Additional data from Smithies et al., (2018). Primitive mantle after Palme and O'Neill, 2013 and dashed line represents MORB after White and Klein, (2013).

highest incompatible trace element concentrations, including substantial LREE enrichments relative to HREE (La/Yb_{CN}=3.21-4.53) (Fig. 1.3). Significant depletions of Nb-Ta compared to La are present in most of these lithostratigraphic units (Nb/La=0.246-0.823), although the most pronounced and uniform Nb-Ta anomalies are found in the basalts and komatiites of the De Grey Supergroup (Nb/La=0.246-0.339). The oldest (~2.78 Ga) Fortescue Group samples are also characterized by low Nb/La ratios (0.29-0.36) and incompatible trace element patterns that are enriched in more incompatible trace elements (La/Yb_{CN}=1.09-9.19). These samples stand in marked contrast to the youngest (~2.63 Ga) Fortescue Group samples (Jeerinah Formation) that have predominantly flat primitive mantle normalized incompatible trace element patterns (La/Yb_{CN}=1.2-8.9) (Fig. 1.3).

1.5.2. Radiogenic isotopes

A total of 63 samples were analyzed for their ^{176}Lu-^{176}Hf and ^{147}Sm-^{143}Nd isotope compositions and a subset of 40 samples were analyzed for their ^{138}La-^{138}Ce isotope compositions (see Appendix A1). Age-corrected $\varepsilon Hf_{(i)}$ and $\varepsilon Nd_{(i)}$ values were normalized to the CHUR value of Bouvier et al. (2008) and $\varepsilon Ce_{(i)}$ values were normalized to the CHUR value of Willig and Stracke (2019) and Israel et al., (2019), giving combined $^{138}La/^{136}Ce$ and $^{138}Ce/^{136}Ce$ ratios of 0.1865 and 1.336878, respectively.

Initial $\varepsilon Hf_{(i)}$ values of EPT basalts range from 0.0 to +4.2 (excluding sample Pil16-24 having an $\varepsilon Hf_{(i)}$ value of +7.4), whereas komatiites tend to have higher $\varepsilon Hf_{(i)}$ values (+1.5 to +8.1; see Appendix A1), in accordance with previous observations by Nebel et al. (2014). Notably, negative $\varepsilon Hf_{(i)}$ and $\varepsilon Nd_{(i)}$ values were only found in the youngest samples (De Grey

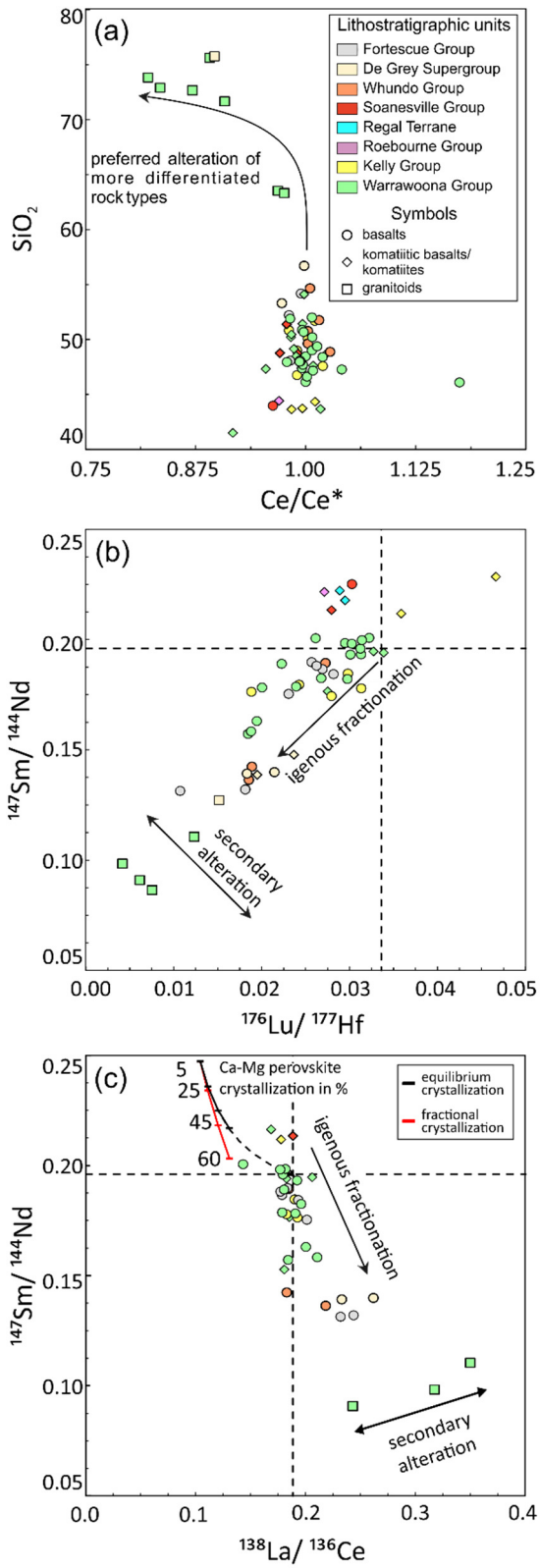

Fig. 1.4: Plots illustrating alteration features in Pilbara rocks. a) Ce/Ce* anomalies increase with increasing SiO_2. b) and c) co-variations of parent/daughter ratios of relevant radiogenic isotope systems indicate, that the majority of samples have preserved their pristine magmatic geochemistry. Additional data from Tusch et al., (2021) for samples that were also analyzed in this study.

Supergroup and Fortescue Group; $\varepsilon Hf_{(i)}$=-2.7 to +5.0; $\varepsilon Nd_{(i)}$=-2.8 to + 3.2). Felsic to intermediate granitic samples of various age yield diverse $\varepsilon Hf_{(i)}$ values (-5.8 to +2.0) and $\varepsilon Nd_{(i)}$ values (-6.3 to +1.3) that are in good agreement with previously reported zircon data (e.g., Kemp et al., 2015; Gardiner et al., 2017; Petersson et al., 2019).

The majority of our samples display negative initial $\varepsilon Ce_{(i)}$ values. Samples without Ce/Ce* anomalies (Fig. 1.4) yield a narrow range in initial $\varepsilon Ce_{(i)}$ values (-0.4 to +0.61), whereas samples with Ce/Ce* anomalies show a significantly higher scatter in $\varepsilon Ce_{(i)}$ values (-7.4 to + 2.3). Generally, all three isotope systems consistent trends between 3.53 Ga and 2.63 Ga, where $\varepsilon Hf_{(i)}$ and $\varepsilon Nd_{(i)}$ broadly increase between 3.5-3.2 Ga, although the majority of 3.34 Ga basalt samples of the Kelly Group deviate towards slightly more unradiogenic values (Fig. 1.5). Cerium isotopes show a complementary trend, with decreasing $\varepsilon Ce_{(i)}$ values between 3.5-3.2 Ga and a slight increase at 3.34 Ga. Between ca. 2.9-2.7 Ga, $\varepsilon Hf_{(i)}$ and $\varepsilon Nd_{(i)}$ decrease sharply, while $\varepsilon Ce_{(i)}$ values increase slightly. The 2.63 Ga Jeerinah Formation deviates from that trend by showing significantly higher $\varepsilon Hf_{(i)}$ and $\varepsilon Nd_{(i)}$, as well as lower $\varepsilon Ce_{(i)}$ values.

1.6. Discussion

1.6.1. Alteration and its effects on radiogenic isotope systematics

Rocks from the Pilbara Craton have experienced a complex geological history, including hydrothermal alteration and metamorphism that subsequently modified the pristine geochemistry of these rocks (Collins and Van Kranendonk, 1999; Van Kranendonk et al., 2002). Thus, it is crucial to evaluate whether the samples analyzed in this study have preserved their primary REE and HFSE budgets. HFSE, Th, and REE display significant co-variations with Zr, indicating that these elements have not been substantially mobilized by secondary processes (Fig. 1.2) (see also Polat et al., 2002). Cerium anomalies in mafic samples are always smaller than 5% (excluding sample Pil16-44a: Ce/Ce*=1.2 and sample 179757: Ce/Ce*=0.92), indicating that the LREE were not substantially mobilized during secondary geological events (Fig. 1.4a) (Polat et al., 2002). Similar to previous studies on Archean rocks (e.g. Vervoort and Blichert-Toft, 1999; Nebel et al., 2014), initial $\varepsilon Hf_{(i)}$ and $\varepsilon Nd_{(i)}$ values (and also $\varepsilon Ce_{(i)}$ values) show a coherent evolution through time (Fig. 1.5). Furthermore, there are no co-variations between $\varepsilon Hf_{(i)}$, $\varepsilon Nd_{(i)}$, and $\varepsilon Ce_{(i)}$ and loss on ignition (LOI) and all three parent/daughter ratios correlate with each other, indicating primary magmatic trends (Figs. 1.4b and 1.4c). In contrast, all large ion lithophile elements were mobile during post-magmatic events, as suggested by poor correlations with Zr (Fig. 1.2f).

In marked contrast to the mafic rocks, most granitoids display negative Ce/Ce* anomalies, as low as 0.835, that increase with increasing SiO_2 (Fig. 1.4a). This is surprising, as the granitoids studied have preserved a seemingly pristine mineralogy and have very low LOIs (<1.5 wt %). The Ce/Ce* anomalies imply that the granitoids are prone to disturbance of the ^{138}La-^{138}Ce system, likely during oxidative weathering, where Ce^{4+} can become decoupled from the other REE^{3+}. We speculate that altered mafic volcanic rocks are less susceptible to terrestrial weathering than granites, as the mafic volcanics contain high amounts of

secondary minerals (e.g., chlorite serpentine, epidote and amphibole) that might be more robust during oxidative terrestrial weathering.

The coupled behavior of $\varepsilon Hf_{(i)}$, $\varepsilon Nd_{(i)}$, and $\varepsilon Ce_{(i)}$ in mafic-ultramafic Pilbara rocks over time (Fig. 1.5) also argues against secondary alteration effects, as the three studied radioactive decay systematics should be variably affected by secondary alteration (e.g., Polat et al., 2002). Most importantly, all whole rock ^{147}Sm-^{143}Nd and ^{176}Lu-^{176}Hf (and ^{138}La-^{138}Ce) age regression lines for individual units yield ages which overlap within error with the reported stratigraphic ages for the formations from which they were sampled (supplementary Figs. 1.1-1.3, Appendix A1). Thus, we conclude that the initial Hf-Nd-Ce isotope compositions determined in this study are sufficiently robust to constrain the depletion history of the Archean mantle beneath the Pilbara Craton, although ^{138}La-^{138}Ce data for samples with Ce/Ce* anomalies are regarded as altered.

1.6.2. Effects of crustal contamination

Crustal contamination can strongly affect radiogenic isotope compositions and consequently obscure the information on parental mantle sources. The oldest mafic-ultramafic samples in our study (3.53-3.18 Ga) show a broad range of $\varepsilon Hf_{(i)}$ and $\varepsilon Nd_{(i)}$, correlating with La/Yb (Fig. 1.6f) but not with Nb/Th (Fig. 1.6d). This implies that the magmatic source mixed with a second isotopically heterogeneous component, but this was unlikely continental crust as it has characteristically low Nb/Th ratios. Similar co-variations are also expected for Ce isotopes, but such changes are not easily analytically resolvable. As most of the 3.53-3.18 Ga mafic samples also fall on the MORB-OIB array in Th/Yb vs. Nb/Yb space (Fig. 1.6a), it seems more plausible that the two components involved were primitive mantle-like source and a more depleted mantle endmember.

Unlike the older mafic samples, younger units (De Grey Supergroup, Fortescue Group, and potentially the Whundo Group) show decreasing Nb/Th with decreasing $\varepsilon Hf_{(i)}$ (Fig. 1.6c). This observation is best explained by the interaction of primary melts with an enriched component, likely continental crust (Arndt et al., 2001; Mole et al., 2018), but possibly also mantle source enrichment (Smithies et al., 2005a).

1.6.3. Cerium isotope constraints

Although the ^{138}La-^{138}Ce system has so far only rarely been applied in geochemistry, it can put additional constraints on the implications that are drawn from combined ^{176}Lu-^{176}Hf and ^{147}Sm-^{143}Nd systematics, e.g. the origin of strongly decoupled Hf and Nd isotope compositions found in Archean mafic rock successions (Vervoort and Blichert-Toft, 1999; Vervoort et al., 2000; Hoffmann et al., 2011b). One process that was inferred for this decoupling is the fractionation of Ca-perovskite during magma ocean crystallization (e.g.,

Hoffmann et al., 2011b; Rizo et al., 2011). In the presence of perovskite, LREE can be strongly fractionated from Lu and Hf (Corgne and Wood, 2002; Corgne et al., 2005). In the lower mantle, the LREE are mainly affected by the fractionation of Ca- and Mg-perovskite that have $D_{La}<D_{Ce}$ and $D_{Sm}>D_{Nd}$, causing pervoskite cumulates to have superchondritic Sm/Nd ratios but subchondritic La/Ce ratios (Fig. 1.4c). Although Ca-perovskite is less abundant than Mg-perovskite, all the LREE are significantly more compatible in the former (D_{LREE} >1) than the latter phase (D_{LREE} <1). Lutetium and Hf show the opposite behavior during perovskite fractionation with D_{Lu}/D_{Hf} ~0.5 for Mg-perovskite, an d D_{Lu}/D_{Hf} ratio of >5 for Ca-perovskite (Corgne and Wood, 2002; Corgne et al., 2005). Consequently, early segregation of Ca- and Mg-perovskite would produce perovskite cumulates that exhibit lower La/Ce and higher Sm/Nd ratios compared to bulk silicate Earth, whereas the Lu/Hf ratio is variable, and strongly dependent on the fractions of Ca- and Mg-perovskite being crystallized (e.g., Hoffmann et al., 2011b; Rizo et al., 2011; Puchtel et al., 2016). Thus, early Ca-Mg-perovskite cumulates would evolve towards negative εCe values, positive εNd values, and variable εHf values.

To further quantify this process, we conducted trace element modeling, assuming crystallization of 4.5% Ca-perovskite, 85% Mg-perovskite, and 10.5% ferropericlase, in accord with previous estimates (e.g., Hoffmann et al., 2011b; Rizo et al., 2011; Puchtel et al., 2016) (see Appendix A1). Higher abundances of Ca-perovskite would generate extremely unradiogenic Hf isotope compositions over time, whereas lower Ca-

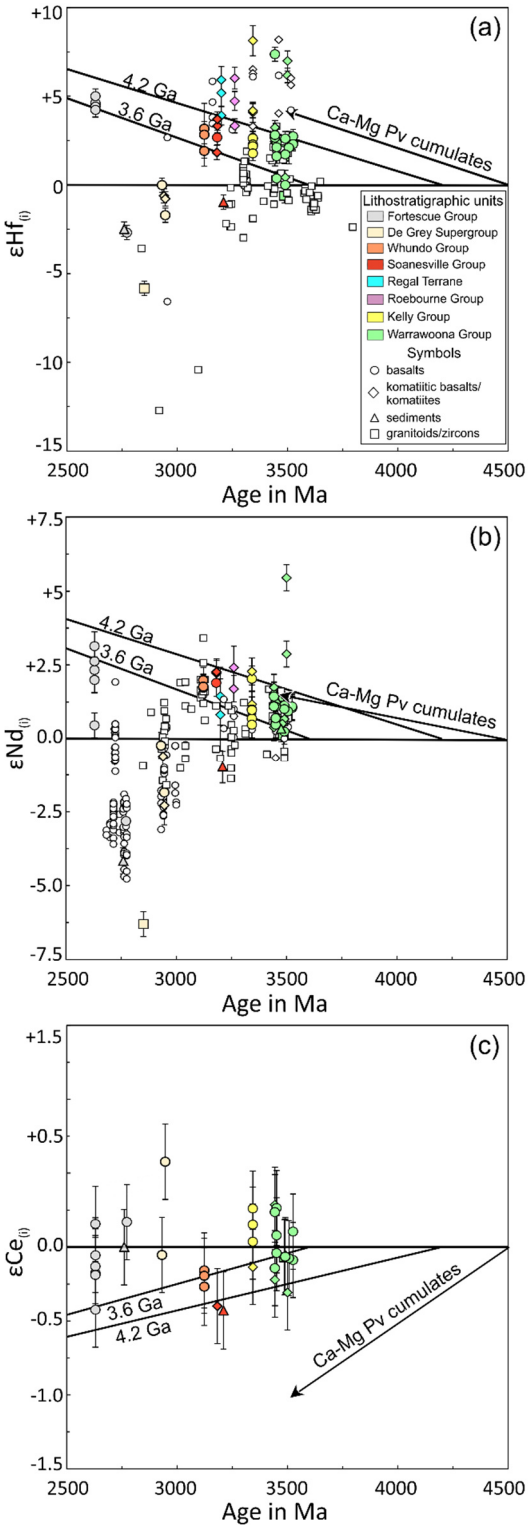

Fig. 1.5: Evolution of radiogenic isotope compositions in Pilbara rocks through geologic time. Panels illustrate a) initial Hf, b) initial Nd, and c) initial Ce isotope compositions. For Hf and Nd isotope compositions, our samples show a constant increase between ca. 3.59-3.18 Ga for most samples with the marked exception of the majority of 3.34 Ga Kelly Group samples. After 3.12 Ga, the Pilbara Craton develops towards more radiogenic Ce and less radiogenic Nd and Hf isotope compositions, reflecting a subduction-like setting and/or crustal contamination of older felsic crust. Errors are only shown for samples of this study and include the propagated errors of the external reproducibility on isotope composition measurements, measured parent/daughter ratios and the errors of the crystallization age of each specific formation. If the individually measured 2 S.E. was larger than the external reproducibility, we chose this error for the error propagation. Additional literature data compiled from Jahn et al., (1981); Gruau et al., (1987); Nelson et al., (1992); Tyler et al., (1992); Amelin et al., (1999); Arndt et al., (2001); Van Kranendonk et al., (2007b); Guitreau et al., (2012); Nebel et al., (2014); Kemp et al., (2015); Gardiner et al., (2017), (2019); Mole et al., (2018); Petersson et al., (2019).

perovskite abundances would result in extremely positive Zr-Hf anomalies relative to REE. The age for the magma ocean crystallization was set to 4.4 Ga, although changing that age by ±100 Ma hardly affects the isotopic outcome at 3.5 Ga. Depending on the style of crystallization (fractional vs. equilibrium crystallization) and the fraction of crystallized melt (5% to 60%), perovskite cumulates in both crystallization modes develop towards positive εNd values (ca. +0.8 to +5.5), variable εHf values (-5.4 to +3.0), and strongly negative εCe values (-1.0 to -1.5) at 3.5 Ga. The εCe values of these modelled cumulates at 3.5 Ga would be significantly lower than εCe values of our oldest 3.53-3.34 Ga samples from the EPT (-0.3 to +0.3) (Fig. 1.5c). The exotic isotope composition that is derived from our model is unmatched by our observed data and thus precludes Ca-Mg perovskite cumulates to be a potential source for Pilbara rocks, which is furthermore consistent with relatively high $^{138}La/^{136}Ce$ ratios in our samples (Fig. 1.4c) and an insignificant fractionation of Zr-Hf from Sm-Nd (Fig. 1.3). Altogether, the geochemical evidence suggests that the decoupling of Hf-Nd isotopes in the Pilbara Craton does not stem from an early magma ocean crystallization event, but rather originates from early differentiation events in the upper mantle.

The combination of Ce, Nd and Hf isotopes provides a powerful tool to gain better insight into the history of the early Earth and demonstrates that Ca-Mg cumulate segregation during magma ocean crystallization can be discarded as a cause for extremely high $\varepsilon Hf_{(i)}$ values found in Archean rocks from the Pilbara Craton. It still remains ambiguous, however, if the decoupling of Hf and Nd isotopes in other Archean rocks can be explained by perovsite segregation (e.g., Hoffmann et al., 2011b; Rizo et al., 2011; Puchtel et al., 2016) or not (e.g., Hoffmann and Wilson, 2017), although future ^{138}La-^{138}Ce isotope studies might help to place better constraints on this issue.

1.6.4. Hafnium, Nd and Ce isotope systematics of Pilbara mafic-ultramafic rocks and their implications for mantle evolution

Some mafic-ultramafic rocks from the Pilbara Craton show a decoupling of their initial Hf-Nd-Ce isotope compositions, with extremely radiogenic $\varepsilon Hf_{(i)}$ values up to +8.1 at significantly lower $\varepsilon Nd_{(i)}$ values (Figs. 1.5a and 1.7b). These findings are in apparent contrast to the studies by Kemp et al. (2015) and Petersson et al., (2019; 2020) who postulated a near-chondritic mantle at ~3.6 Ga. Their studies focused on Hf isotope compositions measured in inherited and detrital zircons from granitoids and sedimentary rocks (Kemp et al., 2015) and zircons from mafic to felsic rock successions (Petersson et al., 2019; Petersson et al., 2020). However, zircons in granitoids may not reveal the full depletion history of the Archean mantle, and in particular the TTGs that are thought to result from remelting of older mafic protoliths (Smithies et al., 2009; Hoffmann et al., 2011a; Gardiner et al., 2017; Johnson et al., 2017). Depending on the time elapsed between mantle melting, formation of mafic proto-crust, and TTG formation (hereafter the crustal residence time), the mafic protoliths may have developed unradiogenic Hf isotope compositions. Consequently, zircons that grew during TTG crystallization may have inherited their initial Hf isotope compositions from the evolved isotope composition of the mafic protolith rather than from the ambient mantle.

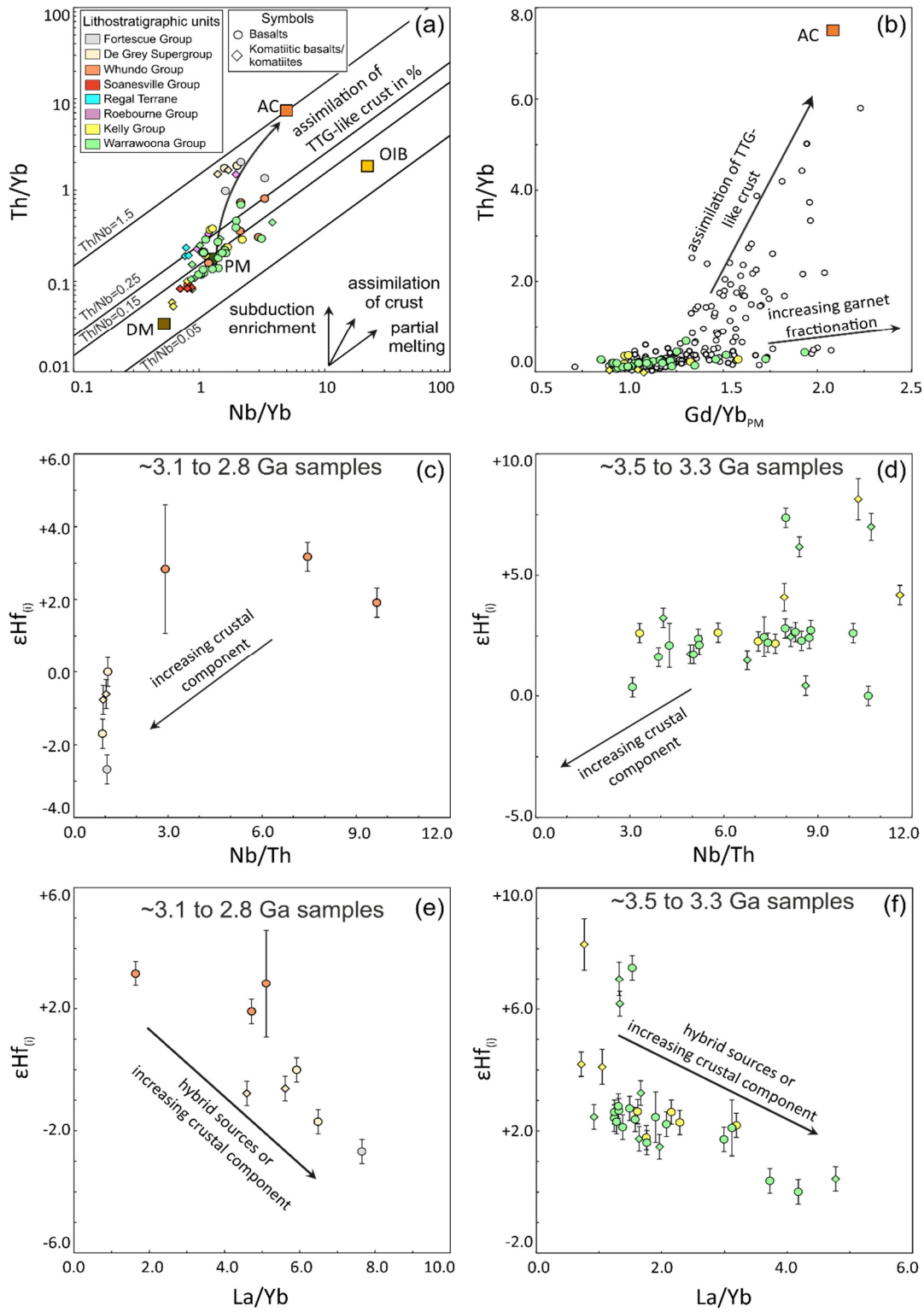

Fig. 1.6: Isotope and trace element variations illustrating effects of crustal contamination for selected suites. a) All ≤2.9 Ga samples b) but only some Paleoarchean samples have inherited an enriched component with high Th/Yb. c) and d) Hybrid mantle sources are likely responsible for decreased $\varepsilon Hf_{(i)}$ values of some EPT samples and not continental crust, as no co-variations between $\varepsilon Hf_{(i)}$ or $\varepsilon Nd_{(i)}$ with Nb/Th are observed, e) and f) but with La/Yb. Co-variations of $\varepsilon Hf_{(i)}$ with La/Yb and Th/Nb in younger successions, however, indicate mixing with crustal components rather than hybrid mantle sources. Additional literature data are taken from Tusch et al., (2020) for samples of this study. Additional literature data from the Pilbara Craton are shown here with smaller symbol sizes and without colors. Error estimates are the same as in Figure 1.5. Additional literature data compiled from Palme and O'Neill, (2013) (primitive mantle = PM); Salters and Stracke, (2004) (depleted mantle = DM); Sun and McDonough, (1989) (ocean island basalts = OIB); Rudnick and Fountain, (1995) (Archean TTG-like crust = AC)

Petersson et al., (2019; 2020) reported chondrite-like Hf isotope compositions for 3.59-3.31 Ga zircons from mafic to intermediate rocks from the Pilbara Craton, from which they argued for a chondritic composition of the ambient mantle until ~3.6 Ga. However, the basalts of their study show significant LREE enrichment and strong Nb-Ta depletions. Based on our study, this is best explained by the interaction with an enriched component, most likely reflecting crustal contamination. This is also in accord with previous work by Smithies et al., (2018) who have found evidence for crustally contaminated ~3.5 Ga Pilbara basalts displaying similarly low Nb/Th ratios as those reported by Petersson et al., (2019). Moreover, the presence of basalts with near-chondritic $\varepsilon Hf_{(i)}$ does not exclude the presence

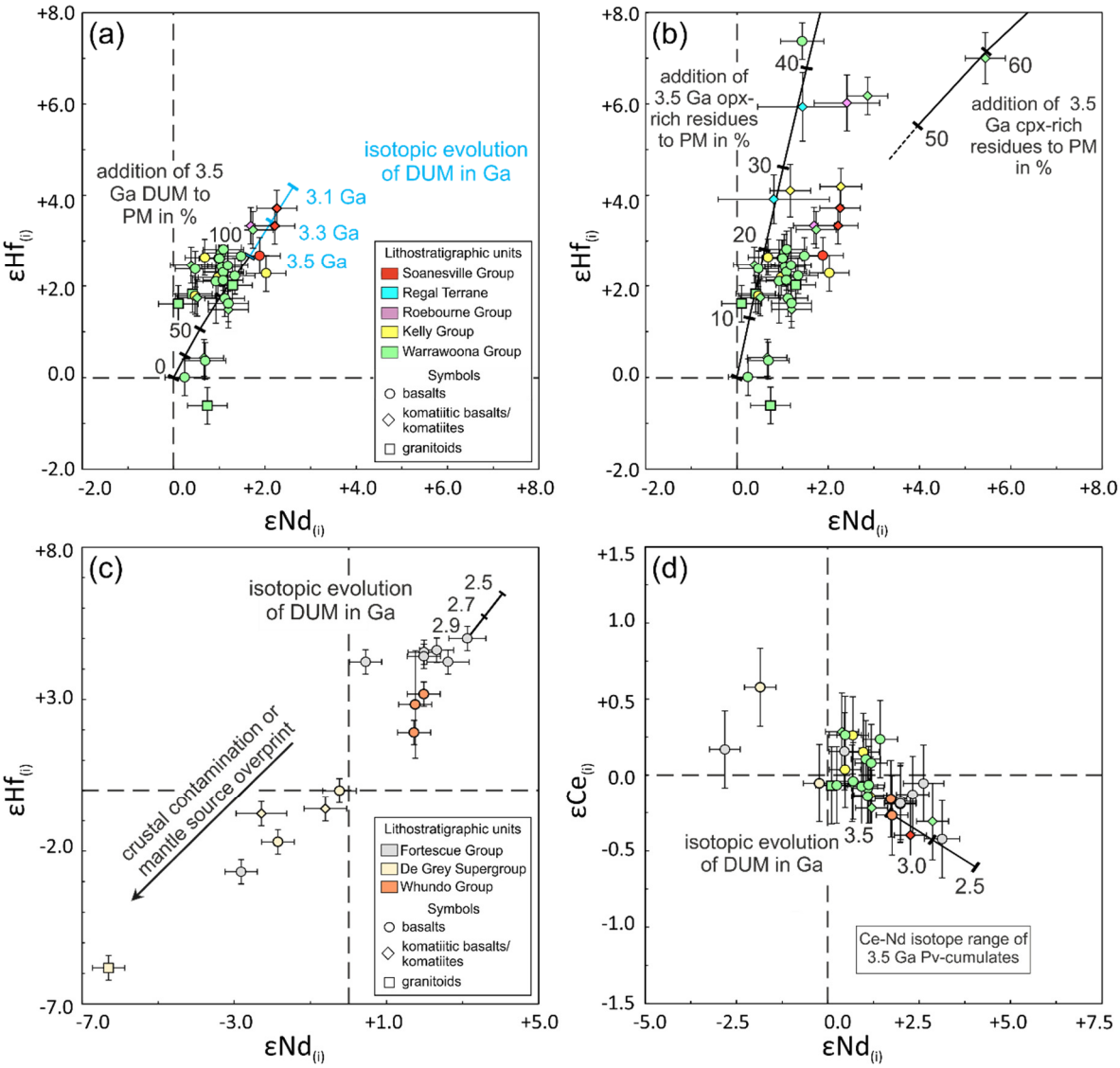

Fig. 1.7: Co-variation diagrams between initial Ce, Nd and Hf isotope compositions. a) $\varepsilon Hf_{(i)}$ vs. $\varepsilon Nd_{(i)}$ for 3.53-3.12 Ga samples show an increase of initial $\varepsilon Hf_{(i)}$ and $\varepsilon Nd_{(i)}$ values for most mafic samples with time that is best explained by an evolving depleted upper mantle (DUM) component. b) Some samples, in particular komatiites, are decoupled in their $\varepsilon Hf_{(i)}$ and $\varepsilon Nd_{(i)}$ composition, which is best explained by mixing of primitive mantle with older (~4.2 Ga) residual mantle domains showing decoupled Hf-Nd isotope compositions due to residual garnet. c) Refertilization of the mantle source or crustal contamination can explain the decreased $\varepsilon Hf_{(i)}$ vs. $\varepsilon Nd_{(i)}$ values found in some 2.94-2.63 Ga samples. d) Values of $\varepsilon Ce_{(i)}$ vs $\varepsilon Nd_{(i)}$ of unaltered samples show a coherent evolution compared to the $\varepsilon Hf_{(i)}$ and $\varepsilon Nd_{(i)}$ trend. Importantly, the Hf-Nd-Ce arrays defined by the Pilbara samples all overlap the chondritic value, with an Hf-Nd array for coupled samples of $\varepsilon Hf_{(i)}$= 1.2 (±0.2) × $\varepsilon Nd_{(i)}$ + 0.53 (±0.6) that is indistinguishable from the modern day Hf-Nd mantle array. The Ce-Nd array is defined by: $\varepsilon Ce_{(i)}$ =-0.14 (±0.07) × $\varepsilon Nd_{(i)}$ -0.08 (±0.3) and also overlaps with the present day Ce-Nd array (Israel et al., 2019). Error estimates are the same as in Figure 1.5.

of more depleted mantle, as shown by our study (Figs. 1.5-1.8). If such rocks are interpreted as crustally contaminated, as we favor, they rather provide evidence for the presence of ≥3.59 Ga felsic basement beneath the Pilbara Craton, which is consistent with inherited zircon data (Van Kranendonk et al., 2002).

Due to the predominantly positive $\varepsilon Hf_{(i)}$ and $\varepsilon Nd_{(i)}$ values in mafic-ultramafic rocks analyzed here, we conclude that the ambient mantle of the Pilbara Craton must have undergone older depletion events prior to 3.5 Ga, as suggested by previously studies (Gruau et al., 1987; Arndt et al., 2001; Smithies et al., 2007b; Tessalina et al., 2010; Nebel et al., 2014; Gardiner et al., 2017). Hafnium and Nd isotope compositions both suggest an onset of mantle-crust differentiation processes at ~4.2 Ga, evolving towards present day εHf and εNd values of +16 and +10, respectively. In contrast, Ce isotopes are not able to place further constraints on that depletion event due to somewhat smaller isotope variations, although Ce isotope evidence is still in accord with a ~4.2 Ga depletion event (assuming a present day εCe of the depleted upper mantle of -1.5). Nevertheless, there are some samples with near-chondritic $\varepsilon Hf_{(i)}$ and $\varepsilon Nd_{(i)}$ values that lack evidence for crustal contamination (Pil16-17 and Pil16-20b). These samples likely originated from more primitive mantle sources, possibly from primitive upwelling mantle material added to the depleted upper mantle (cf. Bédard, 2018). Importantly, however, we observe an increase in $\varepsilon Hf_{(i)}$ and $\varepsilon Nd_{(i)}$ and a decrease in $\varepsilon Ce_{(i)}$ with decreasing crystallization age between 3.53 Ga and 3.12 Ga. This is best explained by a depleted mantle source that evolved through geologic time (*cf.* Smithies et al., 2005b).

Initial Hf and Nd isotope compositions in rocks from the slightly younger (~3.26-3.18 Ga) Roebourne Group, Soanesville Group and Dalton Suite that are all ascribed to a rift-related setting are significantly more radiogenic, with $\varepsilon Ce_{(i)}$ being more unradiogenic, if compared to samples of the 3.34 Ga old Kelly Group (Arndt et al., 2001; Smithies et al., 2007b; Van Kranendonk et al., 2010). In addition, the majority of samples from these younger successions are characterized by elevated Sm/Nd ratios and MORB-like trace element patterns, implying a more depleted mantle source compared to the plume-related rocks of the Warrawoona and Kelly groups, as previously postulated by Smithies et al. (2005b). The observed change in the trace element geochemistry is likely linked to a proposed change in geodynamic setting at ~3.2 Ga from upwelling/plume-like dominated processes to modern style plate tectonics (Smithies et al., 2005a; Smithies et al., 2005b; Van Kranendonk et al., 2007; Van Kranendonk et al., 2010). We conclude that this change from mantle upwelling/plume-related volcanism before ~3.2 Ga to rift-related volcanism after ~3.2 Ga (Smithies et al., 2005b; Van Kranendonk et al., 2010) is mirrored by a change in ambient mantle composition. Such a model is also in accord with observations of increasing PGE abundances (Maier et al., 2009) and decreasing ^{182}W isotope anomalies (Tusch et al., 2021b) at the same time, which are suggested to mirror widespread homogenization of the mantle at this time by more efficient vertical mixing. The long-lived isotope systems analyzed in this study can help to better constrain how the involvement of different mantle reservoirs triggered homogenization of late veneer material. Between 3.5 and 3.2 Ga, deep-rooted upwelling mantle material that was not yet equilibrated with late veneer material mixed with shallower mantle regions that already equilibrated with late veneer material. Due to a change in the geodynamic setting at 3.2 Ga (Van Kranendonk et al., 2010), the

supply in the upper mantle by upwelling mantle with pre-late veneer signature ceased, resulting in decreased $\mu^{182}W$ values (Tusch et al., 2021b)and increased PGE concentrations (Maier et al., 2009) after ~3.2 Ga.

With the emergence of localized subduction by ~3.1 Ga, an arc-like setting led to formation of the 3.12 Ga Whundo Group (Krapez and Eisenlohr, 1998; Smithies et al., 2005a; Smithies et al., 2007c). Our data for Whundo Group samples generally indicate the involvement of an enriched component as implied by somewhat lower Nb/Th ratios and $\varepsilon Hf_{(i)}$ and $\varepsilon Nd_{(i)}$ values in these samples (Figs. 1.3, 1.5, 1.6c). In the context of a subduction-like setting that was previously proposed for the Whundo Group (Krapez and Eisenlohr, 1998; Smithies et al., 2005a; Smithies et al., 2007c), it is possible that this enriched component originates from remelting a subducting crust. However, the small number of samples (n=3) analyzed from the Whundo Group hampers a more detailed interpretation of the tectonic setting of the Whundo Group. After the collision of the WPS and the EPT at 3.07 Ga, volcanics of the ~3.0 Ga De Grey Supergroup tapped a metasomatized mantle that was likely re-enriched within a subduction setting at ~3.12 Ga (Smithies et al., 2004; Smithies et al., 2005a). This is mirrored by significantly lower $\varepsilon Hf_{(i)}$ and $\varepsilon Nd_{(i)}$ and higher $\varepsilon Ce_{(i)}$ values in all of the rocks of the De Grey Supergroup (Fig. 1.5). The absence of samples that have positive $\varepsilon Hf_{(i)}$, $\varepsilon Nd_{(i)}$ and lower $\varepsilon Ce_{(i)}$ values argues against a role of AFC processes and supports evidence that the enriched component must have already been distributed within the mantle source (Smithies et al., 2004).

The older units (2.78-2.63 Ga) of the Fortescue Group were contaminated by significantly older crust, as indicated by AFC processes becoming apparent from strongly negative $\varepsilon Hf_{(i)}$ and $\varepsilon Nd_{(i)}$ and positive $\varepsilon Ce_{(i)}$ values that are found in some samples of the Fortescue Group (Arndt et al., 2001; Smithies et al., 2007b; Mole et al., 2018). In contrast, the majority of the younger ~2.63 Ga Jeerinah Formation within the Fortescue Group show no evidence for crustal contamination (except possibly sample 201476), by generally having elevated $\varepsilon Hf_{(i)}$ (+4.2 to +5.0) and $\varepsilon Nd_{(i)}$ (+0.5 to +3.2), and low $\varepsilon Ce_{(i)}$ values (-0.44 to -1.3), suggesting an origin from a depleted mantle domain.

1.6.5. A genetic model for the evolution of the East Pilbara Terrane

Our Hf and Nd isotope results reveal distinct differences between most komatiites and basalts. As $\varepsilon Hf_{(i)}$ values are significantly higher in komatiites compared to most basalts, different mantle reservoirs must have been involved in the formation of the Pilbara Craton. Furthermore, the majority of basalts from the Warrawoona Group have $\varepsilon Hf_{(i)}$ and $\varepsilon Nd_{(i)}$ values that are best explained by an origin from a shallow, depleted upper mantle domain (Gruau et al., 1987; Nisbet et al., 1993; Arndt et al., 2001; Smithies et al., 2005b; Smithies et al., 2007b; Sossi et al., 2016; Bédard, 2018). Nevertheless, some samples investigated here show near-chondritic $\varepsilon Hf_{(i)}$, $\varepsilon Nd_{(i)}$ and $\varepsilon Ce_{(i)}$ values that cannot be explained by crustal contamination. This observation rather implies near-primitive mantle sources for at least some rocks from the Pilbara Craton that likely represent material from deep-rooted upwelling mantle (see also Van Kranendonk et al., 2007a, 2015). However, it is still ambiguous whether komatiites in general were formed in a plume setting (e.g., Arndt et

al., 1997; Arndt et al., 2001; Smithies et al., 2005b) or as a consequence of mantle overturn events (e.g., Bédard, 2018). As our model can be applied to both scenarios, we refer to this process as '*upwelling mantle*' without preferring any of these two processes.

Interestingly, two Warrawoona Group samples (Pil16-17 and Pil16-20b) of this study that display chondritic Hf-Nd-Ce isotope compositions were melted in deeper parts of the mantle, as indicated by the highest Gd/Yb_{PM}=1.72-1.93 and TiO_2/Yb=0.752-0.738. Pressure and temperature estimates following the approach of Lee et al. (2009) confirm that sample Pil16-20b was melted at P-T conditions exceeding the estimates for all other Warrawoona Group samples from the Pilbara Craton by at least 3 GPa and 150°C (supplementary Fig. 1.4, Appendix A1; sample Pil16-17 could not be calculated). In contrast, all other Warrawoona Group samples with more radiogenic $\varepsilon Hf_{(i)}$ and $\varepsilon Nd_{(i)}$ values were melted in shallower mantle regions as indicated by near-chondritic Gd/Yb_{PM}. As the Paleoarchean basalts from this study show a continuous spectrum from near-chondritic to increasingly positive $\varepsilon Hf_{(i)}$ and $\varepsilon Nd_{(i)}$ values expected for depleted mantle at that time, we conclude that an upper depleted mantle endmember was mixed with a near-chondritic upwelling mantle between 3.53-3.34 Ga (Figs. 1.5-1.8). In contrast to the majority of the basalts analyzed here, most komatiitic rocks and one basalt from the EPT show highly radiogenic initial Hf isotope compositions that are decoupled from their Ce-Nd isotope compositions. This decoupling can be explained by older melt loss from garnet-bearing residual mantle reservoirs that can efficiently fractionate Lu/Hf from Sm/Nd and La/Ce. In order to reconcile our observations, we conducted isotope and trace element modelling to explain the decoupled Hf-Nd-Ce isotope compositions, as well as the trace element characteristics of rocks from the Pilbara Craton. Following Sossi et al. (2016), a non-modal batch melting model was used. The first step comprised extraction of 10% melt from a lherzolite in the garnet stability field at 4.2 Ga, forming residual mantle domains. We have chosen this age based on our data, as it likely reflects the onset of mantle-crust differentiation beneath the Pilbara Craton (Fig. 1.5). Within 700 Ma, such isolated residual mantle domains may have evolved towards extreme $\varepsilon Hf_{(i)}$ $\varepsilon Nd_{(i)}$ and $\varepsilon Ce_{(i)}$ values of +42, +16 and -1.2, respectively, in accord with present day observations from abyssal peridotites (Salters et al., 2011). Due to the refractory nature of such depleted mantle domains, higher melting temperatures are required, which can explain why the decoupling of Hf-Nd-Ce isotope compositions is mainly found in komatiites as they are a product of high temperature mantle melting (e.g., Arndt et al., 1997). This model can also explain the highly radiogenic but coupled Hf and Nd isotope compositions of sample 179757, where the residual mantle contains more clinopyroxene than orthopyroxene (see Appendix A1). Mass balance calculations, as illustrated in supplementary Figure 1.5 (Appendix A1), suggest that in-mixing of more fertile primitive mantle material would efficiently dilute the Hf-Nd-Ce isotope compositions of such residual domains. Our model demonstrates that mixing between primitive mantle with Hadean residual mantle at almost equal proportions (30-50% residual mantle and 50-70% primitive mantle) creates a hybrid mantle source with trace element and Hf-Nd-Ce isotope characteristics that match those observed in rocks from the Pilbara Craton (Fig. 1.7, supplementary Fig. 1.5, Appendix A1).

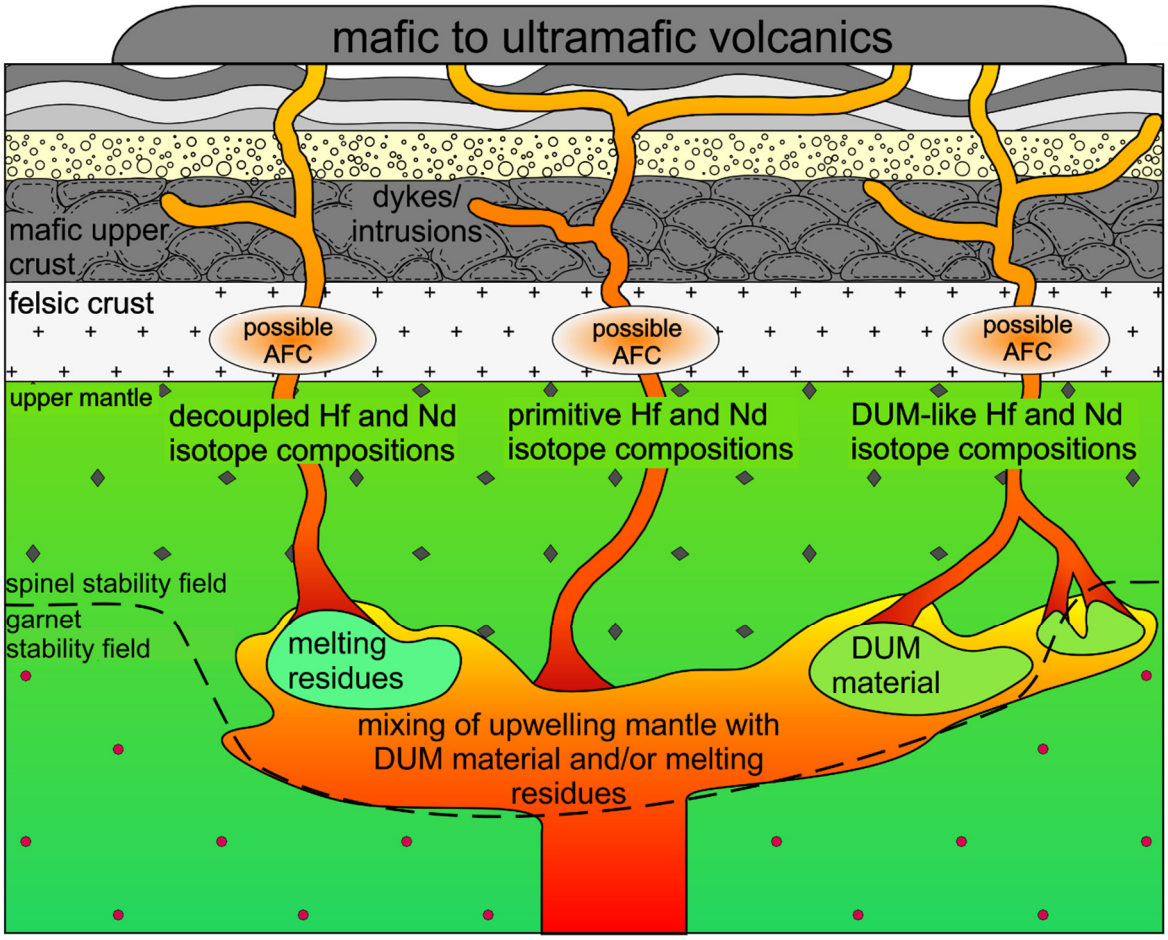

Fig. 1.8: Sketch illustrating our proposed geodynamic model for the early evolution of the Pilbara craton as preserved in the EPT. Between ca. 3.5 to 3.3 Ga, near-primitive upwelling mantle mixes with ca. 4.2 Ga old depleted upper mantle (DUM) material and in some cases with residual mantle domains depleted in the garnet stability field. With such hybrid mantle sources (near primitive and garnet-bearing residual mantle domains), the pooled melts may have decoupled Hf-Nd isotope compositions. In contrast, mixing of near-primitive and DUM material (which is most frequent) generates melts that are not decoupled in their Hf and Nd isotope composition and lie in $\varepsilon Hf_{(i)}$ vs. $\varepsilon Nd_{(i)}$ space somewhere between primitive mantle and DUM recalculated to the time of eruption. Furthermore, the eruption of near-primitive mantle melts that have not mixed with residual domains or DUM material also occurred, although this compositional type must have been rare as only few samples are characterized by near-chondritic Hf and Nd isotope compositions.

Unfractionated Gd/Yb_{PM}=0.851-1.25 and relatively low TiO_2/Yb ratios of all EPT komatiites suggest melting within the spinel stability field, in accord with P-T estimates for the Warrawoona Group (Lee et al., 2009) (supplementary Fig. 1.4, Appendix A1). This apparent contrast to our proposed residual mantle domains from the garnet stability field can be explained by two processes: (1) Anomalously high temperatures of the upwelling mantle shifted the spinel stability field towards significantly higher depths (e.g., Klemme et al., 2009); or (2) convective transport of the residual mantle domains to shallower depths outside the garnet stability field, as previously proposed for the 3.33 Ga Commondale komatiite suite in South Africa (Hoffmann and Wilson, 2017 and references therein). As previously observed by Nebel et al. (2014), and confirmed here, the extremely radiogenic $\varepsilon Hf_{(i)}$ values in Pilbara komatiites are absent after ~3.2 Ga (Fig. 1.5), consistent with the proposed change in plate tectonic regime recorded in the Pilbara Craton. As the onset of Phanerozoic-style plate tectonics has long been interpreted to result from decreasing mantle temperatures (cf. Davies, 1992), we therefore conclude that it was this factor, more

than any other, that reduced the proportions of residual mantle domains tapped by mantle melts after 3.2 Ga.

1.7. Conclusions

A combined Hf-Nd-Ce isotope dataset for mafic-ultramafic rocks from the Pilbara Craton, covering all major stratigraphic units, places new constraints on the geodynamic evolution of the Pilbara Craton and the early Archean mantle in general. In mafic-ultramafic successions of the Pilbara Craton, these isotope systematics were insignificantly affected by post-magmatic alteration, implying that the decoupling of Hf isotopes from Ce-Nd isotopes is a primary magmatic feature. Consistently elevated Nb/La ratios in all samples >3.2 Ga preclude AFC processes to have operated during their formation, possibly reflecting the limited extent of evolved continental crust in the Pilbara Craton during the early Archean.

Perovskite fractionation in an ancient magma ocean cannot explain the observed variability in Hf-Nd-Ce isotope compositions, and the Ce-Nd array of the accessible upper mantle was near-chondritic by early Archean time. Rather, the broad variety of $\varepsilon Hf_{(i)}$, $\varepsilon Nd_{(i)}$ and $\varepsilon Ce_{(i)}$ values imply that at least two distinct mantle reservoirs were involved in the formation of these rocks. One reservoir, most likely ambient upper mantle, must have had a long depletion history, commencing at ~4.2 Ga, as constrained by the most depleted basalt samples. A second reservoir with near-chondritic radiogenic isotope ratios likely tapped the lower mantle by continuous mantle upwelling. Most komatiites have significantly higher $\varepsilon Hf_{(i)}$ values that are decoupled from Nd-Ce compositions. This is likely explained by high temperature melting of residual mantle domains that have experienced a previous melt depletion history in the garnet stability field. Samples younger than 3.2 Ga exhibit significantly lower Nb/Th ratios and, in some cases, unradiogenic Hf and Nd isotope compositions, reflecting the involvement of enriched components via subduction zone recycling and crustal contamination. Collectively, our study demonstrates that the radiogenic isotope composition of mafic-ultramafic rocks from Pilbara Craton provides an unprecedented insight into mantle depletion history, further illustrating that depletion of the mantle may have commenced relatively early in Earth's history, in late Hadean time.

Chapter II

2. Temporal evolution of ^{142}Nd signatures in SW Greenland from high precision MC-ICP-MS measurements

2.1. Abstract

Measurements of ^{142}Nd isotope signatures in Archean rocks are a powerful tool to investigate the earliest silicate differentiation on the early Earth. We introduce a new analytical protocol to perform high precision radiogenic and mass independent Nd isotope measurements by MC-ICPMS. To validate our method, we have measured well-characterized ~3.72 to ~3.8 Ga samples from the ~3.7 to ~3.8 Ga Itsaq Gneiss Complex and associated greenstone belts in SW Greenland, including lithostratigraphic units that were previously analyzed for $^{142\text{-}143}$Nd isotope systematics, by both TIMS and MC-ICPMS. Our μ^{142}Nd values for ~3.72 to ~3.8 Ga rocks from the Isua region range from +9.2±2.6 to +13.2±1.1 ppm and is in accord with previous studies.

Using coupled ^{142,143}Nd/^{144}Nd isotope systematics our data for ~3.8 Ga (ultra-) mafic successions from the Isua region, we can confirm previous age constraints on the earliest silicate differentiation events with a differentiation age T_{diff} of $4.417^{+0.045}_{-0.060}$ Ga. Moreover, we can reveal a statistically significant decrease of ^{142}Nd/^{144}Nd isotope compositions in the ambient mantle of SW Greenland that already started to decrease in the Eoarchean between ~3.8 Ga ($\mu^{142}Nd_{3.8Ga}$ = 13.0±1.1) and ~3.72 Ga ($\mu^{142}Nd_{3.7Ga}$ = +9.8±1.0). Our study reveals that $\varepsilon^{143}Nd_{(i)}$ and $\varepsilon Hf_{(i)}$ values of Isua rocks scatter more than it would be expected from a single stage differentiation event as implied from nearly uniform μ^{142}Nd values, suggesting that the previously described decoupling of Hf and Nd isotopes is not a primordial magma ocean signature. Instead, we conclude that some of the ^{147}Sm-^{143}Nd isotope systematics have been established by second stage processes like younger mantle depletion events or recycling of subducted material. Preservation of pristine isochrons largely rules out an explanation by younger alteration events. Based on isotope and trace element modeling, we argue that temporal evolution of coupled ^{142,143}Nd/^{144}Nd isotope compositions in the ambient mantle of the Isua region is best explained by the progressive admixture of material to the Isua mantle source that must have had present day-like μ^{142}Nd compositions.

2.2. Introduction

The long-lived ^{147}Sm-^{143}Nd isotope system has become a key analytical tool in geochronology and geochemistry issues. Its potential can be significantly increased when it is combined with the short-lived ^{146}Sm-^{142}Nd decay system ($T_{1/2}$ = 103 Ma (Friedman et al., 1966; Meissner et al., 1987; Marks et al., 2014)) that was only active the first few 100 Ma. Since the first discovery of anomalous ^{142}Nd/^{144}Nd compositions in Archean rocks, this short-lived isotope system has been widely applied to numerous Archean terranes (typically expressed in μ-notation, depicting the ppm deviation from a terrestrial reference material). When combined, coupled ^{147,146}Sm-^{143,142}Nd isotope systematics can yield valuable information about early geodynamic processes. Especially the Isua region in SW Greenland has drawn a particular interest in the scientific community, since this Archean remnant shows elevated ^{142}Nd/^{144}Nd compositions that has been interpreted to reflect Hadean silicate differentiation (Caro et al., 2003; Boyet and Carlson, 2005; Caro et al., 2006; Bennett et al., 2007; Rizo et al., 2012). Anomalous ^{142}Nd/^{144}Nd isotope compositions are predominantly found in Paleo- to Eoarchean cratons (Boyet and Carlson, 2006; Caro et al., 2006; Rizo et al., 2011; Rizo et al., 2012; Rizo et al., 2016; Caro et al., 2017; Morino et al., 2017) and their broad disappearance after ~3.5 to ~3.0 Ga has been interpreted to reflect mantle homogenization processes (Boyet and Carlson, 2006; Caro et al., 2006; Bennett et al., 2007; Rizo et al., 2012; Saji et al., 2018; Schneider et al., 2018; Hyung and Jacobsen, 2020). However, with increasing analytical precision and more numbers of rocks being investigated, anomalous ^{142}Nd/^{144}Nd isotope compositions have also rarely been reported for Neoarchean and even present day rocks (Debaille et al., 2013; Horan et al., 2018; Peters et al., 2018). Therefore, ^{142}Nd/^{144}Nd isotope studies can also provide information on the timing and efficiency of mantle homogenization processes. To better understand mantle homogenization processes, Archean rocks from SW Greenland provide an excellent opportunity as there is a variety of rocks preserved with different crystallization ages (3.85-3.6 Ga Itsaq Gneiss Complex (IGC) and associated greenstone belts (Nutman and Friend, 2009; Amelin et al., 2011), ~3.2-3.5 Ga Ameralik dikes (Nutman et al., 2004; Rizo et al., 2012) and multiple younger ~3.1 to 2.8 Ga subduction-related terranes (Szilas, 2018).

Accurate and high-precision isotope measurements are essential to resolve small ^{142}Nd isotope anomalies. In the past thermal ionization mass spectrometry (TIMS) were almost exclusively preferred to conduct such high precision measurements due to small mass fractionation effects. Although the vast majority of recent TIMS studies provided highly precise Nd isotope data (errors usually ≤+/-5 ppm), the accuracy and reliability of TIMS protocols for ^{142}Nd measurement has often been debated, largely due to irreproducible mass fractionation effects. Reported problems included issues with the static mode (Brandon et al., 2009b), reservoir mixing on the filament (Upadhyay et al., 2008) or changes in mass fractionation during acquisition steps (Garçon et al., 2018). All these issues call for additional protocols to verify TIMS-based data.

More recently, there has been an increasing number of MC ICP-MS protocols that enabled high precision isotope measurements (e.g., ^{182}W or ^{142}Nd) with an analytical resolution power similar to that of TIMS analysis (e.g., Willbold, 2007; Saji et al., 2016; Saji et al., 2018; Budde et al., 2019; Tusch et al., 2019). In this present study, we have developed a new MC

ICP-MS protocol to determine mass independent and radiogenic Nd isotope compositions with high precision and accuracy. We applied our newly developed analytical protocol to well characterized ~3.8 to ~3.7 Ga rocks from the IGC and associated greenstone belts, the ~3.3 to ~3.5 Ga Ameralik dikes and several terrestrial reference materials. Due to the high number of existing $^{142}Nd/^{144}Nd$ data on Isua rocks, they allow an assessment of our new protocol in terms of accuracy and precision (e.g., Caro et al., 2003; Boyet and Carlson, 2005; Caro et al., 2006; Bennett et al., 2007; Rizo et al., 2011; Saji et al., 2018). In addition we have measured younger ~3.1 to ~2.0 Ga rocks from subduction zone-related rocks. These data are incorporated into the existing framework that investigates the early differentiation history of Earth and helps to better understand the mechanisms that homogenized initially heterogeneous Eoarchean $^{142}Nd/^{144}Nd$ isotope compositions by the end of the Archean.

2.3. Geological background and sample description

Unlike many other Archean terranes that are usually of Paleoarchean age or younger, the Eoarchean 3.85-3.6 Ga IGC and associated greenstone belts allow insights into Eoarchean evolution of the Earth (Nutman and Friend, 2009). For supracrustal belts within the IGC, the Isua region has attracted increasing attention in the last decades, due to its good preservation (metamorphism up to amphibolite facies at locally little deformation), with some domains having only experienced little to no post-3.5 Ga strain (e.g., Moorbath et al., 1977; Friend et al., 1996; Nutman et al., 1999; Polat et al., 2002; Polat and Hofmann, 2003). Generally, the Isua Supracrustal Belt (ISB) can be divided into two formerly separate terranes, a northern ~3.7 Ga old terrane and a southern ~3.8 Ga old terrane that both show geochemical similarities to modern island arcs (Polat et al., 2002; Polat and Hofmann, 2003; Nutman and Friend, 2009). In the region south of the Isua greenstone belt (SOISB), the IGC contains a mixture of ~3.8 Ga felsic rocks and amphibolites that are preserved as enclaves in low strain domains (Friend et al., 1996; Nutman et al., 2002; Crowley, 2003; van de Löcht et al., 2020) within up to 3.85 Ga old TTG orthogneisses (Amelin et al., 2011) (Figs. 2.1 and Extended Data Fig. 2.1).

An interlayered <3.75 Ga mylonitized sedimentary unit within the ISB separates the northern ~3.7 Ga terrane from the older ~3.8 Ga southern terrane. Its deformation resulted from the 3.69-3.66 Ga juxtaposition of the northern and southern terrane (Nutman et al., 2007; Nutman et al., 2009) (Fig. 2.1). The ~3.7 Ga terrane can be subdivided into three sub-terranes that are associated with the occurrence of boninites, island arc tholeiites and intermediate to felsic schists (Polat et al., 2002; Polat and Hofmann, 2003; Nutman et al., 2009). Due to their strong geochemical similarities with modern analogues from subduction zone settings, the metavolcanic rocks were interpreted to have formed in a similar geodynamic setting (Polat et al., 2002; Polat and Hofmann, 2003; Hoffmann et al., 2010; Hoffmann et al., 2011b; Hoffmann et al., 2012; van de Löcht et al., 2020). Between 3.69 and 3.66 Ga, both terranes were juxtaposed (Crowley, 2003; Nutman and Friend, 2009).

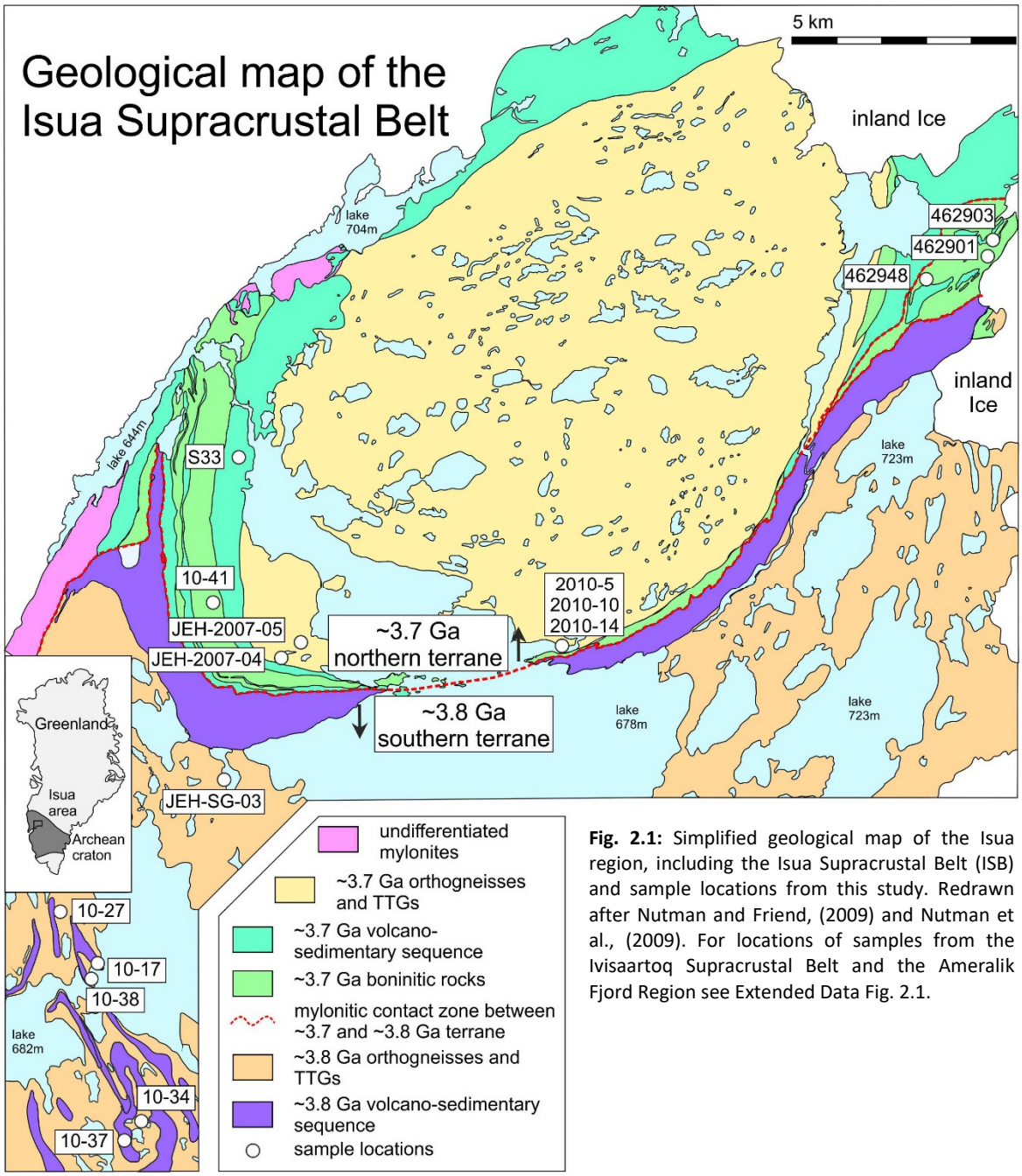

Fig. 2.1: Simplified geological map of the Isua region, including the Isua Supracrustal Belt (ISB) and sample locations from this study. Redrawn after Nutman and Friend, (2009) and Nutman et al., (2009). For locations of samples from the Ivisaartoq Supracrustal Belt and the Ameralik Fjord Region see Extended Data Fig. 2.1.

During the Paleoarchean, the amalgamated terranes were intruded by several generations of east-west oriented dikes that are typically referred to as Ameralik dike swarm (Nutman et al., 2004). The ages for most of the Ameralik dikes near the Isua area cluster around ~3.4 Ga (Rizo et al., 2012) although younger ages as low as 3265±15 Ma have been reported (Nutman et al., 2004).

Increased volcanic activity was reinitiated at ~3.08 to 2.84 Ga and is recorded here by samples from the ~3.08 Ga Ivisaartoq supracrustal belt as well as metavolcanic rocks in the ~2.97 Ga Ameralik Fjord Region that also contains younger, ~2.0 Ga dikes (Polat et al., 2009; Polat et al., 2010). Geochemical data for both terranes revealed the influence of older recycled material, making a subduction zone setting the most likely geodynamic setting for the formation of these younger greenstone belts (Szilas et al., 2015a; Szilas et al., 2016).

2.4. Methods

2.4.1. Sample dissolution and separation of clean Nd cuts

The dissolution of sample powders follows the chemical protocol of Tusch et al., (2019) and will only be summarized in brief (see Extended Data Table 2.1 and Extended Data Fig. 2.2). Each digestion involved 1 g of sample material that was dissolved in 15 ml 24 M HF + 15 ml 14 M HNO_3 for 2 days at 140°C and subsequently evaporated until near dryness. Subsequently, 5 ml 14 M HNO_3 were added and dried down to near dryness. This step was repeated three times to remove residual HF without forming unsolvable fluoride precipitates. Afterwards, the samples were dissolved in 30 ml 6 M HCl at 120 to 150 °C for 48 hours. In case of residual precipitates, this last step was repeated until clear sample solutions were obtained.

The separation for $^{142}Nd/^{144}Nd$ analysis follows a five-step ion exchange protocol to achieve maximum Nd purification (Extended Data Table 2.1). The first separation step (step I) follows the first-stage ion exchange column protocol of Tusch et al., (2019) and provides a rare earth element (REE) cut that is mostly free of matrix elements. In case of analysis that required more than 1g of sample material, REE cuts were combined after this separation step. In a next step (step II), REE were separated from the remaining matrix (mainly residual alkaline and alkaline earth metals) by using cation exchange resin and different HCl molarities. This matrix free REE cut was dried down and re-dissolved in 10 M HNO_3/20 mM $KBrO_3$ to fully oxidize Ce^{3+} to Ce^{4+}. Next (step III), Ce was separated from the remaining REE on Ln spec resin, following a slightly modified separation protocol of Schnabel et al. (2017), where ≥99.95% of Ce is removed from the remaining LREE cut. Subsequently, (step IV), separation step II was repeated, to remove K that was introduced by the $KBrO_3$ from the previous separation. Finally (step V), Nd was separated from the remaining LREE using 30 cm long glass columns that were filled with 6 ml of 50 µm Ln Spec resin. The columns were filled with 400 µl of anion resin on top in order to prevent the Ln Spec resin from floating up, which might broaden the eluted element peaks. This step purifies Nd from Pr and Sm as well as from residual Ce. In order to remove as much Pr as possible and losing the least Nd, we separately collected the last 3-5 ml before the expected onset of the Nd peak in 1 ml steps and analyzed 1‰ aliquots to determine Pr and Nd contents. Eventually, these 1 ml rinsing steps were added to the final Nd cut to obtain the highest Nd yields possible at low Pr monitors. This procedure allowed Nd yields of ~95% during separation V while ~75% of the Pr was removed. After separation steps II-V, we dried down the samples and treated the residue with 80 µl 14 M HNO_3 + 40 µl 30 % H_2O_2 at low temperatures (≤60°C) to destroy possible organic compounds.

For long-lived ^{176}Lu-^{176}Hf and ^{147}Sm-^{143}Nd isotope systematics, 150 mg of sample powder were spiked with mixed ^{150}Nd-^{149}Sm and ^{176}Lu-^{180}Hf isotope tracers and digested in 8 ml 1:1 HF-HNO_3 for one day. After the first digestion step, samples were dried down redissolved in 8 ml 1:1 HF-HNO_3 and digested in Parr© bombs at 180 °C for three days (Hoffmann et al., 2011a). Subsequently, samples were dried to near dryness, when 5 ml of conc. HNO_3 were added and dried down to near dryness again. This step was repeated three times to remove HF without forming insoluble fluoride precipitates. After the removal of HF, samples were redissolved in 8 ml 6 M HCl in which they were fully dissolved. Pure fractions of Lu and Hf

were obtained following the chemical separation protocol of Münker et al., (2001). A light rare earth element-bearing cut was further separated from matrix elements by cation exchange using stage one from the separation protocol of Schnabel et al., (2017). From this LREE-bearing cut, pure fractions of Sm and Nd were obtained following the chemical separation protocol of Pin and Zalduegui (1997).

2.4.2. Mass spectrometry

All Nd isotope measurements were performed on a Neptune Plus MC ICP-MS at University of Cologne. We used a 50 µl/min C-Flow Nebulizer that was connected to an Apex Q desolvation system. For the Apex exhaust, we used an external peristaltic pump. The internal gas line of the Apex was connected to a N_2 gas line. The sample-out gas line of the Apex was attached to a Scott type double pass glass spray chamber by a 1.8 mm injector. In between the Apex and the injector, we connected an additional Ar gas line. We used H-skimmer cones as this has shown to ensure the most stable signals, typically yielding ~7 V on ^{142}Nd per 100 ppb Nd.

All seven Nd isotopes, ^{142}Nd, ^{143}Nd, ^{144}Nd, ^{145}Nd, ^{146}Nd, ^{148}Nd and ^{150}Nd were measured as well as ^{140}Ce and ^{147}Sm monitors to correct for isobaric interferences on masses ^{142}Nd, ^{144}Nd, ^{148}Nd and ^{150}Nd, respectively. For all Nd isotopes, faraday cups were connected to 10^{11} Ω amplifiers, while 10^{13} Ω amplifiers were used for faraday cups that monitored ^{140}Ce and ^{147}Sm. Mass bias was corrected assuming the exponential law and ^{146}Nd/^{144}Nd = 0.7219 or ^{148}Nd/^{144}Nd = 0.241578 (hereafter denoted as 6/4 or 8/4). If not explicitly noted otherwise, all reported ^{142}Nd/^{144}Nd isotope data were corrected for mass bias by using ^{148}Nd/^{144}Nd. A gain calibration among the faraday cups and a baseline (1200 integration steps with 1.05 s each) were measured daily. Individual measurements typically comprised 60 cycles (8.4 s integration time) and were usually run between 25 to 35V on ^{142}Nd. Sample solutions were always bracketed by a referenced JNdi-1 standard solution and individual samples were measured repeatedly (usually 10 to 12 times). Potential ^{141}Pr^{1}H interferences on mass 142 were checked by measuring a Pr-doped JNdi-1 at the beginning of each analysis and the general stability of the instrument was ensured by measuring an LP-1 in house standard (La Palma Basalt) at least every ~36 hours (Extended Data Fig. 2.3). To be able to measure samples repeatedly at such high intensities, ~3 µg Nd were consumed per sample. The intensity of samples and standards were matched within ≤5% to each other and the analysis of samples and standards were interrupted by 300s of wash time. Accordingly, the measurement time for one sample amounts to ~7 hours. Procedural blanks were always less than 16 ng, resulting in negligible blank contributions of ≤0.5%. The typical internal precision of one single measurement typically amounts to a 2 SE of ±5, ±5, ±4, ±3 and ±8 ppm for μ^{142}Nd, μ^{143}Nd, μ^{145}Nd, μ^{146}Nd, and μ^{150}Nd values (8/4), respectively. Reported errors for repeatedly analyzed samples depict the 95% CI, although we consider our intermediate precision of ±1.4 ppm as minimum error.

For long-lived isotope systematics, measured ^{143}Nd/^{144}Nd isotope data was mass bias corrected using the exponential law and assuming a ^{146}Nd/^{144}Nd ratio of 0.7219. All ^{143}Nd/^{144}Nd data are reported relative to the La Jolla reference material, having a

$^{143}Nd/^{144}Nd$ composition of 0.511859. Our intermediate precision for $^{143}Nd/^{144}Nd$ compositions amounts to ±0.4 ε-units and is considered as uncertainty of $^{143}Nd/^{144}Nd$ analysis. Hafnium isotope analyses were corrected using the exponential law and assuming a $^{179}Hf/^{177}Hf$ of 0.7325. All data are given relative to the Münster AMES JMC, having a $^{176}Hf/^{177}Hf$ ratio of 0.282160. The intermediate precision on $^{176}Hf/^{177}Hf$ isotope ratios amounts to ±0.4 ε-units. The errors on parent/daughter ratio amount to 0.2%. Our quoted errors for initial Nd and Hf isotope compositions include the errors from our external reproducibility, errors on parent/daughter ratios, and errors on the crystallization ages. All data are reported relative to the CHUR values of Bouvier et al., (2008). Total procedural blanks were 35 pg for Nd, 56 pg for Sm, 41 pg for Lu and 26 pg for Hf.

2.5. Results

We have obtained $^{142}Nd/^{144}Nd$ isotope data for a variety of previously investigated Archean samples from southwest Greenland, as well as for some modern rocks (including certified reference materials) and standard solutions. The dataset includes 15 different felsic to (ultra-) mafic rocks that lie within the IGC. Measured $\mu^{142}Nd$ values for individual ~3.72 to ~3.8 Ga samples range from +9.2±2.6 to +13.6±1.4, giving a mean value of +11.2±3.4 which is in excellent agreement with previous studies (Fig. 2.2a) (Boyet and Carlson, 2005; Caro et al., 2006; Bennett et al., 2007; Rizo et al., 2011; Saji et al., 2018). This value also overlaps with the analysis of one sample from the Narssaq ultramafic body ($\mu^{142}Nd$ = +11.6 ±2.2). Mantle-derived rock samples from ~3.8 Ga enclaves in the SOISB area yield slightly, but resolvably higher $\mu^{142}Nd$ values of +13.0±1.1 when compared to mantle-derived rocks from the ~100 Ma younger ISB ($\mu^{142}Nd$ = +9.8±1.0). In addition, we have measured three samples from the Ameralik dike swarm (including replicate digestions) that yield homogeneous $\mu^{142}Nd$ compositions of +3.8±1.1). This mean value is also indistinguishable from the value obtained by Saji et al. (2018) ($\mu^{142}Nd$ = +4.9±1.8; Fig. 2.2b). Two mafic rocks from the Ivisaartoq supracrustal belt, two mafic rocks samples from the Ameralik fjord region as well as one 2.0 Ga dike (including one replicate) from SW Greenland all bear small excesses in $\mu^{142}Nd$, ranging from +5.9±2.1 to +2.7±2.2 (Fig. 2.2c). To obtain a coherent set of coupled $^{143,142}Nd$ and ^{176}Hf data, samples that lack available ^{147}Sm-^{143}Nd or ^{176}Lu-^{176}Hf isotope data were also determined here (including all Ameralik dikes and the ~2.0 Ga Proterozoic dike). Ameralik dikes generally have strongly homogeneous $\varepsilon^{143}Nd_{(i)}$ values of +1.9±0.4 to +2.4±0.4, in good agreement with previous studies (Saji et al., 2018). Calculated $\varepsilon Hf_{(i)}$ values are similar to $\varepsilon^{143}Nd_{(i)}$ values but slightly higher (+2.6±0.4 to +2.9±0.4). In contrast, the 2.0 Ga dike show lower $\varepsilon^{143}Nd_{(i)}$ (+0.2±0.4) and $\varepsilon Hf_{(i)}$ values (+0.8±0.4).

Furthermore, two individual digestions of the geological reference material BHVO-2 gave $\mu^{142}Nd$ values of -0.2±2.1 and +1.0±1.8, respectively, in excellent agreement with previous results (Saji et al., 2016; Schneider et al., 2018; Hyung and Tissot, 2021). To further validate our method, we also measured the $\mu^{142}Nd$-$\mu^{143}Nd$ compositions for the different digestions of the reference material BHVO-2 that was doped with different amounts of sample 10-38, having an average $\mu^{142}Nd$ value of +12.5±2.0. Prior to digestion, sample powders were mixed at different proportions (25%, 50% and 75% of added BHVO-2). These mixing ratios should have resulted in $\mu^{142}Nd$ excesses of ~+9, +6 and +3 ppm and are in good agreement

with our observed values of +8.0±1.7, 5.5±1.8 and 1.6±1.9, respectively. The analysis of a La Jolla reference material yields slightly elevated μ^{142}Nd values of +2.6±2.5, in perfect agreement with previous results (Saji et al., 2016). Praseodymium-doped JNdi-1 standards measured here never revealed resolvably elevated μ^{142}Nd compositions (-0.9±3.6 to +1.3±1.4). We have also measured several modern rock samples and certified reference materials (Fig. 2.2d), including one intraplate basalt from the Eifel volcanic field in Germany (Ei-27), one intraplate basalt from the Hyblean Plateau in Italy (IBL-1), as well as the granite reference material JG-1 that have μ^{142}Nd values of +0.9±2.9, +1.0±1.9 and -0.4±1.4, respectively.

2.6. Discussion

2.6.1. Interferences and mass independent isotope effects

High precision ^{142}Nd/^{144}Nd isotope measurements are hampered by four isobaric interferences (^{142}Ce, ^{144}Sm, ^{148}Sm and ^{150}Sm). Due to the highly efficient redox chemistry (step III) and the final REE separation (step V), Ce monitors in our samples were always smaller than Ce monitors in our standard solutions (^{142}Ce/^{142}Nd typically below 4×10^{-7}), except for three samples that had insignificantly higher Ce interferences. For Sm interferences on mass 144, 148 and 150, our samples had always lower Sm monitors than our standard solutions, typically having a ^{144}Sm/^{144}Nd of 2×10^{-6}. Measurements of Ce and Sm doped standards (0.02 ppb Sm or Ce and 400ppb Nd) yielded ^{144}Sm/^{144}Nd and ^{142}Ce/^{142}Nd ratios of 2×10^{-5}. Both doped standards yielded μ^{142}Nd values that were indistinguishable from zero (-0.4±3.4 for Sm-doped JNdi-1, and +0.6±2.4 for Ce-doped JNdi-1).

In addition to isobaric interferences, ^{142}Nd/^{144}Nd analysis can be compromised by molecular interference of ^{141}PrH on ^{142}Nd as previously shown by Saji et al., (2016). To be able to eliminate analytical artifacts of ^{141}PrH on ^{142}Nd, we measured a Pr-doped JNdi-1 standard solution at the beginning of each measurement session that had Pr/Nd ratios slightly higher than chondritic (Pr:Nd > 1:7) which would be expected for highly enriched samples that underwent insufficient Pr-Nd separation. Surprisingly, measured Pr-doped standard solutions never revealed detectable analytical artifacts on ^{142}Nd, although Saji et al., (2016) reported excesses of up to ~+9 ppm in Pr-doped standard solutions with chondritic Pr/Nd ratios. Although the reasons for this discrepancy remain unknown, we speculate that this could be linked to the use of an X-skimmer cone (as done by Saji et al., (2016)) which might promote the formation of ^{141}Pr^{1}H interferences.

For high precision isotope measurements, high yields during chemical separation are essential. First, high yields allow performing replicate measurements at the highest signal intensities possible. Secondly, loss of material during chemical separation can induce mass independent isotope effects that might not be fully correctable, causing artificial isotope anomalies (Thirlwall, 1991; Wombacher and Rehkämper, 2003). We have analyzed the first 15% yield fraction of an LP-1, partly eluted during separation step V, revealing strong mass independent Nd isotope fractionations. This fraction bears strong mass independent

excesses of higher masses (μ^{150}Nd (6/4) = +45.3±5.4) and deficits (although not resolvable) on μ^{142}Nd (6/4) = -4.1±4.8). This finding is in excellent agreement with findings by Saji et al., (2016) who have conducted equivalent tests using the same ion exchange resin. These authors have concluded that this fractionation pattern is produced by nuclear field shift, in accord with results by Garçon et al., (2018), who observed similar nuclear field shift-induced fractionation patterns.

The mass independent fractionation caused by nuclear field shift might also be responsible for small deficits in μ^{150}Nd values found in some of our samples. Consequently, it has to be evaluated if a potential nuclear field would also affect μ^{142}Nd values, since our mass bias correction relies on accurate and unfractionated ^{148}Nd/^{144}Nd ratios. In contrast to the

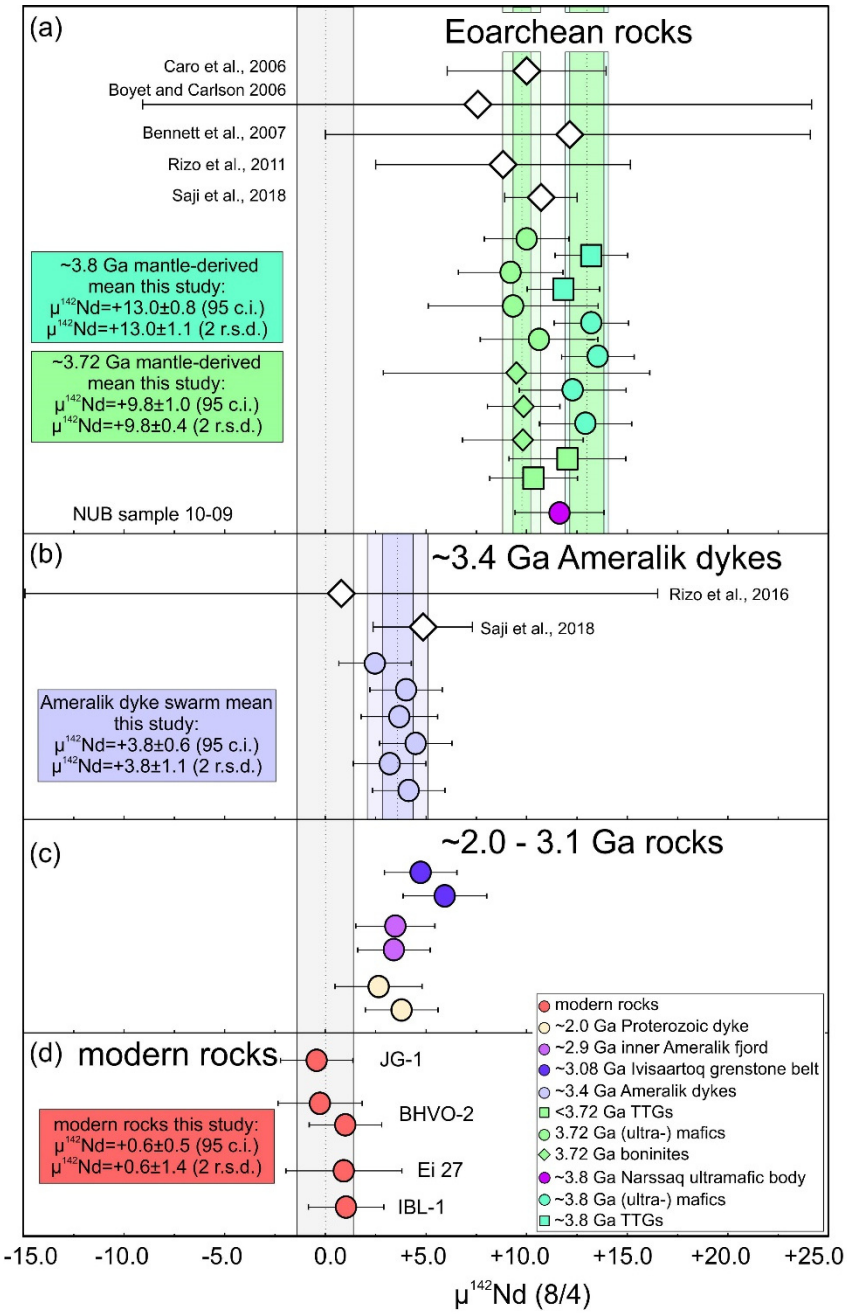

Fig. 2.2: ^{142}Nd/^{144}Nd isotope compositions of samples from SW Greenland and modern rocks. a) comparison of ~3.7 to ~3.8 Ga rocks from the ISB with previously reported literature data. All mean values obtained here overlap within error with previous studies. However, ~3.8 Ga (ultra-) mafic rocks from this study exhibit μ^{142}Nd excesses that can be statistically resolved from ~3.72 Ga mantle-derived rocks. One sample from the Narssaq Ultramafic body (purple) also reveals similar μ^{142}Nd excesses as ~3.7 to ~3.8 Ga Isua rocks, in line with their proposed Eoarchean age (van de Löcht et al., 2020). b) compositions of ~3.4 Ga Ameralik dyke swarm samples c) ^{142}Nd/^{144}Nd isotope composition of Mesoarchean to Proterozoic rocks from SW Greenland d) ^{142}Nd/^{144}Nd isotope composition of various modern terrestrial rocks and reference materials. The grey error band drawn throughout the figure depicts the intermediate precision of ±1.4 ppm (2 r.s.d.). Errors shown for individual samples are the 95% CI intervals, our intermediate precision of ±1.4 ppm is considered as minimum error. For literature means, the 2 r.s.d. are used. Literature data are compiled from several studies (Boyet and Carlson, 2006; Caro et al., 2006; Bennett et al., 2007; Rizo et al., 2011; Rizo et al., 2012; Saji et al., 2018).

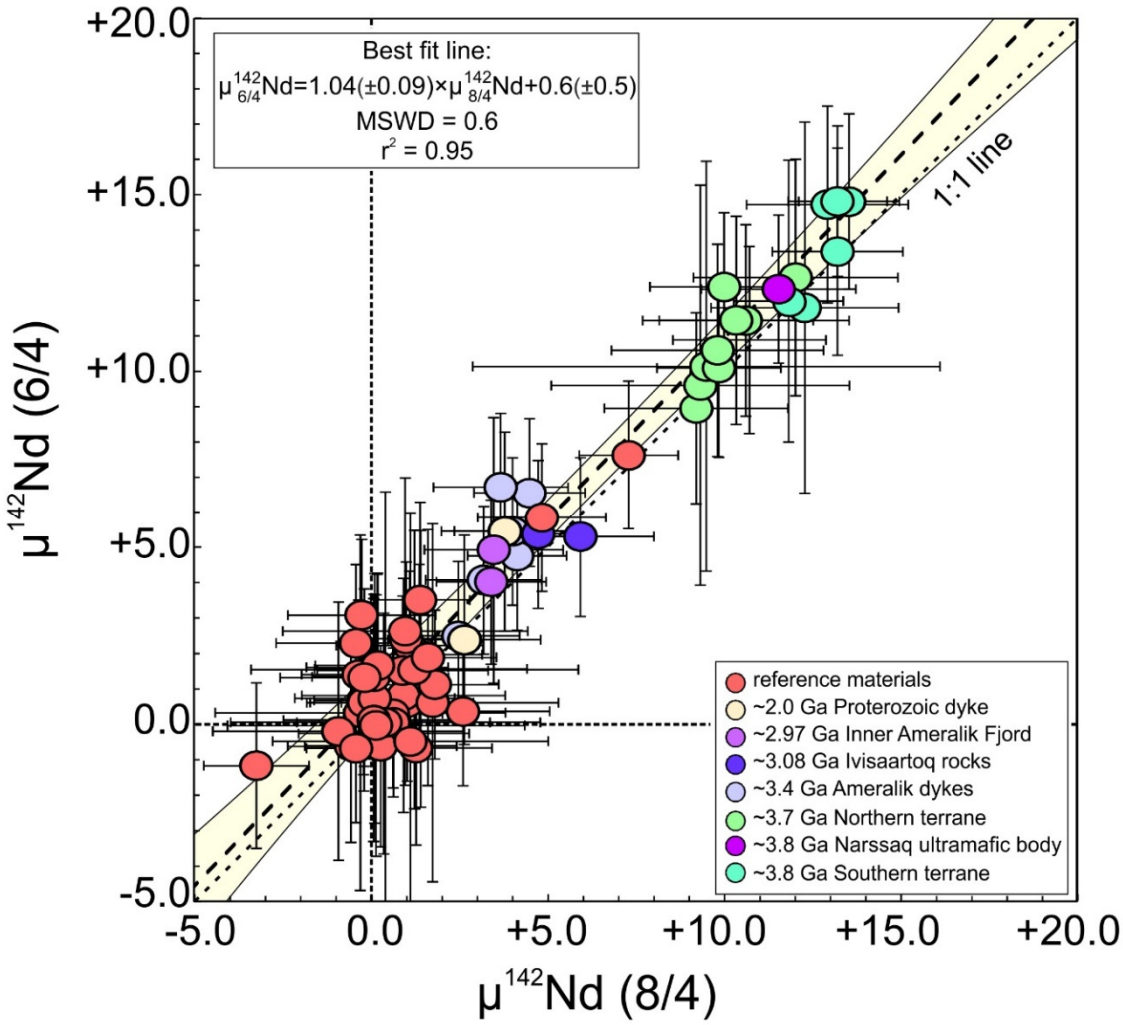

Fig. 2.3: Comparison of $^{148}Nd/^{144}Nd$ vs. $^{146}Nd/^{144}Nd$ corrected $^{142}Nd/^{144}Nd$ data that are expected to plot on a 1:1 line. The best-fit line intersects the x-axis at +0.6±0.5 with a slope of +1.04±0.09, implying that both mass bias corrections work properly.

slightly scattering $\mu^{150}Nd$ (8/4) of LP-1 analysis (+3.0±4.7 to -13.2±1.6), measured $\mu^{148}Nd$ values (6/4) remain unfractionated (-3.3±2.8 to +3.9±2.7). The LP-1 analysis with the strongest $\mu^{150}Nd$ (8/4) deficit -13.4±3.4 ppm still retains a $\mu^{142}Nd$ (8/4) value (+0.1±2.3) and a $\mu^{142}Nd$ (6/4) value (+0.7±3.5) that are indistinguishable from our long-term average for this reference material ($\mu^{142}Nd$ = +0.4±1.4 and $\mu^{142}Nd$ (6/4) = +1.1±2.1) (Extended Data Fig. 2.3). Such a magnitude of $^{150}Nd/^{144}Nd$ fractionation of was only exceeded by one sample (JEH 2007-04), where the $\mu^{150}Nd$ (8/4) value amounts to -14.6±2.3. A replicate digestion and analysis of that sample revealed identical $\mu^{142}Nd$ (8/4) (+4.5±1.6 and 4.0±1.6) and $\mu^{142}Nd$ (6/4) values (+6.6±1.7 and +5.5±1.5) at less fractionated $\mu^{150}Nd$ (8/4) Nd values (-14.6±2.3 and -10.3±3.7). Since fractionated $^{150}Nd/^{144}Nd$ compositions of less than -15 ppm did not induce any artificial effects on $\mu^{142}Nd$ (8/4) values, we take this as evidence that the effects on $^{142}Nd/^{144}Nd$ analysis are negligible, given the magnitude of mass independent Nd isotope fractionation found for our protocol. An insignificant contribution by nuclear field shift effects on ^{148}Nd isotope abundances is further verified in $^{146}Nd/^{144}Nd$ and $^{148}Nd/^{144}Nd$ corrected $^{142}Nd/^{144}Nd$ data as both mass bias corrections yield identical ^{142}Nd results. In $\mu^{142}Nd$ (6/4) vs. ^{142}Nd (8/4) space, all samples plot on the predicted 1:1 line (Fig. 2.3). We therefore conclude that a slight contribution of nuclear field shift might explain

our small scatter in ^{150}Nd isotope abundances for our LP-1 standard (and some other samples) whereas such effects are negligible for ^{148}Nd/^{144}Nd and consequently also for 8/4 corrected ^{142}Nd/^{144}Nd ratios, of which the variations are only caused by our statistical errors.

2.6.2. Method verification

Resolving isotope compositions at the ppm level is challenging due to the different interference and mass independent isotope effects described above. In order to carefully validate our separation and measurement protocol we took three approaches. (1) In order to cross-reference with previous studies (Boyet and Carlson, 2006; Caro et al., 2006; Bennett et al., 2007; Rizo et al., 2016; Saji et al., 2018), we measured ~3.72 to 3.8 Ga Isua rocks and ~3.4 Ga Ameralik dikes that were previously shown to exhibit homogenous μ^{142}Nd excesses of +10.5±1.8 ppm and +4.7±1.7, respectively (Saji et al., 2018) (Figs. 2.2a and b). (2) Additionally, we doped an excess-bearing sample (10-38) with an excess-free terrestrial reference material (BHVO-2) to verify that can we can resolve small predicted

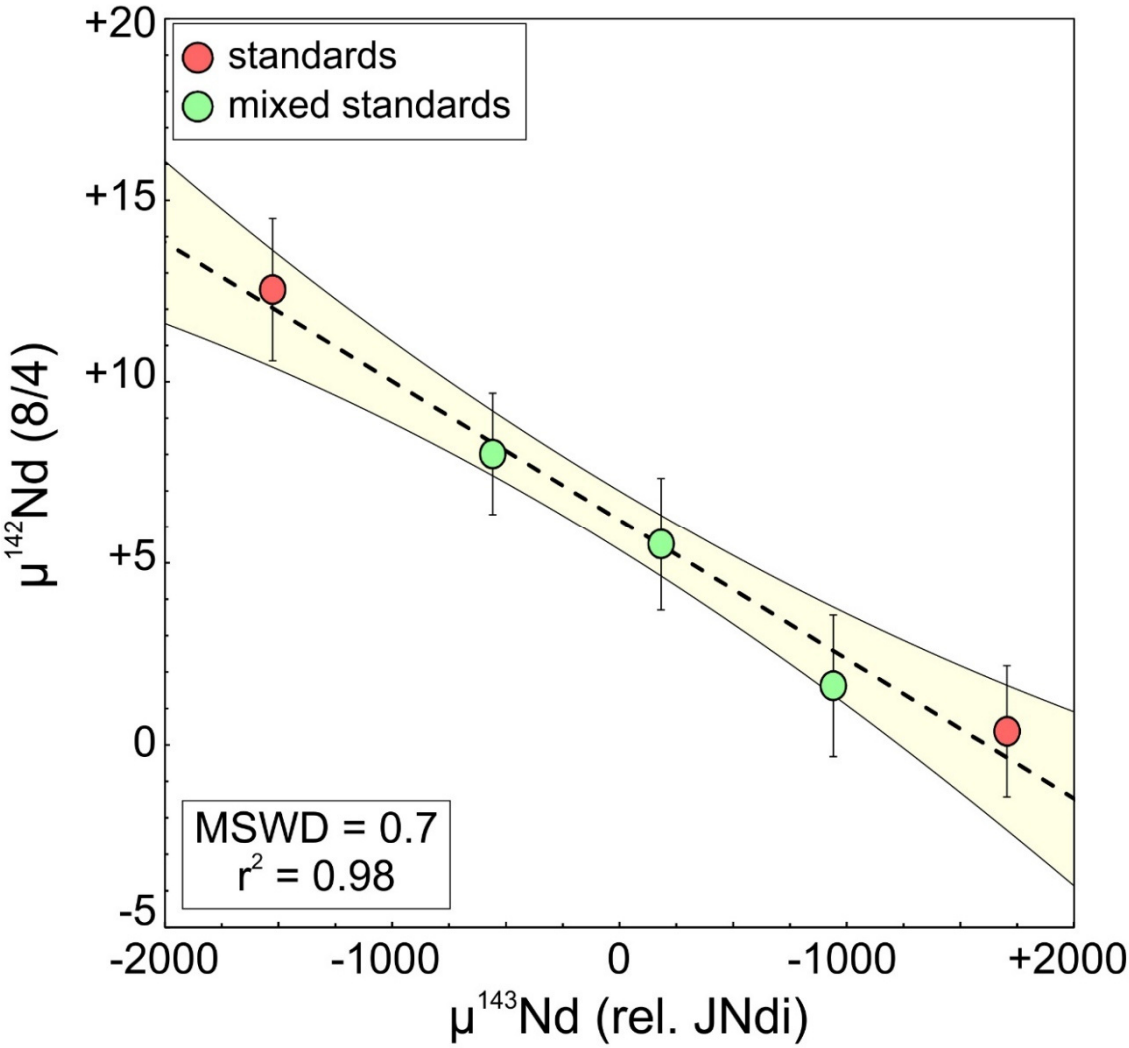

Fig. 2.4: Measured μ^{142}Nd vs. μ^{143}Nd compositions for processed reference material BHVO-2 that was doped with different amounts of SW Greenland sample 10-38 (green). Mean values for sample 10-38 (μ^{142}Nd=12.5±2.0)) and BHVO-2 (+0.4±1.8) are taken from this study (red). Errors for mixed standards are the same as in Figure 3 and for the two standard endmember compositions, the 2 r.s.d. from their respective mean value was used.

anomalies (Fig. 2.4). (3) We performed repeated digestions and analysis of our in-house reference material LP-1 to obtain an intermediate precision of $^{142}Nd/^{144}Nd$ analysis (Extended Data Fig. 2.3).

Individual ~3.7-3.8 Isua samples from this study exhibit $\mu^{142}Nd$ values that range from +9.2±2.6 to +13.6±1.4. Our ~3.7-3.8 Isua rocks yield a mean $\mu^{142}Nd$ value of +11.2±3.4, in good agreement with the mean MC ICP-MS value obtained by Saji et al. (2018) ($\mu^{142}Nd$ = 10.7±1.8) but is also in good agreement with results from previous TIMS studies (Boyet and Carlson, 2006; Caro et al., 2006; Bennett et al., 2007; Rizo et al., 2016) (Fig. 2.2a). Furthermore, we digested, and analyzed three different Ameralik dike samples (10-41, SG-03 and JEH 2007-04) twice, with the individual replicates overlapping with each other within ≤0.5 ppm. Our $\mu^{142}Nd$ mean value for the Ameralik dikes amounts to +3.8±1.1 and is in excellent agreement with the mean value obtained by Saji et al., (2018) ($\mu^{142}Nd$ = +4.7±1.7), but does not confirm the strongly heterogeneous compositions reported by Rizo et al., (2012) (Fig. 2.2b). Considering the strongly fractionated mass-independent Nd isotope compositions ($\mu^{150}Nd$ up to +42.4; $\mu^{145}Nd$ up to +15.3) reported by Rizo et al. (2012), we speculate that their negative $^{142}Nd/^{144}Nd$ isotope compositions reported for Ameralik dikes rather represent analytical artifacts, a conclusion that was previously also drawn by Saji et al. (2018).

The results of the mixing test of the excess-bearing sample 10-38 mixed with different amounts of BHVO-2 reference material is also in good agreement with the expected $^{142}Nd/^{144}Nd$ compositions. When plotted in $\mu^{142}Nd$ vs. $\mu^{143}Nd$ space, combined powders of BHVO-2 and sample 10-38 constitute a straight mixing line between the respective endmember compositions, demonstrating the accuracy and precision of our data (Fig. 2.4).

Finally, we have measured juvenile volcanic rocks that are not expected to carry anomalous $^{142}Nd/^{144}Nd$ compositions, comprising one intraplate basalt from the Quaternary Eifel volcanic field in Germany (Ei-27), one intraplate basalt from the Hyblean Plateau on Sicily (IBL-1) as well as the two terrestrial reference materials JG-1 and BHVO-2 (Fig. 2.2d). Our results for BHVO-2, including a replicate analysis, amount to a mean $\mu^{142}Nd$ = +0.4±1.8 (2r.s.d.), in excellent agreement with previous data (Burkhardt et al., 2016; Saji et al., 2016; Garçon et al., 2018; Schneider et al., 2018; Hyung and Tissot, 2021; Wang and Carlson, 2022). Furthermore, the analysis of a La Jolla reference material reveal mass-independent isotope effects for the different Nd masses ($\mu^{142}Nd$ = +2.6±2.5, $\mu^{145}Nd$ = -5.7±2.1 and $\mu^{150}Nd$= +13.3±4.3), in good agreement with previous MC ICP-MS results (Saji et al., 2016). Multiple analysis (N = 23) of seven different digestions from our in-house reference material LP-1 (historical La Palma basalt) that were processed and analyzed together with our samples, were used to determine our intermediate precision. They yield an average $\mu^{142}Nd$ value of +0.5±1.4 (2r.s.d.) and +1.0±2.2 (2r.s.d.) if normalized to 8/4 and 6/4, respectively (Extended Data Fig. 2.3). We consider this intermediate precision as minimum error for our $^{142}Nd/^{144}Nd$ measurements. Due to its superior intermediate precision, we prefer the 8/4 correction, and, if not stated differently this normalization is used hereafter.

2.6.3. μ^{142}Nd excesses in Greenland rocks

2.6.3.1. ^{142,143}Nd differentiation model ages

Coupled ^{147,146}Sm-^{143,142}Nd isotope systematics are a powerful tool to unravel planetary silicate differentiation processes. By combining these two decay series, it is possible to determine the timing of ancient mantle depletion, since the slope in μ^{142}Nd and $\varepsilon^{143}Nd_{(i)}$ space is a function that depends on the differentiation age (e.g., Harper and Jacobsen, 1992; Caro et al., 2003; Bennett et al., 2007). However, this application relies on determining accurate μ^{142}Nd and $\varepsilon^{143}Nd_{(i)}$ values of a mantle reservoir at a given age.

The major problem for calculating accurate ^{142,143}Nd/^{144}Nd model ages arises from inaccurate $\varepsilon^{143}Nd_{(i)}$ values (Fig. 2.5). To minimalize these effects we did not extrapolate samples to one uniform crystallization age, since the calculation $\varepsilon^{143}Nd_{(t)}$ values at any other time than their crystallization ages creates biased $\varepsilon^{143}Nd_{(t)}$ values. Instead, we have only considered samples that cluster in a very narrow age range (≤±30 Ma), causing insignificant propagated uncertainties on $\varepsilon^{143}Nd_{(i)}$ values. Moreover, TTGs were excluded here since they are the product of remelting older precursor rocks (Hoffmann et al., 2011a). Schneider et al., (2018) were able to show that the μ^{142}Nd anomalies found in TTGs often seem to have a higher magnitude compared to contemporaneous mantle-derived rocks which would cause further bias in our approach (Fig. 2.2a). This is also in accord with a 3.715 Ga TTG sample from this study (229403) that seems to have higher μ^{142}Nd values compared to contemporaneous (ultra-) mafic rocks (Fig. 2.2a). Furthermore, a variable crustal residence time between the emplace of the mafic precursor rocks and the subsequent TTG extraction can also lead to variable $\varepsilon^{143}Nd_{(i)}$ values, causing further scatter in this model age approach.

For the reasons above, our data set is restricted to mantle-derived samples that fall into a narrow age range of 3.8±0.030 Ga. As already suggested in previous studies, we have also included ^{142}Nd-^{143}Nd data from the Eastern Superior Craton as they likely were affected by the same differentiation event (Caro et al., 2017; Morino et al., 2017; Saji et al., 2018). In In this way we can combine our data with literature data from the near-contemporaneous ~3.78 Ga Saglek Block and the 3.78 Ga Nuvvuagittuq Greenstone Belt (O'Neil et al., 2008; Morino et al., 2017) to infer a differentiation model age for the North Atlantic Craton and Eastern Superior Province. We have also included samples from the Ukaliq Greenstone Belt (Caro et al., 2017) for which it was shown to have a close genetic link and a similar emplacement ages as the ~3.78 Ga Nuvvuagittuq Greeenstone Belt (Cates et al., 2013; Chowdhury et al., 2020). Our inferred model age including all samples amounts to $4.347 \pm^{0.005}_{0.005}$ Ga and is in good agreement with previous studies that vary between ~4.32 to ~4.53 Ga (Caro et al., 2003; Boyet and Carlson, 2005; Caro et al., 2006; Bennett et al., 2007; Rizo et al., 2011; Morino et al., 2017; Morino et al., 2018; Saji et al., 2018). Notably the highest inferred model ages of ~4.5 (Boyet and Carlson, 2005; Bennett et al., 2007; Rizo et al., 2012) is likely linked to the assumption that bulk Earth has a 20 ppm lower μ^{142}Nd composition, which created steeper slopes in the ^{142}Nd-^{143}Nd arrays that has led to higher inferred differentiation model ages.

Despite our screening, accurate ^{142}Nd-^{143}Nd differentiation model ages are still hampered by the large scatter of $\varepsilon^{143}Nd_{(i)}$ values (Fig. 2.5). This could imply that in some samples the long-lived ^{147}Sm-^{143}Nd systematics have been modified due to multiple differentiation events, magma mixing (i.e., added slab melts or crustal contamination) or post-magmatic alteration (e.g., Moorbath et al., 1997; Frei et al., 2002; Hoffmann et al., 2011b; Caro et al., 2017). For example, one sample from this study and one sample from the Saglek block (Morino et al., 2017) even plot in the forbidden zone of this isochron (Fig. 2.5a). This is also the case for sample PB-3 from (Saji et al., 2018) that has not been included here as it belongs to the younger ~3.7 Ga ISB. On the other hand, some of the samples from the Nuvvuagittuq Greenstone Belt (O'Neil et al., 2008) have positive $\varepsilon^{143}Nd_{(i)}$ of ~+2 despite negative μ^{142}Nd values. When applying a screening for samples that fall off the ^{142}Nd-^{143}Nd array, a higher inferred age of $4.387 \pm^{0.007}_{0.007}$ Ga can be calculated. Although these ages pretend errors of <10 Ma, they clearly suffer from poor

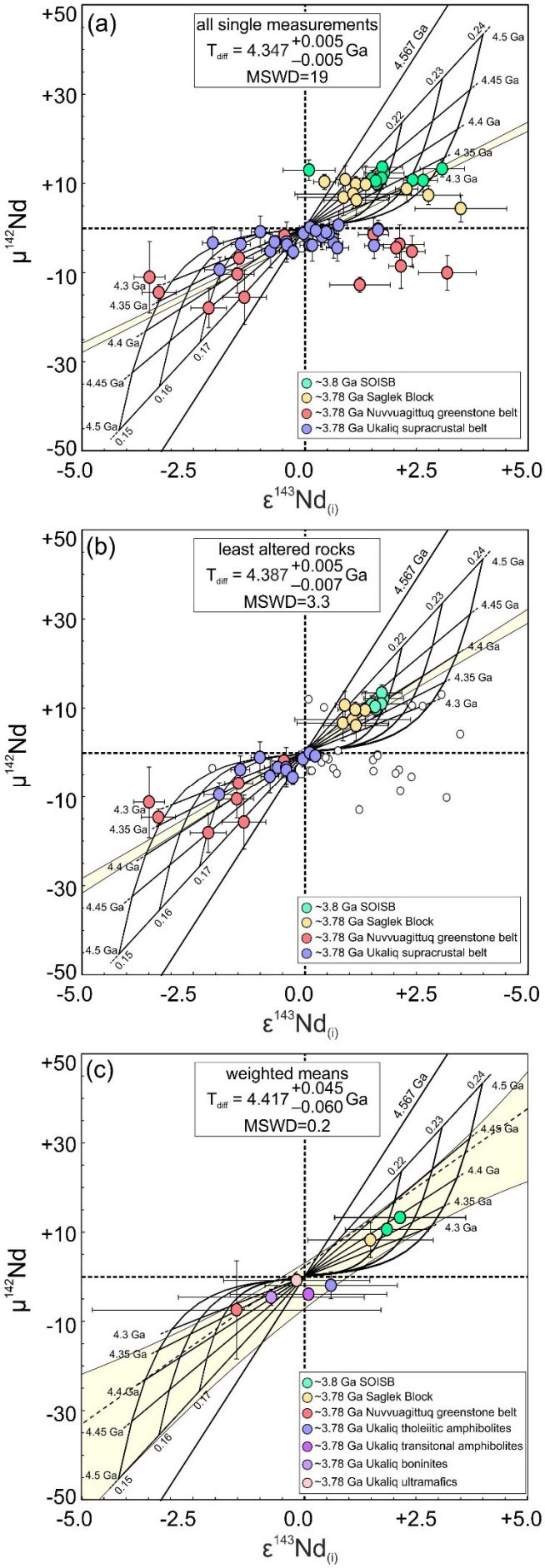

Fig. 2.5: Plot illustrating coupled ^{142}Nd-^{143}Nd data and single stage differentiation ages for samples from the North Atlantic Craton and the Superior Province. a) Plot showing all data from the SOISB, Saglek Block, Superior Province and the Ukaliq Supracrustal Belt, (O'Neil et al., 2008; Caro et al., 2017; Morino et al., 2018; Saji et al., 2018). b) Plot excluding samples that are considered as being altered (still shown as white circles). c) Same datasets as in a) but using weighted means. Data with resolvable negative μ^{142}Nd values at $\varepsilon^{143}Nd_{(i)} \geq +2$ are excluded here since these data clearly indicate open system behavior of the ^{147}Sm-^{143}Nd system or multi-stage evolution. We only included mantle-derived rocks that fall in an age range of 3.78±0.03 Ga. For samples by Saji et al., (2018) the sample locations were re-examined and we included only the samples that belong to the ~3.8 Ga old assemblages from the southern terrane. Errors displayed for μ^{142}Nd are the same as in Figs. 3 and 6.

accuracy since this age does not even overlap within error with the inferred age that comprises all data (Fig. 2.5a-b). High MSWDs from 3.3 to 19 further illustrate scatter far beyond analytical uncertainties. When only considering mean values for different localities as suggested earlier (Caro et al., 2017; Morino et al., 2017; Saji et al., 2018), the inferred model age amounts to $4.417 \pm^{0.045}_{0.060}$ Ga (Fig. 2.5c). Using means for different sample localities seems to provide the best way to calculate coupled ^{142,143}Nd differentiation ages as the errors of the averaged $\varepsilon^{143}Nd_{(i)}$ values for different localities will increase with increasing $\varepsilon^{143}Nd_{(i)}$ heterogeneity. Consequently, a higher scatter in $\varepsilon^{143}Nd_{(i)}$ values will cause a higher error for the inferred means that will be weighted less when calculating error propagated differentiation model ages. We conclude that the calculation of accurate and precise ^{142}Nd-^{143}Nd differentiation model ages is not limited by the precision of ^{142}Nd/^{144}Nd analysis but is mainly controlled by $\varepsilon^{143}Nd_{(i)}$ values that might have been modified by multiple differentiation events or post-magmatic alteration. For this reason, the $4.417^{+0.045}_{-0.060}$ Ga differentiation age seems the most plausible since it offers the best possibility to account for modified $\varepsilon^{143}Nd_{(i)}$ values. This age is also in good agreement with terrestrial differentiation age estimations that were inferred from independent isotope approaches (Wilde et al., 2001; Allègre et al., 2008; Mukhopadhyay, 2012).

2.6.3.2. Significance of long-lived Hf and Nd isotope data

Eoarchean rocks from the Isua area are known to exhibit decoupled $\varepsilon Hf_{(i)}$- $\varepsilon^{143}Nd_{(i)}$ values ratios, showing predominantly elevated $\varepsilon Nd_{(i)}$ values at near-chondritic $\varepsilon Hf_{(i)}$ values. For a long time, it has been argued whether or not this decoupling (especially the Isua region) is a pristine magmatic feature or induced during late-stage metamorphism (Bennett et al., 1993; Moorbath et al., 1997; Hoffmann et al., 2010; Hoffmann et al., 2011b; Rizo et al., 2011; Hoffmann et al., 2012; Hoffmann et al., 2014; Rizo et al., 2016; van de Löcht et al., 2020).

Our high precision ^{142}Nd/^{144}Nd isotope can cast new light on this debate. Previous studies invoked three scenarios to explain the observed Hf Nd isotope decoupling: (I) Perovskite fractionation in a deep magma ocean; (II) fluid-controlled alteration in a subduction-zone-like setting or late-stage metamorphism or (III) slab melt addition in a subduction setting (Hoffmann et al., 2011b; van de Löcht et al., 2020). If the variations and the decoupling $\varepsilon Hf_{(i)}$ and $\varepsilon^{143}Nd_{(i)}$ values is attributed to fractionation in an early magma ocean, this should also produce variable μ^{142}Nd anomalies that correlate with $\varepsilon Hf_{(i)}$ and $\varepsilon^{143}Nd_{(i)}$ values. In contrast, slab melt addition within a subduction zone setting would produce variable scatter in μ^{142}Nd. Depending on the age of the extracted slab melt precursor rocks, ^{146}Sm might have become functionally extinct by that time. In contrast, any late-stage metamorphism (^{146}Sm is completely extinct), will affect ^{147}Sm-^{143}Nd but leave no imprint on ^{142}Nd/^{144}Nd compositions.

It has been experimentally shown by Corgne et al., (2005) that extensive crystallization of perovskite would severely fractionate high field strength elements (HFSE) from REE. The fractionation strongly depends on the proportions of Ca and Mg perovskite since Ca perovskite has a D_{Lu}/D_{Hf} >1 whereas Mg perovskite has a D_{Lu}/D_{Hf} <1. Taking this into

consideration, previous studies (Caro et al., 2005; Hoffmann et al., 2011b; Rizo et al., 2011) have postulated a perovskite-related origin of the Isua source which can account their decoupling of Hf and Nd isotopes. We have remodelled trace element as well as Hf-Nd isotope data in Ca-Mg perovskite cumulates the coherent partition coefficients of (Corgne et al., 2005) and a recently proposed range Ca-Mg perovskite proportions for the terrestrial magma ocean (2% to 10% Ca-perovskite) (Caro et al., 2005; Hoffmann et al., 2011b; Rizo et al., 2011). We assumed different degrees of equilibrium crystallization (5 to 50%) and a primitive mantle composition (Palme and O'Neill, 2013) with previously reported pervoskite partition coefficients (Corgne et al., 2005) (see Appendix A2 for partition coefficients, trace elements and isotope results). In contrast to previous studies, our modelling approach reveals that the perovskite model has three major problems.

(1) The proportions of Ca- and Mg-perovskite used in previous models (Caro et al., 2005; Hoffmann et al., 2011b; Rizo et al., 2011) would severely fractionate Th-Ti and HFSE from the REE (such as Hf/Sm or Th/La; see also Extended Data Fig. 2.4 and 2.5). The ubiquitous negative Nb-Ta anomalies in Isua rocks are inconsistent with a perovskite cumulate origin that would produce no or slightly positive Nb-Ta anomalies. Other HFSE-related geochemical features (e.g. Zr-Hf anomalies) further strongly argue against a perovskite involvement in the petrogenesis of Isua rocks since positive Zr-Hf anomalies should be directly linked to negative $\varepsilon Hf_{(i)}$ values (and vice versa), a feature that is not observed in Isua rocks (Extended Data Fig. 2.4a).

(2) Segregating pervoskite cumulates would have very uniform Nb/Ta ratios of ~10, and Zr/Hf ratios of 33 to 34 fairly independent of Ca and Mg pervoskite proportions or crystallization grades. However, there are only two samples that display Nb/Ta ratios of ~11, whereas all other samples have higher and variable Nb/Ta ratios that often reach values >14 (Hoffmann et al., 2010; Tusch et al., 2019; van de Löcht et al., 2020). Concurrently, many ISB rocks have significantly lower Zr/Hf ratios than 33 with ratios as low as 28, in good agreement with those of modern day MORBs (Münker et al., 2003). The prevalence of ISB rocks with Zr/Hf ratios lower than the modelled perovskite source implies that a perovskite cumulate source is not depleted enough. In fact, this issue exists for many other geochemical parameters, such as Th/La, Hf/Sm or Th/Nb, that are all lower in mantle-derived rocks from the Isua region than the modeled perovskite cumulate. Since all of the aforementioned element ratios increase during partial melting or fractional crystallization, perovskite cumulate sources cannot explain samples with lower Th/La, Hf/Sm, La/Sm or Th/Nb ratios (Extended Data Fig. 2.4).

(3) Most importantly, if the observed variable $\varepsilon^{143}Nd_{(i)}$ values present in ~3.72 and ~3.8 Ga rocks were explained in a single stage perovskite model with varying Ca-perovskite proportions, samples with higher $\varepsilon^{143}Nd_{(i)}$ would also be expected to have the highest $\mu^{142}Nd$ values, an observation that is not matched here by the data. Instead, mantle-derived rocks of the same age show a decoupling of $\mu^{142}Nd$ and $\varepsilon^{143}Nd_{(i)}$ values, with $\mu^{142}Nd$ values remaining constant at variable $\varepsilon^{143}Nd_{(i)}$ values (Figs. 2.5 and 2.6).

Tapping the complementary enriched reservoir (cf. Puchtel et al., 2016) that has formed after perovskite fractionation also does not fit the trace element and isotope constraints. Such a reservoir would have subchondritic Sm/Nd ratios, which should have produced

negative μ^{142}Nd and $\varepsilon^{143}Nd_{(i)}$ values over time, a feature that is not observed (Bennett et al., 1993; Moorbath et al., 1997; Boyet and Carlson, 2005; Caro et al., 2006; Hoffmann et al., 2010; Hoffmann et al., 2011b; Rizo et al., 2011; Hoffmann et al., 2012; Rizo et al., 2012; Hoffmann et al., 2014; Rizo et al., 2016; van de Löcht et al., 2020). Furthermore, due to the high partition coefficients for Th within Ca-Pv (D_{Th} = 8 to 18) (Corgne et al., 2005), Th will be strongly sequestered into the Pv-cumulates, leaving behind a Th-depleted complementary reservoir, also contradicting trace element observations from the ~3.8 to ~3.7 Ga mantle-derived rocks (Polat et al., 2002; Polat and Hofmann, 2003; Hoffmann et al., 2010; Hoffmann et al., 2011b; Tusch et al., 2019; van de Löcht et al., 2020). Considering the trace element and isotope constraints discussed above, we therefore conclude that a perovskite-related origin for the geochemical patterns in Eoarchean rocks from Isua is unlikely.

In addition to the decoupling of long-lived Hf and Nd isotopes, we also observe a decoupling of $\varepsilon^{143}Nd_{(i)}$ and μ^{142}Nd values. While μ^{142}Nd values are uniform in the ~3.7 and ~3.8 Ga terrane, $\varepsilon^{143}Nd_{(i)}$ values are strongly divers. Instead of a magma ocean model, the decoupling of ^{142,143}Nd/^{144}Nd and ^{176}Hf/^{177}Hf compositions can be rather ascribed to two other processes. Either the mantle source was added an enriched component that had a different Nd isotope composition than the Isua source or, alternatively, the decoupling of μ^{142}Nd and $\varepsilon^{143}Nd_{(i)}$ values represents post-magmatic alteration (≤3.72 Ga) of the ^{147}Sm-^{143}Nd systematics that no longer affected the extinct ^{146}Sm-^{142}Nd systematics. Although post-magmatic alteration would cause heterogeneous $\varepsilon^{143}Nd_{(i)}$ values at homogenous μ^{142}Nd values which is similar to our observations, the preservation of whole rock isochrons that are in good agreement with the accepted ages rather argues against wide open system behaviour of the ^{147}Sm-^{143}Nd system (Hoffmann et al., 2010; Hoffmann et al., 2011b). The same decoupling of $\varepsilon^{143}Nd_{(i)}$ and μ^{142}Nd values is also expected when the Isua source is added an enriched component with decreased $\varepsilon^{143}Nd_{(i)}$ values but identical μ^{142}Nd values. This can be achieved when the enriched component was differentiated rather late (after 4.0 Ga), when ^{146}Sm went functionally extinct. Given that many samples have rather too low $\varepsilon^{143}Nd_{(i)}$ (with respect to their elevated μ^{142}Nd values) and show strongly enriched trace element patterns (Polat et al., 2002; Polat and Hofmann, 2003; Hoffmann et al., 2010; Hoffmann et al., 2011b; van de Löcht et al., 2018; Tusch et al., 2019), the admixture of an enriched component (possibly felsic slab melts, or TTG assimilation) seems reasonable, (Polat et al., 2002; Hoffmann et al., 2010; Hoffmann et al., 2011b). We therefore argue that the trace element and Hf-Nd isotope systematics for the northern and southern terrane are rather explained by a complex subduction-like setting for the ISB, involving a depleted Isua mantle source that was overprinted by a more enriched component (likely adakitic melts) (Polat et al., 2002; Hoffmann et al., 2010; Hoffmann et al., 2011b; van de Löcht et al., 2020).

Considering our favored ^{142,143}Nd model age of ~4.42 Ga (Fig. 2.5c) and a μ^{142}Nd excess of ~+13 ppm in ~3.8 Ga rocks, ^{147}Sm/^{144}Nd ratios ≥0.22 are required to reproduce the isotope compositions of the Isua mantle source. At ~3.7 to ~3.8 Ga, this is equivalent to an ε^{143}Nd of ≥+1.8, meaning that any ε^{143}Nd significantly lower than this value rather reflects the increasing influence of an enriched component. This is further supported by the composition of some ISB samples that have μ^{142}Nd-$\varepsilon^{143}Nd_{(i)}$ values that plot in the

forbidden range of the ^{142}Nd-^{143}Nd isochron (i.e. require differentiation ages >4.568Ga) (Fig. 2.5a; sample 10-34 from this study and sample PB-3 from (Saji et al., 2018) (not shown). Our findings are in line with the involvement of an enriched component mixed into the Isua mantle source that is likely also responsible for earlier decoupled Hf-Nd isotopes (Hoffmann et al., 2010; Hoffmann et al., 2011b; Rizo et al., 2012).

2.6.3.3. Neodymium isotope evolution of the Isua mantle source through time

Anomalous ^{142}Nd/^{144}Nd isotope compositions for Eoarchean rocks from SW-Greenland have been reported by several studies (e.g., Caro et al., 2003; Boyet and Carlson, 2006; Caro et al., 2006; Bennett et al., 2007; Rizo et al., 2011; Rizo et al., 2012; Rizo et al., 2016; Morino et al., 2017; Saji et al., 2018). However, the origin of the Nd isotope signature in the mantle and its homogenization by the Archean mantle is still poorly understood. Our study can provide new constraints on the timescales of mantle dynamics.

It is known from several studies that during the Archean, ^{142}Nd/^{144}Nd anomalies have started to disappear, reflecting convective mantle homogenization (e.g., Boyet and Carlson, 2006; Caro et al., 2006; Bennett et al., 2007). Previous studies regarded the diminishing of ^{142}Nd/^{144}Nd anomalies to reflect one global scale process (Rizo et al., 2012; Saji et al., 2018; Schneider et al., 2018). Therefore, such mantle homogenization timescales might be too generalized, as every craton might behave differently. For example, the ~3.4 Ga Ameralik dikes show clearly resolvable μ^{142}Nd excesses, whereas even older 3.5 Ga rocks from the Pilbara Craton already show modern day like μ^{142}Nd values (Archer et al., 2019; Murphy et al., 2021). This either implies that the ~4.42 Ga differentiation signature is only of local significance, or, alternatively, mantle refertilization processes may have operated heterogeneously and locally different. Therefore, we avoid a comparison at a global scale and focused on rocks from the IGC and associated greenstone belts (Fig. 2.6).

To better understand the ^{142}Nd/^{144}Nd isotope mantle evolution over time, we have only considered mantle-derived metavolcanic rocks. Among our analyzed Isua samples, there are two peridotite samples from the ~3.8 Ga terrane of which one (10-34) is highly metasomatized whereas the other peridotite (10-27) belongs to the group of the least metasomatized peridotites (van de Löcht et al., 2020). As shown in Figure 2.2a, both ~3.8 Ga samples display identical μ^{142}Nd values. Considering a subduction-like setting as proposed for the ~3.8 to ~3.7 Ga Isua rocks (Polat et al., 2002; Polat and Hofmann, 2003; Hoffmann et al., 2010; Hoffmann et al., 2011b; Hoffmann et al., 2012; van de Löcht et al., 2020) implies that the refertilizing contaminant and the depleted Isua source must have had μ^{142}Nd compositions similar to that of the ambient Isua mantle. Otherwise, we would expect a higher diversity of μ^{142}Nd values, depending on the influx of subducted material. We conclude that, within analytical precision, these rocks still display the μ^{142}Nd composition of the uncontaminated mantle, despite their incorporated enriched component. Therefore, although contaminated, these rocks can still be used to place new constraints on mantle homogenization processes. The ~3.4 Ga Ameralik dike samples analyzed here have slightly depleted LREE compositions (La/Sm = 1.34 to 1.46) and reveal

Table 2.1: Modelling parameters used to calculate the adjusted Isua mantle source composition for the PRIMA, SCHEM, and SDEM replenishment model.

	PRIMA	SCHEM	SDEM
$^{147}Sm/^{144}Nd$	0.1960	0.2025[1]	0.2045
Adjusted time of Isua differentiation[2]	4.360	4.42	4.42
$\varepsilon^{143}Nd_{(i)}$ BSE at time of differentiation[3]	0.0	+0.1	+0.2
$\mu^{142}Nd$ BSE at time of differentiation[3]	0.0	-2.5	-4.8
$\mu^{142}Nd$ Isua source at 3.8 Ga	+13	+13	+13
Adopted $^{147}Sm/^{144}Nd_{source}$[3]	0.2310	0.2235	0.227
$\varepsilon^{143}Nd_{(3.8)}$ adjusted Isua source	+2.5	+2.3	+2.6

[1]SCHEM (Caro and Bourdon, 2010) was recalculated assuming a 10 ppm difference between BSE and the most terrestrial-like chondrites in contrast to the originally assumed ~20 ppm difference (see also **Chapter III** for further discussion), resulting in lower $^{147}Sm/^{144}Nd$ ratios than previously proposed.
[2]The differentiation age used here is the one calculated in this study (Fig. 2.5c). A slightly younger differentiation age of 4.36 Ga for the PRIMA-based refertilization model was assumed that still lies within our proposed uncertainties for the differentiation event. If the calculated 4.42 Ga differentiation age was assumed instead, the Isua source at 3.8 Ga would require lower Sm/Nd ratios to account for the +13 ppm $\mu^{142}Nd$ excess. This would also create lower $\varepsilon^{143}Nd_{(i)}$ values for the 3.8 Ga Isua source. After replenishing the Isua source with PRIMA material, the 3.4 Ga replenished Isua source would become too unradiogenic to account for a source for the Ameralik dikes. This issue was overcome by using a slightly lower differentiation age of 4.36 Ga.
[3]In a non-chondritic Earth model, $\varepsilon^{143}Nd$ values of BSE will become increasingly positive over time, whereas $\mu^{142}Nd$ will evolve from an initial $\mu^{142}Nd$ deficit of -10 ppm towards a present day $\mu^{142}Nd = 0$ (i.e., ~enstatite chondritic composition, see **Chapter III** for a more detailed discussion). Therefore, a non-chondritic BSE still had a deficit in its $\mu^{142}Nd$ composition that also needs to be considered here when calculating $^{147}Sm/^{144}Nd_{source}$ ratios.

depleted Th/La_{PM} ratios (0.654 to 0.865) (Tusch et al., 2019). We therefore conclude that they were not affected by an enriched component and regard them as mantle-derived rocks (see also Saji et al., 2018 who came to an identical conclusion).

All Mesoarchean to Proterozoic samples analyzed here also show elevated $\mu^{142}Nd$ compositions. These samples have enriched trace element characteristics (Th/La = 1.01 to 1.58; La/Sm = 1.78 to 3.15) and fairly unradiogenic $\varepsilon^{143}Nd_{(i)}$ values (+0.2 to +2.4). Therefore, it has been concluded that they have formed in geological settings where an older, enriched component was involved (Szilas et al., 2015a; Szilas et al., 2016). Considering that the decrease of $\mu^{142}Nd$ values between the oldest rocks of the IGC at ~3.8 Ga to the ~3.4 Ga Ameralik dikes (Nutman et al., 2004; Rizo et al., 2012) occurred rather rapid (Fig. 2.6), we would not expect resolvable $\mu^{142}Nd$ anomalies in these Mesoarchean to Phanerozoic rocks. In some of these Mesoarchean rocks, Szilas et al., (2015) have observed striking similarities of $\varepsilon^{143}Nd_{(3.8Ga)}$ and $\varepsilon^{143}Nd_{(3.8Ga)}$ with those reported for Isua boninites (Hoffmann et al., 2010). Therefore, it is rather likely that reworking of older crustal fragments during subduction reintroduced an older component (i.e. IGC crust) with elevated $\mu^{142}Nd$ values into the mantle. However, this process counteracts the diminishing of anomalous $^{142}Nd/^{144}Nd$ composition by mantle refertilization processes. Therefore, these rocks are not considered here to unravel mantle homogenization processes.

To explain the rapid decrease in ^{142}Nd excess from ~3.8 Ga to ~3.4 Ga mantle-derived rocks, we have conducted coupled $^{142,143}Nd/^{144}Nd$ isotope and trace element modelling (Table 2.1, Figs. 2.6 and 2.7). For ^{146}Sm-^{142}Nd isotope modelling, we have assumed a solar system initial $^{146}Sm/^{144}Sm$ ratio of 0.00828 and used a ^{146}Sm half-life of 103 Ma (Marks et al., 2014). Since the $^{142}Nd/^{144}Nd$ compositions of ~3.8 to ~3.4 Ga Isua mantle-derived rocks seem to

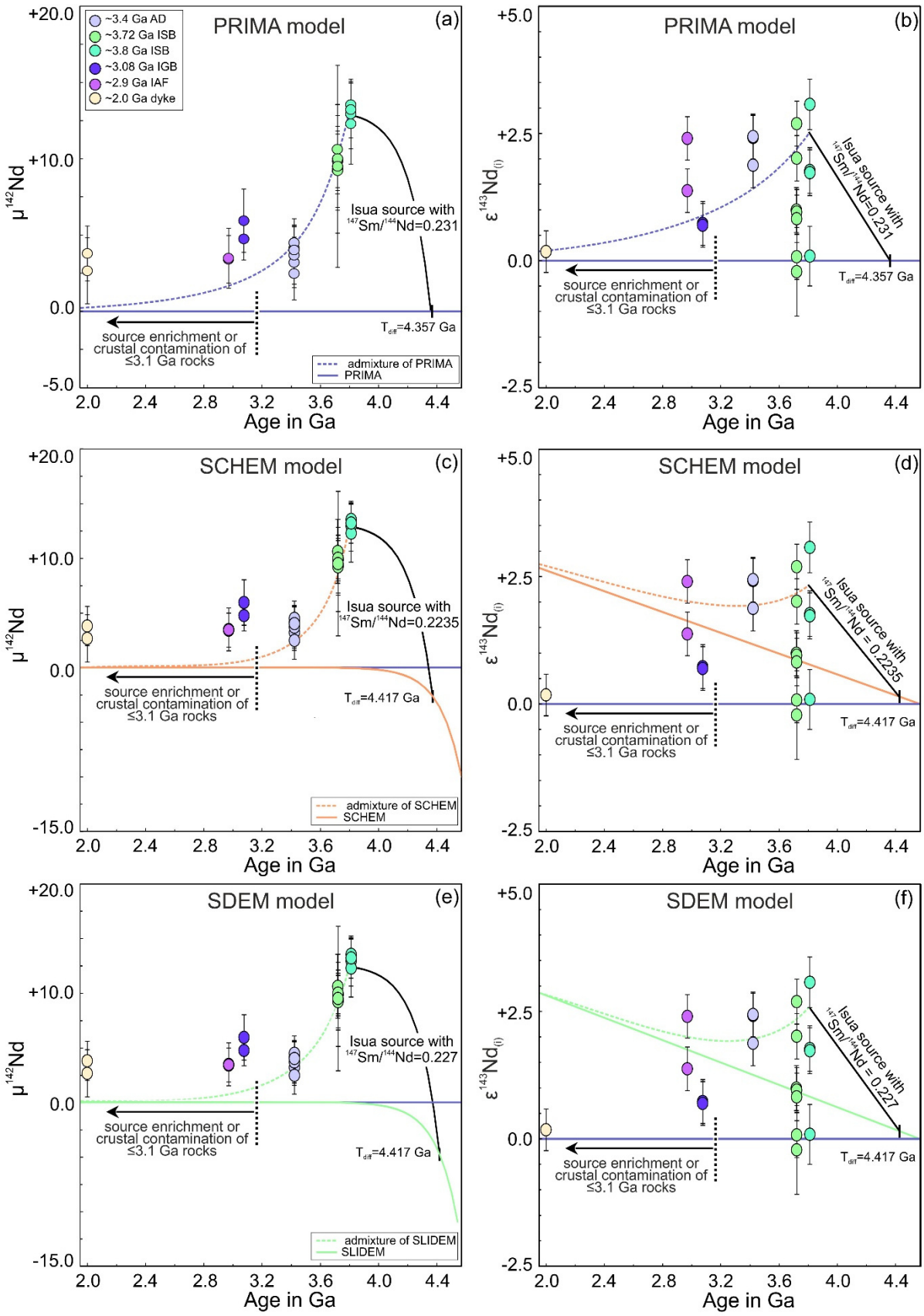

Fig. 2.6: Coupled $^{142,143}Nd/^{144}Nd$ evolution of the different mantle domains covered in this study over time. Shown is the evolution of the depleted Isua mantle source by assuming it was replenished with different bulk Earth compositions. In a) $\mu^{142}Nd$ and b) $\varepsilon^{143}Nd_{(i)}$ values are explained by replenishing the Isua source with primitive mantle material (PRIMA). In c) $\mu^{142}Nd$ and d) $\varepsilon^{143}Nd_{(i)}$ values are explained by replenishing the Isua source with superchondritic Earth Material (SCHEM) (Caro and Bourdon, 2010), whereas in e) $\mu^{142}Nd$ and f) $\varepsilon^{143}Nd_{(i)}$ values are explained by admixing a slightly depleted Earth-Moon composition (SDEM) (**Chapter III**). Isotope ompositions of the different reservoirs over time are

given in the Appendix A2. For our modelling approach, the Isua mantle was replenished with 17% primitive mantle (PRIMA) 30% of SCHEM and 26% SDEM over 100 Ma increments, all assumed to have a bulk Earth $^{142}Nd/^{144}Nd$ composition ($\mu^{142}Nd = 0$) at 3.8 Ga. In the SCHEM model, we assumed a more recently determined $^{142}Nd/^{144}Nd$ difference between Earth and enstatite chondrites of -10 ppm (Boyet et al., 2018) and based on that we re-determined the corresponding $^{147}Sm/^{144}Nd$ ratio of SCHEM to be 0.2025 (see also **Chapter III**). In both superchondritic Earth models, a 2-stage evolution is assumed. The first differentiation lead to a superchondritic BSE that is responsible for the evolution of BSE from $\mu^{142}Nd = -10$ towards $\mu^{142}Nd = 0$. The second differentiation at 4.417 Ga, as constrained here (Fig. 2.5c), is responsible for the elevated $\mu^{142}Nd$ compositions found in Isua rocks. However, at 4.417 Ga the $^{142}Nd/^{144}Nd$ composition of BSE is still decreased by ~2.5 ppm (SCHEM) or 4.8 (SDEM) due to incomplete decay of ^{146}Sm. At the same time, the recalculated $^{143}Nd/^{144}Nd$ composition will have evolved towards $\varepsilon^{143}Nd = +0.12$ (SCHEM) or +0.15 (SDEM). Both of these issues are compensated by using a ~3% (SCHEM) or 4% (SDEM) higher $^{147}Sm/^{144}Nd$ ratio for the Isua source (see also Table 2.1). For $\mu^{142}Nd$, errors are the same as in Fig. 3 and for $\varepsilon^{143}Nd_{(i)}$, errors are the propagated errors including the errors on parent/daughter ratios, crystallization age and our external reproducibility of ±0.4 ε-units on $^{143}Nd/^{144}Nd$ isotope ratios.

converge towards $\mu^{142}Nd = 0$, we assumed that the replenishing component must also had a $\mu^{142}Nd = 0$. Therefore, it seems unlikely that the admixture of sediments within an island arc setting was the driving force for decreasing $\mu^{142}Nd$ values, since ~3.7 to ~3.8 Ga Isua sediments were shown to have identical $^{142}Nd/^{144}Nd$ compositions as mantle derived rocks (Caro et al., 2003). Replenishing the Isua source with enriched material is also difficult, since it would also result in decreased $\varepsilon^{143}Nd$ values at 3.4 Ga, irreconcilable with the elevated $\varepsilon^{143}Nd_{(i)}$ values observed in the Ameralik dikes. Therefore, it seems more likely that bulk Earth material with $\mu^{142}Nd$ near 0 progressively diluted the depleted Isua mantle source. This implies that this material cannot have participated in the previous ~4.42 Ga differentiation event, suggesting that the previous differentiation event was not of

global character (Bennett et al., 2007). With respect to the ongoing debate whether Earth is chondritic or not (Boyet and Carlson, 2006; O'Neill and Palme, 2008; Caro and Bourdon, 2010; Burkhardt et al., 2016; Boyet et al., 2018), we have generated three individual models, with different assumptions for the accessible bulk Earth composition. They include a primitive mantle (PRIMA) (Palme and O'Neill, 2013), a SCHEM composition (Caro and Bourdon, 2010) and a slightly depleted Earth Moon (SDEM) composition (**Chapter III**). Since the SDEM and SCHEM models start with a chondritic, but subterrestrial $^{142}Nd/^{144}Nd$ composition ($\mu^{142}Nd = -10$) but superchondritic $^{147}Sm/^{144}Nd$ ratios, they will evolve towards a $\mu^{142}Nd = 0$ over time. As ^{146}Sm was functionally extinct by 3.8 Ga, all three reservoirs are assumed to have a $\mu^{142}Nd = 0$ (Table 2.1, Figs. 2.6c-f).

In our model, we have refertilized the depleted Isua source by admixing 17% PRIMA, 30% SCHEM or 26% SDEM material to the Isua source in incremental steps every 100 Ma (Fig. 2.6-2.8). For our trace element model, we have used peridotite 10-22 to represent the primordial depleted Isua mantle since that sample belongs to a group of peridotites that have inherited the least amounts of metasomatizing fluids and have been interpreted to be the best representatives of the Isua mantle source (van de Löcht et al., 2020). The admixture of the three less depleted materials will smoothen incompatible trace element patterns by obliterating Ti, Zr-Hf and Nb-Ta anomalies (Fig. 2.7). At ~3.4 Ga the mantle beneath the Isua region has achieved a slightly depleted incompatible trace element composition without significant anomalies, which is in good agreement with the predicted

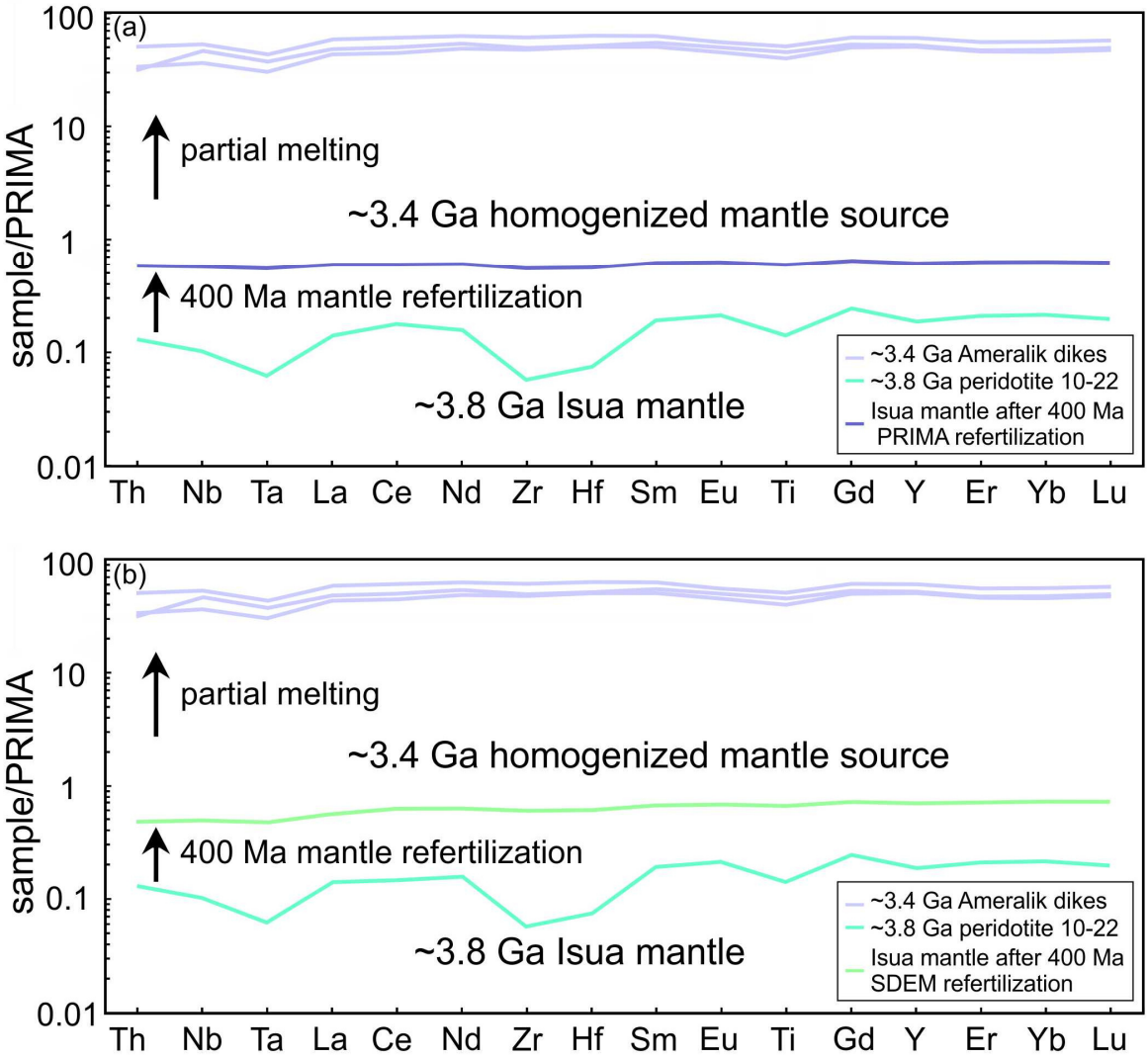

Fig. 2.7: Evolution of trace element compositions for the same model as in Fig. 6. Shown is the trace element composition of the homogenized mantle source at 3.4 Ga after being replenished for 400 Ma with BSE material (i.e. SDEM or PRIMA). At 3.4 Ga, the homogenized mantle source is flat without having any Zr-Hf or Nb-Ta anomalies. The modelled trace element pattern of our homogenized mantle source therefore can well explain the flat trace element patterns of contemporaneous 3.4 Ga Ameralik dykes (shown for comparison). For the Isua mantle source, the composition of a mantle peridotite type 1 (sample 10-22) was assumed to be representative of the mantle beneath the Isua region at 3.8 Ga (van de Löcht et al., 2020). Due to a lack of coherent trace element composition constraints for SCHEM, trace elements were only modelled for PRIMA and SDEM. Trace element data for the Ameralik dikes is taken from Tusch et al., (2019). Trace element compositions are listed in Appendix A2.

one for the Ameralik dikes (Figs. 2.6b, 2.6f and 2.7). At the same time, our replenishing model will cause a decrease of $^{142}Nd/^{144}Nd$ anomalies and buffer $\varepsilon^{143}Nd$ from becoming too radiogenic at 3.4 Ga (Fig. 2.6). The admixture of depleted material (SCHEM or SDEM) both create similar Nd isotope evolutions (Caro and Bourdon, 2010, **Chapter III**). While $\mu^{142}Nd$ values converge towards $\mu^{142}Nd = 0$, $\varepsilon^{143}Nd$ values first decrease over a short period of ~300 Ma and subsequently evolve towards slightly elevated $\varepsilon^{143}Nd_{(i)}$ values. In the PRIMA model, the Isua mantle evolves towards $\varepsilon^{143}Nd$ and $\mu^{142}Nd$ values that both converge at 0 (Figs. 2.6a and 2.6b). All three models can well explain the observed $\varepsilon^{143}Nd$ and $\mu^{142}Nd$

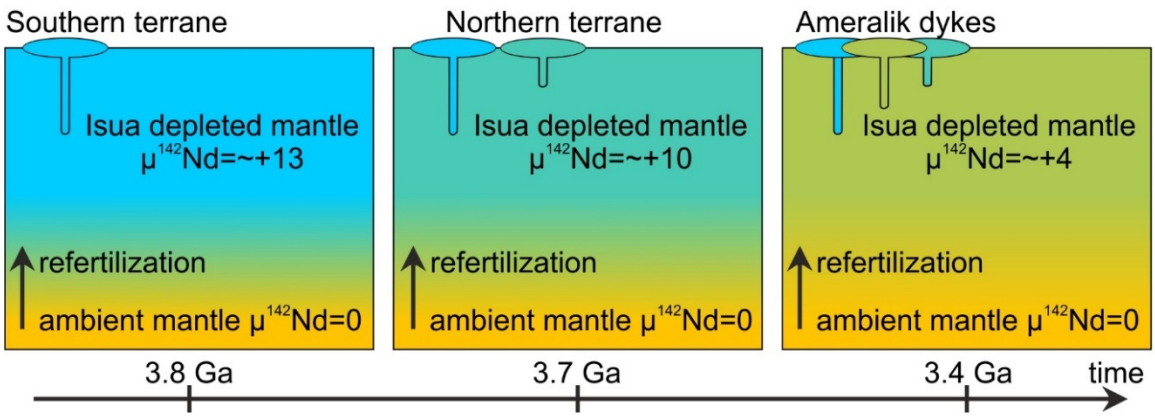

Fig. 2.8: Schematic model illustration the homogenization of $^{142}Nd/^{144}Nd$ anomalies in the Isua mantle region. A differentiation event at ~4.42 Ga created a depleted reservoir that evolved towards $\mu^{142}Nd$ values of +13 at 3.8 Ga. This depleted mantle beneath the Isua region was progressively diluted by admixing primordial mantle material that was not involved in this previous differentiation event.

values over time and the admixture of SDEM or PRIMA can also explain the observed trace element characteristics (SCHEM could not be calculated as there are no trace element constraints). Although all models yield near-identical results at ~3.4 Ga, there is one striking difference between the primitive and the two superchondritic models. The two superchondritic models will evolve towards elevated $\varepsilon^{143}Nd$ values over time whereas $\varepsilon^{143}Nd$ values in the PRIMA model will converge towards 0. At ~3.3 to 3.2 Ga the chondritic and the superchondritic model will have developed to clearly resolvable $\varepsilon^{143}Nd$ values. Since there are Ameralik dikes as young as 3.265 Ga (Nutman et al., 2004), these rocks would be able to provide clear evidence for one model or the other.

2.7. Conclusions

We have developed a new analytical protocol to measure mass-independent isotope composition of Nd at high precision, including radiogenic ^{142}Nd and ^{143}Nd. This method was verified by confirming previous $^{142}Nd/^{144}Nd$ results for samples from the well-characterized Isua region and measuring various mixtures of TTG with known ^{142}Nd excesses and the BHVO-2 reference material. Multiple analysis of 22 La Palma basalt (LP-1) in house standards yield an intermediate precision of ±1.4 ppm, demonstrating that we are able to resolve anomalies at the lower ppm level. We incorporated previous literature data for 3.8 Ga old rocks from Isua into our new dataset to infer an $^{142,143}Nd/^{144}Nd$ differentiation model age of $4.417 \pm^{0.045}_{0.060}$ Ga, in excellent agreement with previous estimates. In addition to previous results, our data reveal a resolvably different distribution of $^{142}Nd/^{144}Nd$ compositions in ~3.72 Ga and ~3.8 Ga rocks. While ~3.8 Ga (ultra-) mafic rocks have $\mu^{142}Nd$ values of 13.0±1.1, ~3.72 Ga (ultra-) mafic rocks show slightly, but resolvably lower $\mu^{142}Nd$ values of 9.8±1.0. Analysis of the ~3.4 Ga Ameralik dikes show even lower $\mu^{142}Nd$ values with an average of 3.8±1.1. With respect to the ongoing debate whether Earth is chondritic or not, our observations are best explained by the progressive admixture of slightly depleted or primitive material bulk Earth material with a non-anomalous $^{142}Nd/^{144}Nd$ composition at 3.8 Ga to the Isua source. This implies that not the whole mantle participated in the ancient differentiation event recorded in Isua rocks. In addition to the previously described $\varepsilon^{143}Nd$-εHf decoupling, ISB rocks are also characterized by a

decoupling of $^{142,143}Nd/^{144}Nd$ compositions by having homogeneous $\mu^{142}Nd$ values but diverse $\varepsilon^{143}Nd_{(i)}$ values. This feature is best explained by supply of material with similar $^{142}Nd/^{144}Nd$ but different $^{143}Nd/^{144}Nd$ systematics via recycling processes that may be similar to modern subduction environments.

2.8. Extended Figures and Tables

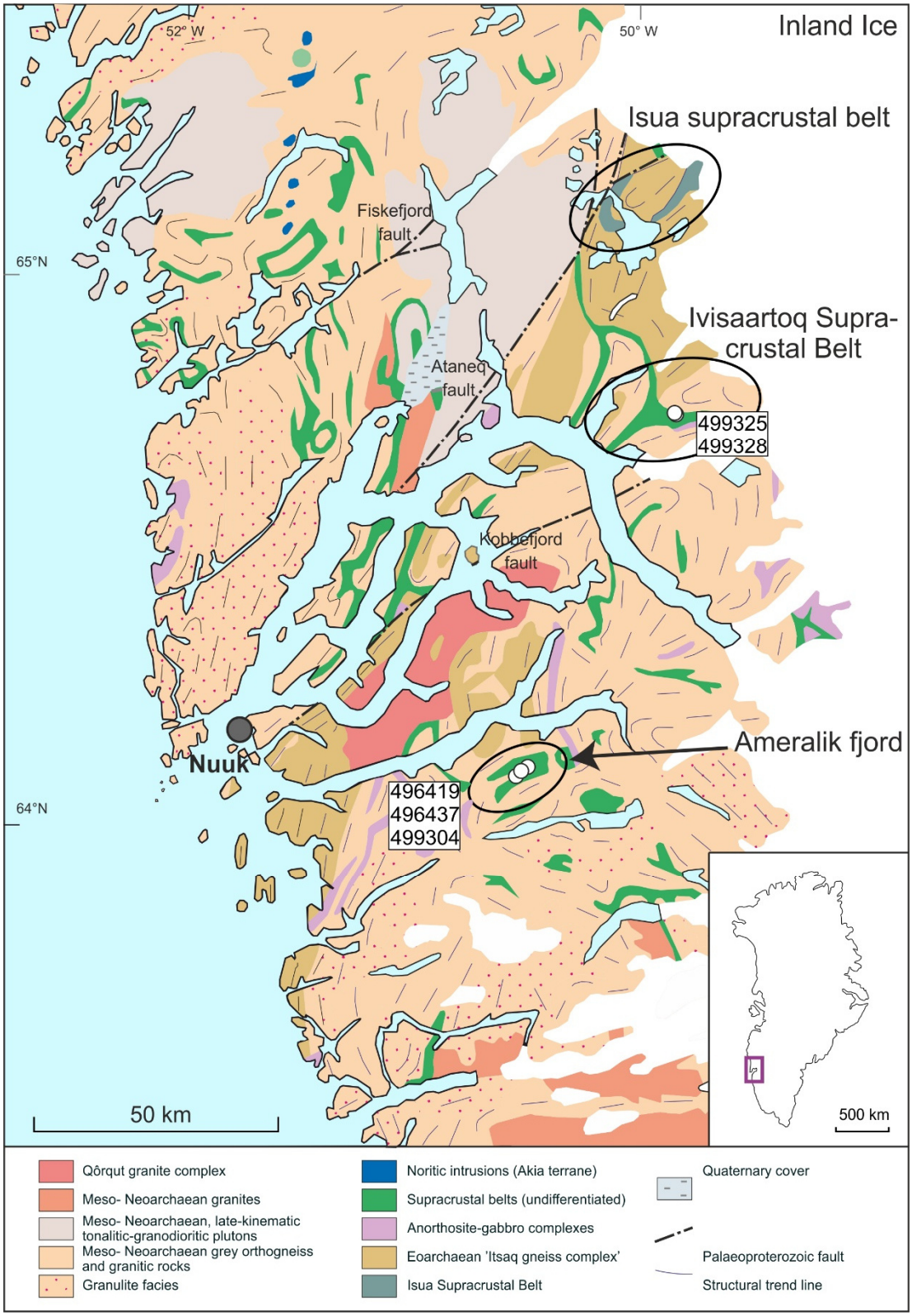

Extended Data Fig. 2.1: Geological map of the Nuuk region, highlighting our studied areas. Shown are the sample locations for samples from the Ameralik Fjord region and the Ivisaartoq Supracrustal Belt. The map is modified after Szilas et al., (2015b) and based on work by the Geological Survey of Denmark and Greenland.

Extended Data Table 2.1:

Stage	Reagent	Volumes [ml]
I Separation of HFSE and matrix		
Column I (15 ml BioRad AG 50 W-X-8)		
Preconditioning	1 M HCl - 0.3% H_2O_2	2 × 20
Load, HFSE & Ti	1 M HCl - 0.3% H_2O_2	20
Elute HFSE & Ti	1 M HCl - 0.3% H_2O_2	15
Elute major element matrix	1.8 M HCl	80
Collect REE, Sr and Ba	6 M HCl	100
II Separation of LREE from remaining matrix and HREE		
Column II (6 ml BioRad AG 50 W-X-8)		
Preconditioning	2.5 M HCl	2 × 10
Load, elute remaining matrix and HREE	2.5 M HCl	5
Elute remaining matrix and HREE	2.5 M HCl	27
Collect LREE and Ba[a]	6 M HCl	35
III Separation of REE from Ce		
Column III (0.5 ml Ln Spec® resin)		
Preconditioning	10 M HNO_3	4
Preconditioning	10 M HNO_3 - 30 mM $KBrO_3$	6
Load, elute LREE, Ba and K	10 M HNO_3 - 30 mM $KBrO_3$	0.5
Elute LREE, Ba and K[a]	10 M HNO_3 - 30 mM $KBrO_3$	7.5
Elute Ce	10 M HNO_3	2
Elute Ce	H_2O	2
Elute Ce	6 M HCl - 1% H_2O_2	6
IV Separation of LREE and Ba from K		
Column II (6 ml BioRad AG 50 W-X-8)		
Preconditioning	2.5 M HCl	2 × 10
Load, elute K	2.5 M HCl	5
Elute K	2.5 M HCl	27
Collect LREE and Ba[a]	6 M HCl	35
V Separation of Nd from other LREE and Ba		
Column IV (6 ml 50µm Ln Spec® resin and 0.4 ml AG ® 1-X8 on top)		
Preconditioning	0.25 calibrated HCl	2 × 10
Load	0.25 calibrated HCl	0.5
Elute Ba, La, residual Ce and Pr[b]	0.25 calibrated HCl	25
Collect Nd[a]	0.25 calibrated HCl	12

[a]Dry down two times with 80µl 14 M HNO_3 + 40 µl 30 % H_2O_2
[b]For Nd cuts, the last 3-5 ml were collected in 1ml steps seperately and recombined to ensure best possible Pr-Nd separation with maximum Nd yields

Elution scheme for purifying Nd from rock samples. Modified after Pin and Zalduegui, (1997), Schnabel et al., (2017) and Tusch et al., (2019).

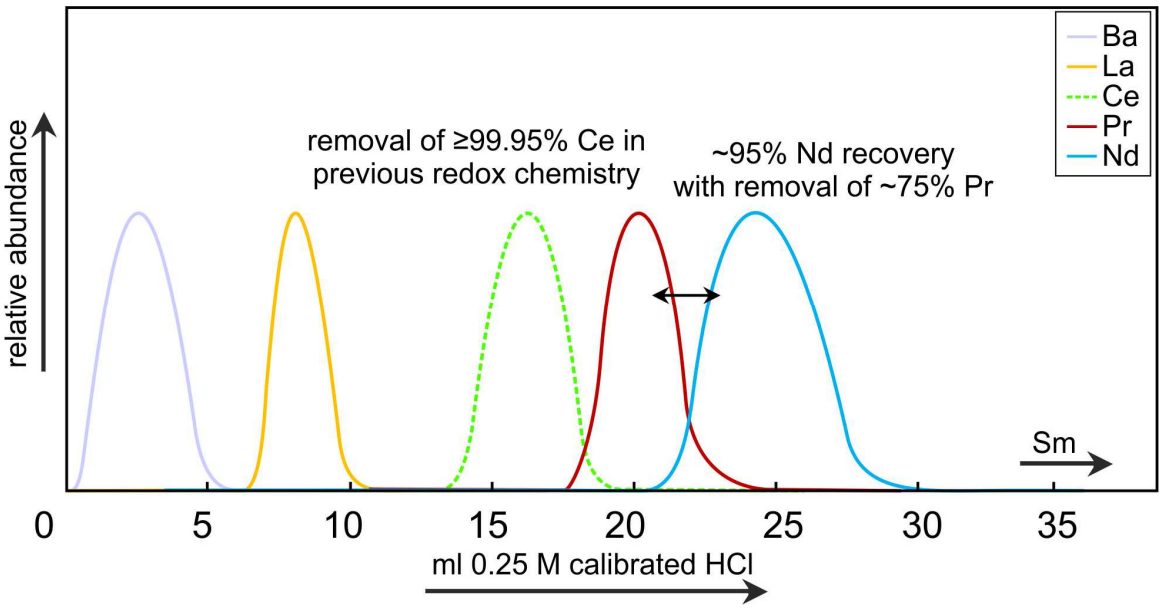

Extended Data Fig. 2.2: Schematic REE elution (separation step V) on Ln® Spec resin. Protocol is modified after Pin and Zalduegui, (1997).

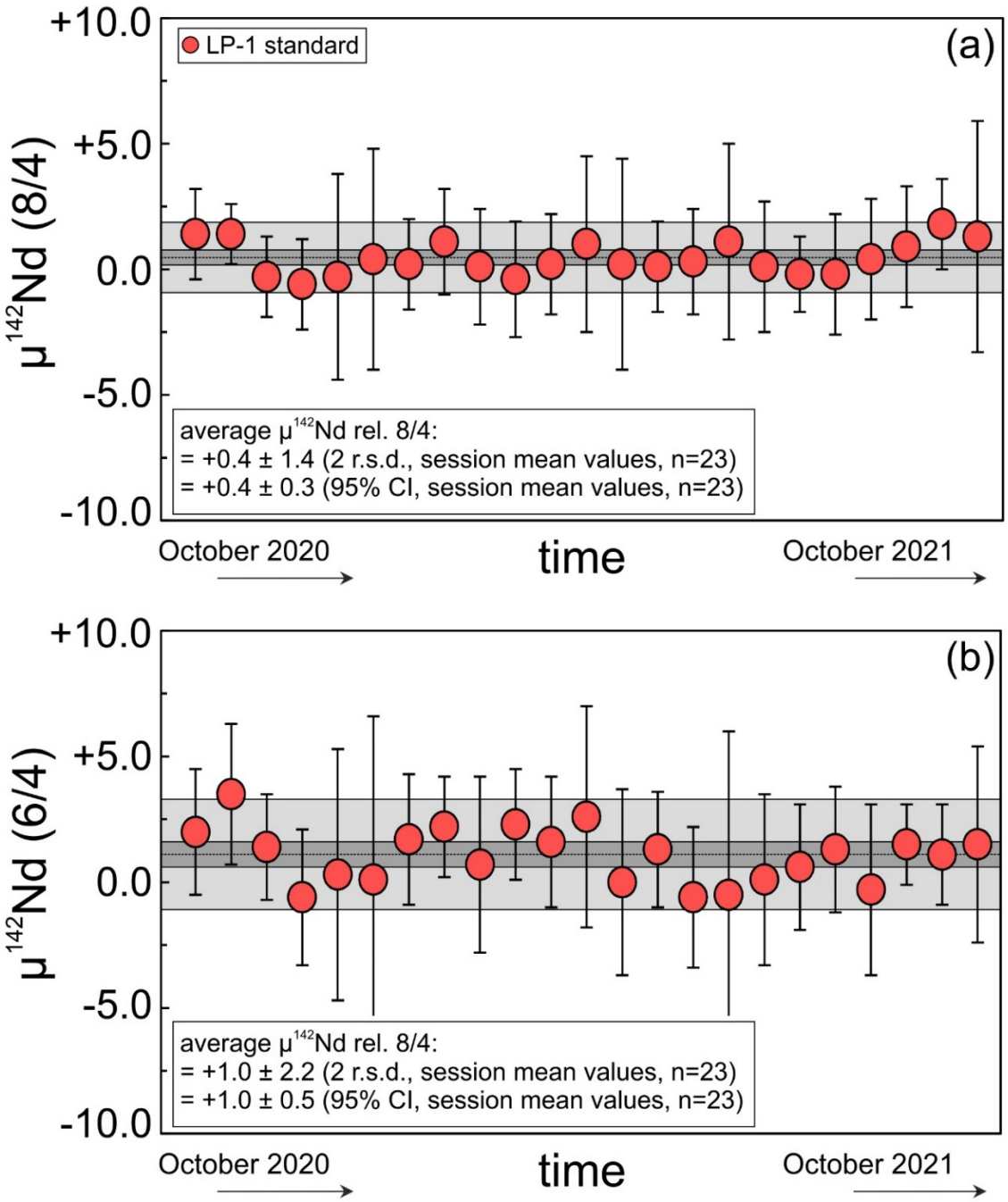

Extended Data Fig. 2.3: Intermediate precision of 22 multiple measurements for our in-house reference material LP-1, using a) $^{148}Nd/^{144}Nd$ (8/4) or b) $^{146}Nd/^{144}Nd$ (6/4) for mass bias correction. The smaller dark grey bars and the larger light grey bars refer to the mean 95% CI and 2 r.s.d. for all session mean values, respectively. Our intermediate precision of ±1.4 ppm on $^{142}Nd/^{144}Nd$ (8/4) analysis is considered as minimum error.

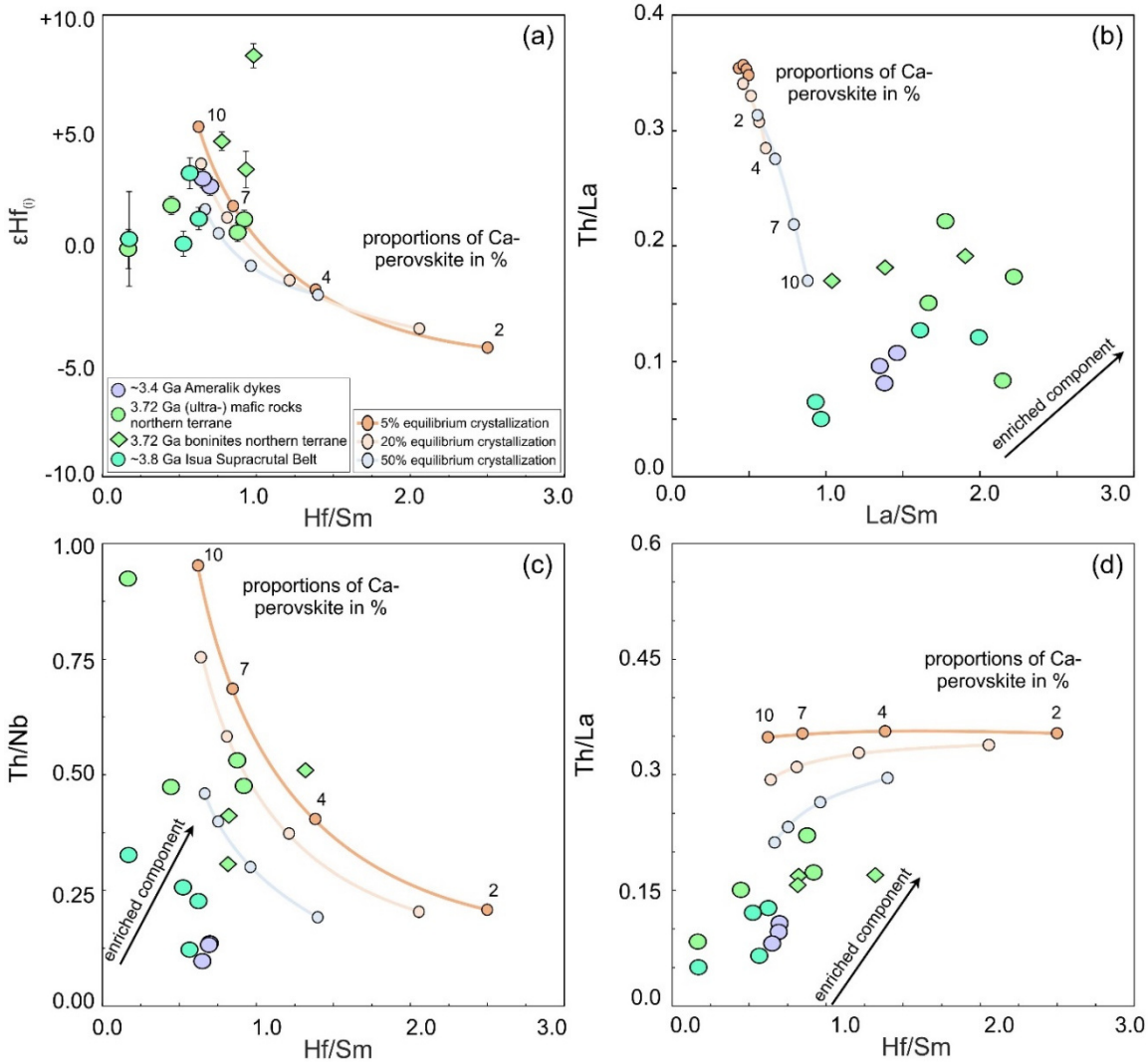

Extended Data Fig. 2.4: Evaluation whether trace element and isotope characteristics of ~3.8 to ~3.4 Ga Isua rocks can be explained by tapping perovskite cumulates with different degrees of crystallization and variable Ca-Mg perovskite proportions. a) Isua rocks show positive covariations between $\varepsilon Hf_{(i)}$ and Hf/Sm, whereas perovskite cumulates would create inverse correlations. b) Th/La vs. La/Sm, c) Th/Nb vs. Hf/Sm and d) Th/La vs. Hf/Sm reveal that some Isua samples are more depleted (i.e., having lower Th/La, Hf/Sm or Th/Nb ratios) than the modelled perovskite cumulates. Since partial melting increases these ratios, perovskite cumulates are too enriched to be a viable source. Notably, we have modelled Ca-Mg perovskite proportions as previously postulated for the Isua region (Caro et al., 2005; Hoffmann et al., 2011b; Rizo et al., 2011) and assuming a wide range of crystallization degrees (5% to 50%). For $\varepsilon Hf_{(i)}$, errors shown are the propagated errors including the errors on parent/daughter ratios, crystallization age and our external reproducibility of ±0.4 ε-units on $^{176}Hf/^{177}Hf$ isotope ratios. See Appendix A2 for model parameters. Additional data from previous studies (Polat et al., 2002; Polat and Hofmann, 2003; Hoffmann et al., 2010; Hoffmann et al., 2011b; van de Löcht et al., 2018; Tusch et al., 2019; van de Löcht et al., 2020).

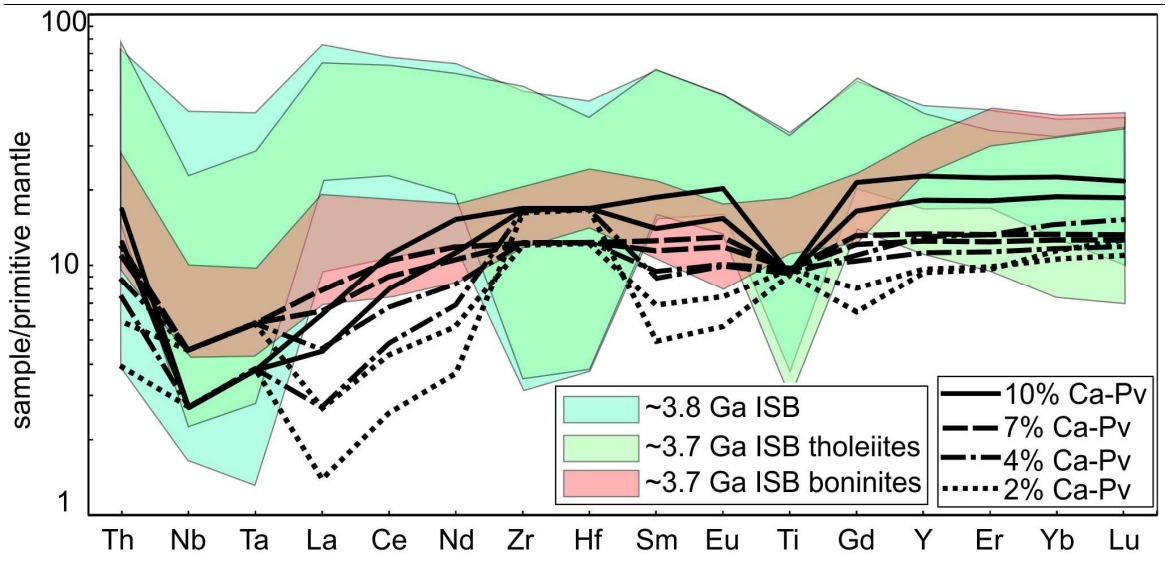

Extended Data Fig. 2.5: Comparison of observed and modelled trace element pattern, assuming a perovskite-related cumulate origin. Perovskite cumulates would create strong fractionations between REE and HFSE. Modelling parameters are as in Extended Data Fig. 2.4 but with an emphasis on trace element characteristics. For the different Ca/Mg-perovskite ratios, two lines are always shown, one assuming 5% and the other assuming 50% Pv equilibrium crystallization. See Appendix A2 for detailed model parameters. Shaded trace element data are from previous studies (Polat et al., 2002; Polat and Hofmann, 2003; Hoffmann et al., 2010; Hoffmann et al., 2011b; van de Löcht et al., 2018; Tusch et al., 2019).

Chapter III

3. Cerium-Nd isotope evidence for an incompatible element depleted Moon

3.1. Abstract

The Moon is a key example of a planetary body that originated from a giant impact collisional event. By better understanding its bulk composition, we can gain critical constraints on the building blocks from which the Earth-Moon system had formed. Combined measurements of long-lived ^{147}Sm-^{143}Nd and short-lived ^{146}Sm-^{142}Nd isotope compositions of Earth and Moon have lead to controversial interpretations in the past and it remains open, whether the Moon is similar to primitive chondrites in its refractory lithophile element composition or not. We investigated coupled ^{138}La-^{138}Ce and ^{147}Sm-^{143}Nd isotope and trace element compositions across a wide range of lunar rock types to provide an independent assessment of the bulk Moon composition. Lunar rocks define a tight array in ^{138}Ce-^{143}Nd space, intersecting initial εNd=0 at an initial εCe of -0.26±0.04, significantly lower than the currently accepted chondritic ^{138}Ce reference value (Israel et al., 2019; Willig and Stracke, 2019). Combined modeling of ^{138}Ce-^{143}Nd-^{176}Hf isotope and trace element behavior during lunar magma ocean (LMO) crystallization (Snyder et al., 1992) can now confirm that the bulk silicate Moon must be slightly depleted in its highly incompatible trace element inventory. Our calculated composition of the silicate Moon evolves towards εCe=-0.25 and εNd=+1.4 at 3.3 Ga, the approximate age of most lunar samples investigated here. This proposed lunar composition is in perfect agreement with the intersection of the lunar array with trends defined by near-contemporaneous terrestrial rocks from the Archean Pilbara and the Kaapvaal Cratons. We take this as evidence that accessible silicate Earth and the Moon may share a common reservoir slightly depleted in highly incompatible trace elements, named here Slightly Depleted Earth-Moon reservoir (SDEM). The SDEM reservoir proposed here is in line with previous models claiming a depleted composition of the accessible silicate Earth (Caro and Bourdon, 2010), but the degree of depletion is significantly smaller than previously proposed.

3.2. Introduction

Unlike the larger terrestrial planets, the Moon formed from the debris of a giant impact event that ejected silicate material from both, a Mars-sized impactor (Canup, 2004) and

proto-Earth into space (Pahlevan and Stevenson, 2007; Stewart et al., 2018). Radiogenic isotope studies can place firm constraints on the origin of the Moon and its building blocks. Amongst these, in particular the two Sm-Nd isotope systems (long-lived ^{147}Sm-^{143}Nd and short-lived ^{146}Sm-^{142}Nd) are of special interest. Distinct isotopic differences between the Earth-Moon system and chondrites have been found for the short-lived ^{146}Sm-^{142}Nd isotope system (Boyet and Carlson, 2007; Brandon et al., 2009a; Caro and Bourdon, 2010; Mcleod et al., 2014; Boyet et al., 2018; Morino et al., 2018; Borg et al., 2019), with modern terrestrial rock displaying a ca. +10 to +30 ppm ^{142}Nd excess relative to various chondrite classes (Boyet et al., 2018). These observations suggest that the bulk Moon and also the Earth may have evolved with non-chondritic Sm/Nd ratios (Caro et al., 2008; Caro and Bourdon, 2010). Alternatively, Earth and Moon may have chondritic Sm/Nd ratios and the different ^{142}Nd abundances may not reflect radiogenic ingrowth, but rather primordial nucleosynthetic heterogeneities inherited from different building blocks that carried variable s-process signatures (Bouvier and Boyet, 2016; Burkhardt et al., 2016; Boyet et al., 2018). Evidence for a chondritic Moon has further been supported by combined isotope systematics of long-lived ^{147}Sm-^{143}Nd and ^{176}Lu-^{176}Hf in lunar rocks (Sprung et al., 2013).

In order to finally unravel whether the Moon is chondritic or not, we investigated combined patterns of the long-lived ^{138}La-^{138}Ce (λ=2.37×10^{-12} a^{-1}) and ^{147}Sm-^{143}Nd isotope systems in a comprehensive suite of lunar rocks. Both isotope systems yield strong inverse correlations in modern mantle-derived (Israel et al., 2019) and Archean rocks (Hasenstab et al., 2021; Tusch et al., 2021a), reflecting the opposite incompatibilities of their respective parent-daughter element pairs. This makes combined ^{138}Ce-^{143}Nd isotope systematics an ideal tool for investigating the incompatible trace element budget of the Moon with two independent isotope systems, and aids clarifying the origin of elevated ^{142}Nd/^{144}Nd isotope compositions in the Earth Moon system. Our sample selection covers all important lunar lithologies such as low- and high-Ti mare basalts as well as enriched basalts (KREEP) and various lunar highland rocks (see Appendix). The samples are well characterized and were previously investigated for their inventory of High Field Strength Elements (HFSE) and other incompatible elements (W, U, Th) (Thiemens et al., 2019). For a total of 32 lunar samples (including two duplicates), we measured ^{138}La-^{138}Ce and ^{147}Sm-^{143}Nd isotope compositions by MC ICP-MS (Schnabel et al., 2017) and determined trace element compositions of sample aliquots by quadrupole ICP-MS (Garbe-Schönberg, 1993) (see also Appendix). Ratios of ^{138}La/^{136}Ce and ^{147}Sm/^{144}Nd were both measured by isotope dilution (Schnabel et al., 2017). Further details on the analytical protocol are given in the method section. Within analytical uncertainty, our εCe value obtained for BHVO-2 (-0.82±0.21) is in excellent agreement with our long-term average (-0.65±0.21) and values obtained by other laboratories (Israel et al., 2019; Willig and Stracke, 2019).

3.3. Sample selection and compositions

We investigated a comprehensive suite of 30 lunar samples that comprise the most common rock types found on the Moon. The collection includes samples from Apollo 11 (three), Apollo 12 (six), Apollo 14 (three), Apollo 15 (six) Apollo 16 (three), Apollo 17 (eight) and one lunar meteorite (NWA 6950). These samples represent chemically distinct

reservoirs from the Moon's interior that provide insight into different phases of lunar evolution. Among the samples are also two Ferroan anorthosites (FANs, samples 60025 and 67076) that represent the oldest lunar crust, built by floating plagioclase cumulates (Wood et al., 1970). FANs are generally characterized by very low incompatible trace element concentrations and strongly positive Eu/Eu* anomalies (9.15 to 32.8), but the strongly heterogeneous trace element systematics suggest some intra-group variations (Extended Data Figs. 3.2 and 3.3). Furthermore, seven KREEP-rich samples were analyzed here (samples 14163, 14305, 14310, 65015, 72275, 73275 and 68115), tapping the highly enriched urKREEP reservoir that formed after the majority of the lunar magma ocean (LMO) had crystallized (McKay and Weill, 1977; Warren and Wasson, 1979). KREEP-rich samples show strongly enriched signatures (La/Sm=2.39-2.47), slightly negative Nb-Ta anomalies (Nb/La=0.641-0.926), negative Eu/Eu* (0.220-0.388) and Ti/Ti* anomalies (0.125-0.211) (Thiemens et al., 2019; Kommescher et al., 2020). In addition, eight high Ti basalts (samples 10020, 79035, 79135, 10017, 10020, 10057, 74255, 74275 and 75035) and 14 low Ti basalts (15058, 15065, 15545, 15556, 15495, 15555, 12004, 12022, 12051, 12053, 12054 and 12063) as well as one lunar meteorite NWA 6950 were analyzed here, all representing volcanic eruptions during younger, prolonged mare activity. While low Ti basalts show broadly unfractionated HFSE compositions (Münker, 2010; Thiemens et al., 2019), most High Ti basalts have positive HFSE anomalies, relative to similar incompatible REEs (Nb/La=1.14 to 4.47; Zr/Sm=24.0-28.6) (Thiemens et al., 2019). High Ti basalts and Apollo 12 low Ti basalts show predominantly depleted light rare earth element (LREE) patterns (La/Sm=0.694-1.50 and 1.08-1.57, respectively), while Apollo 15 low Ti basalts show less fractionated and more uniform REE patterns (La/Sm=1.52-1.76).

3.4. Discussion

3.4.1. Cerium-Nd isotope evidence

As key observation, lunar rocks define a tight, anti-correlated array in ^{138}Ce-^{143}Nd space, where high and low-Ti mare basalts define the incompatible element depleted and KREEP basalts the enriched endmember, respectively (Fig. 3.1). Notably, the present day εCe and εNd values of the array do not intersect at chondritic εCe-εNd compositions, suggesting a non-chondritic composition of the Moon (Fig. 3.1a). Since the present day εCe-εNd array of lunar basalts is controlled by ^{138}La/^{136}Ce and ^{147}Sm/^{144}Nd ratios that might have been modified from the source ratios during partial melting, we also calculated $\varepsilon Ce_{(i)}$-$\varepsilon Nd_{(i)}$ at the time of crystallization (Fig. 3.1b). Interestingly, the slope of the array is shallower than for terrestrial samples (Hasenstab et al., 2021; Tusch et al., 2021a) (Fig. 3.1d, Extended Data Fig. 3.1), possibly a result of different fractionation of La/Ce from Sm/Nd in the terrestrial and lunar mantle. At $\varepsilon Nd_{(i)}$=0, our combined data for lunar rocks intersect at $\varepsilon Ce_{(i)}$=-0.26±0.04, arguing for a slight depletion of the Moon in light rare earth elements. As robust insights from initial $\varepsilon Ce_{(i)}$-$\varepsilon Nd_{(i)}$ values might be biased by the large time interval of crystallization between individual samples, we also provide a time independent approach by calculating $^{138}La/^{136}Ce_{source}$-$^{147}Sm/^{144}Nd_{source}$ ratios of their cumulate sources, assuming a common LMO differentiation age of 4.33 Ga (Boyet and Carlson, 2007; Borg et al., 2019) (Fig. 3.1c). Notably, the array defined by $^{138}La/^{136}Ce_{source}$-$^{147}Sm/^{144}Nd_{source}$ ratios also does

not intersect the chondritic composition. These combined observations clearly demonstrate that the bulk silicate Moon (BSM) cannot be chondritic and must be slightly depleted in highly incompatible trace elements relative to chondrites. Notably, the offset of initial $\varepsilon Ce_{(i)}$ values between our lunar samples and the chondritic composition is relatively small. Therefore, it must be ensured that the offset is not an artifact caused by an inaccurate determination of the chondritic reference composition, usually referred to as chondritic uniform reservoir (CHUR). We therefore compare 3.3±0.25 Ga old lunar

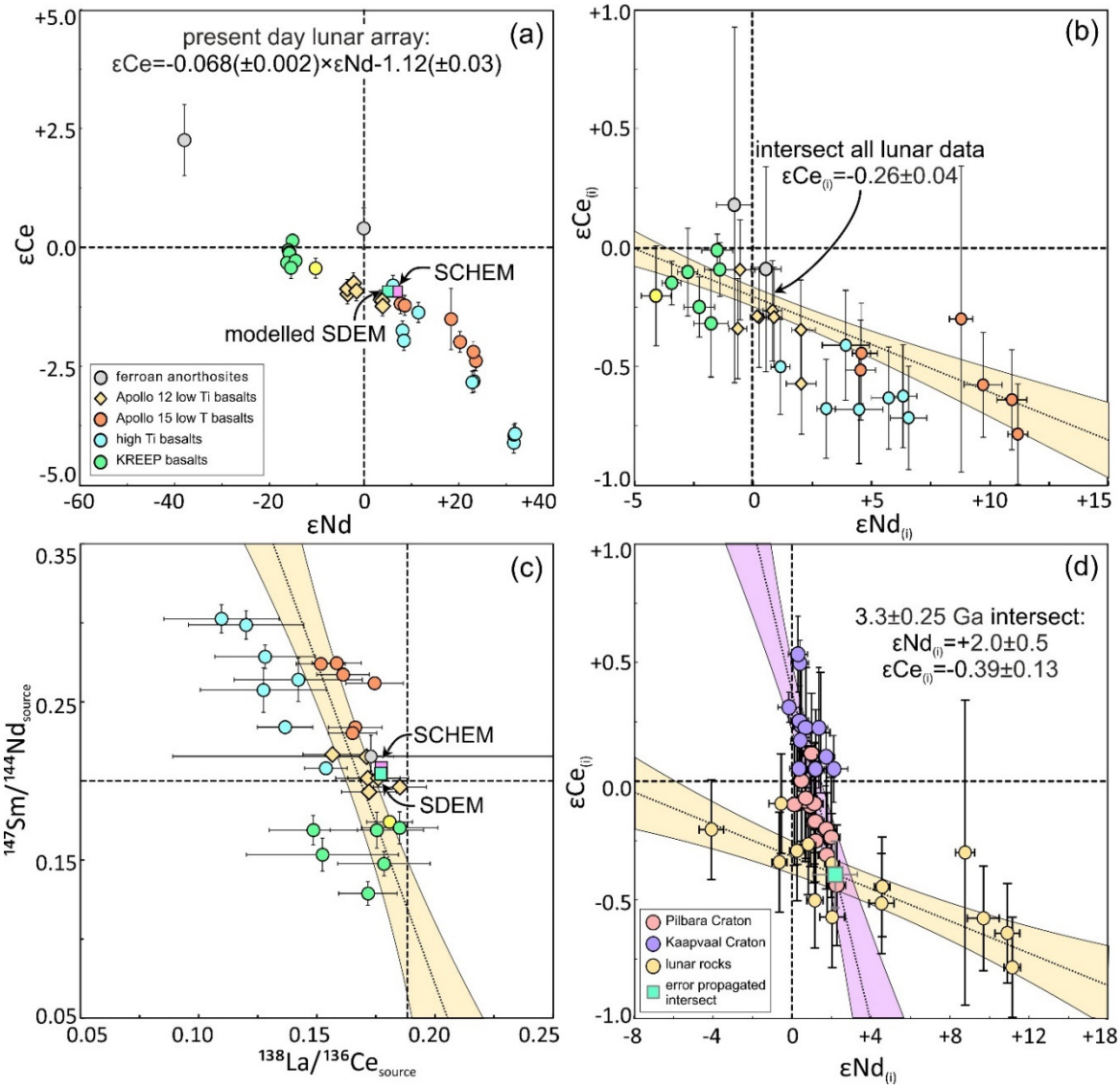

Fig. 3.1: Measured Ce-Nd isotope compositions of lunar rocks. a) Present day εCe-εNd values do not intersect the chondritic compositions but are displaced towards less radiogenic εCe values, similar to our modelled slightly depleted Earth-Moon composition (SDEM) or SCHEM (Caro and Bourdon, 2010). b) Initial $\varepsilon Ce_{(i)}$-$\varepsilon Nd_{(i)}$ values also do not intersect at chondritic compositions. c) Calculated $^{138}La/^{136}Ce_{source}$ and $^{147}Sm/^{144}Nd_{source}$ ratios do also not intersect the chondritic values and confirm a non-chondritic composition of the bulk Moon. Calculated $^{138}La/^{136}Csource$ and $^{147}Sm/^{144}Ndsource$ ratios refer to a LMO crystallization age of 4.33 Ga (Borg et al., 2019) and assume chondritic starting compositions (Bouvier et al., 2008; Willig and Stracke, 2019). The $^{138}Ce/^{136}Ce$ isotope composition for SCHEM was extrapolated, assuming an εNd value of +6.9 (Caro and Bourdon, 2010) and using the recently defined terrestrial Ce-Nd mantle array(Israel et al., 2019). d) Comparison of a subset of near-contemporaneous 3.3±0.25 Ga lunar and terrestrial rocks. For εNd=0, the εCe intersect of both planetary bodies is displaced by ~70 ppm. The arrays of 3.3±0.25 Ga old lunar and Archean (Hasenstab et al., 2021; Tusch et al., 2021a) rocks both intersect at a composition of εCe(3.25Ga)=-0.39±0.13 and εNd(3.25Ga)=+2.0±0.5. This is indistinguishable from our modelled composition for BSM at 3.3 Ga, exhibiting εCe(3.3Ga) and εNd(3.3Ga) values of -0.26 and +1.4, respectively. All data are normalized to the CHUR values of Bouvier et al., (2008) and Willig and Stracke, (2019).

samples from this study with contemporaneous Archean rocks from the Pilbara and the Kaapvaal Craton for which combined Ce and Nd isotope data have been reported previously (Hasenstab et al., 2021; Tusch et al., 2021a). We have chosen this specific age group, because it comprises enough samples to gain representative interpretations. In stark contrast to the subchondritic intersect of lunar rocks (Fig. 3.1d), 3.3 Ga old terrestrial samples from the Pilbara and Kaapvaal Cratons (Hasenstab et al., 2021; Tusch et al., 2021a) intersect the chondritic $\varepsilon Nd_{(3.3Ga)}$=0 value at a superchondritic $\varepsilon Ce_{(i)}$=+0.39±0.06, clearly resolvable from the lunar intersect by ~70 ppm (Fig. 3.1d, Extended Data Fig. 3.1). Furthermore, the two terrestrial suites display a significantly steeper array in εCe- εNd space. Taking these findings into consideration, we conclude that the observed offset for lunar and terrestrial samples in $\varepsilon Ce_{(i)}$-$\varepsilon Nd_{(i)}$ space from CHUR cannot be simply explained by inaccurate $^{138}La/^{136}Ce$ and $^{138}Ce/^{136}Ce$ isotope composition for CHUR. Any adjustment of $^{138}La/^{136}Ce$ or $^{138}Ce/^{136}Ce$ ratios for CHUR would modify the calculated intercepts of $\varepsilon Ce_{(i)}$ values for lunar and terrestrial rocks equally. In addition, the CHUR value by Willig and Stracke, (2019) was previously confirmed in another study (Israel et al., 2019), further confirming its validity. Hence, we arrive at the inescapable conclusion, that the Moon must be depleted in its highly incompatible trace element budget.

In contrast to our claim for a non-chondritic Moon, long-lived Hf and

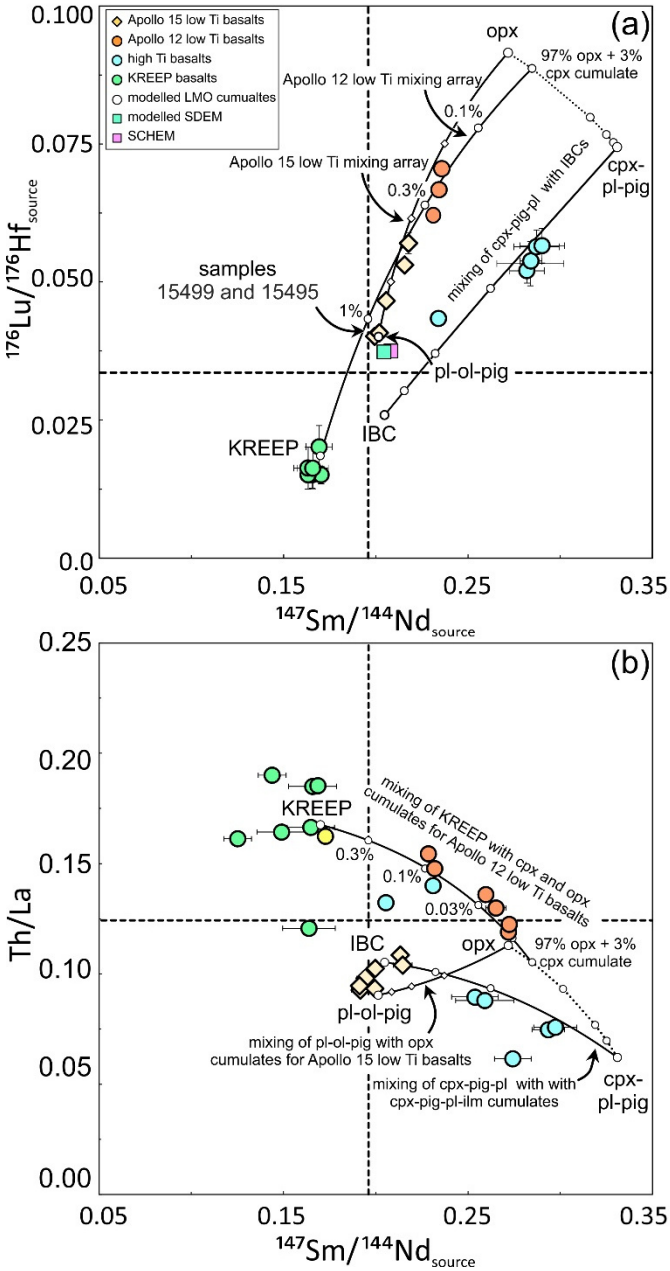

Fig. 3.2: Modelled isotope and trace element compositions of lunar mantle reservoirs in comparison to available data for lunar basalts. a) Shown are different modelled endmember compositions of various LMO cumulates (Snyder et al., 1992) assuming a depleted bulk composition for the Moon. Mixing relationships between the shown cumulates can explain the full range of coupled $^{176}Lu/^{177}Hf_{source}$ vs. $^{147}Sm/^{144}Nd_{source}$ ratios for existing literature data of lunar rocks (Sprung et al., 2013; Carlson et al., 2014). b) Modelled Th/La vs. $^{147}Sm/^{144}Nd_{source}$ data imply that Apollo 12 and 15 low Ti basalts were formed by the involvement of different mantle cumulates, excluding simple mixing models between a single depleted LMO cumulate and different proportions of TIRL, as suggested earlier (Sprung et al., 2013). Parent/daughter$_{source}$ ratios for LMO cumulates were calculated assuming a crystallization age of 4.336 Ga (Borg et al., 2019) and a depleted bulk composition for the Moon as inferred in this study. If not stated otherwise, symbols on the mixing lines correspond to 25, 50 and 75% mixing proportions. Abbreviations: opx = orthopyroxene-rich cumulates, cpx-pl-pig = clinopyroxene-plagioclase-pigeonite-rich cumulates, pl-pig-ol = plagioclase-pigeonite-olivine rich cumulates, IBC = ilmenite-bearing cumulates, KREEP = K-REE-P-rich rocks.

Nd isotope systematics have previously provided strong arguments in favor of a chondritic Moon (Sprung et al., 2013). Sprung et al., (2013) provided $^{176}Hf/^{177}Hf$ and $^{143}Nd/^{144}Nd$ isotope data for different lunar rock types and conducted isotope modelling, evaluating both chondritic and non-chondritic starting compositions (superchondritic Earth model composition; herein referred to as SCHEM (Caro and Bourdon, 2010)). Importantly, some of these samples were also analyzed in this study, yielding identical $^{143}Nd/^{144}Nd$ compositions. While most of the lunar rocks from Sprung et al., (2013) could be explained by both starting compositions, the claim for a chondritic starting composition particularly hinged on two lunar low Ti basalts from Apollo 15 (15499 and 15495; Fig. 3.2a), which were found to be inconsistent with a non-chondritic starting composition.

3.4.2. Modelling approach

Considering the new ^{138}La-^{138}Ce isotope data, a new model is clearly required to explain the apparent inconsistency between Ce-Nd and Hf-Nd isotope systematics. Therefore, we included samples that were previously analyzed for ^{176}Lu-^{176}Hf and ^{147}Sm-^{143}Nd isotope systematics (Sprung et al., 2013; Carlson et al., 2014) in our study and conducted combined trace element and Hf-Nd-Ce isotope modeling, using the same crystallization sequence (Snyder et al., 1992) that was previously used by Sprung et al., (2013) (Fig. 3.2). This previous modeling approach (Sprung et al., 2013) required significant amounts of trapped interstitial liquid (TIRL) to be retained in the LMO cumulates (up to ~20%) in order to explain the observed Hf-Nd systematics. The use of such high amounts of TIRL conflicts with previous studies (Snyder et al., 1992) who suggested significantly lower amounts (≤5%). Taking this into consideration, we explain the compositions of lunar basalts by mixing relationships between different cumulate reservoirs that formed after lunar magma ocean crystallization (Snyder et al., 1992) (see Appendix for detailed modelling parameters). As starting composition for a depleted BSM we assumed a slightly depleted bulk silicate Earth (BSE) composition from the literature (O'Neill and Palme, 2008) mixed with a primitive projectile (Palme and O'Neill, 2013) during the giant impact (Fig. 3.3). Mixing proportions follow previous assumptions and amount to 14% impactor material and 86% terrestrial material (Canup, 2004), assuming complete equilibration between both planetary bodies in the aftermath of the giant impact(Pahlevan and Stevenson, 2007; Stewart et al., 2018). Our modelled depleted BSM composition (hereinafter denoted as slightly depleted Earth-Moon system or SDEM; for further information see below) evolves towards present day εCe, εNd and εHf values of -0.94, +5.0 and +10.1, respectively, which is less depleted than SCHEM (Caro and Bourdon, 2010) (Table 3.1). The modelled $^{147}Sm/^{144}Nd$ composition of the BSM amounts to 0.2045, similar to but slightly lower than previous independent estimates from $^{142}Nd/^{144}Nd$ patterns ($^{147}Sm/^{144}Nd$=0.206 (Caro et al., 2008); $^{147}Sm/^{144}Nd$=0.2054 (Caro and Bourdon, 2010)). In Fig. 3.2a, modelled compositions of $^{176}Lu/^{177}Hf$ and $^{147}Sm/^{144}Nd$ for lunar cumulate reservoirs are compared with the observed range of existing lunar data. Our modelling approach shows that mixing between various types of LMO cumulates can produce hybrid compositions that are able to explain the full range of observed lunar isotope and trace element compositions. Long-lived radiogenic

isotope compositions of our modelled SDEM are reported in Table 3.1 and modelled trace elements are reported in Extended Data 3.1.

Our model can reconcile the parent/daughter$_{source}$ ratios of high Ti basalts by mixing of ilmenite-bearing cumulates (IBCs) (Irving et al., 1978) with clinopyroxene-plagioclase-pigeonite cumulates (Fig. 3.2). Other studies also invoked the involvement of KREEP-rich material (Brandon et al., 2009a) or high amounts of TIRL (Sprung et al., 2013) (similar to KREEP at this late stage of LMO crystallization). However, we consider the involvement of such an enriched material as unlikely since it would have easily overprinted the depleted light rare earth element patterns (La/Sm_{CN}=0.61 to 0.89) of high Ti basalts (Extended Fig. 3.1, see Method section for more information).

Together with our combined isotope and trace element data, our modeling approach now permits new insights into geochemical relationship between different suites of low Ti basalts, which have previously been regarded to represent one petrological group. In contrast to this view, our combined trace element and isotope data reveal distinct differences between Apollo 12 and 15 low Ti basalts, strongly arguing for the involvement of different mantle sources during their petrogenesis. In Th/La vs. $^{147}Sm/^{144}Nd_{source}$ space (Fig. 3.2b), compositions of Apollo 12 low Ti basalts suggest the admixture of KREEP during their petrogenesis. In contrast, our group of Apollo 15 low Ti basalts fall on a different mixing array with plagioclase-pigeonite-olivine cumulates as more plausible endmember. The low Th/La ratios of Apollo 15 low Ti basalts further corroborate an origin from a depleted lunar reservoir, arguing against significant involvement of TIRL as previously proposed (Sprung et al., 2013). The role of different cumulates in the formation of Apollo 12 and 15 low Ti basalts is also in accord with our modelled $^{176}Lu/^{177}Hf_{source}$ and $^{147}Sm/^{144}Nd_{source}$ compositions (Fig. 3.2a). Most importantly, our findings show that even the two critical low Ti samples from Apollo 15 (15499 and 15495) used in previous modelling approaches[18] plot on our proposed cumulate mixing line. Consequently these two key samples from Sprung et al., (2013) can no longer exclude a non-chondritic composition of the Moon (Fig. 3.2a). Collectively, the good agreement between geochemical observations and theoretical modelling predictions strengthen the case for a non-chondritic Moon.

Table 3.1: ^{138}La-^{138}Ce, ^{147}Sm-^{143}Nd, and ^{176}Lu-^{176}Hf parent-daughter ratios and isotope compositions of the modelled SDEM reservoir.

isotope system	parent/daughter ratio	ε-value (3.3 Ga)	ε-value (present day)	isotope composition (present day)
^{138}La-^{138}Ce	0.1768	-0.26	-0.94	$^{138}Ce/^{136}Ce$=1.336771
^{147}Sm-^{143}Nd	0.2045	+1.4	+5.0	$^{143}Nd/^{144}Nd$=0.512889
^{176}Lu-^{176}Hf	0.03680	+2.8	+10.1	$^{176}Hf/^{177}Hf$=0.283070

Modelled parameters are listed in the Method section and Appendix A3.

3.4.3. Implications for short-lived ^{146}Sm-^{142}Nd systematics

Our proposed depleted Moon composition also has implications for short-lived ^{146}Sm-^{142}Nd systematics. The most recent studies explain the ~10 to 30 ppm ^{142}Nd/^{144}Nd excess of the Earth-Moon system compared to the most Earth-like chondrites by nucleosynthetic heterogeneities (Bouvier and Boyet, 2016; Burkhardt et al., 2016; Boyet et al., 2018). When investigating existing Nd isotope data in μ^{142}Nd vs. μ^{145}Nd, μ^{148}Nd or μ^{150}Nd space (Extended Data Fig. 3.4), Earth appears to plot off the s-process mixing line by having elevated ^{142}Nd/^{144}Nd compositions. We reevaluated nucleosynthetic isotope effects by calculating best-fit arrays in μ^{142}Nd vs. μ^{145}Nd, μ^{148}Nd or μ^{150}Nd space (Extended Data Fig. 3.4), based on Nd isotope data compiled from the literature (Boyet et al., 2018) (see also Appendix for a more detailed discussion). The intersects of chondritic μ^{142}Nd values at $\mu^{145,148,150}$Nd=0 amount to a weighted mean of -11.0±1.5 ppm relative to the terrestrial reference (weighted 2 rsd). This value indicates that Earth has a residual excess in μ^{142}Nd relative to the most Earth-like chondrites, even when nucleosynthetic effects are taken into account (Burkhardt et al., 2016; Boyet et al., 2018). These observations imply that part of the μ^{142}Nd excesses found on Earth still require early silicate differentiation, although the offset must be smaller than previously estimated (Caro et al., 2008; Caro and Bourdon, 2010). Assuming that the residual 11.0±1.5 ppm μ^{142}Nd excess of Earth is caused by silicate differentiation that occurred immediately at 4.568 Ga (Caro and Bourdon, 2010), this would correspond to a minimum ^{147}Sm/^{144}Nd ratio of 0.203 for the BSE. This value is in good agreement but slightly lower than the one we modelled for the BSM (^{147}Sm/^{144}Nd=0.2045). However, if a younger differentiation age is assumed, BSE needs to have evolved with a higher ^{147}Sm/^{144}Nd ratio, which would shift the ^{147}Sm/^{144}Nd composition of BSE even closer to our modelled composition. For example, when assuming a differentiation age of 4.525 Ga that is slightly younger than the most recent age estimations of the Moon (Thiemens et al., 2019), the μ^{142}Nd excess of the accessible silicate Earth (and consequently the Moon) would correspond to a ^{147}Sm/^{144}Nd ratio of 0.2042, surprisingly similar to what is claimed here. Collectively, even when considering s-process-related variations in Earth's building blocks, the modelled ^{142}Nd/^{144}Nd isotope compositions are still in accord with our observations from Ce-Nd isotopes.

3.4.4. Comparison with Archean rocks

While lunar rocks intersect chondritic $\varepsilon Nd_{(i)}$ at subchondritic $\varepsilon Ce_{(i)}$ values, near-contemporaneous terrestrial rocks intersect chondritic $\varepsilon Nd_{(i)}$ at significantly higher $\varepsilon Ce_{(i)}$ values. For the Pilbara Craton $\varepsilon Nd_{(i)}$=0 is intersected at $\varepsilon Ce_{(i)}$=+0.22±0.12, while the Kaapvaal Carton gives an intersect of +0.33±0.12. Since the slopes in εCe-εNd are significantly steeper compared to the lunar array, the terrestrial intersects for $\varepsilon Ce_{(i)}$ at $\varepsilon Nd_{(i)}$=0 are less precise, although it is striking that they do not seem to fully overlap chondritic Earth compositions. Interestingly, though, the terrestrial $\varepsilon Ce_{(i)}$-$\varepsilon Nd_{(i)}$ array of 3.3±0.25 Ga rocks from the Pilbara and Kaapvaal Cratons overlaps our modelled SDEM composition. The intersection of the 3.3±0.25 Ga lunar and terrestrial arrays is at $\varepsilon Ce_{(3.3Ga)}$=-0.39±0.13 and $\varepsilon Nd_{(3.3Ga)}$=+2.0±0.5, in good agreement with our modelled composition for the BSM ($\varepsilon Ce_{(3.3Ga)}$=-0.26 and $\varepsilon Nd_{(3.3Ga)}$=+1.4). Importantly, this calculated intersection is

sufficiently robust, since intersections calculated for different age groups of samples and for individual cratons yield identical results (Extended Data Fig. 3.1). Our observations imply the conclusion that not only BSM but also BSE has a superchondritic composition and that our modelled SDEM composition can be interpreted as bulk composition for both planetary bodies, as hypothesized earlier (Brandon et al., 2009a). Our model can also explain why Archean rocks show positive $\varepsilon Ce_{(i)}$ values at chondritic $\varepsilon Nd_{(i)}$ values (Hasenstab et al., 2021; Tusch et al., 2021a). This feature is a consequence of the markedly different slopes in $\varepsilon Ce_{(i)}$-$\varepsilon Nd_{(i)}$ space (3.3 Ga terrestrial rocks m=-0.39±0.07 (Hasenstab et al., 2021; Tusch et al., 2021a); 3.25 Ga lunar rocks m=-0.036±0.014; Fig 1) and normalizing them to a wrong reservoir (CHUR), which will result in different intersections of $\varepsilon Ce_{(i)}$ at $\varepsilon Nd_{(i)}$=0.

Although various chondrite classes were shown to have nearly constant ratios of lithophile refractory elements (Palme and O'Neill, 2013) ($^{138}La/^{136}Ce$ or $^{147}Sm/^{144}Nd$), it remains ambiguous if this also applies to larger planetary bodies (Caro et al., 2008; O'Neill and Palme, 2008; Caro and Bourdon, 2010; Campbell et al., 2012). In this regard, our finding of a depleted lunar composition is of particular interest. Since many recent studies argued that a large proportion of the Moon is made up by terrestrial material (Pahlevan and Stevenson, 2007; Zhang et al., 2012; Stewart et al., 2018), it is most likely that the depletion was inherited from proto-Earth. To account for such depleted terrestrial reservoirs, the most plausible explanation involves early silicate differentiation on the proto-Earth. Evidence for such early silicate differentiation events is provided by terrestrial rocks that exhibit anomalous compositions of short-lived isotope systematics, such as ^{182}Hf-^{182}W, ^{146}Sm-^{142}Nd or ^{129}I-^{129}Xe (Boyet and Carlson, 2005; Mukhopadhyay, 2012; Tusch et al., 2021a). We therefore reevaluate below, if previous models for early terrestrial differentiation can also account for a depleted lunar composition, namely (1) early terrestrial magma ocean crystallization leaving behind a deep enriched reservoir (Labrosse et al., 2007) (2) deeply subducted enriched hidden reservoirs (Tolstikhin and Hofmann, 2005) or (3) a depleted bulk Earth following collisional erosion (O'Neill and Palme, 2008) (Fig. 3.3).

3.4.5. Origin of the depleted lunar component

The first possible model (1) considers the segregation of enriched silicate reservoirs that formed during terrestrial magma ocean crystallization in the deep Earth (Fig. 3.3). In this scenario, the Moon would have preferentially accreted from light rare earth element-depleted domains. Considering that crystallization of a magma ocean on Earth's surface is assumed to have been deep-rooted (reaching the perovskite stability field (Li and Agee, 1996)) or may even have occurred as basal magma ocean (Labrosse et al., 2007), segregation of Ca- Mg-perovskite would have severely fractionated highly incompatible trace elements including element ratios like Th/La or Zr/Sm (Corgne et al., 2005; Hasenstab et al., 2021; Tusch et al., 2021a). Assuming that the Moon has predominantly accreted proto-Earth material (Pahlevan and Stevenson, 2007; Zhang et al., 2012; Stewart et al., 2018), it should have inherited such fractionated incompatible trace element ratios, which is rather not the case (Extended Data Fig. 3.1). Following model (2), proto-Earth may have sequestered enriched crustal material along the core-mantle boundary by subduction in a strongly convecting Hadean mantle (Fig. 3.3). This is supported by the presence of large

low-shear-velocity provinces in the deep mantle and could have resulted in the formation of an enriched hidden reservoir that was not sampled during the Moon-forming giant impact (Tolstikhin and Hofmann, 2005). However, the onset of continuous and large-scale subduction likely postdates the giant impact (Tolstikhin and Hofmann, 2005) and therefore it remains ambiguous whether very early subduction processes could have sequestered

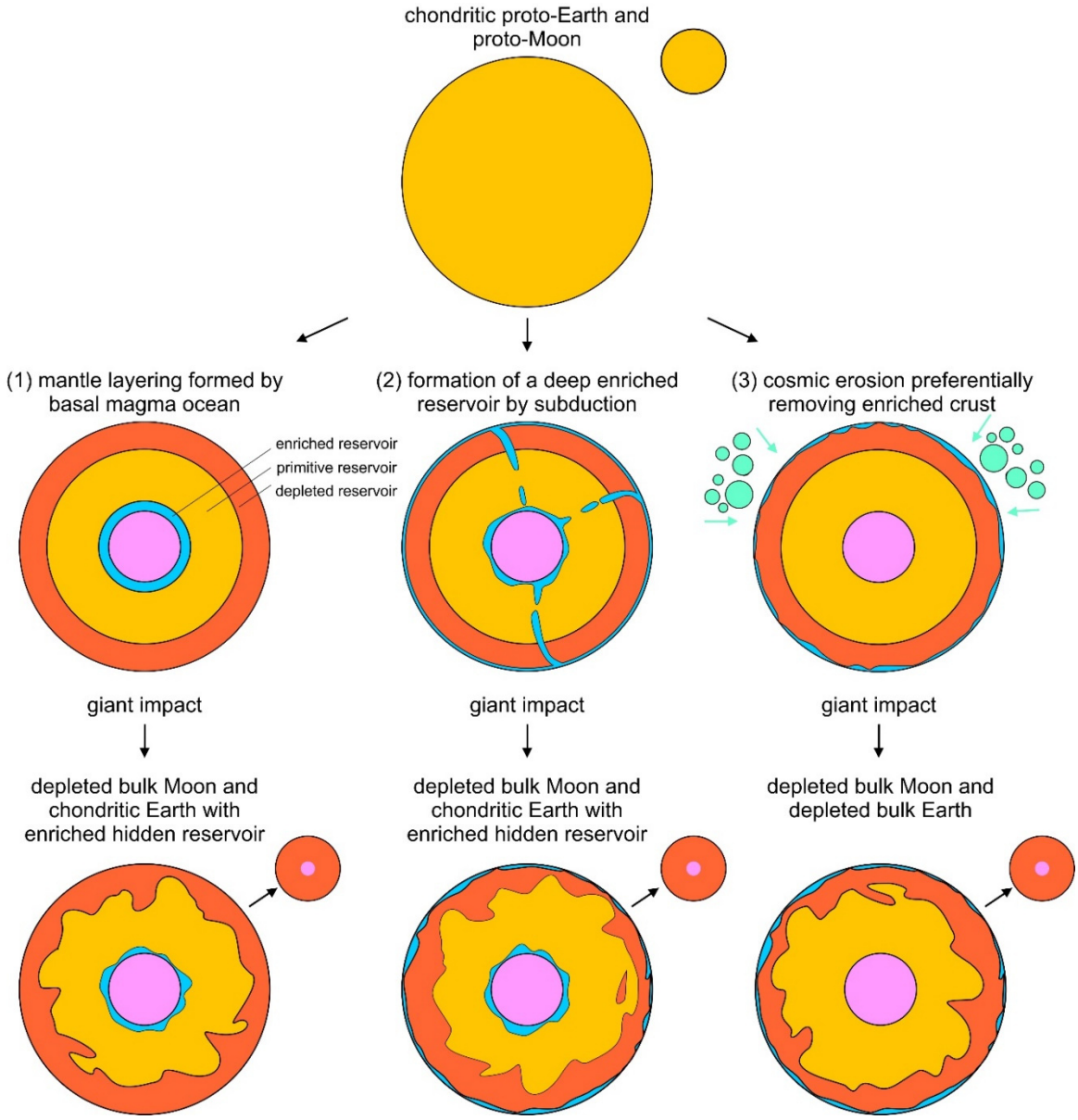

Fig. 3.3: Possible models explaining a slightly depleted composition of the Moon. Early silicate differentiation on a chondritic proto-Earth could account for early depleted reservoirs in three different ways (1) in an early magma ocean where a layered mantle was formed with a deep enriched reservoir (Labrosse et al., 2007); (2) in an early subduction-like setting where enriched crust was transported to lower mantle regions (Tolstikhin et al., 2006); or (3) during cosmic erosion that preferentially removed Earth's upper, enriched proto-crust (O'Neill and Palme, 2008). Due to the preferential sampling of depleted mantle material from the accessible Earth during the giant impact, all three models could account for an incompatible element depleted Moon. However, since it remains ambiguous, if early differentiated reservoirs would have survived the giant impact (Pahlevan and Stevenson, 2007; Stewart et al., 2018), we prefer the cosmic erosion model.

sufficient amounts of enriched material into the deep mantle. Notably, models (1) and (2), require that such hidden enriched reservoirs would have survived the Moon-forming impact (Tolstikhin et al., 2006; Pahlevan and Stevenson, 2007; Stewart et al., 2018), which is geodynamically difficult (Pahlevan and Stevenson, 2007; Stewart et al., 2018). This issue is bypassed in model (3), in which the enriched terrestrial reservoir is not sequestered in the deep Earth, but is rather partly removed by collisional erosion (O'Neill and Palme, 2008), leaving behind a slightly depleted BSE (Fig. 3.3). In this model, the Moon inherited its depleted composition from a depleted bulk proto-Earth. Although all models can in principle account for a depleted Moon, we therefore prefer model 3 due to the geodynamic shortcomings of models (1) and (2).

3.5. Conclusive remarks

In summary, we can explain the slightly depleted composition of the Moon (SDEM) with dynamic models, where the depleted lunar composition might be a vestige from a slightly depleted proto-Earth. This model is in line with previous models for a depleted proto-Earth (e.g., SCHEM or EDR) (Caro et al., 2008; Caro and Bourdon, 2010), but in the earlier models, a substantially higher degree of incompatible element depletion as postulated here was required, which is more difficult to be reconcile with Hf and Nd isotope constraints (Sprung et al., 2013; Burkhardt et al., 2016; Boyet et al., 2018). Our postulated SDEM composition lies in between the previously postulated depleted reservoirs (Caro et al., 2008; Caro and Bourdon, 2010) and primitive chondritic compositions (Palme and O'Neill, 2013). If proven valid by future work on terrestrial samples, our findings have not only implications for lunar research, but also may also shed new light on the mass balance of terrestrial mantle reservoirs.

3.6. Method section

3.6.1. Analytical techniques

For our ^{138}La-^{138}Ce and ^{147}Sm-^{143}Nd isotope study, we processed ca. 100 mg for basaltic samples and ca. 250 mg for FAN samples, as reported in the study of Thiemens et al., (2019). Prior to digestion, an isotope tracer enriched in ^{150}Nd and ^{149}Sm was added to all sample powders. After the samples were fully digested (for digestion technique see Thiemens et al., (2019)), the solutions were split into three aliquots, including a larger 70-80% aliquot (70% for high and low Ti basalts, 75% for FANs and 80% for KREEPs) that was subsequently processed following previous separation protocols (Pin and Zalduegui, 1997; Münker et al., 2001; Schnabel et al., 2017) to obtain pure and unspiked fractions for Ce-IC measurements, as previously summarized by Hasenstab et al., (2021). Compositions of Sm and Nd were also measured from these aliquots. An isotope tracer enriched in ^{138}La and ^{142}Ce was added to the second 10-15% aliquots, and left for two days at 120°C to ensure sample-spike equilibration. This LREE-bearing cut was subsequently processed after Schnabel et al., (2017) to separate pure element fractions for La-ID and Ce-ID analysis. The

remaining 10% aliquots were analyzed at University of Kiel for trace element compositions using an Agilent 7500cs quadruple ICP-MS and following the analytical protocol of Garbe-Schönberg, (1993). Due to total spiking of certain isotopes (^{94}Zr, ^{149}Sm, ^{150}Nd, ^{176}Lu, ^{180}Hf, ^{180}Ta, ^{183}W, ^{229}Th, ^{233}U and ^{236}U), we report the ID data instead (from Thiemens et al., (2019), Appendix A3).

Lanthanum-Ce isotope dilution (ID) and Ce isotope composition (IC) analyses were performed following the analytical protocol of Schnabel et al., (2017) on a Thermo Finnigan Neptune Plus MC ICP-MS at University of Cologne, with some minor modifications to the protocol stated in Hasenstab et al., (2021). The exponential law was used for mass bias correction assuming a ^{136}Ce/^{140}Ce of 0.002124072 (Makishima and Nakamura, 1991). A potential tailing effect of ^{140}Ce on ^{138}Ce was determined by measuring half masses but only yielded negligible tailing effects on ^{138}Ce that lie in the sub-ppm range (Schnabel et al., 2017; Hasenstab et al., 2021). All data are reported relatively to the Mainz AMES standard solution, with a ^{138}Ce/^{136}Ce of 1.33738 (Willbold, 2007). For Ce ID measurements, doped Ba was used for mass bias correction, assuming a ^{137}Ba/^{135}Ba ratio of 1.70383, whereas for La ID measurements doped Nd was used for mass bias correction (^{146}Nd/^{144}Nd=0.7219). The external reproducibilities on ^{138}La/^{136}Ce are better than ±0.2% (2σ) for ID measurements and ±21 ppm (2σ) for Ce IC measurements for single measurements (Schnabel et al., 2017; Hasenstab et al., 2021). To get better accuracy and precision of our measurements, we performed replicate measurements (up to 12 times) for Ce IC as far as it was possible from the available material. For samples analyzed more than four times (most KREEP basalts and some high Ti basalts), we report the 95% confidence interval as uncertainty, while our external reproducibility of ±21 ppm is given as uncertainty for samples measured four times or less.

Neodymium isotope compositions are reported relative to the La Jolla standard, having a ^{143}Nd/^{144}Nd ratio of 0.511859. Mass bias correction was performed by assuming a ^{146}Nd/^{144}Nd of 0.7219, following the exponential law. In contrast to older in house Nd isotope studies (Hasenstab et al., 2021) we used an Apex device, which yielded a significantly better external reproducibility of ±17 ppm while the external reproducibility for ^{147}Sm/^{144}Nd ratios amounts to better than ±0.2% (2σ). The calculated uncertainties on initial Ce and Nd isotope compositions as well as parent/daughter$_{source}$ ratios represent the propagated uncertainties from the measured isotope compositions, the uncertainties of the parent-daughter ratio and the uncertainties of the crystallization ages as well as and neutron capture effects in case they remained uncorrected.

3.6.2. Neutron capture effects

Due to the large amount of elements analyzed from the same sample digestions employed for this study (Zr, Lu, Hf, Nb, Ta, W, U, Th, La, Ce, Nd, Sm) (Thiemens et al., 2019) we have chosen total spiking for Sm-Nd analysis to avoid a more complex chromatographic separation protocol with possibly poor yields. However, total spiking hampers an accurate correction for the neutron capture affected Sm and Nd isotopes. For the samples of this study, for which Sm isotopes have been previously analyzed (Boyet and Carlson, 2007;

Sprung et al., 2013; Gaffney and Borg, 2014; Mcleod et al., 2014; Borg et al., 2019), we corrected neutron capture effects following the approach of Sprung et al., (2010) and Sprung et al., (2013), since previous studies (Brandon et al., 2009a; Mcleod et al., 2014) have shown that secondary neutron fluences vary insignificantly within the same samples. For samples without Sm IC isotope literature data being available, we additionally included an uncertainty of ±0.5 εNd-units to the uncertainty propagation, which is a valid maximum as outlined in a similar approach(Münker, 2010).

For Ce isotopes, we also used the available Sm isotope data (Boyet and Carlson, 2007; Sprung et al., 2013; Gaffney and Borg, 2014; Mcleod et al., 2014; Borg et al., 2019) and if available in conjunction with unspiked Hf isotope data (Sprung et al., 2014; Kruijer and Kleine, 2017) to quantify the effects on La and Ce isotopes. The neutron capture effects on La and Ce isotopes are generally significantly lower than what is observed for Nd or Sm isotopes with the strongest effects lying on ^{136}Ce, showing cross sections and resonance integrals calculated from the derived ENDF/B-VI.8 300°K database (https://www-nds.iaea.org/exfor/endf.htm.), using the ENDF utility code inter_win.exe (https://www-nds.iaea.org/public/endf/utility-7.0/inter/.) (see Extended Data Table 3.1 for detailed parameters). The respective neutron capture effects were calculated using the code of Sprung et al., (2013), extended for La and Ce and adhering to the same boundary conditions listed therein. Similar to the Sm-Nd corrections, for La-Ce corrections, epithermal-to-thermal flux-ratios were calculated from existing Sm-IC data (Boyet and Carlson, 2007; Sprung et al., 2013; Gaffney and Borg, 2014; Mcleod et al., 2014; Borg et al., 2019) and Hf-IC data (Sprung et al., 2014; Kruijer and Kleine, 2017). The strongest neutron capture effect were calculated for sample 15556 where the measured εCe value would be 0.03 ε-units higher than the neutron capture corrected value, which is negligible, given the present analytical uncertainty. This sample is also known to have Sm isotope compositions corresponding to extraordinarily strong neutron irradiations (Sprung et al., 2013). For samples for which Sm IC data exists, a neutron capture correction was applied for the ^{138}La-^{138}Ce systematics. For samples without existing Sm IC data, we added a 3 ppm uncertainty (which is the highest correction in this study) to our uncertainty propagation.

Since Ce-Nd isotope arrays of lunar rocks from this study form a linear trend (Fig. 3.1) as observed in present day igneous rocks (Israel et al., 2019) or Archean rocks (Hasenstab et al., 2021; Tusch et al., 2021a), this observation further corroborates that the uncertainty estimates for neutron capture induced isotope heterogeneity employed here are sufficiently robust, since different cross sections for different isotopes and elements should produce scatter on the $\varepsilon Ce_{(i)}$-$\varepsilon Nd_{(i)}$ array. Therefore, we conclude that neutron capture processes did not affect Ce isotope compositions and that the Ce-Nd isotope compositions of this study only reflect the pristine magmatic events.

3.6.3. Previous modelling constraints on LMO crystallization

Choosing adequate model parameters is crucial, as they exert a strong impact on the inferred model outcome. Previous modelling approaches that addressed long-lived isotope systematics in lunar rocks (Sprung et al., 2013) explained the lunar isotope data by the

formation of distinct LMO cumulate reservoirs (Snyder et al., 1992) that retained variable amounts of trapped interstitial residual liquid (TIRL). However, this approach needs to be treated with caution, as it considers high amounts (≥20%) of TIRL to explain the $^{147}Sm/^{144}Nd_{source}$ and $^{176}Lu/^{177}Hf_{source}$ compositions of some samples (samples 15499 or 15495 and 10057). This is ≥4 times higher than previous estimates for TIRL that amounted to ≤5% (Snyder et al., 1992; Münker, 2010). Due to trace element partitioning, the crystallizing cumulates will become incompatible trace element depleted whereas the remaining melt residue will become increasingly enriched. Consequently, the admixture of high amounts of TIRL to the LMO cumulate would dominate the incompatible trace element budget of the cumulate. However, this is not in accord with trace element constraints provided by our study. We obtained high precision isotope dilution (ID) data for a variety of low Ti basalts, including sample 15495 that, required extremely high amounts of TIRL (ca. 20%) according to Sprung et al., (2013). However, our data reveal a strongly subchondritic Th/La ratio (0.0944) for sample 15495 which is almost 25% lower than chondritic/primitive mantle estimates (Palme and O'Neill, 2013), similar to other low Ti basalts (Fig. 3.2b). Such depleted characteristics cannot be reconciled by high amounts of TIRL, which would cause superchondritic Th/La ratios.

Another issue arises from the choice of partition coefficients used in the model of Sprung et al., (2013). This study assumed a D_{Hf} of 0.28 for ilmenite, resulting in D_{Hf}/D_{Lu} ratios that are ~10 times lower than previous estimates for lunar ilmenite (Klemme et al., 2006). Taking such low D_{Hf} values into consideration, positive Hf/Hf^* anomalies that are diagnostic for high Ti basalts (Extended Data Fig. 3.2) could no longer be related to partial melting of ilmenite (Kommescher et al., 2020). The low partition coefficients for Hf in ilmenite comes from a study that investigated trace element partitioning between ilmenite, armalcolite and silicate melts (van Kan Parker et al., 2011). Similar to ilmenite, armalcolite is also a Ti-oxide in which Zr and Hf are even more compatible than in ilmenite (see van Kan Parker et al., (2011)). We conclude that the low D_{Hf} for ilmenite is related to the presence of armalcolite in the experimental charges of van Kan Parker et al., (2011) that exerts a strong influence on the partitioning behavior of Hf in ilmenite. Accordingly, the D_{Hf} value of 0.28 in ilmenite from van Kan Parker et al., (2011) is expected to be underestimated when armalcolite is not present. These considerations are also in accord with ilmenite partitioning data obtained by another study (Klemme et al., 2006) that reported significantly higher D_{Hf} values in ilmenite (1.24). Notably, when a more realistic D_{Hf} of 1.24 is used for ilmenite (Klemme et al., 2006) the IBC endmember from Sprung et al., (2013) would plot at significantly lower $^{176}Lu/^{177}Hf$ ratios. Consequently, such an IBC endmember composition would define a mixing array that would no longer be able to explain the observed range of $^{176}Lu/^{177}Hf_{source}$ ratios in high Ti basalts.

3.6.4. New modelling constraints

In our model, we assumed a slightly depleted bulk silicate Moon as starting composition. As previously proposed, LMO solidification followed a crystallization sequence (Snyder et al., 1992) that produced geochemically distinct mantle cumulates. The proceeding LMO solidification sequestered a crystallization sequence that formed six geochemically distinct

cumulate reservoirs: Strongly depleted (1) orthopyroxene-rich and (2) clinopyroxene-plagioclase-pigeonite-rich cumulates, moderately depleted (3) olivine-rich and (4) plagioclase-pigeonite-olivine rich cumulates, slightly enriched (5) ilmenite-bearing cumulates, and a highly enriched (6) KREEP-reservoir. As we can show, subsequent mixing of these cumulates forms hybrid reservoirs that are able to explain the full range of isotope and trace element characteristics observed in the most common petrological lunar rock types.

As discussed in the main text, we argue that the depleted character of the Moon may have been inherited from a depleted proto-Earth. A depleted composition for the BSE has previously been suggested by other studies (Caro et al., 2008; O'Neill and Palme, 2008; Caro and Bourdon, 2010; Campbell et al., 2012). To quantify the composition of a depleted proto-Earth, we followed the approach of O'Neill and Palme, (2008). In short, 2.6 % of crust (relative to BSE) is extracted, and partly (54%) removed by collisional erosion (see O'Neill and Palme, (2008) for more details). This causes a depleted composition of a left-over proto-Earth with a superchondritic $^{147}Sm/^{144}Nd$ ratio of 0.2063, ,similar to previous estimates (Caro et al., 2008; Caro and Bourdon, 2010). We expanded the modelled depleted BSE composition from O'Neill and Palme, (2008) now also providing data for Nb, Ta, Ce, Pr, Zr, Eu, Gd, Tb, Dy, Y Ho, Er and Y using the same model parameters and partitioning coefficients as originally used in study (O'Neill and Palme, 2008), with some minor adjustments. The partition coefficients for La were recalculated using the lattice strain model (Blundy and Wood, 1994), since D_{La}/D_{Ce} was unrealistically low (0.45), with D_{La} plotting significantly below the predicted lattice strain hyperbole defined by other rare earth elements. To prevent the slightly depleted proto-Earth from transmitting potential Zr-Hf anomalies to the Moon, D_{Zr} was recalculated so that the inferred composition had a $Zr/Zr^{*}=(Sm_{CN}\times Nd_{CN})^{0.5}=1$ and Hf was recalculated by assuming constant D_{Zr}/D_{Hf} ratios that were previously reported (O'Neill and Palme, 2008). The proposed depleted proto-Earth composition (SDEM) is given in Table 3.1 and Extended Data Table 3.2 and all modelling parameters and outcomes (LMO crystallization compositions) are listed Appendix A3.

Recent studies have shown remarkable nucleosynthetic isotope similarities between Earth and Moon, such as for Cr or Ti that are indistinguishable on both planetary bodies (Zhang et al., 2012; Young et al., 2016; Mougel et al., 2018). Furthermore oxygen isotope compositions of Earth and Moon are also virtually indistinguishable (Young et al., 2016) although previous studies suggested small differences (Greenwood et al., 2018; Cano et al., 2020) that are still clearly much lower compared to compositions of other planetary bodies, such as Mars or Vesta (Mohapatra and Murty, 2003; Zhang et al., 2019). Based on these observations, more recent dynamic models for the Moon-forming giant impact suggest near-complete equilibration between Earth and Moon (Pahlevan and Stevenson, 2007; Stewart et al., 2018). On that basis, we also assumed full equilibration between the lunar impactor and proto-Earth. Our lunar impactor of assumed chondritic composition amounts to ca. 14% of Earth's mass (Canup, 2004), as suggested in a previous study. During accretion, the Moon inherited the depleted incompatible trace element characteristics of the depleted proto-Earth. Our modelled depleted BSM evolves at $^{138}La/^{136}Ce=0.1768$, $^{147}Sm/^{144}Nd=0.2045$ and $^{176}Lu/^{177}Hf=0.03680$, slightly lower than the Superchondritic Earth Model by Caro and Bourdon, (2010). This corresponds to present day εCe, εNd and εHf

values of -0.94, +5.0 and +10.1, respectively. If differentiation directly occurred at 4.568 Ga, a maximum μ^{142}Nd of +13.2 ppm relative to chondrites can be inferred. A younger age for this differentiation event would shift Earth's (and the Moon's) μ^{142}Nd composition towards lower ^{142}Nd excesses. For example, when assuming a differentiation age of 4.525 Ga that is slightly younger than the most recent age estimations of the Moon (Thiemens et al., 2019), the μ^{142}Nd excess of Earth (and consequently the Moon) would decrease to +9.9 ppm.

After the Moon has accreted from depleted Earth material, it underwent planetary differentiation, i.e., lunar magma ocean (LMO) formation. For this event we assumed an age of 4.336 Ga (Borg et al., 2019) and a crystallization sequence as previously suggested (Snyder et al., 1992). The distinct mantle reservoirs formed during LMO crystallization comprise (in order of crystallization) olivine-cumulates, orthopyroxene-cumulates, plagioclase-olivine-pigeonite-cumulates, clinopyroxene-plagioclase-pigeonite-cumulates, pigeonite-plagioclase-clinopyroxene-ilmenite-bearing cumulates and KREEP. It has been shown that fractional crystallization operates imperfectly, as, for examples, anorthosites often still contain olivine. To account for these imperfect conditions, we added 2% entrained plagioclase and 1-5% TIRL to the cumulates as suggested earlier (Snyder et al., 1992). Throughout our modelling we used partition coefficients from recent studies (Phinney and Morrision, 1990; Westrenen et al., 2000; McDade et al., 2003; Klemme et al., 2006; Dygert et al., 2020). For a better overview, we provide all modelling parameters as well as compositions of the different lunar reservoirs in the Appendix A3.

3.6.5. Evaluation of nucleosynthetic contributions to the terrestrial ^{142}Nd inventory

In the past, nucleosynthetic variations have been reported for Nd isotopes (Bouvier and Boyet, 2016; Burkhardt et al., 2016; Boyet et al., 2018), and negative correlations for μ^{145}Nd, μ^{148}Nd and μ^{150}Nd vs. μ^{142}Nd have been observed and were interpreted as mixing lines of differently distributed s-process material. Previous studies (Bouvier and Boyet, 2016; Burkhardt et al., 2016; Fukai and Yokoyama, 2017; Fukai and Yokoyama, 2019) have argued that Earth also falls on this mixing line, leading to the interpretation that Earth must be chondritic as well. However, none of these studies have calculated best fit lines whether Earth really plots on that mixing line or not. Boyet et al., (2018) compiled existing chondrite data and on that basis we have calculated best fit intersects in μ^{142}Nd vs. μ^{145}Nd, μ^{148}Nd and μ^{150}Nd spaces. The weighted intersects at μ^{145}Nd=0, μ^{148}Nd=0, and μ^{150}Nd=0 amount to μ^{142}Nd=-11.0 ±1.5 ppm, indicating that a residual μ^{142}Nd difference of ca. 11 ppm between Earth and the most Earth-like chondrites cannot be fully explained by nucleosynthetic variations alone (Extended Data Fig. 3.4). In these plots, enstatite chondrites are the most Earth-like chondrites, whereas ordinary chondrites as well as carbonaceous chondrites show an increasing s-process deficit, becoming increasingly distinct from Earth's Nd isotope composition. Burkhardt et al., (2016) has argued that the high amounts of CAIs in the CV chondrite Allende distorts the Nd isotope composition of Allende (and that of other CV chondrites). Notably, subtracting CAIs as suggested by Burkhardt et al., (2016) would shift carbonaceous chondrites towards lower μ^{142}Nd but

higher μ^{145}Nd, μ^{148}Nd and ^{150}Nd values, which would result in a rotation of the best fit s-process mixing line (Extended Fig. 3.4). Considering that almost all of the carbonaceous chondrites comprise CV chondrites, this would affect most of the carbonaceous chondrites (Extended Data Fig. 3.4). Since the mean value of these three arrays roughly approximate to the composition of ordinary chondrites in μ^{142}Nd vs. $\mu^{145,148,150}$Nd space, ordinary chondrites would roughly constitute the point of rotation of these arrays, if a CAI correction for CV chondrites was applied. Since the best fit slopes in μ^{142}Nd vs. μ^{145}Nd and μ^{148}Nd space are steeper compared to the CAI subtraction line, the correction for CAI admixture would rotate these best fit lines counterclockwise, resulting in lower μ^{142}Nd intersections. Therefore, the lowest of these intersects (μ^{142}Nd=-5.7±1.3; Extended Data Figs. 3.4a-d) can be considered a minimum residual offset for Earth. In μ^{142}Nd vs. μ^{150}Nd space, however, the calculated best fit lines have a shallower slope compared to the CAI mixing line, which would rotate the best fit line clockwise, resulting in decreased μ^{142}Nd intersections. Therefore, our lowest calculated offset in μ^{142}Nd vs. μ^{150}Nd space (μ^{142}Nd=-12.4±0.6; Extended Data Figs. 4e-f) can be considered a maximum offset for Earth. Combined, this implies that the offset between Earth and the most Earth-like chondrites (μ^{145}Nd=0; μ^{148}Nd=0; μ^{150}Nd=0) in their ^{142}Nd/^{144}Nd compositions must lie between 5.7±1.3 and 12.4±0.6 ppm. In this regard, our superchondritic Earth model provides a viable mechanism to explain this residual offset. Depending on the differentiation age at which Earth must have differentiated, our modeling predictions suggest maximum ^{142}Nd/^{144}Nd difference of ≤13.2 ppm for Earth (assuming earliest possible terrestrial differentiation at 4.568 Ga), which is in excellent agreement with the observed difference between Earth and chondrites.

3.6.6. Extended Data Figures and Tables

Extended Data Fig. 3.1: Combined intersects of terrestrial and lunar Ce-Nd arrays for a) 3.25±0.1 Ga lunar and Pilbara rocks (Hasenstab et al., 2021), b) 3.3±0.25 Ga lunar and Pilbara (Hasenstab et al., 2021) rocks, c) 3.65±0.2 Ga lunar and Kaapvaal rocks (Tusch et al., 2021a). None of the individual arrays intersect the chondritic composition (Willig and Stracke, 2019), but all arrays share a common slightly depleted reservoir (SDEM).

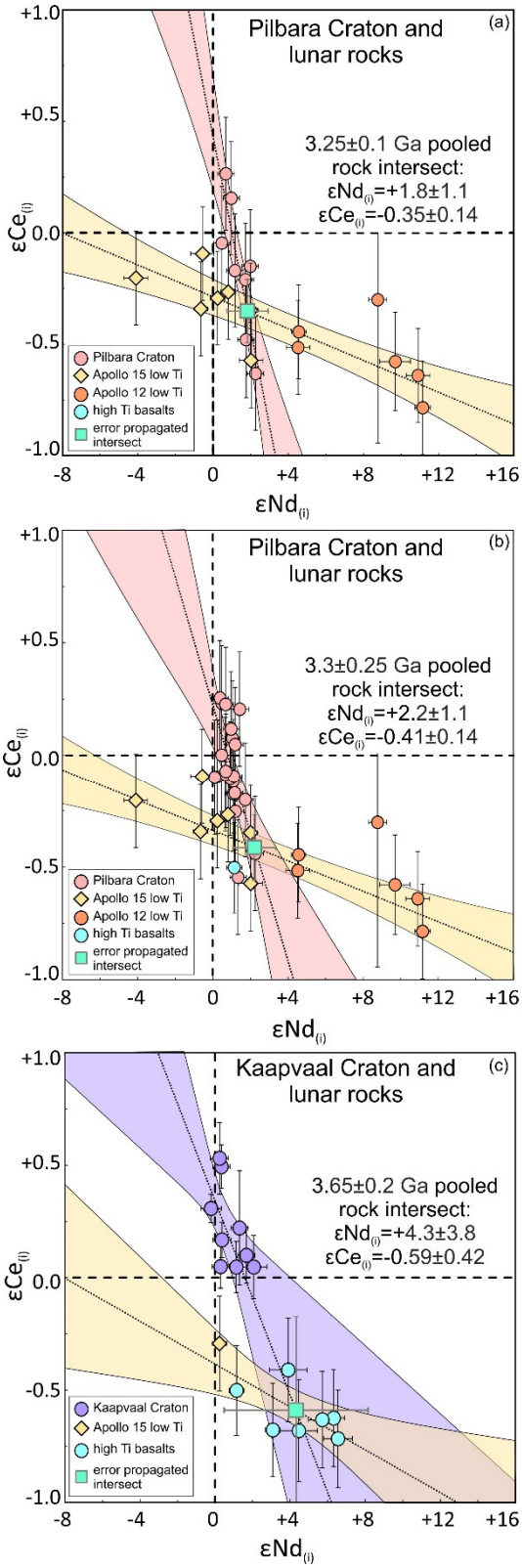

Extended Data Table 3.1

Neutron capture cross sections and resonance integrals used to calculated neutron effects on La and Ce isotope compositions.

isotope	thermal neutron capture cross section @ 300 K	resonance integral
^{134}Ba	1.39E+00	2.14E+01
^{135}Ba	5.76E+00	9.89E+01
^{136}Ba	4.08E-01	1.64E+00
^{137}Ba	5.05E+00	3.87E+00
^{138}Ba	3.56E-01	2.57E-01
^{138}La	5.66E+01	3.64E+02
^{139}La	8.90E+00	1.20E+01
^{136}Ce	7.38E+00	7.66E+01
^{138}Ce	1.02E+00	9.12E+00
^{140}Ce	5.64E-01	3.91E-01
^{142}Ce	9.41E-01	3.00E+00

Extended Data Table 3.2:

Trace element composition of SDEM.

element [ppm]	SDEM
Th	0.0526
Nb	0.386
Ta	0.0279
La	0.499
Ce	1.37
Pr	0.214
Nd	1.10
Zr	8.48
Hf	0.250
Sm	0.371
Eu	0.144
Gd	0.511
Tb	0.0955
Dy	0.652
Y	3.75
Er	0.428
Yb	0.442
Lu	0.0657

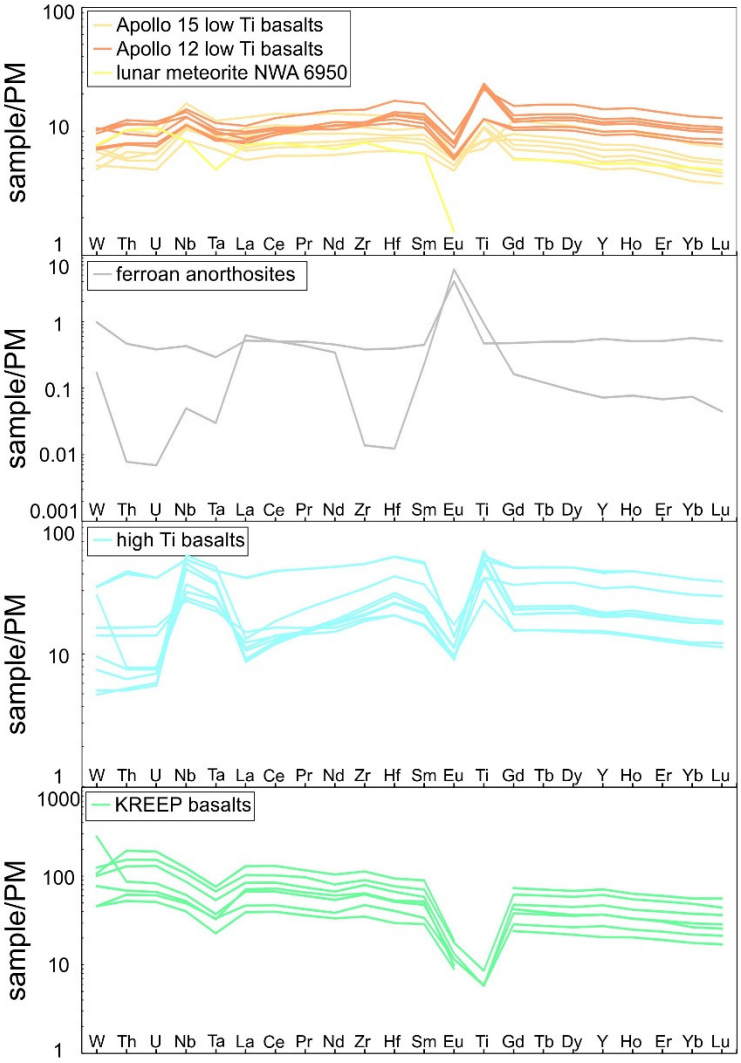

Extended Data Fig. 3.2: Incompatible trace element patterns for various lunar samples analysed here, divided by petrological types. Data for W, Th, U, Nb, Ta Zr, Hf and Lu comprise isotope dilution data from Thiemens et al., (2019) and Ti isotope dilution data is from Kommescher et al., (2020). Lanthanum, Ce, Nd and Sm data comprise isotope dilution data from this study. All combined data were obtained from the same digestion. Primitive mantle was taken from Palme and O'Neill, (2013) with slight modifications: Nb was extrapolated by assuming a Nb/Ta ratio of 17 (Münker et al., 2003) and W was extrapolated by assuming a Hf/W ratio of 25.6 for the BSM (Thiemens et al., 2019).

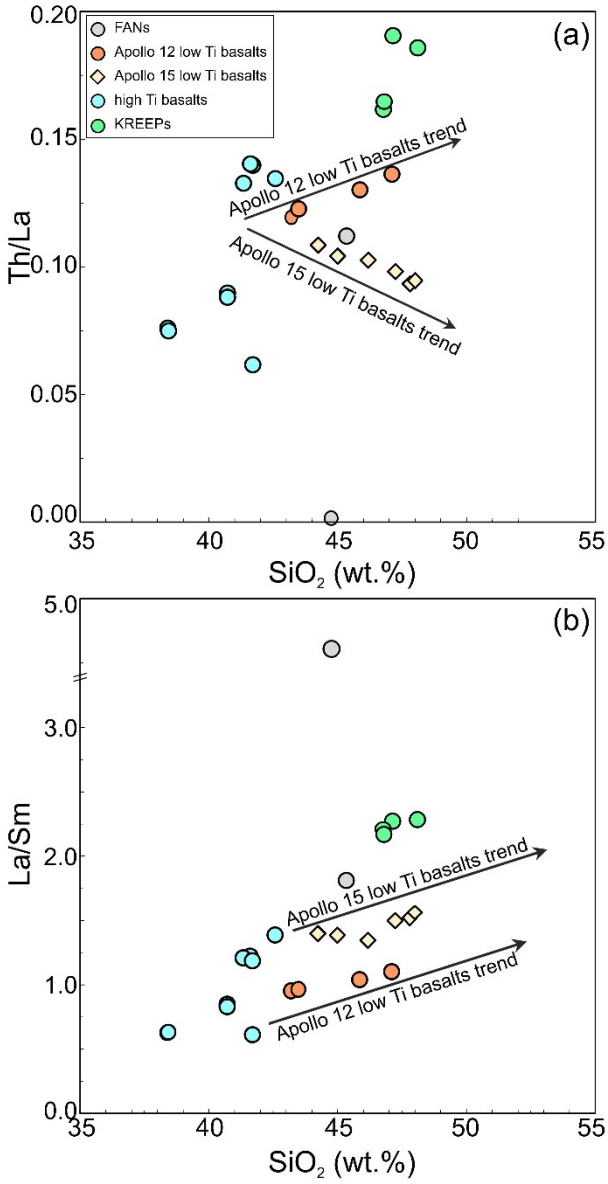

Extended Data Fig. 3.3: Trace element variation diagrams illustrating petrological and geochemical differences between Apollo 12 and 15 low Ti basalts. Plotted are a) Th/La vs. SiO_2 and b) La/Sm vs. SiO_2. The data imply that Apollo 12 and 15 low Ti basalts must have been derived from distinct mantle cumulate reservoirs. Thorium data are from Thiemens et al., (2019) and SiO_2 data from previous studies (Morrison et al., 1971; Wakita et al., 1971; Willis et al., 1971; Mason et al., 1972; Strasheim et al., 1972; Taylor et al., 1972; Willis et al., 1972; Nakamura et al., 1973; Rhodes and Hubbard, 1973; Duncan et al., 1974; Rose et al., 1975; Wänke et al., 1975; Rhodes et al., 1977; Wänke et al., 1977; Snyder et al., 1997; Ryder and Schuraytz, 2001; Norman et al., 2002). SiO_2 data were only considered from studies that also reported incompatible trace element data that are well consistent with our trace element data.

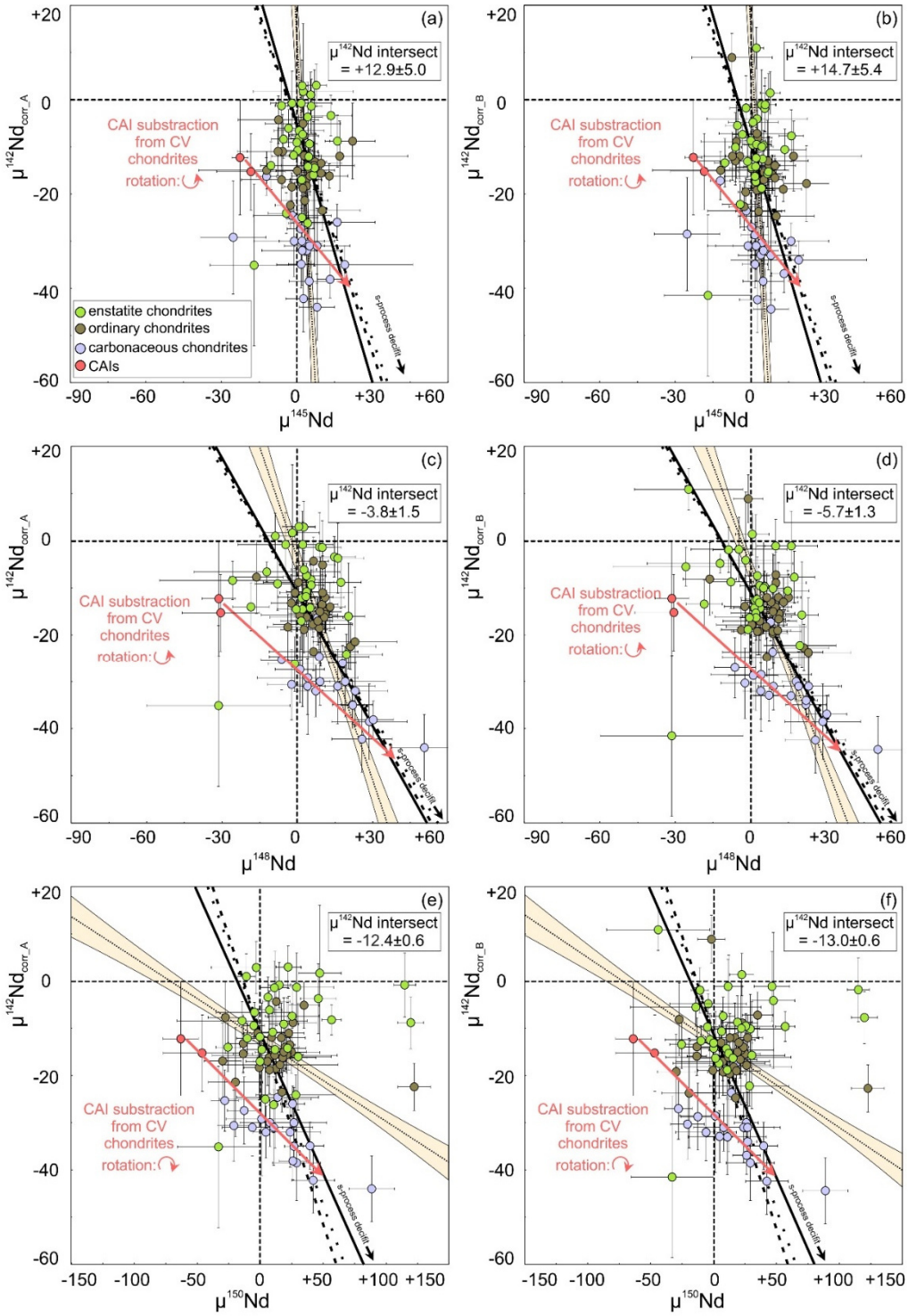

Extended Data Fig. 3.4: Nucleosynthetic variations of Nd isotopes. Reevaluation of different chondrite classes and their implications for Earth's $^{142}Nd/^{144}Nd$ composition from recently compiled data (Boyet et al., 2018). Plotted are a) $\mu^{142}Nd_{corr\_A}$ vs. $\mu^{145}Nd$, b) $\mu^{142}Nd_{\_corr\_B}$ vs. $\mu^{145}Nd$, c) $\mu^{142}Nd_{corr\_A}$ vs. $\mu^{148}Nd$, d) $\mu^{142}Nd_{\_corr\_B}$ vs. $\mu^{148}Nd$, e) $\mu^{142}Nd_{corr\_A}$ vs. $\mu^{150}Nd$ and f) $\mu^{142}Nd_{\_corr\_B}$ vs. $\mu^{150}Nd$. From all six plots, we recalculated a weighted y-axis intersect for $\mu^{142}Nd$ that amounts to -11.0±1.5, with Earth having a $\mu^{142}Nd$ of 0. This implies, that Earth has a $^{142}Nd/^{144}Nd$ isotope composition that is 11 ppm higher than the most Earth-like chondrites, even when nucleosynthetic variations are considered. For carbonaceous chondrites, CAI-uncorrected compositions were used. The effects of CAI subtraction as suggested by Burkhardt et al., (2016) is discussed in the appendix. The abbreviations "corr_A" and "corr_B" refer to the correction of radiogenic ingrowth of ^{146}Sm-^{142}Nd over time by using measured $^{147}Sm/^{144}Nd$ ratios or by using calculated Sm/Nd ratios from the long-lived $^{147}Sm/^{144}Nd$ systematics, respectively (see also Boyet et al., (2018)). Slopes for s-process mixing lines are from Burkhardt et al., (2016) but intersect at $\mu^{142}Nd$=-11 as proposed from the best fit intersects that were recalculated here. Nd isotope data for CAIs are from previous studies (Brennecka et al., 2013; Burkhardt et al., 2016). Colored bands represent the error propagated best fit lines.

References

Alexander E. C., Davis P. K., Lewis R. S. and Reynolds J. H. (1972) Alexander et al., (1972): Rare-gas analysis on neutron irradiated Apollo 12 samples. *Proc. 3rd Lunar Sci. Conf.*, 1787–1795.

Allègre C. J., Manhès G. and Göpel C. (2008) The major differentiation of the Earth at ⍰ 4.45 Ga. *Earth Planet. Sci. Lett.* **267**, 386–398.

Amelin Y., Kamo S. L. and Lee D. C. (2011) Evolution of early crust in chondritic or nonchondritic Earth inferred from U-Pb and Lu-Hf data for chemically abraded zircon from the Itsaq Gneiss Complex, West Greenland. *Can. J. Earth Sci.* **48**, 141–160.

Archer G. J., Brennecka G. A., Gleißner P., Stracke A., Becker H. and Kleine T. (2019) Lack of late-accreted material as the origin of 182W excesses in the Archean mantle: Evidence from the Pilbara Craton, Western Australia. *Earth Planet. Sci. Lett.* **528**, 115841.

Arndt N., Bruzak G. and Reischmann T. (2001) The oldest continental and oceanic plateaus: geochemistry of basalts and komatiites of the Pilbara Craton, Australia. In: *Ernst, R.E., Buchan, K.L. (Eds.), Mantle Plumes Their Identif. Through Time,* **352**, 359–387.

Arndt N. T., Kerr A. C. and Tarney J. (1997) Dynamic melting in plume heads: the formation of Gorgona komatiites and basalts. *Earth Planet. Sci. Lett.* **146**, 289–301.

Arnould M. and Goriely S. (2003) The p-process of stellar nucleosynthesis: Astrophysics and nuclear physics status. *Phys. Rep.* **384**, 1–84.

Baadsgaard H., Nurman A. P., Rosing M., Bridgwater D. and Longstaffe F. J. (1986) Alteration and metamorphism of Amitsoq gneisses from the Isukasia area, West Greenland: Recommendations for isotope studies of the early crust. *Geochim. Cosmochim. Acta* **50**, 2165–2172.

Barosch J., Hezel D. C., Ebel D. S. and Friend P. (2019) Mineralogically zoned chondrules in ordinary chondrites as evidence for open system chondrule behaviour. *Geochim. Cosmochim. Acta* **249**, 1–16.

Bédard J. H. (2018) Stagnant lids and mantle overturns: Implications for Archaean tectonics, magmagenesis, crustal growth, mantle evolution, and the start of plate tectonics. *Geosci. Front.* **9**, 19–49.

Bennett V. C., Brandon A. D. and Nutman A. P. (2007) Coupled 142Nd-143Nd isotopic evidence for hadean mantle dynamics. *Science (80-.).* **318**, 1907–1910.

Bennett V. C., Nutman A. P. and McCulloch M. T. (1993) Nd isotopic evidence for transient, highly depleted mantle reservoirs in the early history of the Earth. *Earth Planet. Sci. Lett.* **119**, 299–317.

Birck J. L. (1986) Precision KRbSr isotopic analysis: Application to RbSr chronology. *Chem. Geol.* **56**, 73–83.

Bisterzo S., Travaglio C., Gallino R., Wiescher M. and Käppeler F. (2014) Galactic chemical evolution and solar s-process abundances: Dependence on the 13c-pocket structure. *Astrophys. J.* **787**.

Bizzarro M., Baker J. A., Haack H. and Lundgaard K. L. (2005) Rapid Timescales for Accretion and Melting of Differentiated Planetesimals Inferred from 26 Al- 26 Mg Chronometry . *Astrophys. J.* **632**, L41–L44.

Blichert-Toft J., Arndt N. T., Wilson A. and Coetzee G. (2015) Hf and Nd isotope systematics of early Archean komatiites from surface sampling and ICDP drilling in the Barberton Greenstone Belt, South Africa. *Am. Mineral.* **100**, 2396–2411.

Blundy J. and Wood B. J. (1994) Prediction of crystal-melt partition coeffiecients. *Lett. to natureature* **372**, 452–454.

Borg L. E., Connelly J. N., Boyet M. and Carlson R. W. (2011) Chronological evidence that the Moon is either young or did not have a global magma ocean. *Nature* **477**, 70–73.

Borg L. E., Gaffney A. M., Kruijer T. S., Marks N. A., Sio C. K. and Wimpenny J. (2019) Isotopic evidence for a young lunar magma ocean. *Earth Planet. Sci. Lett.* **523**.

Bouvier A., Blichert-Toft J., Moynier F., Vervoort J. D. and Albarède F. (2007) Pb-Pb dating constraints on the accretion and cooling history of chondrites. *Geochim. Cosmochim. Acta* **71**, 1583–1604.

Bouvier A. and Boyet M. (2016) Primitive Solar System materials and Earth share a common initial 142Nd abundance. *Nature* **537**, 399–402.

Bouvier A., Vervoort J. D. and Patchett P. J. (2008) The Lu-Hf and Sm-Nd isotopic composition of CHUR: Constraints from unequilibrated chondrites and implications for the bulk composition of terrestrial planets. *Earth Planet. Sci. Lett.* **273**, 48–57.

Bouvier A. and Wadhwa M. (2010) The age of the Solar System redefined by the oldest Pb-b age of a meteoritic inclusion. *Nat. Geosci.* **3**, 637–641.

Boyet M., Bouvier A., Frossard P., Hammouda T., Garçon M. and Gannoun A. (2018) Enstatite chondrites EL3 as building blocks for the Earth: The debate over the 146Sm–142Nd systematics. *Earth Planet. Sci. Lett.* **488**, 68–78.

Boyet M. and Carlson R. W. (2005) 142Nd Evidence for Early (>4.53 Ga) Global Differentiation of the Silicate Earth. *Science (80-.).* **309**, 576–581.

Boyet M. and Carlson R. W. (2007) A highly depleted moon or a non-magma ocean origin for the lunar crust? *Earth Planet. Sci. Lett.* **262**, 505–516.

Boyet M. and Carlson R. W. (2006) A new geochemical model for the Earth's mantle inferred from 146Sm-142Nd systematics. *Earth Planet. Sci. Lett.* **250**, 254–268.

Boyet M. and Gannoun A. (2013) Nucleosynthetic Nd isotope anomalies in primitive enstatite chondrites. *Geochim. Cosmochim. Acta* **121**, 652–666.

Brandon A. D., Lapen T. J., Debaille V., Beard B. L., Rankenburg K. and Neal C. (2009a) Re-evaluating 142 Nd / 144 Nd in lunar mare basalts with implications for the early evolution and bulk Sm / Nd of the Moon. *Geochim. Cosmochim. Acta* **73**, 6421–6445.

Brandon A. D., Lapen T. J., Debaille V., Beard B. L., Rankenburg K. and Neal C. (2009b) Re-evaluating 142Nd/144Nd in lunar mare basalts with implications for the early evolution and bulk Sm/Nd of the Moon. *Geochim. Cosmochim. Acta* **73**, 6421–6445.

Brennecka G. A., Borg L. E. and Wadhwa M. (2013) Evidence for supernova injection into the solar nebula and the decoupling of r -process nucleosynthesis. **110**, 17241–17246.

Budde G., Burkhardt C. and Kleine T. (2019) Molybdenum isotopic evidence for the late accretion of outer Solar System material to Earth. *Nat. Astron.* **3**, 736–741.

Burkhardt C., Borg L. E., Brennecka G. A., Shollenberger Q. R., Dauphas N. and Kleine T. (2016) A nucleosynthetic origin for the Earth's anomalous 142 Nd composition. *Nature* **537**, 394–398.

Campbell I. H., St C. O'Neill H., O'Neill H. S. C. and St C. O'Neill H. (2012) Evidence against a chondritic Earth. *Nature* **483**, 553–558. Available at: http://dx.doi.org/10.1038/nature10901.

Candela P. A. and Bouton S. L. (1990) The influence of oxygen fugacity on tungsten and molybdenum partitioning between silicate melts and ilmenite. *Econ. Geol.* **85**, 633–640.

Cano E. J., Sharp Z. D. and Shearer C. K. (2020) Distinct oxygen isotope compositions of the Earth and Moon. *Nat. Geosci.* **13**, 270–274. Available at: http://dx.doi.org/10.1038/s41561-020-0550-0.

Canup R. M. (2004) Simulations of a late lunar-forming impact. *Icarus* **168**, 433–456.

Canup R. M. and Asphaug E. (2001) Origin of the Moon in a giant impact near the end of the Earth's formation. *Nature* **412**, 708–712.

Carlson R. W., Borg L. E., Gaffney A. M. and Boyet M. (2014) Rb-Sr, Sm-Nd and Lu-Hf isotope systematics of the lunar Mg-suite: The age of the lunar crust and its relation to the time of Moon formation. *Philos. Trans. R. Soc. A Math. Phys. Eng. Sci.* **372**.

Carlson R. W., Boyet M. and Horan M. (2007) Chondrite Barium, Neodymium, and Samarium Isotopic Heterogeneity and Early Earth Differentiation. *Science (80-.).* **316**, 1175–1178.

Caro G. and Bourdon B. (2010) Non-chondritic Sm/Nd ratio in the terrestrial planets: Consequences for the geochemical evolution of the mantle-crust system. *Geochim. Cosmochim. Acta* **74**, 3333–3349. Available at: http://dx.doi.org/10.1016/j.gca.2010.02.025.

Caro G., Bourdon B., Birck J. L. and Moorbath S. (2003) 146Sm-142Nd evidence from Isua metamorphosed sediments for early differentiation of the Earth's mantle. *Nature* **423**, 428–432.

Caro G., Bourdon B., Birck J. L. and Moorbath S. (2006) High-precision 142Nd/144Nd measurements in terrestrial rocks: Constraints on the early differentiation of the Earth's mantle. *Geochim. Cosmochim. Acta* **70**, 164–191.

Caro G., Bourdon B., Halliday A. N. and Quitte G. (2008) Super-chondritic Sm / Nd ratios in Mars , the Earth and the Moon. **452**, 4–7.

Caro G., Bourdon B., Wood B. J. and Corgne A. (2005) Trace-element fractionation in Hadean mantle generated by melt segregation from a magma ocean. *Nature* **436**, 246–249.

Caro G., Morino P., Mojzsis S. J., Cates N. L. and Bleeker W. (2017) Sluggish Hadean geodynamics: Evidence from coupled 146,147Sm–142,143Nd systematics in Eoarchean supracrustal rocks of the Inukjuak domain (Québec). *Earth Planet. Sci. Lett.* **457**, 23–37.

Cates N. L., Ziegler K., Schmitt A. K., Mojzsis S. J. and Lyon D. (2013) Reduced , reused and recycled : Detrital zircons define a maximum age for the Eoarchean (ca . 3750 – 3780 Ma) Nuvvuagittuq Supracrustal Belt , Que. *Earth Planet. Sci. Lett.* **362**, 283–293. Available at: http://dx.doi.org/10.1016/j.epsl.2012.11.054.

Charlier B., Grove T. L., Namur O. and Holtz F. (2018) Crystallization of the lunar magma ocean and the primordial mantle-crust differentiation of the Moon. *Geochim. Cosmochim. Acta* **234**, 50–69. Available at: https://doi.org/10.1016/j.gca.2018.05.006.

Chauvel C., Lewin E., Carpentier M., Arndt N. T. and Marini J. C. (2008) Role of recycled oceanic basalt and sediment in generating the Hf-Nd mantle array. *Nat. Geosci.* **1**, 64–67.

Chowdhury W., Trail D., Guitreau M., Bell E. A., Buettner J. and Mojzsis S. J. (2020) Geochemical and textural investigations of the Eoarchean Ukaliq supracrustals, Northern Québec (Canada). *Lithos* **372–373**, 105673. Available at: https://doi.org/10.1016/j.lithos.2020.105673.

Collins W. J. and Van Kranendonk M. J. (1999) Model for the development of kyanite during partial convective overturn of Archean granite-greenstone terranes: The Pilbara Craton, Australia. *J. Metamorph. Geol.* **17**, 145–156.

Corgne A., Liebske C., Wood B. J., Rubie D. C. and Frost D. J. (2005) Silicate perovskite-melt partitioning of trace elements and geochemical signature of a deep perovskitic reservoir. *Geochim. Cosmochim. Acta* **69**, 485–496.

Corgne A. and Wood B. J. (2002) CaSiO3 and CaTiO3 perovskite-melt partitioning of trace elements: Implications for gross mantle differentiation. *Geophys. Res. Lett.* **29**, 39-1-39–4.

Crowley J. L. (2003) U-Pb geochronology of 3810-3630 Ma granitoid rocks south of the Isua greenstone belt, southern West Greenland. *Precambrian Res.* **126**, 235–257.

Cuk M. and Stewart S. T. (2012) Making the Moon from a Fast-Spinning by Resonant Despinning. *Science (80-.).* **338**, 1047–1052.

Davies G. F. (1992) On the emergence of plate tectonics. *Geology* **20**, 963–966.

Debaille V., O'Neill C., Brandon A. D., Haenecour P., Yin Q. Z., Mattielli N. and Treiman A. H. (2013) Stagnant-lid tectonics in early Earth revealed by 142Nd variations in late Archean rocks. *Earth Planet. Sci. Lett.* **373**, 83–92.

Duncan A. R., Erlank A. J., Willis J. P., Scher M. K. and Ahrens L. H. (1974) Trace element evidence for a two-stage origin of some titaniferous mare basalts. *Proc. 5th Lunar Sci. Conf.*, 1147–1157.

Dygert N., Draper D. S., Rapp J. F., Lapen T. J., Fagan A. L. and Neal C. R. (2020) Experimental determinations of trace element partitioning between plagioclase, pigeonite, olivine, and lunar basaltic melts and an fO2 dependent model for plagioclase-melt Eu partitioning. *Geochim. Cosmochim. Acta* **279**, 258–280.

Elardo S. M., Draper D. S. and Shearer C. K. (2011) Lunar Magma Ocean crystallization revisited: Bulk composition, early cumulate mineralogy, and the source regions of the highlands Mg-suite. *Geochim. Cosmochim. Acta* **75**, 3024–3045. Available at: http://dx.doi.org/10.1016/j.gca.2011.02.033.

Elkins-Tanton L. T., Burgess S. and Yin Q. (2011) The lunar magma ocean : Reconciling the solidi fi cation process with lunar petrology and geochronology. *Earth Planet. Sci. Lett.* **304**, 326–336. Available at: http://dx.doi.org/10.1016/j.epsl.2011.02.004.

Fischer-Gödde M. and Kleine T. (2017) Ruthenium isotopic evidence for an inner Solar System origin of the late veneer. *Nature* **541**, 525–527.

Foley C. N., Wadhwa M., Borg L. E., Janney P. E., Hines R. and Grove T. L. (2005) The early differentiation history of Mars from 182 W- 142 Nd isotope systematics in the SNC meteorites. *Geochemica Cosmochim. Acta* **69**, 4557–4571.

Frei R., Rosing M. T., Waight T. E. and Ulfbeck D. G. (2002) Hydrothermal-metasomatic and tectono-metamorphic processes in the Isua supracrustal belt (West Greenland): A multi-isotopic investigation of their effects on the Earth's oldest oceanic crustal sequence. *Geochim. Cosmochim. Acta* **66**, 467–486.

Friedman A., Milsted J., Metta D., Henderson D., Lerner J. and Harkness A. (1966) Alpha Decay Half Lives of 148Gd 150Gd, and 146Sm*. *Radiochim Acta* **5**, 192–194.

Friend C., Nutman A., Baadsgaard H., Kinny P. and McGregor V. (1996) Meta-igneous (non-gneissic) tonalites and quartz diorites from an extensive ca. 3800 Ma terrain south of the Isua supracrustal belt, southern west Greenland: constraints on early crust formation. *Earth Planet. Sci. Lett.* **142**, 353–365. Available at: http://www.sciencedirect.com/science/article/pii/0012821X96001185.

Friend C. R. L. and Nutman A. P. (2010) Eoarchean ophiolites? New evidence for the debate on the ISUA supracrustal belt, southern west greenland. *Am. J. Sci.* **310**, 826–861.

Friend P., Hezel D. C. and Mucerschi D. (2016) The conditions of chondrule formation, Part II: Open system. *Geochim. Cosmochim. Acta* **173**, 198–209.

Fukai R. and Yokoyama T. (2017) Neodymium isotope heterogeneity of ordinary and carbonaceous

chondrites and the origin of non-chondritic 142Nd compositions in the Earth. *Earth Planet. Sci. Lett.* **474**, 206–214. Available at: http://dx.doi.org/10.1016/j.epsl.2017.06.036.

Fukai R. and Yokoyama T. (2019) Nucleosynthetic Sr–Nd Isotope Correlations in Chondrites: Evidence for Nebular Thermal Processing and Dust Transportation in the Early Solar System. *Astrophys. J.* **879**, 79. Available at: http://dx.doi.org/10.3847/1538-4357/ab0e0d.

Gaffney A. M. and Borg L. E. (2014) A young solidification age for the lunar magma ocean. *Geochemica Cosmochim. Acta* **140**, 227–240.

Gannoun A., Boyet M., Rizo H. and El Goresy A. (2011) 146Sm-142Nd systematics measured in enstatite chondrites reveals a heterogeneous distribution of 142Nd in the solar nebula. *Proc. Natl. Acad. Sci. U. S. A.* **108**, 7693–7697.

Garbe-Schönberg D. (1993) SIMULTANEOUS DETERMINATION OF THIRTY-SEVEN TRACE ELEMENTS IN TWENTY-EIGHT INTERNATIONAL ROCK STANDARDS BY ICP-MS. *Geostand. Newsl.* **17**, 81–97.

Garçon M., Boyet M., Carlson R. W., Horan M. F., Auclair D. and Mock T. D. (2018) Factors influencing the precision and accuracy of Nd isotope measurements by thermal ionization mass spectrometry. *Chem. Geol.* **476**, 493–514. Available at: http://dx.doi.org/10.1016/j.chemgeo.2017.12.003.

Gardiner N. J., Hickman A. H., Kirkland C. L., Lu Y., Johnson T. and Zhao J. X. (2017) Processes of crust formation in the early Earth imaged through Hf isotopes from the East Pilbara Terrane. *Precambrian Res.* **297**, 56–76.

Greenwood R. C., Barrat J., Miller M. F., Anand M., Dauphas N., Franchi I. A., Sillard P. and Starkey N. A. (2018) Erratum: Oxygen isotopic evidence for accretion of Earth's water before a high-energy Moon-forming giant impact (Science Advances DOI: 10.1126/sciadv.aao5928). *Sci. Adv.* **4**.

Gruau G., Jahn B. M., Glikson A. Y., Davy R., Hickman A. H. and Chauvel C. (1987) Age of the Archean Talga-Talga Subgroup, Pilbara Block, Western Australia, and early evolution of the mantle: new SmNd isotopic evidence. *Earth Planet. Sci. Lett.* **85**, 105–116.

Gruau G., Rosing M., Bridgwater D. and Gill R. C. O. (1996) Resetting of Sm-Nd systematics during metamorphism of > 3.7-Ga rocks: Implications for isotopic models of early Earth differentiation. *Chem. Geol.* **133**, 225–240.

Halliday A. N. (2008) A young Moon-forming giant impact at 70–110 million years accompanied by late-stage mixing, core formation and degassing of the Earth. *Philos. Trans. R. Soc.* **A366**, 4163–4181.

Harper C. L. and Jacobsen S. B. (1992) Evidence from coupled 147Sm-143Nd and 146Sm-142Nd systematics for very early (4.5-Gyr) differentiation of the Earth's mantle. **360**, 728–732.

Hasenstab E., Tusch J., Schnabel C., Marien C. S., Van Kranendonk M. J., Smithies H., Howard H., Maier W. D. and Münker C. (2021) Evolution of the early to late Archean mantle from Hf-Nd-Ce isotope systematics in basalts and komatiites from the Pilbara Craton. *Earth Planet. Sci. Lett.* **553**.

Herwartz D., Pack A., Friedrichs B. and Bischoff A. (2014) Identification of the giant impactor Theia in lunar rocks. *Science (80-.).* **344**, 1146–1150.

Herzberg C., Condie K. and Korenaga J. (2010) Thermal history of the Earth and its petrological expression. *Earth Planet. Sci. Lett.* **292**, 79–88. Available at: http://dx.doi.org/10.1016/j.epsl.2010.01.022.

Hezel D. C. and Palme H. (2010) The chemical relationship between chondrules and matrix and the chondrule matrix complementarity. *Earth Planet. Sci. Lett.* **294**, 85–93. Available at: http://dx.doi.org/10.1016/j.epsl.2010.03.008.

Hickman A. H. (2012) Review of the Pilbara Craton and Fortescue Basin, Western Australia: Crustal evolution providing environments for early life. *Isl. Arc* **21**, 1–31.

Hidaka H. and Yoneda S. (2014) Isotopic excesses of proton-rich nuclei related to space weathering observed in a gas-rich meteorite Kapoeta. *Astrophys. J.* **786**.

Hirschmann M. M. (2000) Mantle solidus: Experimental constraints and the effects of peridotite composition. *Geochemistry, Geophys. Geosystems* **1**, 41.

Hoffmann J. E., Münker C., Næraa T., Rosing M. T., Herwartz D., Garbe-Schönberg D., Svahnberg H., M??nker C., N??raa T., Rosing M. T., Herwartz D., Garbe-Sch??nberg D. and Svahnberg H. (2011a) Mechanisms of Archean crust formation inferred from high-precision HFSE systematics in TTGs. *Geochim. Cosmochim. Acta* **75**, 4157–4178.

Hoffmann J. E., Münker C., Polat A., König S., Mezger K. and Rosing M. T. (2010) Highly depleted Hadean mantle reservoirs in the sources of early Archean arc-like rocks, Isua supracrustal belt, southern West Greenland. *Geochim. Cosmochim. Acta* **74**, 7236–7260.

Hoffmann J. E., Münker C., Polat A., Rosing M. T. and Schulz T. (2011b) The origin of decoupled Hf-Nd isotope compositions in Eoarchean rocks from southern West Greenland. *Geochim. Cosmochim. Acta* **75**, 6610–6628.

Hoffmann J. E., Nagel T. J., Münker C., Næraa T. and Rosing M. T. (2014) Constraining the process of Eoarchean TTG formation in the Itsaq Gneiss Complex, southern West Greenland. *Earth Planet. Sci. Lett.* **388**, 374–386. Available at: http://dx.doi.org/10.1016/j.epsl.2013.11.050.

Hoffmann J. E., Svahnberg H., Piazolo S., Scherstén A. and Münker C. (2012) The geodynamic evolution of Mesoarchean anorthosite complexes inferred from the Naajat Kuuat Complex, southern West Greenland. *Precambrian Res.* **196**–**197**, 149–170. Available at: http://dx.doi.org/10.1016/j.precamres.2011.12.002.

Hoffmann J. E. and Wilson A. H. (2017) The origin of highly radiogenic Hf isotope compositions in 3.33 Ga Commondale komatiite lavas (South Africa). *Chem. Geol.* **455**, 6–21. Available at: http://dx.doi.org/10.1016/j.chemgeo.2016.10.010.

Hofmann A. W. (1997) Mantle geochemistry: The message from oceanic volcanism. *Nature* **385**, 218–229.

Hofmann A. W., Class C. and Goldstein S. L. (2022) Size and composition of the MORB + OIB mantle reservoir. *Geochemistry Geophys. Geosystems*.

Horan M. F., Carlson R. W., Walker R. J., Jackson M., Garçon M. and Norman M. (2018) Tracking Hadean processes in modern basalts with 142-Neodymium. *Earth Planet. Sci. Lett.* **484**, 184–191. Available at: https://doi.org/10.1016/j.epsl.2017.12.017.

Horn P., Kirsten T. and Jessberger E. K. (1975) Are there 12 mare basalts younger than 3.1 b.y. unsuccessful search for a 12 mare basalts with crystallization ages below 3.1 b.y. *Meteorit. Planet. Sci.* **10**, 417–418. Available at: http://adsabs.harvard.edu/abs/1975Metic..10..417H.

Hyung E. and Jacobsen S. B. (2020) The 142Nd/144Nd variations in mantle-derived rocks provide constraints on the stirring rate of the mantle from the Hadean to the present. *Proc. Natl. Acad. Sci. U. S. A.* **117**, 14738–14744.

Hyung E. and Tissot F. L. H. (2021) Routine high-precision Nd isotope analyses: an optimized chromatographic purification scheme. *J. Anal. At. Spectrom.*

Irving A. J., Merrill R. B. and Singleton E. (1978) Experimental partitioning of rare earth elements and scandium among armalcolite, ilmenite olivine and mare basalt liquid. *Proc. Lunar Sci. Conf.* **9**, 601–

612. Available at: http://www.ghbook.ir/index.php?name=سراسری اندیشی هم دومین مقالات مجموعه و تلویزیون رسانه سکولاریسم&option=com_dbook&task=readonline&book_id=13629&page=108&chkhashk=03C706812F&Itemid=218&lang=fa&tmpl=component.

Israel C., Boyet M., Doucelance R., Bonnand P., Frossard P., Auclair D. and Bouvier A. (2019) Formation of the Ce-Nd mantle array: Crustal extraction vs. recycling by subduction. *Earth Planet. Sci. Lett.* **1**, 1–12. Available at: https://linkinghub.elsevier.com/retrieve/pii/S0012821X19306338.

Jacobsen B., Yin Q., Moynier F., Amelin Y., Krot A. N., Nagashima K., Hutcheon I. D. and Palme H. (2008) 26Al–26Mg and 207Pb–206Pb systematics of Allende CAIs: Canonical solar initial 26Al/27Al ratio reinstated. *Earth Planet. Sci. Lett.* **272**, 353–364.

Johnson T. E., Brown M., Gardiner N. J., Kirkland C. L. and Smithies R. H. (2017) Earth's first stable continents did not form by subduction. *Nature* **543**, 239–242.

van Kan Parker M., Mason P. R. D. and van Westrenen W. (2011) Trace element partitioning between ilmenite, armalcolite and anhydrous silicate melt: Implications for the formation of lunar high-Ti mare basalts. *Geochim. Cosmochim. Acta* **75**, 4179–4193. Available at: http://dx.doi.org/10.1016/j.gca.2011.04.031.

Kemp A. I., Hickman A. H. and Kirkland C. L. (2015) Report 151: Early Evolution of the Pilbara Craton from Hf isotopes in detrital and inherited zircons. *Precambrian Res.* **261**, 26.

Kinoshita N., Paul M., Kashiv Y., Collon P., Deibel C. M., DiGiovine B., Greene J. P., Henderson D. J., Jiang C. L., Marley S. T., Nakanishi T., Pardo R. C., Rehm K. E., Robertson D., Scott R., Schmitt C., Tang X. D., Vondrasek R. and Yokoyama A. (2012) A Shorter 146Sm Half-Life Measured and Implications for 146Sm-142Nd Chronology in the Solar System. *Science (80-.).* **335**, 1614–1618.

Kirsten T., Deubner J., Horn P., Kaneoka I., Kiko J., Schaeffer O. A. and Thio S. K. (1972) Rare gas record of Apollo 14 and 15 samples. *Proc. 3rd Lunar Sci. Conf.*, 1865–1889.

Kleine T., Mezger K., Münker C., Palme H. and Bischoff A. (2004) 182Hf-182W isotope systematics of chondrites, eucrites, and martian meteorites: Chronology of core formation and early mantle differentiation in Vesta and Mars. *Geochim. Cosmochim. Acta* **68**, 2935–2946.

Kleine T., Touboul M., Bourdon B., Nimmo F., Mezger K., Palme H., Jacobsen S. B., Yin Q. and Halliday A. N. (2009) Hf – W chronology of the accretion and early evolution of asteroids and terrestrial planets. *Geochim. Cosmochim. Acta* **73**, 5150–5188. Available at: http://dx.doi.org/10.1016/j.gca.2008.11.047.

Kleine T., Touboul M., Van Orman J. A., Bourdon B., Maden C., Mezger K. and Halliday A. N. (2008) Hf-W thermochronometry: Closure temperature and constraints on the accretion and cooling history of the H chondrite parent body. *Earth Planet. Sci. Lett.* **270**, 106–118.

Klemme S., Günther D., Hametner K., Prowatke S. and Zack T. (2006) The partitioning of trace elements between ilmenite, ulvospinel, armalcolite and silicate melts with implications for the early differentiation of the moon. *Chem. Geol.* **234**, 251–263.

Klemme S., Ivanic T. J., Connolly J. A. D. and Harte B. (2009) Thermodynamic modelling of Cr-bearing garnets with implications for diamond inclusions and peridotite xenoliths. *Lithos* **112**, 986–991. Available at: http://dx.doi.org/10.1016/j.lithos.2009.05.007.

Klemme S. and O'Neill H. S. C. (2000) The near-solidus transition from garnet lherzolite to spinel lherzolite. *Contrib. to Mineral. Petrol.* **138**, 237–248.

Kommescher S., Fonseca R. O. C., Kurzweil F., Thiemens M. M., Münker C. and Sprung P. (2020) Unravelling lunar mantle source processes via the Ti isotope composition of lunar basalts. , 13–18.

Korenaga J. (2008) UREY RATIO AND THE STRUCTURE AND EVOLUTION OF EARTH'S MANTLE. *Rev. Geophys.* **46**, 1–32.

Kortenkamp S. J., Kokubo E. and Weidenschilling S. J. (2000) Formation of planetary embryos. *Orig. Earth Moon, eds RM Canup K Righter (University Arizona Press. Tucson, AZ)*, 85–100.

Van Kranendonk M. J. V., Hickman A. H., Smithies R. H., Nelson D. R., Pike G., Smithes R. H. and Nelson D. R. (2002) Geology and tectonic evolution of the Archean North Pilbara Terrain, Pilbara Craton, Western Australia. *Econ. Geol.* **97**, 695–732. Available at: http://economicgeology.org/lookup/doi/10.2113/gsecongeo.97.4.695.

Van Kranendonk M. J. (2007) Chapter 8.6 Tectonics of Early Earth. *Dev. Precambrian Geol.* **15**, 1105–1116.

Van Kranendonk M. J. (2010) Two types of Archean continental crust: Plume and plate tectonics on early earth. *Am. J. Sci.* **310**, 1187–1209.

Van Kranendonk M. J., Collins W. J., Hickman A. and Pawley M. J. (2004) Critical tests of vertical vs. horizontal tectonic models for the Archaean East Pilbara Granite-Greenstone Terrane, Pilbara Craton, Western Australia. *Precambrian Res.* **131**, 173–211.

Van Kranendonk M. J., Hugh Smithies R., Hickman A. H. and Champion D. C. (2007) Review: Secular tectonic evolution of Archean continental crust: interplay between horizontal and vertical processes in the formation of the Pilbara Craton, Australia. *Terra Nov.* **19**, 1–38.

Van Kranendonk M. J., Hugh Smithies R., Hickman A. H., Wingate M. T. D. D. and Bodorkos S. (2010) Evidence for Mesoarchean (~3.2 Ga) rifting of the Pilbara Craton: The missing link in an early Precambrian Wilson cycle. *Precambrian Res.* **177**, 145–161.

Van Kranendonk M. J., Smithies R. H., Griffin W. L., Huston D. L., Hickman A. H., Champion D. C., Anhaeusser C. R. and Pirajno F. (2015) Making it thick: a volcanic plateau origin of Palaeoarchean continental lithosphere of the Pilbara and Kaapvaal cratons. *Geol. Soc. London, Spec. Publ.* **389**, 83–111.

Krapez B. and Eisenlohr B. (1998) Tectonic settings of Archaean (3325-2775 Ma) crustal-supracrustal belts in the West Pilbara Block. *Precambrian Res.* **88**, 173–205.

Krot A. N. (2019) Refractory inclusions in carbonaceous chondrites: Records of early solar system processes. *Meteorit. Planet. Sci.* **54**, 1647–1691.

Krot A. N., Petaev M. I., Russell S. S., Itoh S., Fagan T. J., Yurimoto H., Chizmadia L., Weisberg M. K., Komatsu M., Ulyanov A. A. and Keil K. (2004) Amoeboid olivine aggregates and related objects in carbonaceous chondrites: Records of nebular and asteroid processes. *Chemie der Erde* **64**, 185–239.

Kruijer T. S. and Kleine T. (2017) Tungsten isotopes and the origin of the Moon. **475**, 15–24.

Kruijer T. S., Kleine T., Borg L. E., Brennecka G. A., Irving A. J., Bischoff A. and Agee C. B. (2017) The early differentiation of Mars inferred from Hf–W chronometry. *Earth Planet. Sci. Lett.* **474**, 345–354.

Labrosse S., Hernlund J. W. and Coltice N. (2007) A crystallizing dense magma ocean at the base of the Earth's mantle. *Nature* **450**, 866–869. Available at: http://www.nature.com/doifinder/10.1038/nature06355.

Lee C. T. A., Luffi P. and Chin E. J. (2011) Building and destroying continental mantle. *Annu. Rev. Earth Planet. Sci.* **39**, 59–90.

Lee C. T. A., Luffi P., Plank T., Dalton H. and Leeman W. P. (2009) Constraints on the depths and temperatures of basaltic magma generation on Earth and other terrestrial planets using new

thermobarometers for mafic magmas. *Earth Planet. Sci. Lett.* **279**, 20–33.

Li J. and Agee C. B. (1996) Geochemistry of mantle-core differentiation at high pressure. *Nature* **381**, 686–689.

Liou P., Guo, Jinghui, Mitchell R. N., Spencer C. J., Li X., Zhai M., Evans N. J., Li Y., McDonald B. J. and Jin M. (2021) Zircons underestimate mantle depletion of early Earth. *Geochemica Cosmochim. Acta* **317**, 538–551.

van de Löcht J., Hoffmann J. E., Li C., Wang Z., Becker H., Rosing M. T., Kleinschrodt R. and Münker C. (2018) Earth's oldest mantle peridotites show entire record of late accretion. *Geology* **46**, 199–202.

van de Löcht J., Hoffmann J. E., Rosing M. T., Sprung P. and Münker C. (2020) Preservation of Eoarchean mantle processes in ∼3.8 Ga peridotite enclaves in the Itsaq Gneiss Complex, southern West Greenland. *Geochim. Cosmochim. Acta* **280**, 1–25. Available at: https://doi.org/10.1016/j.gca.2020.03.043.

Lugmair G. W. and Marti K. (1978) Lunar initial 143 Nd/ 144 Nd: Differential evolution of the lunar crust and mantle. *Earth Planet. Sci. Lett.* **39**, 349–357. Available at: http://www.sciencedirect.com/science/article/pii/0012821X78900213.

Lugmair G. W. and Shukolyukov A. (1998) Early solar system timescales according to 53Mn-53Cr systematics. *Geochim. Cosmochim. Acta* **62**, 2863–2886.

Maier W. D., Barnes Stephen J., Campbell I. H., Fiorentini M. L., Peltonen P., Barnes Sarah Jane and Smithies R. H. (2009) Progressive mixing of meteoritic veneer into the early Earths deep mantle. *Nature* **460**, 620–623.

Makishima A. and Nakamura E. (1991) Precise measurement of cerium isotope composition in rock samples. *Chem. Geol.* **94**, 1–11. Available at: http://dx.doi.org/10.1016/S0009-2541(10)80012-9.

Marien C. S., Hoffmann J. E., Garbe-Schönberg C. D. and Münker C. (2019) Petrogenesis of plagiogranites from the Troodos Ophiolite Complex, Cyprus. *Contrib. to Mineral. Petrol.* **174**, 1–24. Available at: https://doi.org/10.1007/s00410-019-1569-3.

Marks N. E., Borg L. E., Hutcheon I. D., Jacobsen B. and Clayton R. N. (2014) Samarium-neodymium chronology and rubidium-strontium systematics of an Allende calcium-aluminum-rich inclusion with implications for 146Sm half-life. *Earth Planet. Sci. Lett.* **405**, 15–24. Available at: http://dx.doi.org/10.1016/j.epsl.2014.08.017.

Mason B., Jarosewich E., Melson W. G. and Thompson G. (1972) Mineralogy, petrology, and chemical composition 15476, 15535, 15555, and 15556. *Proc. 3rd Lunar Sci. Conf.*, 785–796.

McDade P., Blundy J. and Wood B. J. (2003) Trace element partitioning between mantle wedge peridodite and hydrous MgO-rich melt. *Am. Mineral.* **88**, 1825–1831.

McKay G. A. and Weill D. F. (1977) KREEP petrogenesis reviseted. *Lunar Sci. Conf.* **2**, 2339–2355.

Mcleod C. L., Brandon A. D. and Armytage R. M. G. (2014) Constraints on the formation age and evolution of the Moon from Nd – 143 Nd systematics of Apollo 12 basalts. *Earth Planet. Sci. Lett.* **396**, 179–189. Available at: http://dx.doi.org/10.1016/j.epsl.2014.04.007.

Meissner F., Schmidt-Ott W. D. and Ziegeler L. (1987) Half-Life and alpha-Ray Energy of 146Sm. *Zeitschrift für Phys.* **174**, 171–174.

Meyer C., Brett R. and Hubbard N. J. (1971) Mineralogy, chemistry, and origin of the KREEP component in soil samples from the Ocean of Storms. *Proc. Second unar Sci. Conf.* **1**, 393–411.

Mezger K., Schönbächler M. and Bouvier A. (2020) Accretion of the Earth—Missing Components? *Space Sci. Rev.* **216**, 1–25. Available at: http://dx.doi.org/10.1007/s11214-020-00649-y.

Mohapatra R. K. and Murty S. V. S. (2003) Precursors of Mars: Constraints from nitrogen and oxygen isotopic compositions of martian meteorites. *Meteorit. Planet. Sci.* **38**, 225–241.

Mole D. R., Barnes S. J., Yao Z., White A. J. R., Maas R. and Kirkland C. L. (2018) The Archean Fortescue large igneous province: A result of komatiite contamination by a distinct Eo-Paleoarchean crust. *Precambrian Res.* **310**, 365–390.

Moorbath S., Allaart J. H., Bridgwater D. and McGregor V. R. (1977) Rb-Sr ages of early Archean supracrustal rocks and Amitsoq gneisses at Isua. *Nature* **270**, 43–45.

Moorbath S., Whitehouse M. J. and Kamber B. S. (1997) Extreme Nd-isotope heterogeneity in the early Archaean - Fact or fiction? Case histories from northern Canada and West Greenland. *Chem. Geol.* **135**, 213–231.

Morino P., Caro G. and Reisberg L. (2018) Differentiation mechanisms of the early Hadean mantle: Insights from combined 176Hf-142,143Nd signatures of Archean rocks from the Saglek Block. *Geochim. Cosmochim. Acta* **240**, 43–63.

Morino P., Caro G., Reisberg L. and Schumacher A. (2017) Chemical stratification in the post-magma ocean Earth inferred from coupled 146,147Sm–142,143Nd systematics in ultramafic rocks of the Saglek block (3.25–3.9 Ga; northern Labrador, Canada). *Earth Planet. Sci. Lett.* **463**, 136–150. Available at: http://dx.doi.org/10.1016/j.epsl.2017.01.044.

Morrison G. H., Gerald J. T., Potter N. M., Gangadharam E. V., Rothenberg A. M. and Burdo R. A. (1971) Elemental abundances of lunar soil and rocks from Apollo 12. *Proc. 2nd Lnar Sci. Conf.*, 1169–1185.

Mougel B., Moynier F. and Göpel C. (2018) Chromium isotopic homogeneity between the Moon, the Earth, and enstatite chondrites. *Earth Planet. Sci. Lett.* **481**, 1–8.

Moyen J. F. and Martin H. (2012) Forty years of TTG research. *Lithos* **148**, 312–336.

Mukhopadhyay S. (2012) Early differentiation and volatile accretion recorded in deep-mantle neon and xenon. *Nature* **486**, 101–104. Available at: http://dx.doi.org/10.1038/nature11141.

Münker C. (2010) A high field strength element perspective on early lunar differentiatio. *GCA* **74**, 7340–7361.

Münker C., Pfänder J. A., Weyer S., Büchl A., Kleine T. and Mezger K. (2003) Evolution of planetary cores and the Earth-Moon system from Nb/Ta systematics. *Science (80-.).* **301**, 84–87.

Münker C., Weyer S., Scherer E. and Mezger K. (2001) Seperation of high field strength elements (Nb, Ta, Zr, Hf) and Lu from rock samples for MC-IPMS measurements. *Geochemistry Geophys. Geosystems* **2**, 1–19.

Murphy D., Rizo H., O'Neil J., Hepple R., Wiemer D., Kemp A. and Vervoort J. (2021) Combined Sm-Nd, Lu-Hf, and 142Nd study of Paleoarchean basalts from the East Pilbara Terrane, Western Australia. *Chem. Geol.* **578**, 120301. Available at: https://doi.org/10.1016/j.chemgeo.2021.120301.

Murphy D. T., Wiemer D., Bennett V. C., Spring T., Trofimovs J. and Cathey H. E. (2021) Paleoarchean variole-bearing metabasalts from the East Pilbara Terrane formed by hydrous fluid phase exsolution and implications for Archean greenstone belt magmatic processes. *Precambrian Res.* **357**, 106114. Available at: https://doi.org/10.1016/j.precamres.2021.106114.

Murthy V. R., Evensen N. M., Jahn B. M. and Coscio M. R. (1972) Apollo 14 and 15 samples: Rb-Sr ages, trace elements, and lunar evolution. *Proc. 3rd Lunar Sci. Conf.1*, 1503–1514.

Næraa T., Scherstén A., Rosing M. T., Kemp A. I. S., Hoffmann J. E., Kokfelt T. F. and Whitehouse M. J. (2012) Hafnium isotope evidence for a transition in the dynamics of continental growth 3.2â €‰Gyr ago. *Nature* **485**, 627–630.

Nakamura N., Masuda A., Tanaka T. and Kurasawa H. (1973) Chemical compositions and rare-earth features of four Apollo 16 samples. *Proc. 4th Lunar Sci. Conf. Lunar Sci. Conf.*, 1407–1414.

Neal C. R. (2017) The composition of KREEP : A detailed study of KREEP basalt 15386. , 17–19.

Nebel O., Arculus R. J., Ivanic T. J. and Nebel-Jacobsen Y. J. (2013) Lu-Hf isotopic memory of plume-lithosphere interaction in the source of layered mafic intrusions, Windimurra Igneous Complex, Yilgarn Craton, Australia. *Earth Planet. Sci. Lett.* **380**, 151–161. Available at: http://dx.doi.org/10.1016/j.epsl.2013.08.019.

Nebel O., Campbell I. H., Sossi P. A. and Van Kranendonk M. J. (2014) Hafnium and iron isotopes in early Archean komatiites record a plume-driven convection cycle in the Hadean Earth. *Earth Planet. Sci. Lett.* **397**, 111–120. Available at: http://dx.doi.org/10.1016/j.epsl.2014.04.028.

Nebel O., Scherer E. E. and Mezger K. (2011) Evaluation of the 87Rb decay constant by age comparison against the U-Pb system. *Earth Planet. Sci. Lett.* **301**, 1–8.

Nisbet E. G., Cheadle M. J., Arndt N. T. and Bickle M. J. (1993) Constraining the potential temperature of the Archaean mantle: A review of the evidence from komatiites. *Lithos* **30**, 291–307.

Norman M. D., Bennett V. C. and Ryder G. (2002) Targeting the impactors: Siderophile element signatures of lunar impact melts from Serenitatis. *Earth Planet. Sci. Lett.* **202**, 217–228.

Nutman A. P., Bennett V. C., Friend C. R. L., Jenner F., Wan Y. and Liu D. (2009) Eoarchaean crustal growth in West Greenland (Itsaq Gneiss Complex) and in northeastern China (Anshan area): Review and synthesis. *Geol. Soc. Spec. Publ.* **318**, 127–154.

Nutman A. P., Bennett V. C., Friend C. R. L. and Norman M. D. (1999) Meta-igneous (non-gneissic) tonalites and quartz-diorites from an extensive ca. 3800 Ma terrain south of the Isua supracrustal belt, southern West Greenland: Constraints on early crust formation. *Contrib. to Mineral. Petrol.* **137**, 364–388.

Nutman A. P. and Friend C. R. L. (2009) New 1:20,000 scale geological maps, synthesis and history of investigation of the Isua supracrustal belt and adjacent orthogneisses, southern West Greenland: A glimpse of Eoarchaean crust formation and orogeny. *Precambrian Res.* **172**, 189–211.

Nutman A. P., Friend C. R. L. and Bennett V. C. (2002) Evidence for 3650-3600 Ma assembly of the northern end of the Itsaq Gneiss Complex, Greenland: Implication for early Archaean tectonics. *Tectonics* **21**, 5-1-5–28.

Nutman A. P., Friend C. R. L., Bennett V. C. and McGregor V. R. (2004) Dating of the Ameralik dyke swarms of the Nuuk district, southern West Greenland; Mafic intrusion events starting from c. 3510 Ma. *J. Geol. Soc. London.* **161**, 421–430.

Nutman A. P., Friend C. R. L., Horie K. and Hidaka H. (2007) Chapter 3.3 The Itsaq Gneiss Complex of Southern West Greenland and the Construction of Eoarchaean Crust at Convergent Plate Boundaries. *Dev. Precambrian Geol.* **15**, 187–218.

Nyquist L. E. (1976) Sr isotopic constraints on the petrogenesis of Apollo 17 mre basalts. *Proc. Lunar Conf. 7th*, 1507–1528.

Nyquist L. E., Wiesmann H., Bansal B., Shih C. Y., Keith J. E. and Harper C. L. (1995) 146Sm-142Nd formation interval for the lunar mantle. *Geochim. Cosmochim. Acta* **59**, 2817–2837.

O'Neil J., Carlson R. W., Francis D. and Stevenson R. K. (2008) Neodymium-142 Evidence for Hadean

Mafic Crust. *Science (80-.).* **321**, 1828–1832.

O'Neill C., Lenardic A., Moresi L., Torsvik T. H. and Lee C. T. A. (2007) Episodic Precambrian subduction. *Earth Planet. Sci. Lett.* **262**, 552–562.

O'Neill H. S. C. and Palme H. (2008) Collisional erosion and the non-chondritic composition of the terrestrial planets. *Philos. Trans. R. Soc. A Math. Phys. Eng. Sci.* **366**, 4205–4238.

Pahlevan K. and Stevenson D. J. (2007) Equilibration in the aftermath of the lunar-forming giant impact. *Earth Planet. Sci. Lett.* **262**, 438–449.

Palme H., Hezel D. C. and Ebel D. S. (2015) The origin of chondrules: Constraints from matrix composition and matrix-chondrule complementarity. *Earth Planet. Sci. Lett.* **411**, 11–19. Available at: http://dx.doi.org/10.1016/j.epsl.2014.11.033.

Palme H. and O'Neill H. (2013) *Cosmochemical Estimates of Mantle Composition*. 2nd ed., Elsevier Ltd. Available at: http://dx.doi.org/10.1016/B978-0-08-095975-7.00201-1.

Papanastassiou D. A. and Wasserburg G. J. (1971) LUNAR CHRONOLOGY AND EVOLUTION FROM Rb-Sr STUDIES OF APOLLO 11 AND 12 SAMPLES. *Earth Planet. Sci. Lett.* **11**, 37–62.

Papanastassiou D. A. and Wasserburg G. J. (1973) Rb-Sr ages and initial strontium in basalts from Apollo 15. *Earth Planet. Sci. Lett.* **17**, 324–337.

Papanastassiou D. A. and Wasserburg G. J. (1972) Rb-Sr systematics of Luna 20 and Apollo 16 samples. *Earth Planet. Sci. Lett.* **17**, 52–63.

Papanastassiou D. A., Wasserburg G. J. and Burnett D. S. (1970) Rb-Sr ages of lunar rocks from the sea of tranquility. *Earth Planet. Sci. Lett.* **8**, 1–19.

Pearce J. A. (2008) Geochemical fingerprinting of oceanic basalts with applications to ophiolite classification and the search for Archean oceanic crust. *Lithos* **100**, 14–48.

Peters B. J., Carlson R. W., Day J. M. D. and Horan M. F. (2018) Hadean silicate differentiation preserved by anomalous 142Nd/144Nd ratios in the Réunion hotspot source. *Nature* **555**, 89–93.

Petersson A., Kemp A. I. S., Gray C. M. and Whitehouse M. J. (2020) Formation of early Archean Granite-Greenstone Terranes from a globally chondritic mantle: Insights from igneous rocks of the Pilbara Craton, Western Australia. *Chem. Geol.* **551**.

Petersson A., Kemp A. I. S., Hickman A. H., Whitehouse M. J., Martin L. and Gray C. M. (2019) A new 3.59 Ga magmatic suite and a chondritic source to the east Pilbara Craton. *Chem. Geol.* **511**, 51–70. Available at: https://doi.org/10.1016/j.chemgeo.2019.01.021.

Phinney W. C. and Morrision D. A. (1990) Partition coefficients for calcic plagioclase : Implications for Archean anorthosites. *Geochemica Cosmochim. Acta* **54**, 1639–1654.

Pin C. and Zalduegui J. (1997) Sequential separation of light rare-earth elements, thorium and uranium by miniatureized extraction chromatography: applicaiton to isotopic analyses of silicate rocks. *Anal. Chim. Acta* **229**, 79–89.

Polat A., Frei R., Fryer B. and Appel P. W. U. (2009) The origin of geochemical trends and Eoarchean (ca. 3700 Ma) zircons in Mesoarchean (ca. 3075 Ma) ocelli-hosting pillow basalts, Ivisaartoq greenstone belt, SW Greenland: Evidence for crustal contamination versus crustal recycling. *Chem. Geol.* **268**, 248–271. Available at: http://dx.doi.org/10.1016/j.chemgeo.2009.09.004.

Polat A., Frei R., Scherstén A. and Appel P. W. U. (2010) New age (ca 2970Ma), mantle source composition and geodynamic constraints on the Archean Fiskenæsset anorthosite complex, SW Greenland. *Chem. Geol.* **277**, 1–20.

Polat A. and Hofmann A. W. (2003) Alteration and geochemical patterns in the 3.7-3.8 Ga Isua greenstone belt, West Greenland. *Precambrian Res.* **126**, 197–218.

Polat A., Hofmann A. W. and Rosing M. T. (2002) Boninite-like volcanic rocks in the 3.7 – 3.8 Ga Isua greenstone belt , West Greenland : geochemical evidence for intra-oceanic subduction zone processes in the early Earth. *Chem. Geol.* **184**, 231–254.

Puchtel I. S., Blichert-Toft J., Touboul M., Horan M. F. and Walker R. J. (2016) The coupled 182W-142Nd record of early terrestrial mantle differentiation Igor. *Geochemistry Geophys. Geosystems* **17**, 1312–1338.

Puchtel I. S., Nicklas R. W., Slagle J., Horan M., Walker R. J., Nisbet E. G. and Locmelis M. (2021) Early global mantle chemical and isotope heterogeneity revealed by the komatiite-basalt record: The Western Australia connection. *Geochim. Cosmochim. Acta*.

Qin L., Carlson R. W. and Alexander C. M. O. D. (2011) Correlated nucleosynthetic isotopic variability in Cr, Sr, Ba, Sm, Nd and Hf in Murchison and QUE 97008. *Geochim. Cosmochim. Acta* **75**, 7806–7828. Available at: http://dx.doi.org/10.1016/j.gca.2011.10.009.

Render J., Fischer-Gödde M., Burkhardt C. and Kleine T. (2017) The cosmic molybdenum-neodymium isotope correlation and the building material of the Earth. *Geochemical Perspect. Lett.* **3**, 170–178.

Rhodes J. M., Blanchard D. P., Dungan M. A., Brannon J. C. and Rodgers K. V. (1977) Chemistry of Apollo 12 mare basalts: Magma types and fractionation processes. *Proc. 8th Lunar Sci. Conf.*, 1305–1338.

Rhodes J. M. and Hubbard N. J. (1973) Chemistry, Classification, and petrogenesis of Apollo 15 mare basalts. *Proc. 4th Lunar Sci. Conf.*, 1127–1148.

Rizo H., Boyet M., Blichert-Toft J., O'Neil J., Rosing M. T. and Paquette J. L. (2012) The elusive Hadean enriched reservoir revealed by 142Nd deficits in Isua Archaean rocks. *Nature* **491**, 96–100.

Rizo H., Boyet M., Blichert-Toft J. and Rosing M. (2011) Combined Nd and Hf isotope evidence for deep-seated source of Isua lavas. *Earth Planet. Sci. Lett.* **312**, 267–279. Available at: http://dx.doi.org/10.1016/j.epsl.2011.10.014.

Rizo H., Walker R. J., Carlson R. W., Touboul M., Horan M. F., Puchtel I. S., Boyet M. and Rosing M. T. (2016) Early Earth differentiation investigated through 142Nd, 182W, and highly siderophile element abundances in samples from Isua, Greenland. *Geochim. Cosmochim. Acta* **175**, 319–336. Available at: http://dx.doi.org/10.1016/j.gca.2015.12.007.

Rodriguez T. R. (2014) Theoretical nuclear structure and astrophysics at FAIR. *J. Phys.* **Conference**, 1–5.

Rose H. J., Baedecker P. A., Berman S., Christian R. P., Dwornik E. J., R.B. F. and Schnepfe M. M. (1975) Chemical composition of rocks and soils returned by the Apollo 15, 16, and 17 missions. *Proc. 6th Lunar Sci. Conf.*, 1363–1373.

Rubie D. C., Frost D. J., Mann U., Asahara Y., Nimmo F., Tsuno K., Kegler P., Holzheid A. and Palme H. (2011) Heterogeneous accretion, composition and core-mantle differentiation of the Earth. *Earth Planet. Sci. Lett.* **301**, 31–42. Available at: http://dx.doi.org/10.1016/j.epsl.2010.11.030.

Rubin A. E. (2010) Physical properties of chondrules in different chondrite groups: Implications for multiple melting events in dusty environments. *Geochim. Cosmochim. Acta* **74**, 4807–4828.

Rufu R., Aharonson O. and Perets H. B. (2017) A multiple-impact origin for the Moon. **10**.

Ryder G. (1991) LUNAR FERROAN ANORTHOSITES AND MARE BASALT SOURCES: THE MIXED CONNECTION. *Geophys. Res. Lett.* **18**, 2065–2068.

Ryder G. and Schuraytz B. C. (2001) Chemical variations of the large Apollo 15 olivine-normative mare

basalt rock samples. *Geophys. Res. Lett.* **106**, 1435–1451.

Saji N. S., Larsen K., Wielandt D., Schiller M., Costa M. M., Whitehouse M. J., Rosing M. T. and Bizzarro M. (2018) Hadean geodynamics inferred from time-varying in the early Earth rock record 142 Nd / 144 Nd. , 43–48.

Saji N. S., Wielandt D., Holst J. C. and Bizzarro M. (2020) Solar system Nd isotope heterogeneity: Insights into nucleosynthetic components and protoplanetary disk evolution. *Geochim. Cosmochim. Acta* **281**, 135–148. Available at: https://doi.org/10.1016/j.gca.2020.05.006.

Saji N. S., Wielandt D., Paton C. and Bizzarro M. (2016) Ultra-high-precision Nd-isotope measurements of geological materials by MC-ICPMS. *J. Anal. At. Spectrom.* **31**, 1490–1504.

Salerno R., Vervoort J., Fisher C., Kemp A. and Roberts N. (2021) The coupled Hf-Nd isotope record of the early Earth in the Pilbara Craton. *Earth Planet. Sci. Lett.* **572**.

Salters V. J. M., Mallick S., Hart S. R., Langmuir C. E. and Stracke A. (2011) Domains of depleted mantle: New evidence from hafnium and neodymium isotopes. *Geochemistry, Geophys. Geosystems* **12**, 1–18.

Scherer E. E., Cameron K. L. and Blichert-Toft J. (2000) Lu-Hf garnet geochronology: Closure temperature relative to the Sm-Nd system and the effects of trace mineral inclusions. *Geochim. Cosmochim. Acta* **64**, 3413–3432.

Schnabel C., Muenker C. and Strub E. (2017) La-Ce isotope measurements by Multicollector-ICPMS. *J. Anal. At. Spectrom.* **32**, 2360–2370. Available at: http://pubs.rsc.org/en/Content/ArticleLanding/2017/JA/C7JA00256D.

Schneider K. P., Hoffmann J. E., Boyet M., Münker C. and Kröner A. (2018) Coexistence of enriched and modern-like 142Nd signatures in Archean igneous rocks of the eastern Kaapvaal Craton, southern Africa. *Earth Planet. Sci. Lett.* **487**, 54–66. Available at: https://doi.org/10.1016/j.epsl.2018.01.022.

Schneider K. P., Hoffmann J. E., Münker C., Patyniak M., Sprung P., Roerdink D., Garbe-Schönberg D. and Kröner A. (2019) Petrogenetic evolution of metabasalts and metakomatiites of the lower Onverwacht Group, Barberton Greenstone Belt (South Africa). *Chem. Geol.* **511**, 152–177. Available at: https://doi.org/10.1016/j.chemgeo.2019.02.020.

Scott E. R. D. and Krot A. N. (2005) Thermal Processing of Silicate Dust in the Solar Nebula: Clues from Primitive Chondrite Matrices. *Astrophys. J.* **623**, 571–578.

Shih C. Y., Nyquist L. E., Bansal B. M. and Wiesmann H. (1992) Rb-Sr and SmNd chronology of an Apollo 17 KREEP basalt. *Earth Planet. Sci. Lett.* **108**, 203–215.

Smithies R. H., Champion D. C. and Van Kranendonk M. J. (2007a) Chapter 4.2 The Oldest Well-Preserved Felsic Volcanic Rocks on Earth: Geochemical Clues to the Early Evolution of the Pilbara Supergroup and Implications for the Growth of a Paleoarchean Protocontinent. *Dev. Precambrian Geol.* **15**, 339–367.

Smithies R. H., Champion D. C. and Van Kranendonk M. J. (2009) Formation of Paleoarchean continental crust through infracrustal melting of enriched basalt. *Earth Planet. Sci. Lett.* **281**, 298–306. Available at: http://dx.doi.org/10.1016/j.epsl.2009.03.003.

Smithies R. H., Champion D. C., Van Kranendonk M. J. and Hickman A. H. (2007b) GEOCHEMISTRY OF VOLCANIC ROCKS OF THE NORTHERN PILBARA CRATON WESTERN AUSTRALIA. *GSWA Rep. 104*, 48.

Smithies R. H., Champion D. C., Van Kranendonk M. J., Howard H. M. and Hickman A. H. (2005a)

Modern-style subduction processes in the Mesoarchaean: Geochemical evidence from the 3.12 Ga Whundo intra-oceanic arc. *Earth Planet. Sci. Lett.* **231**, 221–237.

Smithies R. H., Champion D. C. and Sun S. S. (2004) Evidence for early LREE-enriched mantle source regions: Diverse magmas from the c. 3·0 Ga Mallina Basin, Pilbara Craton, NW Australia. *J. Petrol.* **45**, 1515–1537.

Smithies R. H., Ivanic T. J., Lowrey J. R., Morris P. A., Barnes S. J., Wyche S. and Lu Y.-J. (2018) Two distinct origins for Archean greenstone belts. *Earth Planet. Sci. Lett.* **487**, 106–116. Available at: http://linkinghub.elsevier.com/retrieve/pii/S0012821X18300529.

Smithies R. H., Van Kranendonk M. J. and Champion D. C. (2005b) It started with a plume - Early Archaean basaltic proto-continental crust. *Earth Planet. Sci. Lett.* **238**, 284–297.

Smithies R. H., Van Kranendonk M. J. and Champion D. C. (2007c) The Mesoarchean emergence of modern-style subduction. *Gondwana Res.* **11**, 50–68.

Snape J. F., Nemchin A. A., Bellucci J. J., Whitehouse M. J., Tartèse R., Barnes J. J., Anand M., Crawford I. A. and Joy K. H. (2016) Lunar basalt chronology, mantle differentiation and implications for determining the age of the Moon. *Earth Planet. Sci. Lett.* **451**, 149–158. Available at: http://dx.doi.org/10.1016/j.epsl.2016.07.026.

Snyder G. A., Neal C. R., Taylor L. A. L. A. and Halliday A. N. (1997) Anataxis of lunar cumulate mantle in time and space: Clues from trace-element, strontium and neodymium isotopic chemistry of parental Apollo 12 basalts. *Geochemica Cosmochim. Acta* **61**, 2731–2747.

Snyder G. A., Taylor L. A. and Neal C. R. (1992) A chemical model for generating the sources of mare basalts: Combined equilibrium and fractional crystallization of the lunar magmasphere. *Geochim. Cosmochim. Acta* **56**, 3809–3823.

Söderlund U., Patchett P. J., Vervoort J. D. and Isachsen C. E. (2004) The 176Lu decay constant determined by Lu-Hf and U-Pb isotope systematics of Precambrian mafic intrusions. *Earth Planet. Sci. Lett.* **219**, 311–324.

Sossi P. A., Eggins S. M., Nesbitt R. W., Nebel O., Hergt J. M., Campbell I. H., O'Neill H. S. C., Kranendonk M. Van and Rhodri Davies D. (2016) Petrogenesis and geochemistry of Archean Komatiites. *J. Petrol.* **57**, 147–184.

Sprung P., Kleine T. and Scherer E. E. (2014) EVIDENCE FOR A COMMON INITIAL 176Hf/177Hf OF THE EARTH, MOON, AND CHONDRITES. *45th Lunar Planet. Sci. Conf.*, 2.

Sprung P., Kleine T. and Scherer E. E. (2013) Isotopic evidence for chondritic Lu/Hf and Sm/Nd of the Moon. *Earth Planet. Sci. Lett.* **380**, 77–87. Available at: http://dx.doi.org/10.1016/j.epsl.2013.08.018.

Sprung P., Scherer E. E., Upadhyay D., Leya I. and Mezger K. (2010) Non-nucleosynthetic heterogeneity in non-radiogenic stable Hf isotopes: Implications for early solar system chronology. *Earth Planet. Sci. Lett.* **295**, 1–11. Available at: http://dx.doi.org/10.1016/j.epsl.2010.02.050.

Stewart S. T., Lock S. J., Petaev M. I., Leinhardt Z. and Mace M. T. (2018) The Origin of the Moon Within a Terrestrial Synestia.

Stracke A., Hofmann A. W. and Hart S. R. (2005) FOZO, HIMU, and the rest of the mantle zoo. *Geochemistry, Geophys. Geosystems* **6**.

Strasheim A., Coetzee J. H. J., Jackson P. F. S., Strelow F. W. E., Wybenga F. T., Gricius A. J. and Kokot M. L. (1972) Analysis of lunar samples 15065, 15301, and 15556, with isotopic data for 7Li/6 Li. *Apollo 15 lunar samples*, 257–259.

Szilas K. (2018) A geochemical overview of mid-Archaean metavolcanic rocks from southwest Greenland. *Geosci.* **8**.

Szilas K., Hoffmann J. E., Hansmeier C., Hollis J. A., Münker C., Viehmann S. and Kasper H. U. (2015a) Sm-Nd and Lu-Hf isotope and trace-element systematics of Mesoarchaean amphibolites, inner Ameralik fjord, southern West Greenland. *Mineral. Mag.* **79**, 857–876.

Szilas K., Hoffmann J. E., Schulz T., Hansmeier C., Polat A., Viehmann S., Kasper H. U. and Münker C. (2016) Combined bulk-rock Hf- and Nd-isotope compositions of Mesoarchaean metavolcanic rocks from the Ivisaartoq Supracrustal Belt, SW Greenland: Deviations from the mantle array caused by crustal recycling. *Chemie der Erde* **76**, 543–554. Available at: http://dx.doi.org/10.1016/j.chemer.2016.09.004.

Szilas K., Kelemen P. B. and Rosing M. T. (2015b) The petrogenesis of ultramafic rocks in the >3.7Ga Isua supracrustal belt, southern West Greenland: Geochemical evidence for two distinct magmatic cumulate trends. *Gondwana Res.* **28**, 565–580. Available at: http://dx.doi.org/10.1016/j.gr.2014.07.010.

Tanimizu M. (2000) Geophysical determination of the 138La β- decay constant. **62**, 140–143.

Taylor L. A., Shervais J. W., Hunter R. H., Shih C., Bansal B. M., Nyquist L. E. and Laul L. C. (1983) Pre-4.2 AE mare-basalt volcanism in the lunar highlands. *Earth Planet. Sci. Lett.* **66**, 33–47.

Taylor S. R., Kaye M., Muir P., Nance W., Rudowski R. and Ware N. (1972) Composition of the lunar uplands: Chemistry of Apollo 14 samples from Fra Mauro. *Proc. 3rd Lunar Sci. Conf.*, 1231–1249.

Tessalina S. G., Bourdon B., Van Kranendonk M., Birck J. L. and Philippot P. (2010) Influence of Hadean crust evident in basalts and cherts from the Pilbara Craton. *Nat. Geosci.* **3**, 214–217. Available at: http://dx.doi.org/10.1038/ngeo772.

Thiemens M. M. Isotope Planetology. *PhD thesis*, University of Cologne.

Thiemens M. M., Sprung P., Fonseca R. O. C., Leitzke F. P. and Münker C. (2019) Early Moon formation inferred from hafnium–tungsten systematics. *Nat. Geosci.* **12**, 696–700. Available at: http://dx.doi.org/10.1038/s41561-019-0398-3.

Thirlwall M. F. (1991) Long-term reproducibility of multicollector Sr and Nd isotope ratio analysis. *Chem. Geol.* **94**, 85–104. Available at: http://linkinghub.elsevier.com/retrieve/pii/S000925411080021X.

Thorne A. M. and Trendall A. F. (2001) Geology of the Fortescue Group, Pilbara Craton, Western Australia. *Geol. Surv. West. Aust. Bull.* **144**, 1–249.

Tolstikhin I. and Hofmann A. W. (2005) Early crust on top of the Earth's core. *Phys. Earth Planet. Inter.* **148**, 109–130.

Tolstikhin I. N., Kramers J. D. and Hofmann A. W. (2006) A chemical Earth model with whole mantle convection: The importance of a core-mantle boundary layer (D") and its early formation. *Chem. Geol.* **226**, 79–99.

Trieloff M., Jessberger E. K., Herrwerth I., Hopp J., Flénl C., Ghélis M., Bourot-Denise M. and Pellas P. (2003) Structure and thermal history of the H-chondrite parent asteroid revealed by thermochronometry. *Nature* **422**, 502–506.

Trinquier A., Birck J. and Allegre C. J. (2007) Widespread 54 Cr Heterogeneity in the Inner Solar System . *Astrophys. J.* **655**, 1179–1185.

Trinquier A., Elliott T., Ulfbeck D., Coath C. D., Krot A. N. and Bizzarro M. (2009) The origin of s-process isotope heterogeneity in the solar protoplanetary disk. *Science (80-.).* **324**, 374–377.

Turner G. and Cadogan P. H. (1975) The history of lunar bombardment inferred from 40Ar-39Ar dating of highland rocks. *Proc. 6th Lunar Sci. Conf.*, 1509–1538.

Turner G., Cadogan P. H. and Yonge C. J. (1973) Argon selenchronology. *Proc. 4th Lunar Sci. Conf.*, 1889–1914.

Tusch J., Hoffmann J. E., Hasenstab E., Münker C., Fischer-Gödde M. and Marien C. S. (2021a) Long-term preservation of Hadean protocrust in Earth's mantle. *Unpubl. Prepr.* Available at: https://doi.org/10.1002/essoar.10507464.2.

Tusch J., Münker C., Hasenstab E., Jansen M., Marien C. S., Kurzweil F., Van Kranendonk M. J., Smithies R. H., Maier W. D. and Garbe-Schönberg D. (2021b) Convective isolation of Hadean mantle reservoirs through Archean time. *PNAS* **118**, 1–6.

Tusch J., Sprung P., van de Löcht J., Hoffmann J. E., Boyd A. J., Rosing M. T. and Münker C. (2019) Uniform 182W isotope compositions in Eoarchean rocks from the Isua region, SW Greenland: The role of early silicate differentiation and missing late veneer. *Geochim. Cosmochim. Acta* **257**, 284–310.

Upadhyay D., Scherer E. E. and Mezger K. (2008) Fractionation and mixing of Nd isotopes during thermal ionization mass spectrometry: Implications for high precision 142Nd/144Nd analyses. *J. Anal. At. Spectrom.* **23**, 561–568.

Vervoort J. D. and Blichert-Toft J. (1999) Evolution of the depleted mantle: Hf isotope evidence from juvenile rocks through time. *Geochim. Cosmochim. Acta* **63**, 533–556.

Vervoort J. D., Patchett P. J., Albarède F., Blichert-Toft J., Rudnick R. and Downes H. (2000) Hf-Nd isotopic evolution of the lower crust. *Earth Planet. Sci. Lett.* **181**, 115–129.

Vockenhuber C., Oberli F., Bichler M., Ahmad I., Quitte G., Meier M., Halliday A. N., Lee D. C., Kutschera W., Steier P., Gehrke R. J. and Helmer R. G. (2004) New half-life measurement of182 Hf: Improved chronometer for the early solar system. *Phys. Rev. Lett.* **93**, 4–7.

Wakita H., Rey P. and Schmitt R. A. (1971) Abundances of the 14 rare earth elements and 12 other trace elements in Apollo 12 samples: Five igneous and one breccia rocks and four soils. *Proc. 2nd Lnar Sci. Conf.*, 1319–1329.

Walter M. J., Nakamura E., Trønnes R. G. and Frost D. J. (2004) Experimental constraints on crystallization differentiation in a deep magma ocean. *Geochim. Cosmochim. Acta* **68**, 4267–4284.

Wang D. and Carlson R. W. (2022) Tandem-column extraction chromatography for Nd separation: minimizing mass-independent isotope fractionation for ultrahigh-precision Nd isotope-ratio analysis. *J. Anal. At. Spectrom.* **37**, 185–193.

Wänke H., Baddenhausen H., Blum K., Cendales M., Dreibus G., Hofmeister H., Kruse H., Jagoutz E., Palme C., Spettel B. and Thacker, R. Vilcsek E. (1977) On the chemistry of lunar samples and achondrites. Primary matter in the lunar highlands: A re-evaluation. *Proc. 8th Lunar Sci. Conf.*, 2191–2213.

Wänke H., Palme H., Baddenhausen H., Dreibus G., Jagoutz E., Kruse H., Palme C., Spettel B., Teschke F. and Thacker R. (1975) New data on the chemistry of lunar samples: Primary matter in the lunar highlands and the bulk composition of the moon. *Proc. 6th Lunar Sci. Conf.*, 1313–1340.

Warren P. H. and Wasson J. T. (1979) The origin of KREEP. *Rev. Geophys.* **17**, 73–88.

Wasserburg G. J. and Papanastassiou D. A. (1971) AGE OF AN APOLLO 15 MARE BASALT; LUNAR CRUST AND MANTLE EVOLUTION. *Earth Planet. Sci. Lett.* **13**, 97–104.

Weidenschilling S. J. (2011) Initial sizes of planetesimals and accretion of the asteroids. *Icarus* **214**, 671–

684.

Westrenen W. Van, Blundy J. D. and Wood B. J. (2000) Effect of Fe2q on garnet–melt trace element partitioning: experiments in FCMAS and quantification of crystal-chemical controls in natural systems. *Lithos* **53**, 189–201.

White W. M. and Klein E. M. (2013) *Composition of the Oceanic Crust*. 2nd ed., Elsevier Ltd. Available at: http://dx.doi.org/10.1016/B978-0-08-095975-7.00315-6.

Wiemer D., Schrank C. E., Murphy D. T., Wenham L. and Allen C. M. (2018) Earth's oldest stable crust in the Pilbara Craton formed by cyclic gravitational overturns. *Nat. Geosci.* **11**, 357–361.

Wilde S. A., Valley J. W., Peck W. H. and Graham C. M. (2001) Evidence from detrital zircons for the existence of continental crust and oceans on the Earth 4.4 Gyr ago. *Nature* **409**, 175–178.

Willbold M. (2007) Determination of Ce isotopes by TIMS and MC-ICPMS and initiation of a new, homogeneous Ce isotopic reference material. *J. Anal. At. Spectrom.* **22**, 1364–1372.

Willig M. and Stracke A. (2019) Earth's chondritic light rare earth element composition: Evidence from the Ce–Nd isotope systematics of chondrites and oceanic basalts. *Earth Planet. Sci. Lett.* **509**, 55–65. Available at: https://doi.org/10.1016/j.epsl.2018.12.004.

Willis J. P., Ahrens L. H., Danchin R. V., Erlank A. J., Gurney J. J., Hofmeyr P. K., McCarthy T. S. and Orren M. J. (1971) Some inter-element relationships between lunar rocks and fines, and stony meteorites. *Proc. 2nd Lnar Sci. Conf.1*, 1123–1138.

Willis J. P., Erlank A. J., Gurney J. J. and Ahrens L. H. (1972) Geochemical features of Apollo 15 materials. *Apollo 15 lunar samplesolo 15 Lunar samples*, 268–271.

Wombacher F. and Rehkämper M. (2003) Investigation of the mass discrimination of multiple collector ICP-MS using neodymium isotopes and the generalised power law. *J. Anal. At. Spectrom.* **18**, 1371–1375.

Wood J. A., Dickey J. S., Marvin U. B. and Powell B. N. (1970) Lunar anorthosites and a geophysical model of the Moon. *Proc. Apollo 11 Lunar Sci. Conf.* **1**, 965–988.

Yin Q., Jacobsen S. B., Yamashita K., Blichert-Toft J., Télouk P. and Albarède F. (2002) A short timescale for terrestrial planet formation from Hf-W chronometry of meteorites. *Nature* **418**, 949–952.

York D. (1967) THE BEST ISOCHRON. *Earth Planet. Sci. Lett.* **2**, 479–482.

Young E. D., Kohl I. E., Warren P. H., Rubie D. C., Jacobson S. A. and Morbidelli A. (2016) Oxygen isotopic evidence for vigorous mixing during the Moon-forming giant impact.

Yu G. and Jacobsen S. B. (2011) Fast accretion of the Earth with a late Moon-forming giant impact. *Proc. Natl. Acad. Sci. U. S. A.* **108**, 17604–17609.

Zhang C., Holtz F., Koepke J., Wolff P. E., Ma C. and Bédard J. H. (2013) Constraints from experimental melting of amphibolite on the depth of formation of garnet-rich restites, and implications for models of Early Archean crustal growth. *Precambrian Res.* **231**, 206–217.

Zhang C., Miao B. and He H. (2019) Oxygen isotopes in HED meteorites and their constraints on parent asteroids. *Planet. Space Sci.* **168**, 83–94.

Zhang J., Dauphas N., Davis A. M., Leya I. and Fedkin A. (2012) The proto-Earth as a significant source of lunar material. *Nat. Geosci.* **5**, 251–255.

Appendix A1

Supplementary Figures

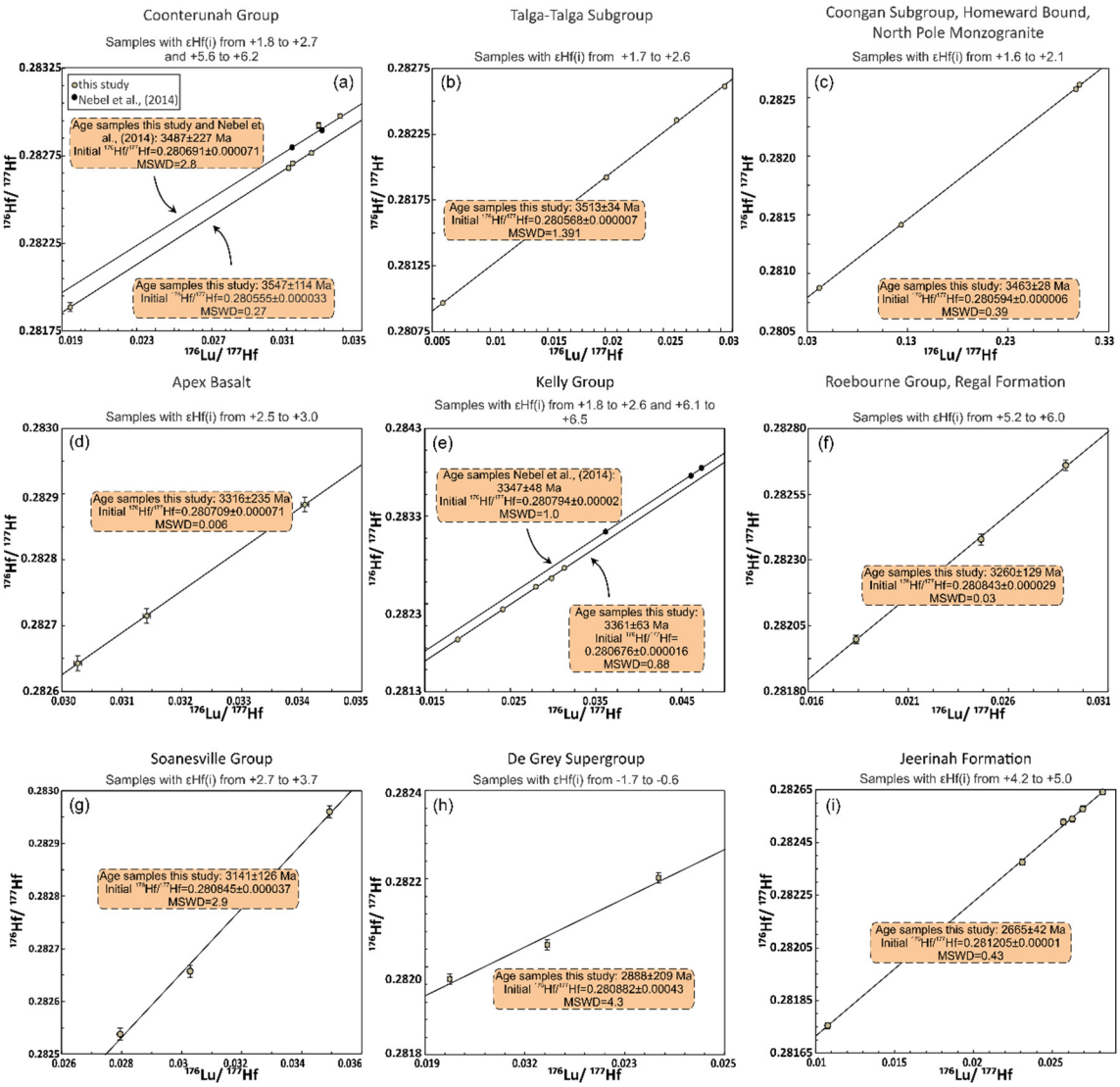

Supplementary Figure 1.1: ^{176}Lu-^{176}Hf whole rock errorchrons for all major stratigraphic units after York, (1967), where at least three samples were analyzed. In this regard, we discarded samples that have strongly heterogeneous $\varepsilon Hf_{(i)}$ values. If less than three samples were available for some formations, we grouped formations if the age differences were less than 20 Ma for ^{147}Sm-^{143}Nd and ^{176}Lu-^{176}Hf and less than 50 Ma for ^{138}La-^{138}Ce. Additional data are from Nebel et al., (2014). Errors used are the external reproducibilities, however if individual 2s.e. were larger than the external reproducibility, these uncertainties were chosen.

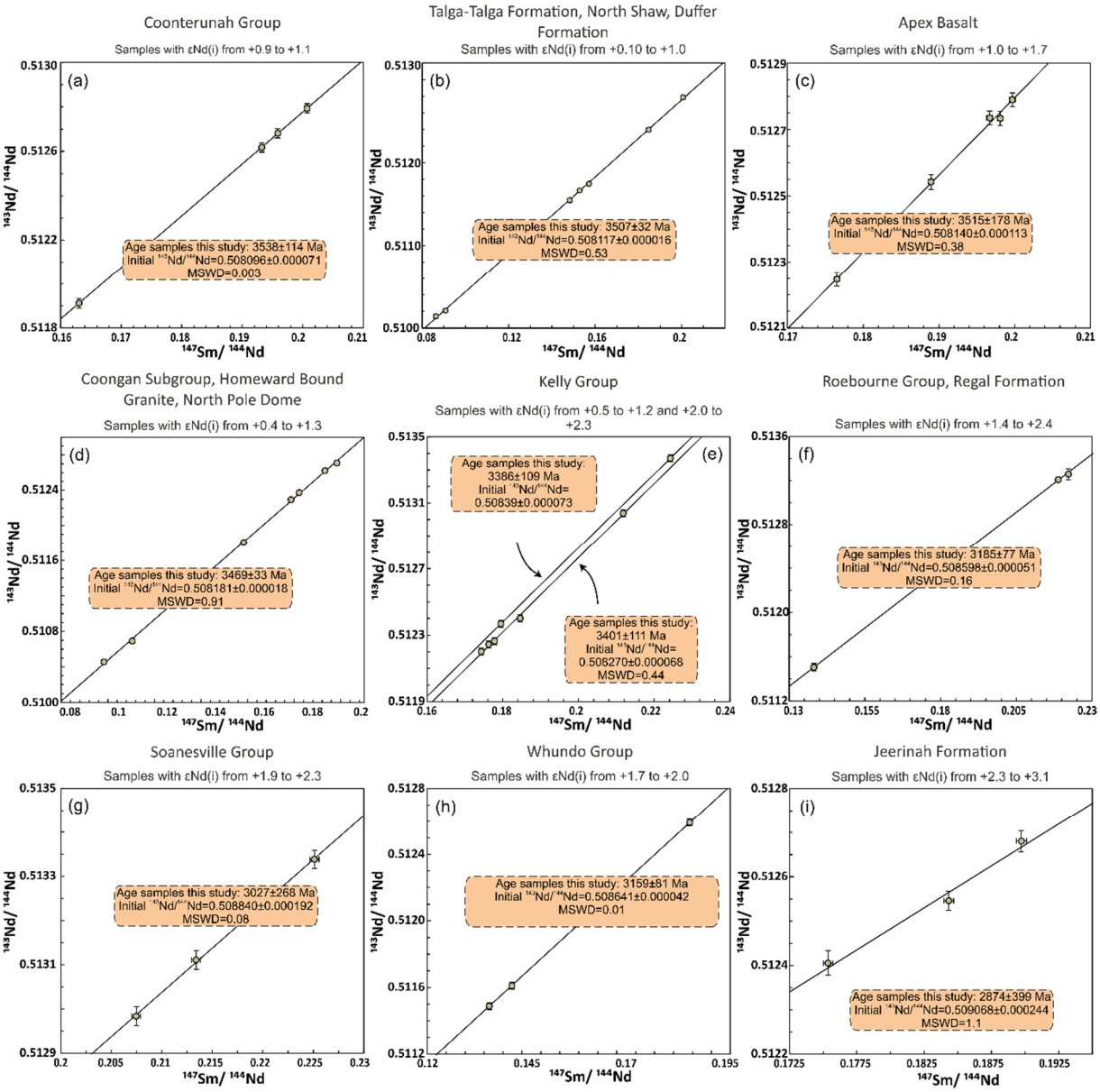

Supplementary Figure 1.2: ^{147}Sm-^{143}Nd whole rock errorchrons for all major stratigraphic units. For further information, see supplementary Figure 1.1.

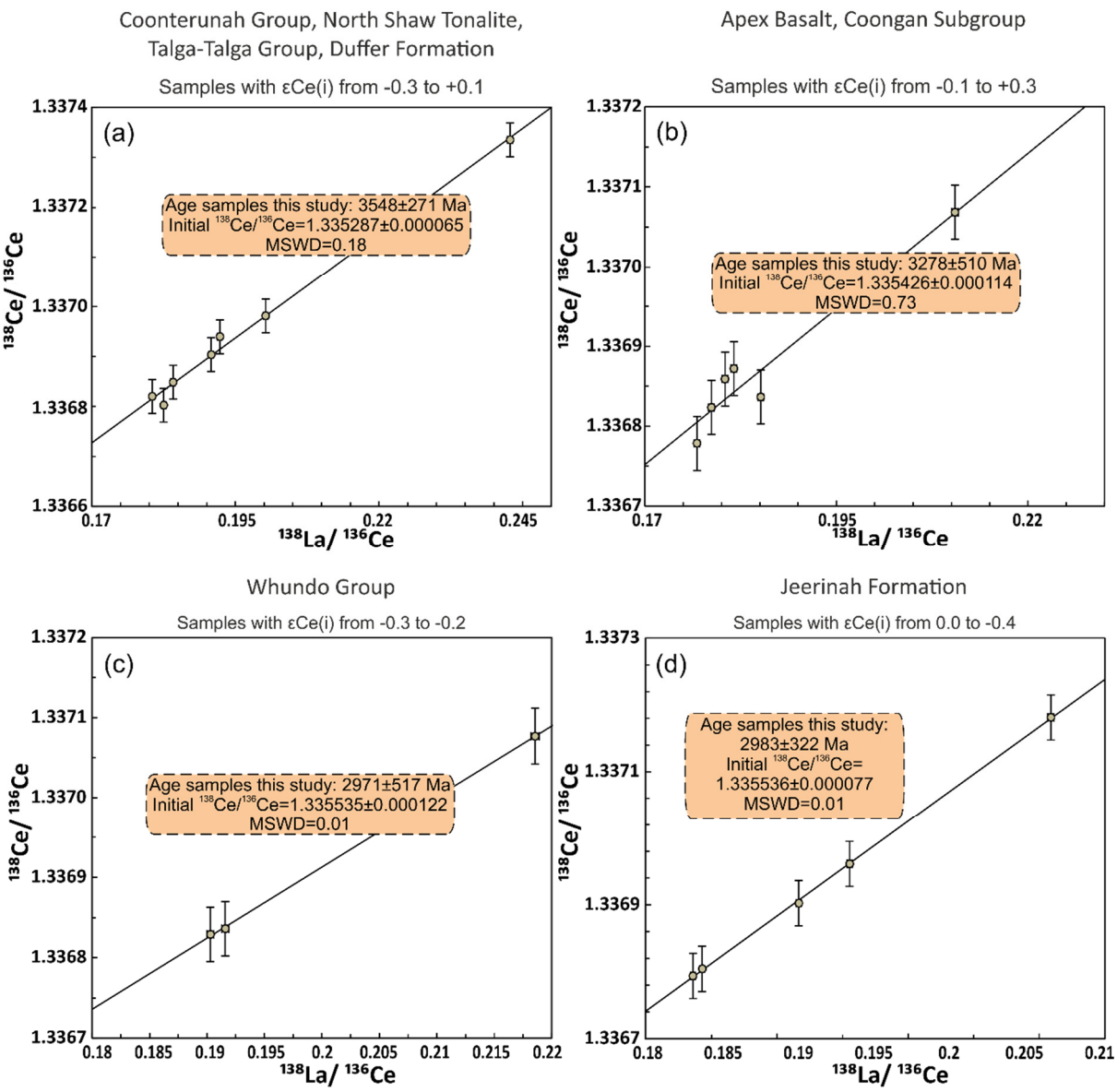

Supplementary Figure 1.3: ^{138}La-^{13843}Ce whole rock errorchrons for all major stratigraphic units. For further information, see supplementary Figure 1.1.

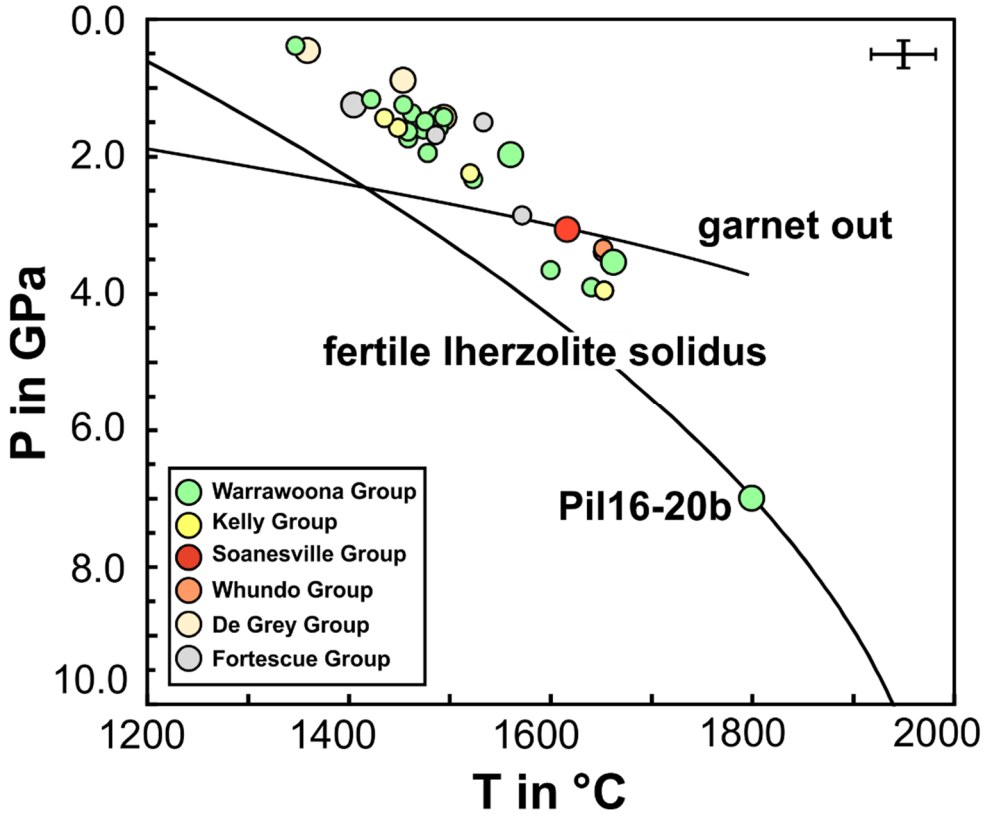

Supplementary Fig. 1.4: Pressure and temperature calculations after (Lee et al., 2009) for Pilbara mafic-ultramafic rocks. Only samples with MgO≥9.5 wt. % and LOI<3 wt. % were chosen to ensure no fractionation of pyroxene and near-pristine magmatic compositions. All magma compositions were corrected for olivine fractionation using olivine Mg# of 0.90, demonstrating that sample Pil16-20b was melted from significantly deeper mantle domains compared to all other Pilbara samples. Fertile lherzolite solidus from Hirschmann, (2000) and garnet out line from Klemme et al., (2009) and Klemme and O'Neill, (2000). Large dots are samples from the studies of Maier et al., (2009) and Tusch et al., (in review) that were also analyzed in this study. Small dots represent samples from the study of Smithies et al., (2018).

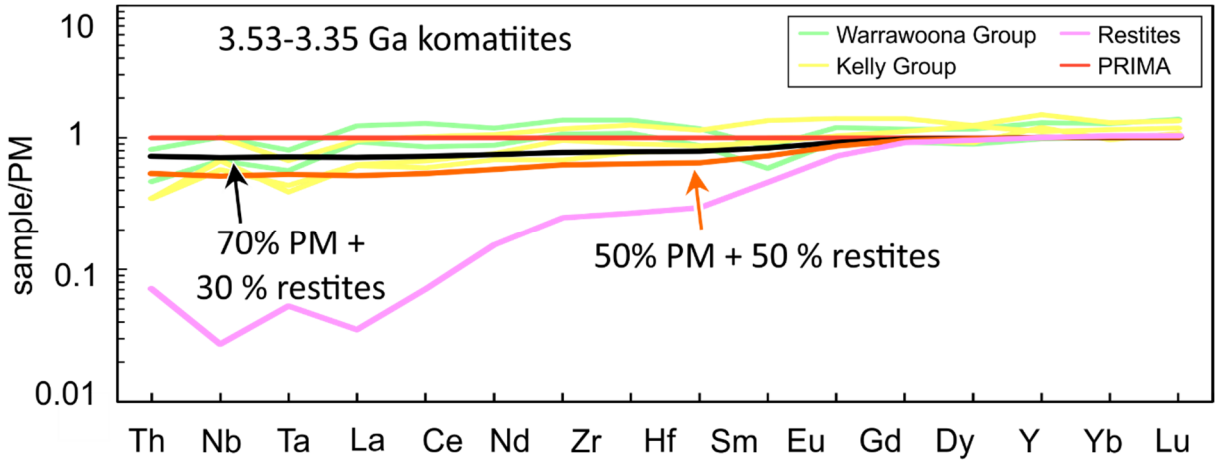

Supplementary Fig. 1.5: Mixing model for hybrid melts tapping ca. 50-70% primitive mantle (PM) and 30-50% residual mantle that was formed from an orthopyroxene-rich mantle in the garnet stability field (Appendix A1). This compositional range can reproduce trace element compositions of Warrawoona and Kelly Group komatiites. Warrawoona Group and Kelly Group komatiite and basalt trace element compositions are from Maier et al., (2009) and Tusch et al., (2021). Normalized to primitive mantle (PM) after Palme and O'Neill, (2013).

Group	Warrawoona Group	Warrawoona Group			Warrawoona Group
Formation	Mount Webber Gabbro	Tabletop Formation			Tabletop Formation
Age [Ma]	3578?	3525			3525
Error [Ma]	10	10			10
Longitude	21°28.426'	21°06.440'			21°06.37'
Latitude	119°20.691'	119°03.373'			119°03.418'
Rock Type	amphibolite	basalt			basalt
Sample	Pil17-007	Pil16-054a	duplicate[d]	average	Pil16-55
La [ppm]	4.280				3.564
Ce [ppm]	10.64				9.021
$^{138}La/^{136}Ce$	0.1959				0.1923
$^{138}Ce/^{136}Ce$	1.336888				1.336940
(±2SE, 6th digit)	±11				±9
$\varepsilon Ce_{(i)}$	-0.5				+0.1
(±2σ)	±0.3				±0.3
Sm [ppm]	2.177	2.311			2.045
Nd [ppm]	7.213	6.962			6.399
$^{147}Sm/^{144}Nd$	0.1824	0.200695991			0.1932
$^{143}Nd/^{144}Nd$	0.512377	0.512793			0.512618
(±2SE, 6th digit)	±19	±8			±20
$\varepsilon Nd_{(i)}$	+1.3	+1.1			+1.0
(±2σ)	±0.6	±0.6			±0.6
Lu [ppm]	0.3063	0.4215	0.4203	0.4209	0.3671
Hf [ppm]	1.623	1.8470	1.8503	1.8487	1.664
$^{176}Lu/^{177}Hf$	0.02678	0.03239	0.03224	0.03232	0.03131
$^{176}Hf/^{177}Hf$	0.282377	0.282776	0.282755	0.282766	0.282706
(±2SE, 6th digit)	±6	±5	±7	±6	±7
$\varepsilon Hf_{(i)}$	+2.2	+2.6	+2.2	+2.4	+2.7
(±2σ)	±0.2	±0.3	±0.3	±0.3	±0.3

Group	Warrawoona Group			Warrawoona Group			Warrawoona Group
Formation	Tabletop Formation			Coucal Formation			Coonterunah Group
Age [Ma]	3525			3507			3500
Error [Ma]	10			20			30
Longitude	21°06.440'			21°07.276'			n.a.
Latitude	119°03.373'			119°02.505'			n.a.
Rock Type	basalt			basalt			komatiite
Sample	Pil16-054b	duplicate[d]	average	Pil16-056	duplicate[d]	average	179756
La [ppm]	3.075			12.69	12.72	12.71	0.8421
Ce [ppm]	8.348			30.88	30.89	30.88	2.246
$^{138}La/^{136}Ce$	0.1792			0.2000	0.2005	0.2002	0.1825
$^{138}Ce/^{136}Ce$	1.336805			1.336947	1.337017	1.336982	1.336803
(±2SE, 6th digit)	±33			±20	±20	±0	±12
$\varepsilon Ce_{(i)}$	-0.1			-0.3	+0.2	-0.1	-0.3
(±2σ)	±0.3			±0.3	±0.3	±0.3	±0.3
Sm [ppm]	1.965			4.965			0.5090
Nd [ppm]	6.066			18.41			1.586
$^{147}Sm/^{144}Nd$	0.1958			0.1630			0.1940
$^{143}Nd/^{144}Nd$	0.512682			0.511912			0.512729
(±2SE, 6th digit)	±7			±8			±17
$\varepsilon Nd_{(i)}$	+1.1			+0.9			+2.9
(±2σ)	±0.6			±0.6			±0.6
Lu [ppm]	0.3701	0.3690	0.3695	0.6152			0.09787
Hf [ppm]	1.696	1.676	1.686	4.488			0.4102
$^{176}Lu/^{177}Hf$	0.03096	0.03125	0.03111	0.01945			0.03386
$^{176}Hf/^{177}Hf$	0.282685	0.282675	0.282680	0.281887			0.282976
(±2SE, 6th digit)	±7	±6	±6	±25			±11
$\varepsilon Hf_{(i)}$	+2.8	+1.8	+2.3	+2.1			+6.2
(±2σ)	±0.3	±0.3	±0.3	±0.9			±0.4

Group	Warrawoona Group	Warrawoona Group	Warrawoona Group	Warrawoona Group		
Formation	Coonterunah Group	North Star Basalt	North Star Basalt	North Star Basalt		
Age [Ma]	3500	3490	3490	3490		
Error [Ma]	25	20	10	10		
Longitude	n.a.	21°10.080'	21°09.047'	21°22.873'		
Latitude	n.a.	119°23.982'	119°24.508'	119°33.614'		
Rock Type	komatiite	basalt	komatiitic basalt	basalt		
Sample	179757	Pil16-017	Pil16-20b	Pil16-037a	duplicate[d]	average
La [ppm]	0.6348	6.901	6.985	6.201	6.604	6.402
Ce [ppm]	1.501	18.24	18.87	15.95	16.71	16.33
$^{138}La/^{136}Ce$	0.2059	0.1841	0.1802	0.1891	0.1924	0.1908
$^{138}Ce/^{136}Ce$	1.336743	1.336849	1.336832	1.336874	1.336934	1.336904
(±2SE, 6th digit)	±11	±24	±29	±24	±21	±0
$\varepsilon Ce_{(i)}$	-2.2	-0.1	+0.1	-0.2	+0.1	-0.1
(±2σ)	±0.3	±0.3	±0.3	±0.3	±0.3	±0.3
Sm [ppm]	0.3793	3.168	3.277	3.233		
Nd [ppm]	1.178	12.18	12.96	10.97		
$^{147}Sm/^{144}Nd$	0.1946	0.1571	0.1528	0.1782		
$^{143}Nd/^{144}Nd$	0.512875	0.511745	0.511666	0.512275		
(±2SE, 6th digit)	±17	±9	±9	±9		
$\varepsilon Nd_{(i)}$	+5.4	+0.2	+0.7	+1.1		
(±2σ)	±0.6	±0.6	±0.6	±0.6		
Lu [ppm]	0.07514	0.2449	0.2148	0.3134		
Hf [ppm]	0.3259	1.883	1.800	2.217		
$^{176}Lu/^{177}Hf$	0.03272	0.01846	0.01694	0.02006		
$^{176}Hf/^{177}Hf$	0.282922	0.281766	0.281675	0.281922		
(±2SE, 6th digit)	±15	±6	±7	±5		
$\varepsilon Hf_{(i)}$	+7.0	0.0	+0.4	+1.7		
(±2σ)	±0.6	±0.3	±0.3	±0.2		

Group	Warrawoona Group	Callina Supersuite			Warrawoona Group		
Formation	North Star Basalt	North Shaw Tonalite			Dresser Formation		
Age [Ma]	3490	3485			3481		
Error [Ma]	10	10			15		
Longitude	21°00.465'	21°21.415'			21°5.567'		
Latitude	119°49.908'	119°27.249'			119°26.761'		
Rock Type	basalt	tonalite			komatiitic basalt		
Sample	Pil16-44a	Pil16-35	duplicate[r,d]	average	Pil16-21	duplicate[d]	average
La [ppm]	3.439	66.26					
Ce [ppm]	11.69	132.8					
$^{138}La/^{136}Ce$	0.1432	0.2428					
$^{138}Ce/^{136}Ce$	1.336864	1.337357	1.337312	1.337335			
(±2SE, 6th digit)	±15	±13	±18				
$\varepsilon Ce_{(i)}$	+2.6	+0.1	-0.2	-0.1			
(±2σ)	±0.3	±0.3	±0.3	±0.3			
Sm [ppm]	2.491	7.917			0.9895		
Nd [ppm]	7.508	52.68			3.238		
$^{147}Sm/^{144}Nd$	0.2006	0.09080			0.1847		
$^{143}Nd/^{144}Nd$	0.512786	0.510210			0.512397		
(±2SE, 6th digit)	±9	±8			±6		
$\varepsilon Nd_{(i)}$	+1.0	+0.1			+0.5		
(±2σ)	±0.6	±0.6			±0.6		
Lu [ppm]	0.4202	0.1583	0.1555	0.1569	0.1971	0.2004	0.1987
Hf [ppm]	2.281	3.978	3.586	3.782	0.9226	0.9341	0.9284
$^{176}Lu/^{177}Hf$	0.02615	0.005645	0.006154	0.005900	0.03033	0.03044	0.03039
$^{176}Hf/^{177}Hf$	0.282357	0.280946	0.280990	0.280968	0.282614	0.282611	0.282613
(±2SE, 6th digit)	±7	±5	±8	±6	±7	±8	±7
$\varepsilon Hf_{(i)}$	+2.6	+1.4	+1.8	+1.6	+1.7	+1.4	+1.6
(±2σ)	±0.3	±0.3	±0.3	±0.3	±0.3	±0.3	±0.3

Group	Warrawoona Group	Warrawoona Group	Callina Supersuite		
Formation	Mount Ada Basalt	Duffer formation	Homeward Bound Granite		
Age [Ma]	3481	3475	3466		
Error [Ma]	15	20	10		
Longitude	21°12.300'	20°57.470'	21°10.443'		
Latitude	119°18.582'	119°52.485'	119°45.636'		
Rock Type	basalt	banded iron formation	granitoid		
Sample	Pil16-007	Pil16-62	Pil16-41	duplicate[r]	average
La [ppm]			64.76		
Ce [ppm]			90.17		
$^{138}La/^{136}Ce$			0.3496		
$^{138}Ce/^{136}Ce$			1.337333	1.337243	1.337288
(±2SE, 6th digit)			±11	±17	±14
$\varepsilon Ce_{(i)}$			-6.7	-7.3	-7.0
(±2σ)			±0.3	±0.3	±0.3
Sm [ppm]	1.185	0.4821	12.04		
Nd [ppm]	3.933	1.967	65.86		
$^{147}Sm/^{144}Nd$	0.1821	0.1481	0.1105		
$^{143}Nd/^{144}Nd$	0.512374	0.511548	0.510691		
(±2SE, 6th digit)	±19	±8	±8		
$\varepsilon Nd_{(i)}$	+1.2	+0.3	+0.4		
(±2σ)	±0.6	±0.6	±0.6		
Lu [ppm]	0.2526		0.9072		
Hf [ppm]	1.205		10.45		
$^{176}Lu/^{177}Hf$	0.02976		0.01232		
$^{176}Hf/^{177}Hf$	0.282575		0.281414		
(±2SE, 6th digit)	±5		±5		
$\varepsilon Hf_{(i)}$	+1.6		+1.8		
(±2σ)	±0.2		±0.2		

Group	Warrawoona Group			-	Warrawoona Group	Warrawoona Group
Formation	North Pole Monzogranite			Spearhill Monzogranite	Mount Ada Basalt	Mount Ada Basalt
Age [Ma]	3466			3466	3451	3451
Error [Ma]	10			10	30	30
Longitude	21°06.971'			21°31.112'	21°21.893'	21°22.150'
Latitude	119°22.409'			119°24.228'	119°34.345'	119°34.416'
Rock Type	monzogranite			monzogranite	basalt	basalt
Sample	Pil16-012	duplicate[r]	average	Pil16-36a	Pil16-028	Pil16-030a
La [ppm]	27.67				6.099	2.284
Ce [ppm]	42.48				16.61	6.124
$^{138}La/^{136}Ce$	0.3171				0.1787	0.1816
$^{138}Ce/^{136}Ce$	1.337515	1.337459	1.337487		1.336823	1.336872
(±2SE, 6th digit)	±15	±18	±16		±21	±17
$\varepsilon Ce_{(i)}$	-3.3	-3.7	-3.5		+0.1	+0.3
(±2σ)	±0.3	±0.3	±0.3		±0.3	±0.3
Sm [ppm]	3.135			5.464	3.619	1.423
Nd [ppm]	19.27			25.99	12.25	4.337
$^{147}Sm/^{144}Nd$	0.0983			0.1270	0.1786	0.1983
$^{143}Nd/^{144}Nd$	0.510456			0.511012	0.512294	0.512708
(±2SE, 6th digit)	±8			±8	±6	±11
$\varepsilon Nd_{(i)}$	+1.3			-6.3	+1.2	+0.5
(±2σ)	±0.6			±0.6	±0.6	±0.6
Lu [ppm]	0.1135			0.6162	0.4904	0.2183
Hf [ppm]	3.861			5.768	2.907	1.050
$^{176}Lu/^{177}Hf$	0.004171			0.01516	0.02394	0.02949
$^{176}Hf/^{177}Hf$	0.280874			0.281613	0.282211	0.282578
(±2SE, 6th digit)	±4			±6	±22	±8
$\varepsilon Hf_{(i)}$	+2.0			-5.8	+2.5	+2.4
(±2σ)	±0.3			±0.3	±0.8	±0.3

Group	Warrawoona Group	Warrawoona Group	Warrawoona Group			Warrawoona Group
Formation	Mount Ada Basalt	Mount Ada Basalt	Apex Basalt			Apex Basalt
Age [Ma]	3451	3451	3443			3443
Error [Ma]	30	30	30			30
Longitude	21°22.150'	21°12.113'	21°06,760'			21°10.624'
Latitude	119°34.416'	119°19.069'	119°22,667'			119°41.762'
Rock Type	basalt	basalt	dolerite			basaltic andesite
Sample	Pil16-30c	Pil17-10	Pil16-009	duplicate[d]	average	Pil16-22a
La [ppm]		8.559				1.156
Ce [ppm]		19.79				3.340
$^{138}La/^{136}Ce$		0.2105				0.1685
$^{138}Ce/^{136}Ce$		1.337069				1.336768
(±2SE, 6th digit)		±11				±11
$\varepsilon Ce_{(i)}$		0.0				+0.3
(±2σ)		±0.3				±0.3
Sm [ppm]	1.090	2.952	0.8359			0.9884
Nd [ppm]	3.411	11.27	2.569			2.762
$^{147}Sm/^{144}Nd$	0.1932	0.1583	0.1967			0.2163
$^{143}Nd/^{144}Nd$	0.512621	0.511805	0.512735			0.513113
(±2SE, 6th digit)	±8	±12	±12			±12
$\varepsilon Nd_{(i)}$	+1.1	+0.7	+1.7			+0.4
(±2σ)	±0.6	±0.6	±0.6			±0.6
Lu [ppm]	0.1869	0.3386	0.1305	0.1304	0.1304	0.1926
Hf [ppm]	0.8811	2.555	0.6662	0.6643	0.6652	0.8030
$^{176}Lu/^{177}Hf$	0.03011	0.01881	0.02779	0.02787	0.02783	0.03405
$^{176}Hf/^{177}Hf$	0.282613	0.281811	0.282498	0.282488	0.282493	0.282884
(±2SE, 6th digit)	±8	±5	±4	±7	±6	±6
$\varepsilon Hf_{(i)}$	+2.1	+0.4	+3.5	+3.0	+3.2	+2.5
(±2σ)	±0.3	±0.4	±0.3	±0.3	±0.3	±0.3

Group	Warrawoona Group	Warrawoona Group			Warrawoona Group		
Formation	Apex Basalt	Apex Basalt			Apex Basalt		
Age [Ma]	3443	3443			3443		
Error [Ma]	30	30			30		
Longitude	21°10.530'	21°10.552'			21°10.641'		
Latitude	119°41.933'	119°42.011'			119°42.124'		
Rock Type	basalt	basalt			basalt		
Sample	Pil16-023a	Pil16-24	duplicate[d]	average	Pil16-025	duplicate[d]	average
La [ppm]	3.013	1.906			3.118		
Ce [ppm]	8.022	5.141			8.583		
$^{138}La/^{136}Ce$	0.1828	0.1804			0.1768		
$^{138}Ce/^{136}Ce$	1.336934	1.336859			1.336779		
(±2SE, 6th digit)	±23	±13			±27		
$\varepsilon Ce_{(i)}$	+0.7	+0.2			-0.1		
(±2σ)	±0.3	±0.3			±0.3		
Sm [ppm]	1.940	1.128			2.051		
Nd [ppm]	5.873	3.608			6.259		
$^{147}Sm/^{144}Nd$	0.1997	0.1890			0.1981		
$^{143}Nd/^{144}Nd$	0.512789	0.512542			0.512733		
(±2SE, 6th digit)	±10	±23			±10		
$\varepsilon Nd_{(i)}$	+1.5	+1.4			+1.1		
(±2σ)	±0.6	±0.6			±0.6		
Lu [ppm]	0.3467	0.2167	0.2153	0.2160	0.3658	0.3657	0.3657
Hf [ppm]	1.566	1.386	1.371	1.378	1.715	1.701	1.708
$^{176}Lu/^{177}Hf$	0.03142	0.02219	0.02229	0.02224	0.03027	0.03052	0.03040
$^{176}Hf/^{177}Hf$	0.282715	0.282233	0.282242	0.282238	0.282643	0.282640	0.282641
(±2SE, 6th digit)	±6	±5	±6	±6	±6	±8	±7
$\varepsilon Hf_{(i)}$	+2.7	+7.3	+7.4	+7.4	+2.8	+2.1	+2.5
(±2σ)	±0.3	±0.3	±0.3	±0.3	±0.3	±0.3	±0.3

Group	Warrawoona Group	Kelly Group	Kelly Group			Kelly Group		
Formation	Apex Basalt	Euro Basalt	Euro Basalt			Euro Basalt		
Age [Ma]	3443	3343	3343			3343		
Error [Ma]	25	15	15			15		
Longitude	n.a.	21°12.933'	21°07.871'			21°21.709'		
Latitude	n.a.	119°18.448'	119°03.724'			119°48.040'		
Rock Type	komatiite	dolerite	basalt			basalt		
Sample	179738	Pil16-001	Pil16-53a	duplicate[d]	average	Pil16-39a	duplicate[d]	average
La [ppm]	2.527		6.036	6.003	6.019			
Ce [ppm]	6.646		16.09	16.00	16.05			
$^{138}La/^{136}Ce$	0.1851		0.1826	0.1826	0.1826			
$^{138}Ce/^{136}Ce$	1.336836		1.336877	1.336886	1.336881			
(±2SE, 6th digit)	±9		±22	±25				
$\varepsilon Ce_{(i)}$	-0.2		+0.2	+0.3	+0.3			
(±2σ)	±0.3		±0.3	±0.3	±0.3			
Sm [ppm]	1.269	1.143	3.126			2.520		
Nd [ppm]	4.346	3.966	10.63			8.486		
$^{147}Sm/^{144}Nd$	0.1765	0.1743	0.1778			0.1795		
$^{143}Nd/^{144}Nd$	0.512248	0.512200	0.512263			0.512368		
(±2SE, 6th digit)	±13	±8	±7			±12		
$\varepsilon Nd_{(i)}$	+1.2	+1.0	+0.7			+2.0		
(±2σ)	±0.6	±0.6	±0.6			±0.6		
Lu [ppm]	0.1961	0.1935	0.5387	0.5361	0.5374	0.3001	0.2950	0.2976
Hf [ppm]	1.011	0.9820	2.447	2.429	2.438	1.775	1.726	1.751
$^{176}Lu/^{177}Hf$	0.02752	0.02796	0.03125	0.03133	0.03129	0.02399	0.02426	0.02412
$^{176}Hf/^{177}Hf$	0.282423	0.282495	0.282713	0.282707	0.282710	0.282241	0.282237	0.282239
(±2SE, 6th digit)	±8	±9	±7	±8	±7	±6	±6	±6
$\varepsilon Hf_{(i)}$	+1.5	+2.6	+2.8	+2.4	+2.6	+2.6	+1.9	+2.3
(±2σ)	±0.3	±0.4	±0.3	±0.3	±0.3	±0.3	±0.3	±0.3

Group	Kelly Group			Kelly Group			Kelly Group	Kelly Group
Formation	Euro Basalt			Euro Basalt			Euro Basalt	Euro Basalt
Age [Ma]	3343			3343			3343	3343
Error [Ma]	15			15			15	15
Longitude	21°21.551'			21°08.300'			21°12.853'	n.a.
Latitude	119°47.963'			119°00.484'			119°18.398'	n.a.
Rock Type	peridotite			gabbro			gabbro	komatiite
Sample	Pil16-040	duplicate[d]	average	Pil16-058b	duplicate[d]	average	Pil17-009	179815
La [ppm]				7.349	7.132	7.240	2.668	
Ce [ppm]				18.54	18.06	18.30	6.831	
$^{138}La/^{136}Ce$				0.1929	0.1922	0.1925	0.1901	
$^{138}Ce/^{136}Ce$				1.336932	1.336959	1.336945	1.336911	
(±2SE, 6th digit)				±24	±18		±14	
$\varepsilon Ce_{(i)}$				0.0	+0.3	+0.2	0.0	
(±2σ)				±0.3	±0.3	±0.3	±0.3	
Sm [ppm]	0.378			3.623			1.416	
Nd [ppm]	1.020			12.42			4.639	
$^{147}Sm/^{144}Nd$	0.2242			0.1763			0.1846	
$^{143}Nd/^{144}Nd$	0.513370			0.512244			0.512401	
(±2SE, 6th digit)	±21			±11			±19	
$\varepsilon Nd_{(i)}$	+2.3			+1.0			+0.5	
(±2σ)	±0.6			±0.6			±0.6	
Lu [ppm]	0.08420	0.08392	0.08406	0.3270			0.2320	0.07668
Hf [ppm]	0.2750	0.2717	0.2734	2.463			1.105	0.2334
$^{176}Lu/^{177}Hf$	0.04346	0.04385	0.04365	0.01885			0.02981	0.04663
$^{176}Hf/^{177}Hf$	0.283548	0.283552	0.283550	0.281896			0.282591	0.283853
(±2SE, 6th digit)	±8	±9	±8	±6			±6	±22
$\varepsilon Hf_{(i)}$	+4.6	+3.8	+4.2	+2.2			+1.8	+8.1
(±2σ)	±0.4	±0.4	±0.4	±0.3			±0.2	±0.9

Group	Kelly Group	Roebourne Group	Roebourne Group	Roebourne Group		
Formation	Euro Basalt	Ruth Well Formation	Ruth Well Formation	Ruth Well Formation		
Age [Ma]	3343	3261	3261	3261		
Error [Ma]	15	25	25	25		
Longitude	n.a.	n.a.	n.a.	20°47.265'		
Latitude	n.a.	n.a.	n.a.	117°11.940		
Rock Type	komatiite	komatiite	komatiite	komatiite		
Sample	179816	160242	160245	Pil16-66b	duplicate[d]	average
La [ppm]	0.6521					
Ce [ppm]	1.787					
$^{138}La/^{136}Ce$	0.1777					
$^{138}Ce/^{136}Ce$	1.336789					
(±2SE, 6th digit)	±10					
$\varepsilon Ce_{(i)}$	-0.1					
(±2σ)	±0.3					
Sm [ppm]	0.4952		0.351	0.879		
Nd [ppm]	1.414		1.537	2.428		
$^{147}Sm/^{144}Nd$	0.2118		0.1382	0.2189		
$^{143}Nd/^{144}Nd$	0.513038		0.511506	0.513209		
(±2SE, 6th digit)	±16		±35	±13		
$\varepsilon Nd_{(i)}$	+1.2		+2.4	+1.7		
(±2σ)	±0.6		±0.7	±0.6		
Lu [ppm]	0.09493	0.05497	0.03884	0.1014	0.1015	0.1014
Hf [ppm]	0.3757	0.2876	0.2998	0.6241	0.6178	0.6209
$^{176}Lu/^{177}Hf$	0.03587	0.02713	0.01839	0.02305	0.02332	0.02318
$^{176}Hf/^{177}Hf$	0.283046	0.282512	0.281999	0.282222	0.282228	0.282225
(±2SE, 6th digit)	±15	±14	±16	±10	±9	±9
$\varepsilon Hf_{(i)}$	+4.1	+4.7	+6.0	+3.5	+3.1	+3.3
(±2σ)	±0.6	±0.5	±0.6	±0.4	±0.4	±0.4

Group	Soanesville Group	Soanesville Group	Soanesville Group	Soanesville Group		
Formation	Paddy Market Formation	Honeyeater Basalt	Honeyeater Basalt	Honeyeater Basalt		
Age [Ma]	3210	3182	3182	3182		
Error [Ma]	30	10	10	10		
Longitude	21°08.522'	21°07.696'	21°08.058'	21°08.058'		
Latitude	119°12.125'	119°12.319'	119°13.112'	119°13.112'		
Rock Type	shale	basalt	ultramfite	gabbro		
Sample	Pil16-50b	Pil16-51	Pil16-052a	Pil16- 52b	duplicate[d]	average
La [ppm]	35.55			1.666	1.656	1.661
Ce [ppm]	60.39			4.295	4.291	4.293
$^{138}La/^{136}Ce$	0.2866			0.1889	0.1879	0.1884
$^{138}Ce/^{136}Ce$	1.337584			1.336862	1.336814	1.336838
(±2SE, 6th digit)	±33			±11	±14	
$\varepsilon Ce_{(i)}$	-0.4			-0.2	-0.5	-0.4
(±2σ)	±0.3			±0.3	±0.3	±0.3
Sm [ppm]	3.994	1.096	0.4845	1.200		
Nd [ppm]	22.93	2.945	1.412	3.401		
$^{147}Sm/^{144}Nd$	0.1053	0.2251	0.2075	0.2134		
$^{143}Nd/^{144}Nd$	0.510656	0.513338	0.512984	0.513111		
(±2SE, 6th digit)	±8	±14	±15	±18		
$\varepsilon Nd_{(i)}$	-1.0	+1.9	+2.2	+2.3		
(±2σ)	±0.7	±0.6	±0.6	±0.6		
Lu [ppm]	0.3678	0.1943	0.09426	0.2013	0.1978	0.1996
Hf [ppm]	2.979	0.9108	0.3830	1.028	1.004	1.016
$^{176}Lu/^{177}Hf$	0.01752	0.03028	0.03494	0.02780	0.02795	0.02788
$^{176}Hf/^{177}Hf$	0.281765	0.282657	0.282960	0.282540	0.282538	0.282539
(±2SE, 6th digit)	±5	±9	±6	±6	±8	±7
$\varepsilon Hf_{(i)}$	-1.0	+2.7	+3.3	+3.9	+3.5	+3.7
(±2σ)	±0.4	±0.3	±0.3	±0.3	±0.3	±0.3

Group	Dalton Suite	Whundo Group	Whundo Group	Whundo Group	De Grey Supergroup
Formation	Dalton Suite	Whundo Group	Whundo Group	Whundo Group	Opaline Well Intrusion
Age [Ma]	3180	3123	3123	3123	2940
Error [Ma]	10	15	15	15	10
Longitude	n.a.	20°55.196'	20°57.717'	20°56.862'	20°50.816'
Latitude	n.a.	117°04.128'	117°02.232'	117°02.890'	117°47.701'
Rock Type	olivine pyroxenite	basalt	basalt	basalt	gabbroic cumulate
Sample	Pil16-49	Pil16-67	Pil16-73	Pil16-74	Pil16-63
La [ppm]		14.71	6.477	12.66	
Ce [ppm]		39.15	17.09	28.24	
$^{138}La/^{136}Ce$		0.1829	0.1845	0.2182	
$^{138}Ce/^{136}Ce$		1.336829	1.336836	1.337077	
(±2SE, 6th digit)		±26	±27	±35	
$\varepsilon Ce_{(i)}$		-0.2	-0.2	-0.3	
(±2σ)		±0.3	±0.3	±0.3	
Sm [ppm]		5.714	3.860	3.252	0.3371
Nd [ppm]		24.26	12.33	14.42	1.469
$^{147}Sm/^{144}Nd$		0.1423	0.1893	0.1363	0.1387
$^{143}Nd/^{144}Nd$		0.511610	0.512593	0.511488	0.511486
(±2SE, 6th digit)		±8	±9	±7	±28
$\varepsilon Nd_{(i)}$		+1.7	+2.0	+1.8	-0.6
(±2σ)		±0.6	±0.6	±0.6	±0.6
Lu [ppm]	0.1627	0.4696	0.6004	0.3847	0.04665
Hf [ppm]	0.7850	3.525	3.125	2.942	0.3396
$^{176}Lu/^{177}Hf$	0.02941	0.01891	0.02727	0.01855	0.01950
$^{176}Hf/^{177}Hf$	0.282580	0.281956	0.282494	0.281961	0.281972
(±2SE, 6th digit)	±9	±6	±9	±49	±8
$\varepsilon Hf_{(i)}$	+1.8	+1.9	+3.2	+2.8	-0.6
(±2σ)	±0.3	±0.3	±0.3	±1.8	±0.3

Group	De Grey Supergroup	De Grey Supergroup	De Grey Supergroup	Callina Supersuite		
Formation	Bookingarra Group	Bookingarra Group	Mount Negro Volcanics	North Shaw Tonalite		
Age [Ma]	2946	2946	2931	2851		
Error [Ma]	15	15	20	10		
Longitude	20°43.372'	20°43.054'	20°59.936'	21°21.290'		
Latitude	117°51.616'	117°52.056'	117°33.440'	119°27.321'		
Rock Type	ultramafic cumulate	spinifex pyroxenite	basalt	tonalite		
Sample	Pil16-064	Pil16-65	Pil16-75	Pil16-34	duplicate[d]	average
La [ppm]		5.997	8.528			
Ce [ppm]		11.16	17.83			
$^{138}La/^{136}Ce$		0.2615	0.2328			
$^{138}Ce/^{136}Ce$		1.337480	1.337193			
(±2SE, 6th digit)		±11	±10			
$\varepsilon Ce_{(i)}$		+0.6	-0.1			
(±2σ)		±0.3	±0.3			
Sm [ppm]	0.4290	0.9761	1.886	9.592		
Nd [ppm]	1.755	4.219	8.190	67.08		
$^{147}Sm/^{144}Nd$	0.1478	0.1398	0.1392	0.08638		
$^{143}Nd/^{144}Nd$	0.511575	0.511444	0.511519	0.510141		
(±2SE, 6th digit)	±33	±17	±16	±8		
$\varepsilon Nd_{(i)}$	-2.3	-1.9	-0.2	+0.7		
(±2σ)	±0.7	±0.6	±0.6	±0.6		
Lu [ppm]	0.06986	0.1439	0.2214	0.1914	0.1925	0.1920
Hf [ppm]	0.4188	0.9521	1.712	3.336	3.625	3.480
$^{176}Lu/^{177}Hf$	0.02368	0.02145	0.01835	0.008141	0.007536	0.007838
$^{176}Hf/^{177}Hf$	0.282202	0.282050	0.281927	0.281040	0.281032	0.281036
(±2SE, 6th digit)	±9	±6	±7	±5	±6	±5
$\varepsilon Hf_{(i)}$	-0.8	-1.7	0.0	-1.2	0.0	-0.6
(±2σ)	±0.4	±0.3	±0.3	±0.3	±0.3	±0.3

Group	Fortescue Group	Fortescue Group	Fortescue Group	Fortescue Group	Fortescue Group
Formation	Black Range Dolerite	Jeerinah Formation	Jeerinah Formation	Hardey Formation	Jeerinah Formation
Age [Ma]	2772	2630	2630	2760	2630
Error [Ma]	10	10	10	15	10
Longitude	21°26.823'	23°13.741'	23°12.986'	21°19.882'	23°14.319'
Latitude	119°32.209'	117°44.846'	117°47.570'	119°36.015'	117°48.292'
Rock Type	dolerite	gabbro	dolerite	shale	dolerite
Sample	Pil16-31	201474	201483	Pil16-38	201487
La [ppm]	13.66	2.877	3.785	38.06	3.220
Ce [ppm]	27.31	7.842	9.532	68.08	8.544
$^{138}La/^{136}Ce$	0.2435	0.1786	0.1933	0.2721	0.1834
$^{138}Ce/^{136}Ce$	1.337276	1.336804	1.336902	1.337369	1.336802
(±2SE, 6th digit)	±25	±13	±11	±21	±10
$\varepsilon Ce_{(i)}$	+0.2	-0.2	-0.1	-0.5	-0.4
(±2σ)	±0.3	±0.3	±0.3	±0.3	±0.3
Sm [ppm]	2.560	1.759	1.960	5.492	1.923
Nd [ppm]	11.72	5.699	6.428	28.45	6.127
$^{147}Sm/^{144}Nd$	0.1320	0.1866	0.1843	0.1167	0.1897
$^{143}Nd/^{144}Nd$	0.511316	0.512568	0.512546	0.510973	0.512680
(±2SE, 6th digit)	±8	±15	±22	±8	±24
$\varepsilon Nd_{(i)}$	-2.8	+2.0	+2.3	-4.2	+3.1
(±2σ)	±0.6	±0.6	±0.6	±0.6	±0.6
Lu [ppm]	0.2752	0.1354	0.1488	0.3836	0.1273
Hf [ppm]	2.151	0.7136	0.7494	3.442	0.7034
$^{176}Lu/^{177}Hf$	0.01816	0.02692	0.02818	0.01581	0.02569
$^{176}Hf/^{177}Hf$	0.281890	0.282577	0.282642	0.281775	0.282528
(±2SE, 6th digit)	±7	±6	±7	±6	±7
$\varepsilon Hf_{(i)}$	-2.7	+4.6	+4.6	-2.5	+5.0
(±2σ)	±0.3	±0.3	±0.3	±0.3	±0.3

Group	Fortescue Group	Fortescue Group	Fortescue Group
Formation	Jeerinah Formation	Jeerinah Formation	Jeerinah Formation
Age [Ma]	2630	2630	2630
Error [Ma]	10	10	10
Longitude	23°13.604'	23°13.549'	23°12.572'
Latitude	117°47.623'	117°47.549'	117°47.593'
Rock Type	dolerite	dolerite	dolerite
Sample	201496	201497	201476
La [ppm]	3.471	4.423	18.39
Ce [ppm]	8.401	12.15	38.62
$^{138}La/^{136}Ce$	0.2011	0.1772	0.2318
$^{138}Ce/^{136}Ce$	1.336961	1.336794	1.337181
(±2SE, 6th digit)	±13	±11	±14
$\varepsilon Ce_{(i)}$	-0.1	-0.2	+0.2
(±2σ)	±0.3	±0.3	±0.3
Sm [ppm]	1.575	2.740	3.814
Nd [ppm]	5.429	8.807	17.55
$^{147}Sm/^{144}Nd$	0.1754	0.1881	0.1313
$^{143}Nd/^{144}Nd$	0.512405	0.512594	0.511531
(±2SE, 6th digit)	±28	±21	±17
$\varepsilon Nd_{(i)}$	+2.6	+2.0	+0.5
(±2σ)	±0.6	±0.6	±0.6
Lu [ppm]	0.1096	0.1687	0.0730
Hf [ppm]	0.6735	0.9119	0.9619
$^{176}Lu/^{177}Hf$	0.02309	0.02626	0.01076
$^{176}Hf/^{177}Hf$	0.282375	0.282540	0.281755
(±2SE, 6th digit)	±8	±5	±7
$\varepsilon Hf_{(i)}$	+4.2	+4.4	+4.2
(±2σ)	±0.3	±0.2	±0.3

*excluded from further interpretation due to uncertain age.

Duplicate[r] repeated measurements.

Duplicate[d] duplicate digestions treated with $HClO_4$.

Duplicate[r,d] repeated measurements for Ce isotopes and duplicate digestions and measurements for ^{176}Lu-^{176}Hf.

All data normalized relative to recent CHUR values (Bouvier et al., 2008; Israel et al., 2019; Willig and Stracke, 2019).

Reference material	BHVO-2	BHVO-2	BHVO-2	BHVO-2	BHVO-2	BHVO-2
Digestion	#1	#2	#3	#4	#5	#6
$^{176}Hf/^{177}Hf$	0.283115	0.283113	0.283116	0.283115	0.28311	
2 SE (last digit)	(7)	(6)	(6)	(7)	(8)	n.d.
εHf	+11.7±0.2	+11.6±0.2	+11.7±0.2	+11.7±0.2	+11.5±0.3	n.d.
Lu [ppm]	0.2718	0.2703	0.2764	0.1075	0.2765	n.d.
Hf [ppm]	4.409	4.373	4.460	1.798	5.214	n.d.
$^{176}Lu/^{177}Hf$	0.008750	0.008772	0.008795	0.008489	0.007527	n.d.
$^{143}Nd/^{144}Nd$	0.512997	0.513003	n.d.	0.512991	n.d.	0.512969
2 SE (last digit)	(8)	(13)	n.d.	(8)	n.d.	(16)
εNd	+7.2±0.1	+7.3±0.2	n.d.	+7.1±0.2	n.d.	+6.6±0.3
Sm [ppm]	5.640	5.599	n.d.	5.622	n.d.	5.638
Nd [ppm]	22.78	22.61	n.d.	22.71	n.d.	22.76
$^{147}Sm/^{144}Nd$	0.1497	0.1497	n.d.	0.1497	n.d.	0.1498
$^{138}Ce/^{136}Ce$	1.336807	1.336816	1.336794	1.336841	1.336792	1.336826
2 SE (last digit)	(11)	(9)	(10)	(8)	(20)	(9)
εCe	-0.7±0.1	-0.6±0.1	-0.8±0.1	-0.4±0.1	-0.8±0.2	-0.5±0.1
La [ppm]	15.37	15.14	n.d.	15.16	15.16	n.d.
Ce [ppm]	37.97	37.47	n.d.	37.64	37.64	n.d.
$^{138}La/^{136}Ce$	0.1965	0.1966	n.d.	0.1961	0.1961	n.d.

All data normalized relative to recent CHUR values (Bouvier et al., 2008; Israel et al., 2019; Willig and Stracke, 2019).

In the following model, equilibrium or fractional crystallization of Mg-Ca perovskite cumulates are formed at 4.4 Ga as a possible source for the decoupling found in ~3.5 Ga Pilbara mafic-ultramafic rocks, assuming a primitive mantle composition (Palme and O'Neill, 2013) as starting composition. It is shown that event over a wide range of crystallizing fractions, neither equilibrium crystallization nor fractional crystallization can reproduce the Hf-Nd-Ce isotope data of these rocks.

Fractional crystallization model	Ferropericlase	Ca-Pv	Mg-Pv													
Mineral modes	0.105	0.045	0.85													
	Th	Nb	Ta	La	Ce	Nd	Zr	Hf	Sm	Eu	Gd	Ti	Y	Er	Yb	Lu
Ferropericlase[1*]	0	0.002	0	0.011	0.016	0.051	0.15	0.076	0.049	0.023	0.07	0.004	0.027	0.04	0.05	0.11
Ca-Pv[2]	18	0.25	0.3	6	11	16	3	2.1	20	22	23	1.1	22	21	19	16
Mg-Pv[2]	0.005	0.21	0.3	0.011	0.023	0.02	2.5	2.5	0.05	0.09	0.14	0.86	0.55	0.67	1.01	1.21

Fraction Pv-cumulate crystallized	$^{138}La/^{136}Ce$	$\varepsilon Ce_{(3.5Ga)}$	$^{147}Sm/^{144}Nd$	$\varepsilon Nd_{(3.5Ga)}$	$^{176}Lu/^{177}Hf$	$\varepsilon Hf_{(3.5Ga)}$	Zr/Sm
0.05	0.104	-1.3	0.248	+5.5	0.0265	-5.7	53.2
0.25	0.110	-1.2	0.236	+4.1	0.0298	-3.6	38.8
0.45	0.119	-1.1	0.221	+2.4	0.0349	-0.6	25.7
0.6[2*]	0.128	-1.0	0.207	+0.8	0.0409	+3.0	16.9

Equilibrium crystallization model	Ferropericlase	Ca-Pv	Mg-Pv	Sum												
Mineral modes	0.105	0.045	0.85	1												
Mineral Phasen	Th	Nb	Ta	La	Ce	Nd	Zr	Hf	Sm	Eu	Gd	Ti	Y	Er	Yb	Lu
Ferropericlase[1*]	0	0.002	0	0.011	0.016	0.051	0.15	0.076	0.049	0.023	0.07	0.004	0.027	0.04	0.05	0.11
Ca-Pv[2]	18	0.25	0.3	6	11	16	3	2.1	20	22	23	1.1	22	21	19	16
Mg-Pv[2]	0.005	0.21	0.3	0.011	0.023	0.02	2.5	2.5	0.05	0.09	0.14	0.86	0.55	0.67	1.01	1.21

Fraction Pv-cumulate crystallized	$^{138}La/^{136}Ce$	$\varepsilon Ce_{(3.5Ga)}$	$^{147}Sm/^{144}Nd$	$\varepsilon Nd_{(3.5Ga)}$	$^{176}Lu/^{177}Hf$	$\varepsilon Hf_{(3.5Ga)}$	Zr/Sm
0.05	0.104	-1.3	0.248	+5.5	0.0269	-5.4	53.3
0.25	0.110	-1.2	0.237	+4.3	0.0289	-4.2	42.6
0.45	0.119	-1.1	0.226	+3.0	0.0305	-3.3	35.3
0.6	0.129	-1.0	0.218	+2.1	0.0314	-2.7	31.2

If partition coefficients were not available from an experiment, they were extrapolated using the lattice strain model after (Blundy and Wood, 1994).

[1*]For Ferropericlase, D^{Th} and D^{Ta} were assumed to be 0 since Nb is extremely incompatible and they could not be calculated after Blundy and Wood, (1994). This assumption will have no significant influence on our model, since D^{Nb}, D^{Th} and D^{Ta} are significantly higher in Ca-Perovskite (Pv) and Mg-Pv.

[2*]60% of segregating Pv-cumulates is considered the maximum amount of Pv-segregation possible as Pv is only stable in ~2/3 of Earth's mantle.

[1]Walter et al., (2004)

[2]Corgne et al., (2005)

Fractional crystallization model	Ferropericlase	Ca-Pv	Mg-Pv													
Mineral modes	0.105	0.045	0.85													
	Th	Nb	Ta	La	Ce	Nd	Zr	Hf	Sm	Eu	Gd	Ti	Y	Er	Yb	Lu
Ferropericlase[1*]	0	0.002	0	0.011	0.016	0.051	0.15	0.076	0.049	0.023	0.07	0.004	0.027	0.04	0.05	0.11
Ca-Pv[2]	18	0.25	0.3	6	11	16	3	2.1	20	22	23	1.1	22	21	19	16
Mg-Pv[2]	0.005	0.21	0.3	0.011	0.023	0.02	2.5	2.5	0.05	0.09	0.14	0.86	0.55	0.67	1.01	1.21

Fraction Pv-cumulate crystallized	$^{138}La/^{136}Ce$	εCe(3.5)	$^{147}Sm/^{144}Nd$	εNd(3.5)	$^{176}Lu/^{177}Hf$	εHf(3.5)	Zr/Sm
0.05	0.104	-1.3	0.248	+5.5	0.0265	-5.7	53.2
0.25	0.110	-1.2	0.236	+4.1	0.0298	-3.6	38.8
0.45	0.119	-1.1	0.221	+2.4	0.0349	-0.6	25.7
0.6[2*]	0.128	-1.0	0.207	+0.8	0.0409	+3.0	16.9

Equilibrium crystallization model	Ferropericlase	Ca-Pv	Mg-Pv	Sum												
Mineral modes	0.105	0.045	0.85	1												
Mineral Phasen	Th	Nb	Ta	La	Ce	Nd	Zr	Hf	Sm	Eu	Gd	Ti	Y	Er	Yb	Lu
Ferropericlase[1*]	0	0.002	0	0.011	0.016	0.051	0.15	0.076	0.049	0.023	0.07	0.004	0.027	0.04	0.05	0.11
Ca-Pv[2]	18	0.25	0.3	6	11	16	3	2.1	20	22	23	1.1	22	21	19	16
Mg-Pv[2]	0.005	0.21	0.3	0.011	0.023	0.02	2.5	2.5	0.05	0.09	0.14	0.86	0.55	0.67	1.01	1.21

Fraction Pv-cumulate crystallized	$^{138}La/^{136}Ce$	$\varepsilon Ce_{(3.5Ga)}$	$^{147}Sm/^{144}Nd$	$\varepsilon Nd_{(3.5Ga)}$	$^{176}Lu/^{177}Hf$	$\varepsilon Hf_{(3.5Ga)}$	Zr/Sm
0.05	0.104	-1.3	0.248	+5.5	0.0269	-5.4	53.3
0.25	0.110	-1.2	0.237	+4.3	0.0289	-4.2	42.6
0.45	0.119	-1.1	0.226	+3.0	0.0305	-3.3	35.3
0.6	0.129	-1.0	0.218	+2.1	0.0314	-2.7	31.2

In the following, two mantle residues are formed at 4.2 Ga that will later individually mix with upwelling primitive mantle. Here, the composition of the melts with strongly decoupled Hf-Nd isotope compositions are reproduced. This model assumes a primitive mantle composition (Palme and O'Neill, 2013) as starting composition.

Deep melting of primitive mantle at 4.2 Ga
Extraction of 15% Batch melt after[1]

Phase	CPx	OPX	Grt	Ol												
Abundance	0.1	0.3	0.05	0.55												
Partition coefficients	Th	Nb	Ta	La	Ce	Nd	Zr	Hf	Sm	Eu	Gd	Dy	Y	Er	Yb	Lu
Clinopyroxene[2]	0.104	0.007	0.028	0.028	0.059	0.115	0.125	0.208	0.259	0.341	0.422	0.57	0.603	0.64	0.635	0.617
Orthopyroxene[3]	0.002	0.004	0.004	0.0031	0.004	0.012	0.024	0.03	0.02	0.009	0.0065	0.011	0.015	0.045	0.08	0.12
Garnet[2]	0.0075	0.04	0.08	0.028	0.08	0.222	0.537	0.431	0.537	1.54	4.84	11.5	14.1	18.8	23.2	24.1
Olivine[3]	0.00005	0.0005	0.0005	0.0005	0.0005	0.00042	0.0011	0.0011	0.0011	0.0005	0.0011	0.0027	0.0082	0.013	0.02	0.02

Isotope composition at 3.5 Ga:	Ce [ppm]	$\varepsilon Ce_{(3.5Ga)}$	Nd [ppm]	$\varepsilon Nd_{(3.5Ga)}$	Hf [ppm]	$\varepsilon Hf_{(3.5Ga)}$
Garnet-bearing residual mantle	0.12	-1.2	0.21	16.5	0.08	44.8
Primitive mantle[4]	1.753	0.0	1.341	0.0	0.3014	0.0

Mixing of garnet-bearing residual mantle with primitive mantle at 3.5 Ga

Fraction of garnet-bearing residual mantle	$\varepsilon Ce_{(3.5Ga)}$	$\varepsilon Nd_{(3.5Ga)}$	$\varepsilon Hf_{(3.5Ga)}$
0.0	0.0	0.0	0.0
0.1	0.0	0.3	1.3
0.2	-0.0	+0.6	+2.8
0.3	-0.0	+1.0	+4.6
0.4	-0.1	+1.5	+6.8
0.5	-0.1	+2.2	+9.5
0.6	-0.1	+3.1	+12.8
0.7	-0.2	+4.3	+17.2
0.8	-0.3	+6.3	+23.2
0.9	-0.5	+9.6	+31.7
1.0	-1.2	+16.5	+44.8

Extraction of 30 to 40% batch melt from hybrid mantle at ~3.5 Ga to from komatiites

Phase	CPx	OPX	Grt	Ol												
Abundance	0.1	0.35	0	0.55												
Partition coefficients	Th	Nb	Ta	La	Ce	Nd	Zr	Hf	Sm	Eu	Gd	Dy	Y	Er	Yb	Lu
Clinopyroxene[2]	0.0059	0.015	0.015	0.03	0.08	0.088	0.274	0.2835	0.299	0.278	0.35	0.4	0.45	0.42	0.45	0.511
Orthopyroxene[3]	0.00200	0.00400	0.00400	0.00310	0.00400	0.0120	0.024	0.0300	0.0200	0.019	0.00650	0.0110	0.050	0.045	0.080	0.12
Garnet[2]	0.00750	0.04	0.08	0.028	0.08	0.222	0.537	0.431	0.537	1.540	4.84	11.500	14.1	18.8	23.200	24.1
Olivine[3]	0.00005	0.0005	0.0005	0.0005	0.0005	0.00042	0.002	0.0022	0.0011	0.001	0.0011	0.0027	0.005	0.013	0.02	0.02

Fraction of batch melt extracted*	Th	Nb	Ta	La	Ce	Nd	Zr	Hf	Sm	Eu	Gd	Dy	Y	Er	Yb	Lu
0.2	0.187	1.22	0.0916	1.41	3.74	3.13	24.6	0.728	1.09	0.494	2.13	2.92	16.0	1.86	1.82	0.256
0.3	0.125	0.820	0.0614	0.949	2.53	2.13	17.4	0.515	0.770	0.347	1.50	2.08	11.6	1.36	1.36	0.194
0.4	0.0939	0.616	0.0462	0.714	1.91	1.62	13.4	0.398	0.594	0.268	1.16	1.61	9.17	1.07	1.08	0.157

*No further fractional crystallization of the ascending melts was modelled, since the crystallization of almost exclusively olivine will not have an effect on the resulting trace
If partition coefficients were not available from an experiment, they were extrapolated using the lattice strain model after[5]

[1]Shaw, (1970)

[2]Zhang et al., (2013)

[3]Salters and Stracke, (2004)

[4]Palme and O'Neill, (2013)

[4]Blundy and Wood, (1994)

In the following, two mantle residues are formed at 4.2 Ga that will later individually mix with upwelling primitive mantle. Here, the composition of a melt with strongly radiogenic but coupled Hf-Nd isotope composition of sample 179757 is reproduced. This model assumes a primitive mantle composition (Palme and O'Neill, 2013) as starting composition.

Shallow melting of primitive mantle at 4.2 Ga
Extraction of 15% Batch melt after[1]

Phase	CPx	OPX	Grt	Ol												
Abundance	0.35	0.1	0.03	0.52												
Partition coefficients	Th	Nb	Ta	La	Ce	Nd	Zr	Hf	Sm	Eu	Gd	Dy	Y	Er	Yb	Lu
Clinopyroxene[2]	0.0059	0.015	0.015	0.03	0.08	0.088	0.204	0.2835	0.299	0.115	0.35	0.4	0.738	0.42	0.45	0.511
Orthopyroxene[3]	0.002	0.004	0.004	0.0031	0.004	0.012	0.024	0.03	0.02	0.009	0.0065	0.011	0.015	0.045	0.08	0.12
Garnet[2]	0.00005	0.0005	0.0005	0.0005	0.0005	0.00042	0.0011	0.0011	0.0011	0.0005	0.0011	0.0027	0.0082	0.013	0.02	0.02
Olivine[3]																

Isotope composition at 3.5 Ga:	Ce [ppm]	εCe(3.5)	Nd [ppm]	εNd(3.5)	Hf [ppm]	εHf(3.5)
Garnet-bearing residual mantle	0.309	-1.3	0.285	22.6	0.140	17.4
Primitive mantle[4]	1.753	0.0	1.341	0.0	0.301	0.0

Mixing of garnet-bearing residual mantle with primitive mantle at 3.5 Ga

Fraction Spinel residual mantle	εCe(3.5)	εNd(3.5)	εHf(3.5)
0.0	0.0	0.0	0.0
0.1	0.0	0.5	0.9
0.2	-0.1	+1.1	+1.8
0.3	-0.1	+1.9	+2.9
0.4	-0.2	+3.3	+4.8
0.5	-0.2	+4.0	+5.5
0.6	-0.3	+5.5	+7.1
0.7	-0.4	+7.5	+9.1
0.8	-0.6	+10.4	+11.3
0.9	-0.8	+14.9	+14.0
1.0	-1.3	+22.6	+17.4

Extraction of 30 to 40% batch melt from hybrid mantle at ~3.5 Ga to from komatiites

Phase	CPx	OPX	Grt	Ol												
Abundance	0.1	0.35	0	0.55												
Partition coefficients	Th	Nb	Ta	La	Ce	Nd	Zr	Hf	Sm	Eu	Gd	Dy	Y	Er	Yb	Lu
Clinopyroxene[2]	0.0059	0.015	0.015	0.03	0.08	0.088	0.274	0.2835	0.299	0.278	0.35	0.4	0.45	0.42	0.45	0.511
Orthopyroxene[3]	0.00200	0.00400	0.00400	0.00310	0.00400	0.0120	0.024	0.0300	0.0200	0.019	0.00650	0.0110	0.050	0.045	0.080	0.12
Garnet[2]	0.00750	0.04	0.08	0.028	0.08	0.222	0.537	0.431	0.537	1.540	4.84	11.500	14.1	18.8	23.200	24.1
Olivine[3]	0.00005	0.0005	0.0005	0.0005	0.0005	0.00042	0.002	0.0022	0.0011	0.001	0.0011	0.0027	0.005	0.013	0.02	0.02

Fraction of batch melt extracted*	Th	Nb	Ta	La	Ce	Nd	Zr	Hf	Sm	Eu	Gd	Dy	Y	Er	Yb	Lu
0.2	0.00489	0.0937	0.00786	0.175	1.04	0.947	14.6	0.424	0.640	0.272	1.26	1.85	10.4	1.23	1.22	0.173
0.3	0.00327	0.0628	0.00527	0.117	0.704	0.645	10.3	0.300	0.451	0.191	0.892	1.32	7.57	0.897	0.911	0.131
0.4	0.00246	0.0472	0.00396	0.088	0.532	0.489	7.92	0.232	0.349	0.147	0.689	1.02	5.96	0.706	0.726	0.106

*No further fractional crystallization of the ascending melts was modelled, since the crystallization of almost exclusively olivine will not have an effect on the resulting trace
If partition coefficients were not available from an experiment, they were extrapolated using the lattice strain model after[5]

[1]Shaw, (1970)

[2]Zhang et al., (2013)

[3]Salters and Stracke, (2004)

[4]Palme and O'Neill, (2013)

[4]Blundy and Wood, (1994)

Appendix A2

Group	Isua Supracrustal Belt	Isua Supracrustal Belt	Isua Supracrustal Belt	Isua Supracrustal Belt	Isua Supracrustal Belt	Isua Supracrustal Belt	Isua Supracrustal Belt	Isua Supracrustal Belt
Subgroup	Southern terrane	Southern terrane	Southern terrane	Southern terrane	Southern terrane	Southern terrane	Northern terrane	Northern terrane
Rock Type	peridotite	amphibolite	amphibolite	ultramafic cumulate	TTG	TTG	boninite	boninite
Sample name	10-34	10-17	10-37	10-27	10-38	10-38	462901	462903
Longitude (N)	65° 0'44.7"	65° 2'28.1"	65° 0'21.8"	65° 2'57.9"	65°00' 49.62"	65°00' 49.62"	65°5'60"	65°10'806"
Latitude (W)	50°11'57.9"	50° 13'18.7"	50° 12'26.3"	50°14'15.0"	50°13' 44.64"	50°13' 44.64"	50°	49°47'347"
Age in Ma	3810	3810	3810	3810	3806	3806	3720	3720
Age uncertainty	50	50	50	50	8	8	20	20
Age reference	[1,2,3]	[1,2,3]	[1,2,3]	[1,2,3]	[3]	[3]	[4,5]	[4,5]
Sm [ppm]	0.649	2.029	2.117	0.394	n.d.	n.d.	0.4000	0.6000
Nd [ppm]	1.58	6.326	6.976	1.06	n.d.	n.d.	1.06	1.88
$^{147}Sm/^{144}Nd$	0.2483	0.1939	0.1834	0.2243	0.1401	0.1401	0.225	0.194
$^{143}Nd/^{1443}Nd$	0.513954	0.512667	0.512401	0.5135	0.51129	0.51129	0.513386	0.512683
(±2SE)	0.000005	0.000005	0.000004	0.000004	0.00001	0.00001	0.000006	0.000016
$\varepsilon Nd_{(i)}$	+0.1	+1.8	+1.7	+3.1	+1.4	+1.4	+0.8	+2
Err. εNd	±0.6	±0.4	±0.5	±0.5	±0.4	±0.4	±0.5	±0.4
Lu [ppm]	0.0688	0.308	0.2458	0.0886	n.d.	n.d.	0.2335	0.2533
Hf [ppm]	0.111	1.747	1.399	0.254	n.d.	n.d.	0.4115	0.7126
$^{176}Lu/^{177}Hf$	0.08789	0.02502	0.02493	0.04944	0.002391	0.002391	0.07986	0.04959
$^{176}Hf/^{177}Hf$	0.286796	0.282185	0.282149	0.284041	0.280498	0.280498	0.286205	0.284166
(±2SE)	0.000013	0.00001	0.000012	0.000007	0.000005	0.000005	0.000004	0.000011
$\varepsilon Hf_{(i)}$	+0.3	+1.2	+0.1	+3.1	+0.4	+0.4	+3.3	+8.2
Err. εHf	±2.0	±0.5	±0.5	±0.7	±0.4	±0.4	±0.9	±0.5
^{147}Sm-^{143}Nd and	[1]	[1]	[1]	[1]	[11]	[11]	[12]	[12]
^{176}Lu-^{177}Hf data from:								

Group	Isua Supracrustal Belt	Isua Supracrustal Belt	Isua Supracrustal Belt	Isua Supracrustal Belt	Isua Supracrustal Belt	Narssaq utramafic Body	Isua Supracrustal Belt	Isua Supracrustal Belt
Subgroup	Northern terrane	Northern terrane	Northern terrane	Northern terrane	Northern terrane		Northern terrane	Northern terrane
Rock Type	boninite	amphibolite	metabasalt	meztabasalt	ultramafic cumulate	peridotite	TTG	TTG
Sample name	462948	2000-10	2000-5	2000-14	S33	10-09	JEH 2007-05	229403
Longitude (N)	65°10'368	65°8'21.90"			65°10'650"	63°58'06.0"	64°42'53.88"	
Latitude (W)	49°49'364	50°9'7.80"			49°47'495"	51°28'17.3"	50°7'27.3"	
Age in Ma	3720	3718	3720	3720	3720	3931	3677	3715
Age uncertainty	20	20	20	20	20	150	9	10
Age reference	[4,5]	[4,5]	[4,5]	[4,5]	[4,5]	[1]	[6]	[7]
Sm [ppm]	0.588	1.734	1.644	2.106	0.5943	0.166		
Nd [ppm]	1.71	5.799	5.565	6.734	2.197	0.440		
$^{147}Sm/^{144}Nd$	0.2079	0.1807	0.1786	0.1891	0.1635	0.2168	0.1025	0.1151
$^{143}Nd/^{144}Nd$	0.512912	0.512304	0.51225	0.512464	0.511968	0.513268	0.510301	0.510716
(±2SE)	0.000043	0.000008	0.000007	0.000008	0.000003	0.000007	0.000012	0.000011
$\varepsilon Nd_{(i)}$	-0.2	+1.0	+1.0	+0.1	+2.7	+1.9	-1.1	+1.5
Err. εNd	±0.9	±0.4	±0.4	±0.4	±0.4	±0.6	±0.4	±0.4
Lu [ppm]	0.2598	0.1665	0.1525	0.2123	0.04562	0.0307		
Hf [ppm]	0.7065	1.585	1.517	1.120	0.1246	0.120		
$^{176}Lu/^{177}Hf$	0.05125	0.01491	0.01425	0.01983	0.05199	0.03440	0.05991	0.006757
$^{176}Hf/^{177}Hf$	0.284182	0.281474	0.28141	0.281844	0.284104	0.282955	0.280823	0.280858
(±2SE)	0.000005	0.000005	0.000007	0.000007	0.000021	0.000009	0.000005	0.000007
$\varepsilon Hf_{(i)}$	+4.5	+1.2	+0.6	+1.8	-0.1	+3.9	0.0	0.0
Err. εHf	±0.5	±0.5	±0.5	±0.5	±0.5	±0.4	±0.4	±0.4
^{147}Sm-^{143}Nd and	[12]	[13]	[13]	[13]	this study	[1]	[14]	[14]
^{176}Lu-^{177}Hf data from:								

Group	Isua Supracrustal Belt	Isua Supracrustal Belt	Isua Supracrustal Belt	inner Ameralik Fjord Region	inner Ameralik Fjord Region	inner Ameralik Fjord Region
Subgroup	Ameralik Dyke	Ameralik Dyke	Ameralik Dyke			Proterozoic dyke
Rock Type	amphibolite	amphibolite	amphibolite	amphibolite	amphibolite	dyke
Sample name	10-41	SG 03	JEH 2007-04	496419	496437	499304
Longitude (N)	65° 6'36.72"	65°5'50.82''	65°5'50.82''			
Latitude (W)	50° 9'57.78"	50°7'32.64	50°7'32.64			
Age in Ma	3421	3421	3421	2970	2970	2000
Age uncertainty	34	34	34	28	28	
Age reference	[8]	[8]	[8]	[10]	[10]	
Sm [ppm]	2.525	2.211	2.034	1.367	3.887	4.582
Nd [ppm]	7.849	6.786	6.116	4.492	13.08	19.3
$^{147}Sm/^{144}Nd$	0.1945	0.1970	0.2010	0.1840	0.1797	0.1435
$^{143}Nd/^{144}Nd$	0.512719	0.512777	0.512839	0.512465	0.512433	0.511947
(±2SE)	0.000004	0.000004	0.000004	0.000005	0.000005	0.000005
$\varepsilon Nd_{(i)}$	+2.4	+2.4	+1.9	+1.4	+2.4	+0.2
Err. εNd	±0.4	±0.4	±0.4	±0.4	±0.4	±0.4
Lu [ppm]	0.4112	0.3520	n.d.	0.2584	0.5475	0.4452
Hf [ppm]	1.987	1.680	n.d.	0.9832	3.487	3.764
$^{176}Lu/^{177}Hf$	0.02937	0.02974	n.d.	0.03731	0.02228	0.01679
$^{176}Hf/^{177}Hf$	0.282578	0.282612	n.d.	0.283103	0.282298	0.282167
(±2SE)	0.00001	0.00001	n.d.	0.000006	0.000007	0.000007
$\varepsilon Hf_{(i)}$	+2.6	+2.9	n.d.	+3.8	+5.6	+0.8
Err. εHf	±0.4	±0.4	n.d.	±0.4	±0.5	±0.4
^{147}Sm-^{143}Nd and ^{176}Lu-^{177}Hf data from:	this study	this study	this study	[16]	[16]	this study

[1] van de Löcht et al., (2018)
[2] Amelin et al., (2011)
[3] Nutman et al., (1999)
[4] Nutman and Friend, (2009)
[5] Friend and Nutman, (2010)
[6] Næraa et al., (2012)
[7] Baadsgaard et al., (1986)
[8] Rizo et al., (2012)
[9] Polat et al., (2009)
[10] Polat et al., (2010)
[11] Hoffmann et al., (2014)
[12] Hoffmann et al., (2010)
[13] Hoffmann et al., (2011b)
[14] Hoffmann et al., (2011a)
[15] Szilas et al., (2016)
[16] Szilas et al., (2015)

Group	Isua Supracrustal Belt	Isua Supracrustal Belt	Isua Supracrustal Belt	Isua Supracrustal Belt	Isua Supracrustal Belt	Isua Supracrustal Belt	Isua Supracrustal Belt
Subgroup	Southern terrane	Southern terrane	Southern terrane	Southern terrane	Southern terrane	Southern terrane	Northern terrane
Rock Type	peridotite	amphibolite	amphibolite	ultramafic cumulate	TTG	TTG	boninite
Sample name	10-34	10-17	10-37	10-27	10-38	10-38	462901
Longitude (N)	65° 0'44.7"	65° 2'28.1"	65° 0'21.8"	65° 2'57.9"	65°00' 49.62"	65°00' 49.62"	65°5'60"
Latitude (W)	50°11'57.9"	50° 13'18.7"	50° 12'26.3"	50°14'15.0"	50°13' 44.64"	50°13' 44.64"	50°
Age in Ma	3810	3810	3810	3810	3806	3806	3720
Age uncertainty	50	50	50	50	8	8	20
Age reference	[1,2,3]	[1,2,3]	[1,2,3]	[1,2,3]	[3]	[3]	[4,5]
N	10	11	9	9	9	12	10
V [^{142}Nd]	25	18	9	30	13	25	5
μ^{142}Nd (8/4)	+12.9	+12.3	+13.6	+13.2	+11.8	+13.2	+9.5
95 c.i.	±2.3	±2.7	±1.4	±1.8	±1.6	±1.1	±6.6
μ^{143}Nd (8/4)	+3389.9	+1086.5	-1526.0	+2658.2	-1518.9	-1525.8	+2156.7
95 c.i.	±2.1	±2.3	±2.7	±3.3	±3.2	±2.2	±6.6
μ^{145}Nd (8/4)	+3.8	+2.3	+0.9	-0.6	-0.1	+1.8	+4.3
95 c.i.	±2.6	±2.1	±1.4	±2.6	±2.5	±1.6	±3.2
μ^{146}Nd (8/4)	+2.0	-0.1	+1.5	+1.2	+1.6	+1.8	+1.7
95 c.i.	±1.8	±3.0	±1.9	±2.5	±3.2	±1.8	±5.0
μ^{150}Nd (8/4)	-10.0	+2.1	-9.2	-5.9	-3.0	-8.7	-8.3
95 c.i.	±4.3	±4.4	±3.7	±6.8	±5.9	±1.9	±13.4
μ^{142}Nd (6/4)	+14.7	+11.8	+14.8	+13.4	+12.0	+14.8	+10.1
95 c.i.	±2.8	±5.3	±2.5	±2.9	±4.0	±2.1	±5.8
μ^{143}Nd (6/4)	+3390.3	+1087.9	-1525.4	+2659.0	-1518.9	-1525.0	+2157.8
95 c.i.	±2.1	±3.2	±3.1	±2.9	±4.9	±2.7	±6.6
μ^{145}Nd (6/4)	+2.7	+2.3	-0.3	-0.6	-0.2	+0.4	+2.8
95 c.i.	±2.9	±1.9	±1.4	±2.4	±3.2	±1.2	±3.2
μ^{148}Nd (6/4)	-3.7	+0.3	-2.7	-2.2	-2.9	-3.4	-3.2
95 c.i.	±3.5	±5.9	±3.8	±4.9	±6.4	±3.6	±9.9
μ^{150}Nd (6/4)	-12.5	+0.9	-14.7	-8.7	-3.8	-14.1	-9.8
95 c.i.	±4.4	±9.8	±4.9	±5.4	±7.2	±4.0	±16.9

Group	Isua Supracrustal Belt	Isua Supracrustal Belt	Isua Supracrustal Belt	Isua Supracrustal Belt	Isua Supracrustal Belt	Narssaq utramafic Body	Isua Supracrustal Belt	Isua Supracrustal Belt
Subgroup	Northern terrane	Northern terrane	Northern terrane	Northern terrane	Northern terrane		Northern terrane	Northern terrane
Rock Type	boninite	amphibolite	metabasalt	metabasalt	ultramafic cumulate	peridotite	TTG	TTG
Sample name	462948	2000-10	2000-5	2000-14	S33	10-09	JEH 2007-05	229403
Longitude (N)	65°10'368	65°8'21.90"			65°10'650"	63°58'06.0"	64°42'53.88"	
Latitude (W)	49°49'364	50°9'7.80"			49°47'495"	51°28'17.3"	50°7'27.3"	
Age in Ma	3720	3718	3720	3720	3720	3931	3677	3715
Age uncertainty	20	20	20	20	20	150	9	10
Age reference	[4,5]	[4,5]	[4,5]	[4,5]	[4,5]	[1]	[6]	[7]
N	9	10	10	11	3	11	11	11
V [^{142}Nd]	27	21	28.93	31.24	12	28	33	34
μ^{142}Nd (8/4)	+9.9	+10.6	+9.2	+10.0	+9.3	+11.6	+10.4	+12.0
95 c.i.	±1.8	±2.9	±2.6	±2.1	±4.2	±2.2	±2.2	±2.9
μ^{143}Nd (8/4)	+1440.2	+371.5	+211.8	+686.1	-309.1	+2253.2	-3528.2	-2785.7
95 c.i.	±2.9	±1.8	±2.0	±1.6	±7.6	±1.9	±2.6	±2.7
μ^{145}Nd (8/4)	+9.9	+0.7	-0.1	+0.3	+1.6	+2.1	+2.0	+3.1
95 c.i.	±4.1	±2.0	±2.6	±1.8	±16.6	±1.9	±2.1	±1.8
μ^{146}Nd (8/4)	+0.9	+1.3	-0.4	+2.6	-1.5	+0.7	+0.5	+0.0
95 c.i.	±2.2	±1.9	±2.0	±1.7	±9.2	±1.6	±2.1	±2.1
μ^{150}Nd (8/4)	-8.6	-5.6	-10.6	-4.3	-10.9	-8.2	-3.6	-6.7
95 c.i.	±5.9	±3.7	±4.9	±3.8	±37.7	±3.7	±3.7	±3.1
μ^{142}Nd (6/4)	+10.1	+11.4	+9.0	+12.4	+9.6	+12.3	+11.5	+12.7
95 c.i.	±2.5	±2.7	±2.7	±2.0	±5.7	±1.9	±3.0	±3.4
μ^{143}Nd (6/4)	+1441.3	+371.4	+211.7	+687.9	-308.4	+2254.2	-3528.1	-2785.6
95 c.i.	±2.7	±2.0	±2.8	±1.7	±6.4	±2.2	±2.6	±2.1
μ^{145}Nd (6/4)	+9.7	+0.1	+0.0	-0.9	+0.1	+1.9	+2.0	+3.2
95 c.i.	±3.9	±1.9	±1.8	±1.5	±7.7	±1.7	±2.1	±1.6
μ^{148}Nd (6/4)	-1.6	-2.4	+1.1	-5.1	+0.2	-2.0	-0.7	+0.1
95 c.i.	±4.4	±3.8	±3.9	±3.2	±13.3	±3.4	±4.3	±4.2
μ^{150}Nd (6/4)	-11.8	-5.5	-7.5	-11.1	-15.8	-9.3	-5.5	-5.9
95 c.i.	±5.1	±3.5	±3.1	±2.9	±13.3	±5.4	±5.5	±5.5

Group	Isua Supracrustal Belt	Isua Supracrustal Belt	Isua Supracrustal Belt	Isua Supracrustal Belt	Isua Supracrustal Belt	Isua Supracrustal Belt	Ivisaartoq Supra-crustal Belt	Ivisaartoq Supra-crustal Belt
Subgroup	Ameralik Dyke	Ameralik Dyke	Ameralik Dyke	Ameralik Dyke	Ameralik Dyke	Ameralik Dyke		
Rock Type	amphibolite	amphibolite	amphibolite	amphibolite	amphibolite	amphibolite	amphibolite	metagabbro
Sample name	10-41	10-41	SG 03	SG 03	JEH 2007-04	JEH 2007-04	499325	499328
Longitude (N)	65° 6'36.72"	65° 4'27.72"	65°5'50.82''	65° 6'36.72"	65°5'50.82''	65° 4'27.72"	64°44'46.08"	64°44'53.94"
Latitude (W)	50° 9'57.78"	50° 9'8.40"	50°7'32.64	50° 9'57.78"	50°7'32.64	50° 9'8.40"	49°51'20.16"	49°51'50.7"
Age in Ma	3421	3421	3421	3421	3421	3421	3075	3075
Age uncertainty	34	34	34	34	34	34	15	15
Age reference	[8]	[8]	[8]	[8]	[8]	[8]	[9]	[9]
N	12	12	11	12	11	11	10	12
V [^{142}Nd]	36	31	36	31	33	31	35	31
μ^{142}Nd (8/4)	+4.2	+3.7	+3.2	+3.2	+4.5	+4.0	+5.9	+4.8
95 c.i.	±1.3	±1.9	±1.6	±2.1	±1.6	±1.6	±2.1	±0.9
μ^{143}Nd (8/4)	+893.0	+1160.5	+1273.7	+1274.3	+1410.8	+1416.2	+851.6	+813.4
95 c.i.	±2.1	±2.3	±2.3	±2.2	±1.6	±1.8	±1.1	±1.6
μ^{145}Nd (8/4)	+4.1	+3.1	+4.3	+1.3	+4.8	+2.6	+4.2	+1.6
95 c.i.	±1.2	±2.4	±2.1	±1.3	±1.8	±1.1	±2.0	±2.4
μ^{146}Nd (8/4)	+1.1	+3.0	+0.8	-0.7	+2.2	+1.4	+0.5	+1.1
95 c.i.	±1.2	±1.0	±0.9	±1.2	±1.3	±1.2	±1.2	±1.4
μ^{150}Nd (8/4)	-8.1	-4.9	-5.0	-9.0	-14.6	-10.3	-9.3	-8.0
95 c.i.	±3.1	±2.8	±2.5	±3.9	±2.3	±3.7	±3.4	±3.6
μ^{142}Nd (6/4)	+4.8	+6.7	+4.1	+2.5	+6.6	+5.5	+5.3	+5.4
95 c.i.	±1.5	±1.3	±2.1	±1.8	±1.7	±1.5	±2.3	±2.0
μ^{143}Nd (6/4)	+893.4	+1162.1	+1274.2	+1273.6	+1412.3	+1417.8	+852.0	+813.5
95 c.i.	±2.0	±2.1	±2.5	±2.0	±1.8	±1.7	±1.7	±2.0
μ^{145}Nd (6/4)	+3.6	+1.8	+4.3	+2.0	+4.0	+2.2	+3.7	+0.9
95 c.i.	±1.6	±2.4	±1.9	±1.5	±1.8	±1.2	±1.9	±2.0
μ^{148}Nd (6/4)	-2.0	-5.7	-1.4	+1.7	-4.2	-2.5	-0.9	-2.0
95 c.i.	±2.3	±2.0	±1.8	±2.5	±2.6	±2.4	±2.4	±2.8
μ^{150}Nd (6/4)	-9.3	-13.4	-7.8	-6.2	-21.8	-13.7	-10.8	-10.4
95 c.i.	±3.3	±1.9	±2.9	±3.0	±2.9	±2.5	±3.6	±3.7

Group	inner Ameralik Fjord Region	inner Ameralik Fjord Region	inner Ameralik Fjord Region	inner Ameralik Fjord Region
Subgroup			Proterozoic dyke	Proterozoic dyke
Rock Type	amphibolite	amphibolite	dyke	dyke
Sample name	496419	496437	499304	499304
Longitude (N)				
Latitude (W)				
Age in Ma	2970	2970	2000	2000
Age uncertainty	28	28	0	0
Age reference	[10]	[10]		
N	12	11	12	12
V [^{142}Nd]	23	27	30	30
μ^{142}Nd (8/4)	+3.4	+3.5	+3.8	+2.7
95 c.i.	±1.6	±2.0	±1.8	±2.2
μ^{143}Nd (8/4)	+648.0	+588.1	-324.2	-325.6
95 c.i.	±1.5	±2.0	±1.0	±2.7
μ^{145}Nd (8/4)	+0.0	+1.0	+2.4	+0.8
95 c.i.	±2.2	±2.3	±1.6	±1.7
μ^{146}Nd (8/4)	+0.6	+1.1	+1.8	+0.4
95 c.i.	±2.5	±1.7	±2.0	±1.8
μ^{150}Nd (8/4)	-10.1	-1.8	-8.5	-4.7
95 c.i.	±3.3	±2.4	±3.5	±1.7
μ^{142}Nd (6/4)	+4.0	+4.9	+5.5	+2.4
95 c.i.	±2.3	±3.8	±2.8	±3.0
μ^{143}Nd (6/4)	+648.4	+588.5	-322.9	-326.0
95 c.i.	±2.1	±2.2	±1.7	±2.3
μ^{145}Nd (6/4)	+0.0	+0.9	+0.9	+1.2
95 c.i.	±2.1	±2.6	±1.9	±2.0
μ^{148}Nd (6/4)	-0.9	-2.0	-3.3	-0.6
95 c.i.	±4.9	±3.5	±3.9	±3.6
μ^{150}Nd (6/4)	-11.9	-4.6	-13.5	-5.3
95 c.i.	±4.9	±6.2	±3.3	±4.3

Type	modern rocks	modern rocks	modern rocks	modern rocks	modern rocks	single element solutions	single element solutions	single element solutions	single element solutions	single element solutions	single element solutions
Rock Type	basalt	basalt	basalt	basalt	basalt	-	-	-	-	-	-
Sample name	IBL-2	Ei27	BHVO-2	BHVO-2	52 JG 1	La Jolla	Aldrich chemical company Nd	Aldrich chemical company Nd	Aldrich chemical company Nd	Pr-doped JNdi (1:10)	Pr-doped JNdi (33:225)
Digestion	-	-	-	-	-	-	-	-	-	-	-
N	12	13	11	11	11	11	14	11	10	14	10
V [^{142}Nd]	37	18	36	33	37	33	34	35	26	28	36
μ^{142}Nd (8/4)	+1.0	+0.9	+1.0	-0.2	-0.4	+2.6	-0.2	-3.2	-0.9	+1.3	+0.7
95 c.i.	±1.9	±2.9	±1.8	±2.1	±1.4	±2.5	±1.0	±1.5	±3.6	±2.2	±2.7
μ^{143}Nd (8/4)	+2118.6	+1372.4	+1703.2	+1704.5	+520.3	-503.7	-1175.3	-1176.5	-1174.4	+0.4	+0.3
95 c.i.	±1.7	±2.7	±1.3	±1.8	±1.5	±3.4	±1.1	±2.0	±5.5	±1.5	±1.7
μ^{145}Nd (8/4)	+1.2	-1.7	+1.4	+4.0	+1.0	-5.7	+0.4	-0.4	+2.5	-2.0	+0.1
95 c.i.	±1.0	±2.5	±1.8	±2.0	±1.4	±2.1	±1.2	±2.2	±4.7	±1.8	±1.4
μ^{146}Nd (8/4)	+0.1	-0.7	+2.1	+2.5	-0.5	-3.2	+1.2	+1.1	+1.1	-1.8	-0.4
95 c.i.	±1.7	±2.3	±1.5	±1.0	±1.3	±2.7	±0.8	±1.5	±2.6	±1.5	±2.7
μ^{150}Nd (8/4)	-4.0	-1.3	-10.0	-8.0	-5.6	+13.3	+0.7	+3.5	+2.9	+8.1	+2.9
95 c.i.	±4.0	±4.2	±2.6	±2.9	±2.0	±4.3	±2.5	±4.5	±5.9	±2.7	±3.5
μ^{142}Nd (6/4)	+0.6	+0.8	+2.4	+3.1	-0.7	+0.4	+0.7	-1.2	-0.2	-0.7	+0.1
95 c.i.	±2.2	±3.3	±2.2	±2.1	±1.6	±2.1	±1.4	±2.3	±3.6	±2.7	±1.1
μ^{143}Nd (6/4)	+2118.6	+1372.4	+1704.7	+1705.6	+519.9	-505.4	-1174.8	-1176.2	-1174.0	-0.8	+0.0
95 c.i.	±1.4	±2.9	±1.4	±1.6	±1.8	±4.2	±1.3	±1.2	±5.7	±2.0	±1.9
μ^{145}Nd (6/4)	+1.3	-0.7	+0.4	+2.4	+1.4	-4.0	+0.1	-1.1	+2.1	-0.8	+0.8
95 c.i.	±1.1	±2.5	±1.3	±2.1	±1.4	±1.5	±1.2	±2.3	±5.3	±1.7	±2.3
μ^{148}Nd (6/4)	+0.1	+1.5	-4.0	-4.8	+1.3	+6.6	-2.2	-2.1	-2.1	+3.5	+0.7
95 c.i.	±3.3	±4.5	±2.9	±2.0	±2.5	±5.3	±1.6	±3.0	±5.2	±3.0	±5.4
μ^{150}Nd (6/4)	-2.5	+3.1	-14.7	-15.7	-2.5	+21.2	-2.1	-2.1	+0.3	+13.6	+6.3
95 c.i.	±4.6	±6.7	±4.1	±2.7	±4.8	±6.0	±3.4	±6.3	±7.9	±4.5	±5.9

Type	single element solutions	single element solutions	single element solutions	modern rocks	modern rocks	modern rocks	modern rocks	modern rocks	modern rocks	modern rocks	modern rocks
Rock Type	-	-	-	basalt	basalt	basalt	basalt	basalt	basalt	basalt	basalt
Sample name	Pr-doped JNdi (33:225)	Pr-doped JNdi (33:225)	Pr-doped JNdi (75:500)	11=23 LP-1	10-23 LP-1	35 LP-1	47 LP-1	47 LP-1	47 LP-1	47 LP-1	11 60 LP-1
Digestion				#1	#1	#2	#3	#3	#3	#3	#4
N	11	10	11	13	13	12	12	9	7	11	9
V [^{142}Nd]	20	25	30	37	36	31	29	20	24	26	40
μ^{142}Nd (8/4)	+1.8	-0.9	+1.4	+1.4	+1.4	-0.3	-0.6	-0.3	+0.4	+0.2	+1.1
95 c.i.	±3.6	±3.6	±3.0	±1.8	±1.2	±1.6	±1.8	±4.1	±4.4	±1.8	±2.1
μ^{143}Nd (8/4)	+1.6	-1174.4	+3.7	+1539.3	+1538.2	+1535.8	+1536.2	+1537.1	+1534.2	+1532.3	+1541.0
95 c.i.	±4.5	±5.5	±5.1	±1.6	±1.7	±2.7	±1.7	±3.2	±4.0	±2.5	±1.4
μ^{145}Nd (8/4)	-1.6	+2.5	+0.9	+0.7	+1.8	+0.7	-1.8	+0.4	+1.8	+0.2	+4.1
95 c.i.	±2.7	±4.7	±3.2	±1.2	±1.1	±2.5	±1.6	±2.7	±3.9	±2.1	±1.9
μ^{146}Nd (8/4)	-0.2	+1.1	+1.4	-0.3	+1.5	+1.5	-1.3	+1.4	-0.8	+0.5	+1.3
95 c.i.	±2.2	±2.6	±2.1	±1.4	±1.7	±1.1	±1.4	±1.7	±3.4	±1.6	±1.4
μ^{150}Nd (8/4)	-3.7	+2.9	+1.5	-7.3	-2.8	+1.2	+0.8	+0.3	-2.6	+3.0	-13.2
95 c.i.	±4.7	±5.9	±4.7	±3.7	±2.7	±3.4	±3.4	±7.9	±5.6	±4.7	±1.6
μ^{142}Nd (6/4)	+0.6	-0.2	+1.6	+2.0	+3.5	+1.4	-0.6	+0.3	+0.1	+1.7	+2.2
95 c.i.	±5.1	±3.6	±3.9	±2.5	±2.8	±2.1	±2.7	±5.0	±6.5	±2.6	±2.0
μ^{143}Nd (6/4)	+0.7	-1174.0	+2.5	+1539.2	+1538.4	+1536.7	+1536.1	+1537.4	+1534.0	+1533.1	+1541.5
95 c.i.	±5.4	±5.7	±4.3	±1.9	±2.2	±2.8	±2.2	±3.8	±5.2	±2.6	±1.8
μ^{145}Nd (6/4)	-1.5	+2.1	+0.8	+0.2	+1.4	+0.6	-1.5	+0.6	+2.2	-0.3	+3.1
95 c.i.	±2.8	±5.3	±3.2	±1.5	±1.1	±2.3	±2.1	±3.2	±3.0	±1.9	±2.4
μ^{148}Nd (6/4)	+0.4	-2.1	-2.8	+0.8	-2.7	-2.8	+2.7	-2.6	+1.7	-0.8	-2.3
95 c.i.	±4.4	±5.2	±4.3	±2.8	±3.3	±2.2	±2.9	±3.3	±6.8	±3.2	±2.8
μ^{150}Nd (6/4)	-0.2	+0.3	-0.4	-7.4	-4.3	-2.1	+0.9	+0.6	+0.8	+1.6	-15.8
95 c.i.	±7.4	±7.9	±5.7	±5.4	±5.8	±2.9	±4.5	±4.9	±8.8	±5.3	±4.6

Type	modern rocks	modern rocks	modern rocks	modern rocks	modern rocks	modern rocks	modern rocks	modern rocks	modern rocks	modern rocks	modern rocks	modern rocks
Rock Type	basalt	basalt	basalt	basalt	basalt	basalt	basalt	basalt	basalt	basalt	basalt	basalt
Sample name	60 LP-1	60 LP-1	71 LP-1	71 LP-1	83 LP-1	83 LP-1	83 LP-1	83 LP-1	83 LP-1	95 LP-1	95 LP-1	95 LP-1
Digestion	#4	#4	#5	#5	#6	#6	#6	#6	#6	#7	#7	#7
N	11	12	12	8	12	11	12	12	5	10	11	12
V [^{142}Nd]	28	29	38	32	39	37	38	38	37	34	36	31
μ^{142}Nd (8/4)	+0.1	-0.4	+0.2	+1.0	+0.2	+0.1	+0.3	+1.1	+0.1	-0.2	-0.2	+0.4
95 c.i.	±2.3	±2.3	±2.0	±3.5	±4.2	±1.8	±2.1	±3.9	±2.6	±1.5	±2.4	±2.4
μ^{143}Nd (8/4)	+1536.7	+1537.0	+1539.2	+1541.3	+1527.7	+1533.0	+1532.1	+1533.8	+1536.9	+1537.1	+1534.8	+1525.8
95 c.i.	±2.4	±1.6	±1.7	±5.8	±8.5	±4.8	±4.8	±11.7	±3.7	±2.8	±2.5	±5.2
μ^{145}Nd (8/4)	+2.2	+2.2	+0.2	+1.1	-1.7	+0.8	-0.9	-1.0	-0.1	+2.5	+2.5	-2.8
95 c.i.	±1.8	±2.0	±1.2	±3.5	±5.2	±3.5	±2.5	±6.0	±2.4	±1.7	±1.9	±3.5
μ^{146}Nd (8/4)	+0.4	+2.2	+1.3	+1.4	-0.6	+1.0	-1.5	-1.9	-0.4	+1.8	+1.6	-0.4
95 c.i.	±1.6	±1.3	±1.4	±2.6	±1.8	±1.9	±1.8	±1.3	±1.8	±1.4	±1.5	±1.0
μ^{150}Nd (8/4)	-13.4	-8.1	-5.8	-6.9	-4.9	-4.2	-5.9	-10.7	-8.2	-10.1	-11.3	-4.7
95 c.i.	±3.4	±3.1	±2.6	±4.5	±5.6	±4.1	±4.2	±6.1	±6.1	±2.6	±3.3	±4.2
μ^{142}Nd (6/4)	+0.7	+2.3	+1.6	+2.6	+0.0	+1.3	-0.6	-0.5	+0.1	+0.6	+1.3	-0.3
95 c.i.	±3.5	±2.2	±2.6	±4.4	±3.7	±2.3	±2.8	±6.5	±3.4	±2.5	±2.5	±3.4
μ^{143}Nd (6/4)	+1537.4	+1537.8	+1539.6	+1542.3	+1527.8	+1533.2	+1532.9	+1533.3	+1537.0	+1538.2	+1536.1	+1525.2
95 c.i.	±2.1	±1.9	±1.9	±6.4	±7.8	±5.4	±6.8	±13.0	±4.6	±2.8	±2.7	±5.5
μ^{145}Nd (6/4)	+1.5	+1.1	+0.2	+0.6	-1.7	+0.3	-0.5	-2.5	+0.5	+1.9	+2.2	-4.0
95 c.i.	±1.6	±1.8	±1.9	±3.8	±4.8	±2.9	±2.1	±6.9	±2.1	±1.3	±1.9	±3.0
μ^{148}Nd (6/4)	-0.6	-2.8	-2.4	-2.6	+1.5	-1.8	+3.2	+3.9	+1.1	-3.3	-2.9	+1.0
95 c.i.	±3.1	±2.3	±2.7	±5.2	±3.6	±3.8	±3.7	±2.7	±3.5	±2.8	±3.0	±2.0
μ^{150}Nd (6/4)	-14.9	-14.4	-8.8	-10.3	-4.1	-7.2	-3.4	-6.6	-8.4	-12.9	-15.3	-5.3
95 c.i.	±4.4	±4.9	±5.0	±5.7	±5.2	±5.4	±8.7	±11.2	±8.3	±4.0	±3.2	±4.7

Type	modern rocks	modern rocks	modern rocks	doped reference materials	doped reference materials	doped reference materials	doped reference materials	doped reference materials
Rock Type	basalt	basalt	basalt	-	-	-	-	-
Sample name	95 LP-1	95 LP-1	95 LP-1	BHVO-2+ 10-38 mix	BHVO-2+ 10-38 mix	BHVO-2+ 10-38 mix	400ppb JNdi+ 0.02ppb Sm	400ppb JNdi+ 0.02ppb Ce
Digestion	#7	#7	#7					
N	12	12	10	12	11	11	12	12
V [^{142}Nd]	37	33	35	33	31	32	12	12
μ^{142}Nd (8/4)	+0.9	+1.8	+1.3	+8.0	+5.5	+1.6	-0.4	+0.4
95 c.i.	±2.4	±1.8	±4.6	±1.7	±1.8	±1.9	±3.4	±2.2
μ^{143}Nd (8/4)	+1531.1	+1533.0	+1536.5	-558.0	+182.7	+940.2	+0.4	-0.3
95 c.i.	±3.1	±3.3	±3.4	±2.7	±2.0	±2.2	±2.9	±2.9
μ^{145}Nd (8/4)	-1.3	-0.7	+1.4	+0.7	+1.7	+1.4	-3.3	+1.4
95 c.i.	±2.9	±2.3	±1.8	±1.6	±1.7	±2.6	±2.3	±2.5
μ^{146}Nd (8/4)	-0.4	-0.9	+0.3	+0.2	+0.4	+0.3	-2.7	-0.8
95 c.i.	±1.5	±1.4	±1.6	±1.6	±1.5	±1.6	±3.1	±4.0
μ^{150}Nd (8/4)	-5.6	-8.8	-6.1	-4.8	-7.3	-8.4	+5.5	+1.0
95 c.i.	±3.5	±3.4	±6.6	±3.3	±2.9	±4.1	±8.5	±6.0
μ^{142}Nd (6/4)	+1.5	+1.1	+1.5	+7.6	+5.9	+1.9	-3.2	+0.3
95 c.i.	±1.6	±2.0	±3.9	±1.9	±1.9	±3.6	±3.6	±3.8
μ^{143}Nd (6/4)	+1530.7	+1532.2	+1536.8	-557.3	+182.5	+940.4	+0.3	-0.3
95 c.i.	±3.3	±3.1	±4.1	±2.6	±1.6	±2.1	±2.7	±3.5
μ^{145}Nd (6/4)	-1.8	-0.1	+1.4	+0.2	+1.5	+1.0	-2.1	+1.4
95 c.i.	±2.7	±2.2	±2.0	±1.7	±1.9	±2.7	±2.3	±2.3
μ^{148}Nd (6/4)	+1.0	+2.0	-0.3	+0.2	-0.6	-0.4	+1.7	+1.6
95 c.i.	±2.9	±2.8	±3.1	±3.1	±3.0	±3.2	±5.7	±7.9
μ^{150}Nd (6/4)	-4.6	-6.7	-6.7	-5.9	-9.0	-9.9	+6.2	+1.3
95 c.i.	±3.3	±3.9	±7.5	±3.5	±4.7	±3.7	±7.0	±9.6

partition coefficient	Th	Nb	Ta	La	Ce	Nd	Zr	Hf	Sm	Eu	Ti	Gd	Y	Er	Yb	Lu
Ca-Pv[1]	18	0.25	0.3	6	11	16	3	2.1	20	22	1.1	23	22	21	19	16
Mg-Pv[1]	0.006	0.25	0.36	0.007	0.015	0.023	1.7	1.8	0.07	0.1	0.9	0.17	0.49	0.55	0.8	1

In the following model, equilibrium and fractional crystallization of Mg-Ca perovskite cumulates are calculated to account for a possible source for isotope and trace element systematics of the ~3.7 to 3.8 Ga Isua rocks, assuming a primitive mantle composition (Palme and O'Neill, 2013) as starting composition, assuming a differentiation event that occurred at 4.53 Ga (Labrosse et al., 2007). It is shown that event over a wide range of crystallizing fractions of Ca-perovskite (Pv) varying between 2 to 10%, neither equilibrium crystallization nor fractional crystallization can reproduce trace element and isotope characteristics of the investigated rocks. Partition coefficients for Ca and Mg-Pv from (Corgne et al., 2005). FC refers to fractional crystallization and EC refers to equilibrium crystallization. Elemental compositions are given as ppm.

[1]Corgne et al., (2005)

2% Ca-perovskite

Fraction fractional crystallization	Th	Nb	Ta	La	Ce	Nd	Zr	Hf	Sm	Eu	Ti	Gd	Y	Er	Yb	Lu
0.05	0.032	0.155	0.016	0.091	0.43	0.48	17.1	0.522	0.209	0.092	4359	0.374	3.816	0.450	0.551	0.091
0.1	0.033	0.161	0.017	0.095	0.45	0.49	16.5	0.500	0.215	0.094	4382	0.382	3.833	0.451	0.546	0.089
0.2	0.036	0.176	0.018	0.105	0.49	0.53	15.1	0.455	0.229	0.099	4431	0.399	3.869	0.453	0.536	0.086
0.3	0.039	0.194	0.019	0.118	0.54	0.58	13.7	0.408	0.246	0.106	4489	0.419	3.910	0.456	0.524	0.083
0.4	0.043	0.218	0.021	0.135	0.61	0.64	12.3	0.361	0.267	0.113	4555	0.444	3.959	0.459	0.511	0.079
0.5	0.048	0.250	0.024	0.159	0.70	0.72	10.7	0.311	0.294	0.123	4636	0.475	4.017	0.462	0.496	0.075
0.6	0.056	0.296	0.028	0.193	0.83	0.84	9.14	0.260	0.331	0.137	4736	0.517	4.089	0.466	0.478	0.070

4% Ca-perovskite

Fraction fractional crystallization	Th	Nb	Ta	La	Ce	Nd	Zr	Hf	Sm	Eu	Ti	Gd	Y	Er	Yb	Lu
0.05	0.062	0.155	0.016	0.175	0.82	0.90	17.4	0.524	0.380	0.163	4377	0.632	5.478	0.629	0.710	0.110
0.1	0.063	0.161	0.016	0.182	0.84	0.92	16.7	0.501	0.382	0.163	4399	0.629	5.375	0.616	0.690	0.106
0.2	0.066	0.176	0.018	0.199	0.90	0.96	15.3	0.456	0.388	0.163	4447	0.623	5.158	0.590	0.648	0.099
0.3	0.068	0.194	0.019	0.221	0.97	1.00	13.8	0.409	0.395	0.164	4502	0.616	4.922	0.562	0.604	0.091
0.4	0.071	0.218	0.021	0.248	1.05	1.06	12.3	0.361	0.403	0.165	4566	0.608	4.663	0.531	0.557	0.083
0.5	0.075	0.250	0.024	0.284	1.16	1.12	10.7	0.311	0.413	0.165	4643	0.599	4.375	0.497	0.506	0.075
0.6	0.079	0.296	0.028	0.336	1.31	1.21	9.06	0.260	0.426	0.166	4740	0.588	4.046	0.457	0.450	0.065

7% Ca-perovskite

Fraction fractional crystallization	Th	Nb	Ta	La	Ce	Nd	Zr	Hf	Sm	Eu	Ti	Gd	Y	Er	Yb	Lu
0.05	0.106	0.155	0.016	0.300	1.39	1.52	17.7	0.526	0.62	0.26	4405	1.00	7.83	0.88	0.94	0.14
0.1	0.104	0.161	0.016	0.310	1.41	1.51	17.0	0.503	0.61	0.25	4425	0.95	7.42	0.84	0.88	0.13
0.2	0.101	0.176	0.018	0.331	1.44	1.48	15.5	0.457	0.57	0.24	4470	0.87	6.60	0.75	0.78	0.11
0.3	0.098	0.194	0.019	0.358	1.48	1.46	13.9	0.410	0.54	0.22	4522	0.79	5.78	0.65	0.68	0.10
0.4	0.094	0.218	0.021	0.391	1.53	1.42	12.3	0.361	0.50	0.20	4582	0.70	4.96	0.56	0.57	0.08
0.5	0.089	0.250	0.024	0.434	1.60	1.39	10.7	0.311	0.46	0.18	4655	0.61	4.13	0.47	0.47	0.07
0.6	0.084	0.296	0.028	0.493	1.68	1.34	8.94	0.259	0.42	0.15	4745	0.51	3.31	0.38	0.37	0.06

10% Ca-perovskite

Fraction fractional crystallization	Th	Nb	Ta	La	Ce	Nd	Zr	Hf	Sm	Eu	Ti	Gd	Y	Er	Yb	Lu
0.05	0.147	0.155	0.016	0.423	1.94	2.11	18.1	0.529	0.8	0.4	4432	1.3	10.0	1.1	1.2	0.2
0.1	0.141	0.161	0.016	0.432	1.93	2.04	17.3	0.505	0.8	0.3	4452	1.2	9.2	1.0	1.1	0.2
0.2	0.128	0.176	0.018	0.452	1.90	1.89	15.7	0.458	0.7	0.3	4494	1.0	7.6	0.9	0.9	0.1
0.3	0.115	0.194	0.019	0.477	1.87	1.74	14.0	0.410	0.6	0.2	4542	0.9	6.1	0.7	0.7	0.1
0.4	0.102	0.218	0.021	0.506	1.84	1.58	12.3	0.361	0.5	0.2	4598	0.7	4.7	0.5	0.5	0.1
0.5	0.088	0.250	0.024	0.544	1.80	1.41	10.6	0.310	0.4	0.2	4666	0.5	3.5	0.4	0.4	0.1
0.6	0.073	0.296	0.028	0.594	1.76	1.23	8.81	0.258	0.3	0.1	4750	0.4	2.4	0.3	0.3	0.0

2% Ca-perovskite

Fraction equilibrium crystallization	Th	Nb	Ta	La	Ce	Nd	Zr	Hf	Sm	Eu	Ti	Gd	Y	Er	Yb	Lu
0.05	0.032	0.155	0.016	0.091	0.428	0.475	17.2	0.523	0.209	0.092	4358	0.374	3.816	0.450	0.551	0.0907
0.1	0.033	0.161	0.016	0.095	0.445	0.492	16.6	0.504	0.215	0.094	4379	0.381	3.831	0.451	0.547	0.0894
0.2	0.036	0.175	0.018	0.105	0.486	0.529	15.5	0.469	0.228	0.099	4422	0.396	3.862	0.453	0.538	0.0869
0.3	0.038	0.192	0.019	0.117	0.534	0.572	14.6	0.438	0.242	0.104	4466	0.413	3.894	0.455	0.530	0.0845
0.4	0.042	0.213	0.021	0.133	0.593	0.623	13.8	0.412	0.259	0.110	4511	0.431	3.926	0.457	0.521	0.0822
0.5	0.045	0.238	0.023	0.154	0.666	0.684	13.0	0.388	0.277	0.116	4556	0.451	3.958	0.459	0.514	0.0801
0.6	0.050	0.270	0.025	0.182	0.761	0.759	12.4	0.367	0.299	0.124	4603	0.473	3.992	0.461	0.506	0.0780

4% Ca-perovskite

Fraction equilibrium crystallization	Th	Nb	Ta	La	Ce	Nd	Zr	Hf	Sm	Eu	Ti	Gd	Y	Er	Yb	Lu
0.05	0.062	0.155	0.016	0.175	0.819	0.903	17.4	0.525	0.379	0.163	4377	0.632	5.481	0.629	0.711	0.110
0.1	0.063	0.161	0.016	0.182	0.842	0.919	16.8	0.505	0.382	0.163	4397	0.629	5.388	0.618	0.693	0.107
0.2	0.065	0.175	0.018	0.198	0.894	0.952	15.7	0.470	0.387	0.163	4438	0.624	5.212	0.597	0.660	0.101
0.3	0.067	0.192	0.019	0.218	0.952	0.988	14.7	0.439	0.393	0.164	4480	0.619	5.047	0.577	0.630	0.0960
0.4	0.069	0.213	0.021	0.241	1.02	1.03	13.9	0.412	0.398	0.164	4523	0.614	4.892	0.559	0.602	0.0914
0.5	0.071	0.238	0.023	0.270	1.10	1.07	13.1	0.388	0.404	0.164	4567	0.609	4.746	0.541	0.577	0.0872
0.6	0.074	0.270	0.025	0.308	1.18	1.11	12.4	0.367	0.410	0.165	4611	0.604	4.608	0.525	0.554	0.0833

7% Ca-perovskite fraction equilibrium crystallization	Th	Nb	Ta	La	Ce	Nd	Zr	Hf	Sm	Eu	Ti	Gd	Y	Er	Yb	Lu
0.05	0.106	0.155	0.016	0.300	1.39	1.52	17.7	0.527	0.622	0.264	4404	1.00	7.85	0.885	0.940	0.138
0.1	0.105	0.161	0.016	0.309	1.40	1.51	17.1	0.507	0.609	0.256	4423	0.961	7.50	0.845	0.894	0.131
0.2	0.102	0.175	0.018	0.329	1.44	1.49	15.9	0.471	0.583	0.241	4462	0.897	6.87	0.776	0.815	0.120
0.3	0.100	0.192	0.019	0.352	1.47	1.47	14.9	0.440	0.559	0.229	4502	0.841	6.35	0.717	0.749	0.110
0.4	0.097	0.213	0.021	0.378	1.50	1.45	14.0	0.413	0.537	0.217	4542	0.792	5.89	0.666	0.693	0.102
0.5	0.095	0.238	0.023	0.409	1.54	1.43	13.2	0.389	0.517	0.207	4582	0.748	5.50	0.623	0.644	0.0952
0.6	0.093	0.270	0.025	0.444	1.58	1.41	12.5	0.368	0.498	0.197	4624	0.709	5.16	0.584	0.602	0.0891

10% Ca-perovskite Fraction equilibrium crystallization	Th	Nb	Ta	La	Ce	Nd	Zr	Hf	Sm	Eu	Ti	Gd	Y	Er	Yb	Lu
0.05	0.147	0.155	0.016	0.423	1.94	2.11	18.1	0.530	0.852	0.358	4432	1.34	10.1	1.13	1.16	0.165
0.1	0.142	0.161	0.016	0.431	1.93	2.05	17.4	0.509	0.811	0.338	4450	1.25	9.37	1.05	1.08	0.154
0.2	0.132	0.175	0.017	0.450	1.91	1.93	16.2	0.473	0.740	0.303	4486	1.11	8.21	0.922	0.945	0.136
0.3	0.123	0.192	0.019	0.470	1.89	1.83	15.1	0.442	0.680	0.275	4523	1.00	7.31	0.822	0.842	0.122
0.4	0.116	0.213	0.021	0.492	1.87	1.74	14.2	0.414	0.629	0.252	4560	0.908	6.58	0.742	0.759	0.111
0.5	0.109	0.238	0.022	0.516	1.85	1.66	13.3	0.390	0.586	0.232	4598	0.832	5.99	0.676	0.691	0.101
0.6	0.103	0.270	0.025	0.542	1.83	1.58	12.6	0.368	0.548	0.215	4637	0.767	5.50	0.621	0.634	0.0932

5% Fractional crystallization	$\varepsilon Hf_{3.8Ga}$	$\varepsilon^{143}Nd_{3.8Ga}$	$\varepsilon Ce_{3.8Ga}$	$\mu^{142}Nd$
2% Ca-Pv	-4.4	+6.6	-1.1	+84.9
4% Ca-Pv	-1.9	+5.5	-1.1	+70.0
7% Ca-Pv	+1.7	+4.8	-1.1	+62.0
10% Ca-Pv	+5.1	+4.5	-1.1	+57.7

5% Equilibrium crystallization	$\varepsilon Hf_{3.8Ga}$	$\varepsilon^{143}Nd_{3.8Ga}$	$\varepsilon Ce_{3.8Ga}$	$\mu^{142}Nd$
2% Ca-Pv	-4.4	+6.6	-1.1	+84.9
4% Ca-Pv	-1.9	+5.5	-1.1	+70.0
7% Ca-Pv	+1.7	+4.9	-1.1	+62.2
10% Ca-Pv	+5.2	+4.5	-1.1	+58.2

20% Fractional crystallization	$\varepsilon Hf_{3.8}$	$\varepsilon^{143}Nd_{3.8}$	$\varepsilon Ce_{3.8}$	$\mu^{142}Nd$
2% Ca-Pv	-3.3	+6.1	-1.1	+78.0
4% Ca-Pv	-1.3	+4.6	-1.0	+59.3
7% Ca-Pv	+1.0	+3.6	-1.0	+45.9
10% Ca-Pv	+2.8	+2.8	-0.9	+36.2

20% Equilibrium crystallization	$\varepsilon Hf_{3.8Ga}$	$\varepsilon^{143}Nd_{3.8Ga}$	$\varepsilon Ce_{3.8Ga}$	$\mu^{142}Nd$
2% Ca-Pv	-3.6	+6.1	-1.1	+77.8
4% Ca-Pv	-1.5	+4.7	-1.0	+60.1
7% Ca-Pv	+1.2	+3.8	-1.0	+49.0
10% Ca-Pv	+3.6	+3.3	-1.0	+42.5

50% Fractional crystallization	$\varepsilon Hf_{3.8Ga}$	$\varepsilon^{143}Nd_{3.8Ga}$	$\varepsilon Ce_{3.8Ga}$	$\mu^{142}Nd$
2% Ca-Pv	+0.2	+4.7	-1.0	+59.9
4% Ca-Pv	+0.3	+2.5	-0.9	+32.2
7% Ca-Pv	-0.8	+0.5	-0.7	+6.0
10% Ca-Pv	-2.4	-1.2	-0.5	-15.0

50% Equilibrium crystallization	$\varepsilon Hf_{3.8Ga}$	$\varepsilon^{143}Nd_{3.8Ga}$	$\varepsilon Ce_{3.8Ga}$	$\mu^{142}Nd$
2% Ca-Pv	-2.1	+4.6	-1.0	+59.2
4% Ca-Pv	-0.9	+3.1	-0.9	+39.2
7% Ca-Pv	+0.6	+2.1	-0.8	+27.1
10% Ca-Pv	+1.6	+1.6	-0.7	+21.0

In the following, the diminishing of $^{142}Nd/^{144}Nd$ anomalies is modelled by assuming continuous replenishment of the Isua mantle source with bulk silicate Earth material, either represented by primitive mantle (1) (Palme and O'Neill, 2013), SCHEM (2) (Caro and Bourdon, 2010) or SDEM (3) material (Chapter III). For models (1), (2) and (3), the most realistic replenishment rate amounted to 22, 30 and 26%, respectively. For trace element modelling, the composition of sample 10-27 (van de Löcht et al., 2020) was used to represent the uncontaminated Isua mantle.

SDEM replenishment rate: 0.26 / 100 Ma

	Isua	SDEM	replenished Isua mantle		
Age in Ga	$^{147}Sm/^{144}Nd$	$^{147}Sm/^{144}Nd$	$^{147}Sm/^{144}Nd$	$\mu^{142}Nd$	$\varepsilon Nd_{(3.8)}$
>3.8	0.2270	0.2045			
3.8			0.2270	+13.1	+2.6
3.7			0.2195	+8.7	+2.3
3.6			0.2148	+6.0	+2.1
3.5			0.2118	+4.2	+2.0
3.4			0.2097	+3.0	+2.0
3.3			0.2083	+2.2	+1.9
3.2			0.2072	+1.6	+1.9
3.1			0.2065	+1.2	+2.0
3.0			0.2060	+0.8	+2.0
2.9			0.2056	+0.6	+2.0
2.8			0.2053	+0.5	+2.1
2.7			0.2051	+0.3	+2.2
2.6			0.2050	+0.2	+2.3
2.5			0.2048	+0.2	+2.3
2.4			0.2048	+0.1	+2.4
2.3			0.2047	+0.1	+2.5
2.2			0.2047	+0.1	+2.6
2.1			0.2046	+0.1	+2.7
2.0			0.2046	+0.0	+2.8
1.9			0.2046	+0.0	+2.9

SCHEM

replenishment rate:		0.3 / 100 Ma			
	Isua	SCHEM	replenished Isua mantle		
Age in Ga	$^{147}Sm/^{144}Nd$	$^{147}Sm/^{144}Nd$	$^{147}Sm/^{144}Nd$	$\mu^{142}Nd$	$\varepsilon Nd_{(3.8)}$
>3.8	0.2235	0.2025			
3.8			0.2154	+13.0	+2.3
3.7			0.2025	+8.0	+2.1
3.6			0.2108	+5.2	+2.0
3.5			0.2080	+3.4	+1.9
3.4			0.2062	+2.3	+1.9
3.3			0.2050	+1.6	+1.9
3.2			0.2043	+1.1	+1.9
3.1			0.2037	+0.8	+2.0
3.0			0.2033	+0.5	+2.0
2.9			0.2031	+0.4	+2.0
2.8			0.2029	+0.3	+2.1
2.7			0.2028	+0.2	+2.2
2.6			0.2027	+0.1	+2.2
2.5			0.2026	+0.1	+2.3
2.4			0.2026	+0.1	+2.4
2.3			0.2026	+0.0	+2.5
2.2			0.2025	+0.0	+2.5
2.1			0.2025	+0.0	+3.0
2.0			0.2025	+0.0	+3.4
1.9			0.2025	+0.0	+3.8

PRIMA

Replenishment rate: 0.20 / 100 Ma

	Isua	PRIMA	Replenished Isua mantle		
Age in Ga	$^{147}Sm/^{144}Nd$	$^{147}Sm/^{144}Nd$	$^{147}Sm/^{144}Nd$	$\mu^{142}Nd$	$\varepsilon Nd_{(3.8)}$
>3.8	0.231	0.196			
3.8			0.2310	+13.2	+2.5
3.7			0.2226	+9.5	+2.1
3.6			0.2168	+7.1	+1.8
3.5			0.2126	+5.4	+1.6
3.4			0.2095	+4.2	+1.4
3.3			0.2070	+3.3	+1.2
3.2			0.2051	+2.7	+1.0
3.1			0.2036	+2.1	+0.9
3.0			0.2023	+1.7	+0.8
2.9			0.2013	+1.4	+0.7
2.8			0.2005	+1.1	+0.6
2.7			0.1998	+0.9	+0.5
2.6			0.1992	+0.8	+0.5
2.5			0.1987	+0.6	+0.4
2.4			0.1983	+0.5	+0.3
2.3			0.1980	+0.4	+0.3
2.2			0.1977	+0.4	+0.3
2.1			0.1974	+0.3	+0.2
2.0			0.1972	+0.2	+0.2
1.9			0.1971	+0.2	+0.2

Isua source replenished by	Th	Nb	Ta	La	Ce	Pr	Nd	Zr	Hf	Sm	Eu	Ti	Gd	Tb	Dy	Y	Er	Yb	Lu
SDEM[1]	0.0526	0.386	0.0279	0.499	1.37	0.214	1.10	8.48	0.250	0.371	0.144	1107	0.511	0.0955	0.652	3.75	0.428	0.442	0.0657
3.8 Ga Isua source[2]	0.0110	0.0603	0.00265	0.0961	0.256	0.0463	0.211	0.586	0.0224	0.0832	0.0352	180	0.142	0.0261	0.169	0.766	0.0980	0.102	0.0139
3.7 Ga Isua source (replenished)	0.0218	0.145	0.00922	0.201	0.546	0.0898	0.441	2.64	0.0815	0.158	0.0634	421	0.238	0.0441	0.294	1.54	0.184	0.190	0.0274
3.6 Ga Isua source (replenished)	0.0298	0.208	0.0141	0.279	0.761	0.122	0.6112	4.16	0.125	0.213	0.0842	599	0.309	0.0575	0.387	2.12	0.247	0.256	0.0373
3.5 Ga Isua source (replenished)	0.0357	0.254	0.0177	0.336	0.920	0.146	0.74	5.28	0.158	0.254	0.0997	731	0.361	0.0674	0.456	2.54	0.295	0.304	0.0447
3.4 Ga Isua source (replenished)	0.0401	0.288	0.0203	0.379	1.0379	0.163	0.830	6.11	0.182	0.284	0.111	829	0.400	0.0747	0.507	2.86	0.329	0.340	0.0502
Isua source replenished by																			
PRIMA[3]	0.0849	0.595	0.043	0.683	1.75	0.266	1.34	10.3	0.301	0.435	0.167	1280	0.586	0.108	0.724	4.13	0.468	0.477	0.0708
3.8 Ga Isua source[2]	0.0110	0.0603	0.00265	0.0961	0.256	0.0463	0.211	0.586	0.0224	0.0832	0.0352	180	0.142	0.0261	0.169	0.766	0.0980	0.102	0.0139
3.7 Ga Isua source (replenished)	0.0236	0.151	0.00951	0.196	0.510	0.0836	0.403	2.24	0.0698	0.143	0.0575	367	0.217	0.0399	0.263	1.34	0.161	0.166	0.0236
3.6 Ga Isua source (replenished)	0.0340	0.227	0.0152	0.279	0.722	0.115	0.563	3.61	0.109	0.193	0.0760	522	0.280	0.0514	0.342	1.81	0.213	0.219	0.0316
3.5 Ga Isua source (replenished)	0.0426	0.289	0.0199	0.348	0.897	0.140	0.695	4.75	0.142	0.234	0.091	651	0.332	0.0610	0.407	2.21	0.257	0.263	0.0383
3.4 Ga Isua source (replenished)	0.0498	0.341	0.0239	0.405	1.04	0.162	0.805	5.69	0.169	0.268	0.104	758	0.375	0.0689	0.461	2.53	0.293	0.299	0.0438

[1]SDEM composition from **Chapter III**.

[2]Composition of sample 10-22 from (van de Löcht et al., 2020).

[3]Primitive mantle composition from (Palme and O'Neill, 2013).

Appendix A3

sample name	15058	15065.189	15495	15545.103	15556	15495	15555
classification	low Ti basalt	low Ti basalt	low Ti basalt	low Ti basalt	low Ti basalt	low Ti basalt	low Ti basalt
rock type	basalt	coarse gabbro	porphyric basalt	basalt	basalt	porphyric basalt	basalt
Li	7.18	7.19	7.82	6.64	7.22	7.59	6.50
Sc	42.0	46.0	41.0	37.8	41	40.3	35.7
V	160	186	157	190	201	151	186
Cr	2616	4410	2678	3368	3533	2420	3307
Co	36.6	44.8	38.9	48.0	43.6	39.1	48.3
Ni	27.4	47.3	34.5	58.6	50.5	35.5	66.5
Cu	7.87	10.9	8.02	15.0	9.21	7.87	10.6
Zn	11.6	9.61	10.9	10.6	13.8	9.39	6.73
Ga	3.50	3.50	3.75	3.35	3.74	3.66	3.15
Rb	0.961[a]	1.38[a]	1.20[a]	0.870[a]	0.900[a]	1.12[a]	0.717[a]
Sr	110[a]	96.5[a]	120[a]	94.0[a]	106[a]	115[a]	91.9[a]
Y	29.0	41.0	31.4	23.3	25.6	32.1	20.3
Zr-ID	97.8[b]	139.3[b]	110.2[b]	84.57[b]	89.04[b]	110.2[b]	70.09[b]
Nb-ID	6.620[b]	139.3[b]	6.799[b]	6.150[b]	6.381[b]	6.799[b]	5.006[b]
Mo	0.118	0.0732	0.0741	0.113	0.078	0.0611	0.0782
Cd	n.d.	n.d.	n.d.	n.d.	n.d.	n.d.	n.d.
Sn	n.d.	n.d.	n.d.	n.d.	n.d.	n.d.	n.d.
Sb	n.d.	n.d.	n.d.	n.d.	n.d.	n.d.	n.d.
Cs	0.0603	0.0885	0.0692	0.0611	0.0539	0.0607	0.0547
Ba	67.7	96.2	76.2	50.5	55.4	74.6	43.6
La-ID	6.178[c]	8.812[c]	7.094[c]	4.723[c]	4.995[c]	7.227[c]	3.988[c]
Ce-ID	16.84[c]	24.18[c]	19.25[c]	12.94[c]	13.93[c]	19.55[c]	11.07[c]
Pr	2.52	3.63	2.86	1.98	2.15	2.90	1.68
Nd-ID	12.80[c]	18.53[c]	14.47[c]	10.29[c]	11.03[c]	14.72[c]	8.610[c]
Sm-ID	4.062[c]	5.880[c]	4.544[c]	3.409[c]	3.712[c]	4.618[c]	2.851[c]
Eu	1.00	1.06	1.09	0.876	0.971	1.07	0.797
Gd	4.99	7.14	5.49	4.16	4.53	5.53	3.52
Tb	0.884	1.25	0.958	0.735	0.814	0.968	0.630
Dy	5.63	7.95	6.1	4.74	5.18	6.24	4.00
Ho	1.13	1.59	1.24	0.935	1.02	1.24	0.800
Er	2.99	4.18	3.23	2.45	2.68	3.28	2.10
Tm	0.431	0.596	0.459	0.35	0.378	0.457	0.301
Yb	2.73	3.75	2.87	2.19	2.40	2.91	1.89
Lu-ID	0.3836[b]	0.5276[b]	0.417[a]	0.3049[b]	0.3255[b]	0.4086[b]	0.2668[b]
Hf-ID	2.761[b]	3.959[b]	3.071[b]	2.534[b]	2.667[b]	3.071[b]	2.087[b]
Ta-ID	0.3662[b]	0.5220[b]	0.3805[b]	0.3741[b]	0.3915[b]	0.3805[b]	0.3042[b]
W-ID	0.05918[b]	0.08946[b]	0.06917[b]	0.08102[b]	0.08821[b]	0.06917[b]	0.06328[b]
Tl	0.0351	0.0298	0.0357	0.043	0.0339	0.0219	0.0276
Pb	0.265	0.372	0.358	0.253	0.262	0.319	0.195
Th-ID	12.00[b]	9.778[b]	12.32[b]	14.19[b]	10.60[b]	8.367[b]	9.437[b]
U-ID	0.1498[b]	0.2158[b]	0.1693[b]	0.1324[b]	0.1544[b]	0.1693[b]	0.1120[b]

sample name	12004	12022	12051	12053	12054	12063	NWA 6950
classification	low Ti basalt	low Ti basalt	low Ti basalt	low Ti basalt	low Ti basalt	low Ti basalt	lunar meteorite
rock type	olivine-basalt	ilmenite-basalt	ilmenite-basalt	pigeonite-basalt	ilmenite-basalt	ilmenite-basalt	
Li	7.46	8.65	8.51	7.79	9.27	8.40	6.51
Sc	43.3	51.7	55.7	49.4	58.5	52.4	26.5
V	154	140	131	155	111	136	125
Cr	2816	2709	1887	2349	1410	2477	2415
Co	42.5	44.0	30.6	32.1	24.7	39.6	73.1
Ni	45.0	39.0	11.9	11.5	4.08	30.5	174
Cu	7.05	8.58	9.23	7.77	10.4	8.07	3.40
Zn	11.0	6.92	8.67	7.79	10.3	6.51	15.5
Ga	3.21	3.73	3.81	3.5	4.44	3.76	1.88
Rb	1.25[a]	0.899[a]	0.934[a]	1.24[a]	1.15[a]	0.840[a]	0.972[a]
Sr	107[a]	150[a]	138[a]	114[a]	171[a]	150[a]	51.9[a]
Y	38.2	51.6	46.6	40.8	62.0	48.6	22.4
Zr-ID	114.3[b]	120.8[b]	120.7[b]	122.2[b]	153.3[b]	115.4[b]	83.06[b]
Nb-ID	7.783[b]	6.676[b]	7.669[b]	8.502[b]	8.914[b]	6.616[b]	4.973[b]
Mo	0.0699	0.059	0.0790	0.0699	0.0615	0.0614	0.0789
Cd	n.d.	n.d.	n.d.	n.d.	n.d.	n.d.	n.d.
Sn	n.d.	n.d.	n.d.	n.d.	n.d.	n.d.	n.d.
Sb	n.d.	n.d.	n.d.	n.d.	n.d.	n.d.	n.d.
Cs	0.0701	0.0565	0.0591	0.0724	0.0767	0.0568	0.0554
Ba	73.7	61.7	62.4	76.3	81.9	58.5	92.9
La-ID	6.486[c]	5.679[c]	5.914[c]	6.741[c]	7.524[c]	5.402[c]	5.325[c]
Ce-ID	17.95[c]	17.25[c]	17.16[c]	18.64[c]	22.35[c]	16.31[c]	14.06[c]
Pr	2.74	2.87	2.75	2.83	3.62	2.70	2.02
Nd-ID	13.82[c]	15.89[c]	14.79[c]	14.69[c]	19.73[c]	15.02[c]	9.572[c]
Sm-ID	4.649[c]	5.957c	5.364[c]	5.000[c]	7.229[c]	5.603[c]	2.858[c]
Eu	0.983	1.36	1.22	1.04	1.57	1.33	0.256
Gd	5.96	7.84	6.93	6.24	9.36	7.27	3.45
Tb	1.10	1.47	1.31	1.16	1.76	1.39	0.627
Dy	7.29	9.87	8.84	7.81	11.9	9.31	4.12
Ho	1.50	2.03	1.83	1.60	2.44	1.93	0.877
Er	4.10	5.52	5.00	4.35	6.63	5.21	2.45
Tm	0.599	0.811	0.738	0.641	0.96	0.769	0.369
Yb	3.90	5.28	4.77	4.16	6.28	5.02	2.41
Lu-ID	0.5563[b]	0.7601[b]	0.6894[b]	0.6061[b]	0.9021[b]	0.7273[b]	0.3436[b]
Hf-ID	3.488[b]	4.290[b]	4.039[b]	3.764[b]	5.305[b]	4.101[b]	2.108[b]
Ta-ID	0.4062[b]	0.3591[b]	0.4269[b]	0.4460[b]	0.4993[b]	0.3759[b]	0.2104[b]
W-ID	0.1152[b]	0.08806[b]	0.1268[b]	0.1218[b]	0.1229[b]	0.08500[b]	0.09266[b]
Tl	0.0290	0.0353	0.0274	0.0276	0.0306	0.0274	0.0316
Pb	0.387	0.294	0.318	0.397	0.406	0.266	0.363
Th-ID	9.226[b]	9.474[b]	9.737[b]	9.861[b]	9.727[b]	9.660[b]	9.601[b]
U-ID	0.2599[b]	0.1818[b]	0.2077[b]	0.2718[b]	0.2552[b]	0.1724[b]	0.2434[b]

sample name	60025	67075	10020	79035	79135	10017.395	10020.25
classification	ferroan anorthosite	ferroan anorthosite	high Ti basalt	high Ti basalt	high Ti basalt	high Ti basalt	high Ti basalt
rock type	anorthosite	anorthosite	olivine basalt	soil-breccia	breccia-regolith	vesicular basalt	olivine basalt
Li	1.44	2.56	8.95	9.48	10.6	17.2	8.79
Sc	0.631	8.65	88.9	52.0	43.6	81.0	79.7
V	5.87	18.7	86.3	89.2	86.1	64.0	91.8
Cr	29.3	314	2641	2788	2766	2163	2181
Co	1.36	6.76	19.4	36.3	39.5	25.2	17.1
Ni	1.84	5.11	3.02	198	163	5.70	2.71
Cu	1.93	0.671	11.9	23.8	29.3	11.3	10.2
Zn	1.95	6.21	27.9	60.4	106	28.4	11.7
Ga	3.69	2.92	4.09	6.16	9.23	5.70	3.73
Rb	0.0883[a]	0.539[a]	0.776[a]	1.83[a]	2.15[a]	5.98[a]	0.913[a]
Sr	218[a]	155[a]	148[a]	171[a]	188[a]	174[a]	141[a]
Y	0.297	2.27	85.0	61.3	59.4	173	78.2
Zr-ID	0.1411[b]	3.927[b]	201.0[b]	181.9[b]	189.7[b]	490.9[b]	204.3[b]
Nb-ID	0.02957[b]	0.2552[b]	17.46[b]	15.81[b]	14.98[b]	30.42[b]	19.91[b]
Mo	0.0387	0.0438	0.0586	0.0851	0.0736	0.130	0.0858
Cd	0.0454	0.0312	0.309	0.301	0.388	n.d.	n.d.
Sn	0.0513	0.0661	0.0811	0.172	0.0959	n.d.	n.d.
Sb	0.0145	0.0155	0.0474	0.0447	0.0587	n.d.	n.d.
Cs	0.0043	0.0383	0.043	0.0896	0.109	0.194	0.0522
Ba	12.8	8.79	68.9	108	128	302	69.2
La-ID	0.4230[c]	0.3526[c]	7.238[c]	8.324[c]	9.946[c]	25.70[c]	7.581[c]
Ce-ID	0.8927[c]	0.8781[c]	22.52[c]	23.75[c]	27.67[c]	74.05[c]	24.08[c]
Pr	0.114	0.133	3.89	3.75	4.16	11.6	3.91
Nd-ID	0.4594[c]	0.6044[c]	22.43[c]	19.66[c]	21.06[c]	60.71[c]	23.08[c]
Sm-ID	0.09895[c]	0.1946[c]	8.716[c]	7.010[c]	7.169[c]	21.27[c]	8.931[c]
Eu	1.01	0.676	1.50	1.53	1.62	2.24	1.55
Gd	0.0953	0.278	11.6	8.77	8.87	26.1	11.6
Tb	0.0131	0.0533	2.17	1.62	1.62	4.85	2.18
Dy	0.0663	0.360	14.7	10.8	10.6	32.4	14.8
Ho	0.0123	0.0807	3.07	2.22	2.17	6.71	3.08
Er	0.0319	0.238	8.48	6.09	5.85	18.5	8.49
Tm	0.00481	0.0373	1.24	0.894	0.854	2.69	1.25
Yb	0.0353	0.269	8.15	5.79	5.59	17.4	8.21
Lu-ID	0.00316[b]	0.03603[b]	1.221[b]	0.8558[b]	0.7962[b]	2.483[b]	1.235[b]
Hf-ID	0.003707[b]	0.1185[b]	7.188[b]	5.884[b]	5.885[b]	16.34[b]	7.310[b]
Ta-ID	0.001284[b]	0.01254[b]	1.101[b]	0.9609[b]	0.9009[b]	1.815[b]	1.127[b]
W-ID	0.00204[b]	0.01173[b]	0.1145[b]	0.1648[b]	0.1887[b]	0.3824[b]	0.3313[b]
Tl	0.0135	0.00569	0.0177	0.0195	0.0248	0.0563	0.0395
Pb	0.170	0.274	0.619	1.93	2.48	1.31	0.324
Th-ID	0.1445[b]	0.9187[b]	1.048[b]	1.031[b]	1.027[b]	13.81[b]	12.00[b]
U-ID	0.00016[b]	0.00872[b]	0.1743[b]	0.3152[b]	0.3676[b]	0.8581[b]	0.1805[b]

sample name	10057.279	74255	74275	75035.24	14163	14305	14310
classification	high Ti basalt	high Ti basalt	high Ti basalt	high Ti basalt	KREEP basalt	KREEP basalt	KREEP basalt
rock type	vesicular basalt	ilmenite-basalt	ilmenite-basalt	ilmenite-basalt	KREEP soil	crystalline breccia	feldspathic basalt
Li	16.7	8.16	8.26	11.0	33.7	33.3	26.8
Sc	77.6	70.3	73.3	73.4	25.8	19.4	20.2
V	61.0	119	123	25.1	51.0	37.2	36.8
Cr	2065	3469	3566	1200	1491	1137	1112
Co	24.8	23.1	20.3	14.1	37.2	33.5	27.5
Ni	6.25	6.96	4.78	0.982	367	327	251
Cu	12.6	10.8	10.6	8.72	14.0	5.44	5.32
Zn	23.4	10.7	14.4	14.6	50.3	12.3	28.1
Ga	5.56	3.50	3.55	5.00	11.1	9.07	5.89
Rb	5.8[a]	1.34[a]	1.32[a]	1.04[a]	17.3[a]	8.60[a]	13.1[a]
Sr	171[a]	160[a]	160[a]	231[a]	221[a]	214[a]	201[a]
Y	168	80.9	84.2	129	254	292	193
Zr-ID	489.8[b]	221.0[b]	233.1[b]	321.8[b]	931.1[b]	1163.2[b]	817.3[b]
Nb-ID	30.7[b]	25.93[b]	28.63[b]	32.9[b]	63.73[b]	73.56[b]	51.37[b]
Mo	0.0745	0.115	0.0699	0.0606	0.272	0.105	0.116
Cd	n.d.	n.d.	n.d.	n.d.	0.998	0.962	0.722
Sn	n.d.	n.d.	n.d.	n.d.	0.117	0.173	0.0768
Sb	n.d.	n.d.	n.d.	n.d.	0.0533	0.0537	0.0481
Cs	0.187	0.072	0.0692	0.0525	0.805	0.390	0.570
Ba	296	71.6	73.1	119	978	970	695
La-ID	25.45[c]	5.937[c]	6.234[c]	8.869[c]	70.08[c]	88.59[c]	57.47[c]
Ce-ID	73.42[c]	20.81[c]	21.70[c]	30.94[c]	178.4[c]	228.9[c]	148.2[c]
Pr	11.6	3.86	4.02	5.81	25.8	30.8	19.9
Nd-ID	60.72[c]	23.17[c]	24.17[c]	35.10[c]	108.0[c]	140.0[c]	89.66[c]
Sm-ID	20.83[c]	9.445[c]	9.877[c]	14.50[c]	30.67[c]	38.8[c]	25.29[c]
Eu	2.22	1.84	1.87	2.76	2.96	3.12	2.22
Gd	26.1	12.6	13.2	19.4	36.2	42.8	27.8
Tb	4.82	2.35	2.47	3.69	6.48	7.59	4.98
Dy	32.4	15.9	16.6	24.9	42.2	49.1	32.4
Ho	6.70	3.23	3.39	5.13	8.72	10.1	6.68
Er	18.4	8.75	9.16	13.9	24.3	28.0	18.6
Tm	2.67	1.27	1.33	2.02	3.57	4.10	2.76
Yb	17.4	8.28	8.7	13.3	23.3	26.6	18.0
Lu-ID	2.487[b]	1.191[b]	1.246[b]	1.932[b]	3.125[b]	3.947[b]	2.582[b]
Hf-ID	16.23[b]	8.209[b]	8.675[b]	11.6[b]	23.2[b]	28.35[b]	20.10[b]
Ta-ID	1.815[b]	1.433[b]	1.496[b]	1.935[b]	2.889[b]	3.261[b]	2.305[b]
W-ID	0.3860[b]	0.06358[b]	0.05902[b]	0.09065b	1.493[b]	1.279[b]	1.212[b]
Tl	0.0392	0.0355	0.0343	0.0312	0.0463	0.0234	0.0299
Pb	1.36	0.269	0.248	0.334	12.0	9.30	6.66
Th-ID	11.27[b]	11.70[b]	10.69[b]	9.773[b]	0.9636[b]	1.045[b]	1.031[b]
U-ID	0.8557[b]	0.1317[b]	0.1382[b]	0.1628[b]	3.500[b]	4.328[b]	2.983[b]

sample name	65015	72275	73275	68115
classification	KREEP basalt	KREEP basalt	KREEP basalt	KREEP basalt
rock type	impact breccia	polymict Breccia	Impact melt breccia	polymict breccia
Li	19.2	15.4	17.7	10.7
Sc	15.1	48.6	19.0	10.9
V	39.1	131	47.0	29.5
Cr	1197	2994	1486	987
Co	190	33.9	34.2	56.9
Ni	3099	56.6	305	907
Cu	17.5	16.7	4.49	15.7
Zn	11.1	12.7	21.3	32.9
Ga	6.08	5.31	5.72	4.91
Rb	7.80[a]	14.1[a]	5.92[a]	5.19[a]
Sr	168[a]	113[a]	179[a]	157[a]
Y	152	152	113	84.7
Zr-ID	639.7[b]	658.1[b]	486.2[b]	359.8[b]
Nb-ID	36.6[b]	31.02[b]	29.45[b]	23.79[b]
Mo	0.572	0.072	0.122	0.264
Cd	0.566	0.548	0.46	n.d.
Sn	0.129	0.0948	0.142	n.d.
Sb	0.0809	0.0536	0.0577	n.d.
Cs	0.418	0.701	0.217	0.255
Ba	512	415	368	275
La-ID	45.59[c]	48.37[c]	31.81[c]	26.71[c]
Ce-ID	117.4[c]	127[c]	82.24[c]	69.49[c]
Pr	15.9	17.3	11.3	9.6
Nd-ID	72.42[c]	81.06[c]	51.50[c]	44.76[c]
Sm-ID	20.64[c]	22.4[c]	14.66[c]	12.50[c]
Eu	1.92	1.64	1.93	1.50
Gd	22.3	24.8	16.7	14.0
Tb	3.96	4.20	2.95	2.47
Dy	25.7	26.3	19.2	15.8
Ho	5.29	5.3	3.98	3.25
Er	14.7	14.3	11.0	8.92
Tm	2.16	2.01	1.61	1.3
Yb	14.0	12.7	10.4	8.42
Lu-ID	2.021[b]	1.808[b]	1.507[b]	1.202[b]
Hf-ID	15.51[b]	15.90[b]	12.17[b]	8.916[b]
Ta-ID	1.599[b]	1.402[b]	1.431[b]	0.9736[b]
W-ID	3.374[b]	0.9238[b]	0.5496[b]	0.5493[b]
Tl	0.0189	0.0196	0.0195	0.0494
Pb	3.83	3.33	3.42	1.88
Th-ID	1.033[b]	1.030[b]	1.031[b]	9.594[b]
U-ID	1.897[b]	1.513[b]	1.389[b]	1.169[b]

[a]trace element data with uncorrected residual spike that might be slightly too high.
[b]isotope dilution data from Thiemens et al., (2019).
[c]isotope dilution data from this study, Chapter III.

Sample name	15058	15065.189	15495	15545.103	15556	15495
Classification	low Ti basalts	low Ti basalts	low Ti basalts	low Ti basalts	low Ti basalts	low Ti basalts
Rock type	basalt	coarse gabbro	porphyric basalt	basalt	basalt	porphyric basalt
Age [Ma]	3460	3272	3312	3370	3400	3312
Error [Ma]	40	40	60	150	100	60
Reference	[1]	[2]	[2]	[2]	[3]	[2]
$^{138}La/^{136}Ce$	0.1781	0.1770	0.1790	0.1773	0.1741	0.1795
$^{138}Ce/^{136}Ce^{*}$	1.336766	1.336783	1.336770	1.336731	1.336725	1.336788
$^{138}Ce/^{136}Ce^{*}$	1.336788	1.336808			1.336775	
$^{138}Ce/^{136}Ce^{*}$	1.336768					
$^{138}Ce/^{136}Ce$ (mean*)	1.336774	1.336796	1.336770	1.336731	1.336750	1.336788
Measurement numbers	3	2	1	1	2	1
2.S.E. (mean 6th digit)	18	19	50	23	15	16
Neutron capture effect [ε-deviation]	0.005[20]	n.d.	0.014[20]	n.d.	0.031[20]	n.d.
εCe(t) (NC corrected)	-0.29	-0.09	-0.34	-0.57	-0.27	-0.29
Err. εCe	±0.21	±0.21	±0.21	±0.21	±0.21	±0.21
$^{147}Sm/^{144}Nd^{*}$	0.1919	0.1918	0.1898	0.2002	0.2035	0.1897
$^{143}Nd/^{144}Nd^{*}$	0.512542	0.512512	0.512447	0.512826	0.512808	0.512447
2 S.E. (6th digit)ppm	±8	±10	±9	±9	±9	±11
Neutron capture effect [ε-deviation]	-0.11[20]	n.d.	-0.30[20]	n.d.	-0.65[20]	n.d.
εNd(t) (NC corrected)	+0.3	-0.6	-0.6	+2.0	+0.8	-0.9
±2σ[a]	±0.4	±0.5	±0.4	±0.5	±0.4	±0.5

Sample name	15555	12004	12022	12051	12053	12054
Classification	low Ti basalts	low Ti basalts	low Ti basalts	low Ti basalts	low Ti basalts	low Ti basalts
Rock type	basalt	olivine-basalt	ilmenite-basalt	ilmenite-basalt	pigeonite-basalt	ilmenite-basalt
Age [Ma]	3312	3282	3180	3252	3170	3210
Error [Ma]	60	70	40	100	60	150
Reference	[4]	[5]	[6]	[6]	[7]	estimated from other Apollo 12 low Ti basalts
$^{138}La/^{136}Ce$	0.1749	0.1755	0.1599	0.1673	0.1757	0.1635
$^{138}Ce/^{136}Ce^{*}$	1.336743	1.336718	1.336573	1.336686	1.336715	1.336641
$^{138}Ce/^{136}Ce^{*}$	1.336746	1.336756	1.336579	1.336702	1.336749	1.336618
$^{138}Ce/^{136}Ce$ (mean*)	1.336745	1.336737	1.336576	1.336694	1.336732	1.33663
Measurement numbers	2	2	2	2	2	2
2.S.E. (mean 6th digit)	17	18	19	86	28	17
Neutron capture effect [ε-deviation]	0.002[20]	0.000[20]	n.d.	n.d.	n.d.	n.d.
εCe(t) (NC corrected)	-0.35	-0.44	-0.78	-0.30	-0.52	-0.58
Err. εCe	±0.21	±0.21	±0.21	±0.64	±0.21	±0.22
$^{147}Sm/^{144}Nd^{*}$	0.2002	0.2034	0.2268	0.2194	0.2059	0.2215
$^{143}Nd/^{144}Nd^{*}$	0.512822	0.513021	0.513834	0.513568	0.513067	0.513664
2 S.E. (6th digit)ppm	±8	±8	±9	±9	±8	±10
Neutron capture effect [ε-deviation]	-0.04[20]	-0.01[20]	-0.20[26]	-0.20[26]	n.d.	n.d.
εNd(t) (NC corrected)	+2.0	+4.6	+11.2	+8.8	+4.5	+9.7
±2σ[a]	±0.4	±0.4	±0.4	±0.5	±0.6	±0.8

Sample name	12063	NWA 6950	60025	67075	10020	79035
Classification	low Ti basalts	lunar meteorite	ferroan anorthosite	ferroan anorthosite	high Ti basalts	high Ti basalts
Rock type	ilmenite-basalt	0	anorthosite	anorthosite	olivine basalt	soil-breccia
Age [Ma]	3193	3103	4360	4040	3720	-
Error [Ma]	11	39	3	50	150	-
Reference	[8]	[9]	[10]	[11]	estimated from other high Ti basalts	-
$^{138}La/^{136}Ce$	0.1608	0.1839	0.2149	0.1950	0.1560	0.1702
$^{138}Ce/^{136}Ce^{*}$	1.336615	1.336842	1.337196	1.336947	1.336515	1.336717
$^{138}Ce/^{136}Ce^{*}$	1.336589	1.336831			1.336524	1.336708

$^{138}Ce/^{136}Ce$ (mean*)	1.336602	1.336837	1.337197	1.336948	1.336519	1.336712
Measurement numbers	2	2	1	1	2	2
2.S.E. (mean 6th digit)	17	25	100	57	19	18
Neutron capture effect [ε-deviation]	n.d.	n.d.	0.000[21]	n.d.	n.d.	n.d.
εCe(t) (NC corrected)	-0.64	-0.20	+0.18	-0.09	-0.68	n.d.
Err. εCe	±0.21	±0.21	±0.75	±0.43	±0.23	n.d.
$^{147}Sm/^{144}Nd^*$	0.2255	0.1805	0.1302	0.1947	0.2350	0.2155
$^{143}Nd/^{144}Nd^*$	0.513808	0.512103	0.510685	0.512622	0.513816	0.513214
2 S.E. (6th digit)ppm	±10	±9	±39	±15	±10	±11
Neutron capture effect [ε-deviation]	n.d.	n.d.	0.00[21]	n.d.	n.d.	n.d.
εNd(t) (NC corrected)	+10.9	-4.1	-0.8	+0.5	+4.5	n.d.
±2σ[a]	±0.6	±0.6	±0.8	±0.6	±1.0	n.d.

Sample name	79135	10017.395	10020.25	10057.279	74255	74275
Classification	high Ti basalts	high Ti basalts	high Ti basalts	high Ti basalts	high Ti basalts	high Ti basalts
Rock type	breccia-regolith	vesicular basalt	olivine basalt	vesicular basalt	ilmenite-basalt	ilmenite-basalt
Age [Ma]	-	3554	3720	3622	3830	3830
Error [Ma]	-	50	150	20	60	60
Reference	-	[5]	estimated from other high Ti basalts	[12]	[13]	[13]
$^{138}La/^{136}Ce$	0.1745	0.1685	0.1529	0.1683	0.1385	0.1395
$^{138}Ce/^{136}Ce^*$	1.33678	1.336651	1.33651	1.336674	1.336347	1.336368
$^{138}Ce/^{136}Ce^*$	1.336798	1.336702	1.336523	1.336663		
$^{138}Ce/^{136}Ce^*$	1.336786	1.336672		1.336627		
$^{138}Ce/^{136}Ce^*$		1.336703		1.336632		
$^{138}Ce/^{136}Ce^*$		1.33669		1.336671		
$^{138}Ce/^{136}Ce^*$		1.336654		1.336619		
$^{138}Ce/^{136}Ce^*$		1.336631		1.336583		
$^{138}Ce/^{136}Ce^*$		1.336607				
$^{138}Ce/^{136}Ce^*$		1.336647				
$^{138}Ce/^{136}Ce$ (mean*)	1.336788	1.336662	1.336516	1.336633	1.336347	1.336368
Measurement numbers	3	9	2	8	1	1
2.S.E. (mean 6th digit)	20	14	14	18	17	13
Neutron capture effect [ε-deviation]	n.d.	n.d.	n.d.	0.002[20]	0.000[20]	0.001[20]
εCe(t) (NC corrected)	n.d.	-0.50	-0.41	-0.68	-0.72	-0.62
Err. εCe	n.d.	±0.20	±0.23	±0.21	±0.22	±0.22
$^{147}Sm/^{144}Nd^*$	0.2058	0.2119	0.2340	0.2074	0.2466	0.2471
$^{143}Nd/^{144}Nd^*$	0.51294	0.513041	0.513796	0.513057	0.514246	0.514246
2 S.E. (6th digit)ppm	±10	±10	±10	±8	±10	±7
Neutron capture effect [ε-deviation]	n.d.	-0.40[22]	n.d.	-0.03[20]	0.00[20]	-0.02[20]
εNd(t) (NC corrected)	n.d.	+1.2	+3.9	+3.1	+6.6	+6.3
±2σ[a]	n.d.	±0.4	±1.0	±0.4	±0.8	±0.6
Sample name	75035.24	14163	14305	14310	65015	72275
Classification	high Ti basalts	KREEP basalts	KREEP basalts	KREEP basalts	KREEP basalts	KREEP basalts
Rock type	ilmenite-basalt	KREEP soil	crystalline breccia	feldspathic basalt	impact breccia	polymict Breccia
Age [Ma]	3760	-	3946	3897	3920	3990
Error [Ma]	50	-	50	60	40	30
Reference	[14]	-	[15]	[16]	[17]	[18]
$^{138}La/^{136}Ce$	0.1392	0.1908	0.1879	0.1883	0.1885	0.1850
$^{138}Ce/^{136}Ce^*$	1.336374	1.336939	1.336871	1.336847	1.336854	1.336855
$^{138}Ce/^{136}Ce^*$	1.336373	1.336925	1.336878	1.336862	1.336888	1.336848
$^{138}Ce/^{136}Ce^*$	1.336407	1.336918	1.336906	1.336863	1.336889	1.336823

$^{138}Ce/^{136}Ce^{*}$	1.336335	1.33689	1.336897	1.336902	1.336876	1.336859
$^{138}Ce/^{136}Ce^{*}$		1.336896	1.336888	1.336912	1.336876	1.33687
$^{138}Ce/^{136}Ce^{*}$		1.336946	1.336882	1.336889	1.336885	1.336856
$^{138}Ce/^{136}Ce^{*}$		1.336937	1.336886	1.336925	1.33689	
$^{138}Ce/^{136}Ce^{*}$			1.336863	1.336869		
$^{138}Ce/^{136}Ce^{*}$			1.336894			
$^{138}Ce/^{136}Ce^{*}$			1.336887			
$^{138}Ce/^{136}Ce^{*}$			1.336928			
$^{138}Ce/^{136}Ce$ (mean*)	1.336372	1.336916	1.336891	1.336883	1.33688	1.336852
Measurement numbers	4	8	11	8	7	7
2.S.E. (mean 6th digit)	21	16	18	25	16	17
Neutron capture effect [ε-deviation]	0.003[20,23]	0.014[24]	n.d.	0.011[20]	0.012[20]	0.002[25]
εCe(t) (NC corrected)	-0.63	n.d.	-0.01	-0.10	-0.15	-0.09
Err. εCe	±0.21	n.d.	±0.07	±0.18	±0.09	±0.11
$^{147}Sm/^{144}Nd^{*}$	0.2497	0.1716	0.1676	0.1705	0.1722	0.167
$^{143}Nd/^{144}Nd^{*}$	0.514258	0.511853	0.511809	0.51182	0.511819	0.511793
2 S.E. (6th digit)ppm	±6	±9	±9	±8	±11	±10
Neutron capture effect [ε-deviation]	n.d.	n.d.	n.d.	-0.22[20]	-0.38[20]	0.0[25]
εNd(t) (NC corrected)	+5.7	n.d.	-1.5	-2.8	-3.4	-1.4
$\pm 2\sigma^{a}$	±0.7	n.d.	±0.7	±0.4	±0.4	±0.6

Sample name	73275	68115
Classification	KREEP basalts	KREEP basalts
Rock type	Impact melt breccia	polymict breccia
Age [Ma]	3960	3900
Error [Ma]	50	100
Reference	[19]	estimated from other KREEP basalts
$^{138}La/^{136}Ce$	0.1878	0.1866
$^{138}Ce/^{136}Ce^{*}$	1.336871	1.336838
$^{138}Ce/^{136}Ce^{*}$	1.336892	1.336848
$^{138}Ce/^{136}Ce^{*}$	1.336847	1.336869
$^{138}Ce/^{136}Ce^{*}$	1.336841	1.336811
$^{138}Ce/^{136}Ce^{*}$	1.336849	1.336824
$^{138}Ce/^{136}Ce^{*}$	1.336847	
$^{138}Ce/^{136}Ce^{*}$	1.336858	
$^{138}Ce/^{136}Ce$ (mean$^{*)}$	1.336858	1.336838
Measurement numbers	7	5
2.S.E. (mean 6th digit)	18	19
Neutron capture effect [ε-deviation]	n.d.	0.000[20]
εCe(t) (NC corrected)	-0.25	-0.32
Err. εCe	±0.13	±0.22
$^{147}Sm/^{144}Nd^{*}$	0.1721	0.1688
$^{143}Nd/^{144}Nd^{*}$	0.511887	0.511836
2 S.E. (6th digit)ppm	±9	±9
Neutron capture effect [ε-deviation]	n.d.	0.0[20]
εNd(t) (NC corrected)	-2.3	-1.8
±2σ[a]	±0.7	±0.7

all lunar ^{87}Rb-^{87}Sr ages were recalculated using the decay constant given by Nebel et al., (2011).
*neutron capture uncorrected
[a]errors include propagated errors on parent daughter ratios, age uncertainties and external reproducibilities.
[b]For n≤4 an external reproducibility of 21ppm was assumed (Hasenstab et al., 2021, **Chapter I**), whereas for n>4, the 95 C.I was used for further error propagation

[1] Birck, (1986)
[2] Papanastassiou and Wasserburg, (1973)
[3] Kirsten et al. (1972)
[4] Wasserburg and Papanastassiou, (1971)
[5] Papanastassiou and Wasserburg, (1971)
[6] Alexander et al. (1972)
[7] Horn et al. (1975)
[8] Snape et al. (2016)
[9] Thiemens M. M., (unpublished)
[10] Borg et al. (2011)
[11] Turner et al. (1973)
[12] Papanastassiou et al. (1970)
[13] Nyquist, (1976)
[14] Turner and Cadogan, (1975)
[15] Taylor et al. (1983)
[16] Murthy et al. (1972)
[17] Papanastassiou and Wasserburg, (1972)
[18] Shih et al. (1992)
[19] Turner and Cadogan, (1975)

Neutron capture corrections were calculated with the data given below:
[20] Sprung et al. (2013)
[21] Boyet and Carlson, (2007)
[22] Borg et al. (2019)
[23] Kruijer and Kleine, (2017)
[24] Sprung, P. unpublished data

[25] Gaffney and Borg, (2014)
[26] Mcleod et al. (2014)

In the following, the depleted composition of the Moon is calculated, following the approach of O'Neill and Palme, (2008).

	W	Th	U	Nb	Ta	La	Ce	Pr	Nd	Zr	Hf	Sm	Eu	Ti	Gd	Tb	Dy	Y	Er	Yb	Lu
partition coefficients for early Earth differentiation																					
Partition coefficient[3]	0.0005	0.001	0.0011	0.0034	0.0034	0.0126[1]	0.022	0.027	0.03	0.0374[2]	0.0396[2]	0.045	0.05	0.058	0.056	0.068	0.079	0.088	0.097	0.115	0.12
starting composition[4]	0.012	0.085	0.0229	0.595	0.043	0.683	1.75	0.267	1.34	10.3	0.301	0.435	0.167	1265	0.586	0.108	0.724	4.13	0.468	0.477	0.0708
early depleted mantle	0.00023	0.0032	0.00093	0.069	0.00499	0.225	0.813	0.137	0.74	6.17	0.185	0.28	0.111	889	0.407	0.079	0.556	3.25	0.377	0.398	0.0595
early enriched crust	0.453	3.15	0.846	20.3	1.47	17.9	37	5.08	23.9	165	4.67	6.23	2.23	15335	7.27	1.17	7.03	37	3.89	3.46	0.496
collisional erosion of 54% crust	0.0066	0.0473	0.0128	0.352	0.0255	0.47	1.31	0.205	1.06	8.33	0.246	0.36	0.14	1082	0.499	0.094	0.64	3.69	0.422	0.436	0.0649
depleted proto-Earth																					
mixing of 86% proto Earth with 14% impactor[4]																					
SDEM*	0.0073	0.0526	0.0142	0.386	0.0279	0.499	1.37	0.214	1.1	8.6	0.253	0.371	0.144	1107	0.511	0.096	0.652	3.75	0.428	0.442	0.066

[1]The partition coefficient for La was recalculated using the lattice strain model (Blundy and Wood, 1994).

[2]D_{Zr} was recalculated so that the inferred composition had a $Zr/Zr^{*}=(Sm_{CN}\times Nd_{CN})^{0.5}=1$ and Hf was recalculated by assuming constant D_{Zr}/D_{Hf} ratios as previously reported (Workman and Hart, 2005).

[3]Workman and Hart, (2005)

[4]Palme and O'Neill, (2013)

[5]Canup, (2004)

***S**lightly **D**epleted **E**arth-**M**oon composition

In the following, the lunar magma ocean crystallization was modelled assuming the crystallization sequence of Snyder et al., 1992) and using our calculated SDEM composition as starting composition.

Cumulate	Pl[1]	TIRL	W	Th	U	Nb	Ta	La	Ce	Pr	Nd	Zr	Hf	Sm	Eu	Ti	Gd	Tb	Dy	Y	Er	Yb	Lu
Ol	0.02	0.03	0.0004	0.0027	0.0008	0.0198	0.0015	0.0262	0.0715	0.0111	0.0569	0.443	0.0131	0.0192	0.00817	66.4	0.027	0.0051	0.036	0.216	0.0258	0.0313	0.0054
Opx	0.02	0.025	0.001	0.0073	0.0022	0.0496	0.0041	0.065	0.203	0.0361	0.198	2.14	0.0853	0.0891	0.0304	1114	0.161	0.0369	0.29	1.86	0.24	0.348	0.0542
Pl-ol-pig	0.02	0.05	0.0033	0.0267	0.0109	0.175	0.0145	0.296	0.749	0.113	0.574	3.89	0.12	0.192	0.156	568	0.266	0.0504	0.341	2.02	0.226	0.232	0.0335
Cpx-pig	0.02	0.01	0.0027	0.023	0.0097	0.138	0.0149	0.37	1.31	0.314	1.8	10.8	0.554	0.989	0.308	2553	1.86	0.384	2.8	16.1	2	1.92	0.287
IBC	0.02	0.02	0.0436	0.31	0.0828	2.72	0.22	2.95	8.09	1.26	6.47	58.6	1.86	2.19	0.836	30347	3.01	0.555	3.73	21.2	2.38	2.29	0.334
KREEP			2.06	14.5	3.49	86	4.96	125	324	43.3	210	1468	27.8	50.9	20.8	714	49.1	7.65	45.3	248	23.5	22.1	3.11

Abbreviations as follows: Plag refers to amounts of entrained plagioclase; TIRL refers to trapped interstitial residual liquid

Pl[1] refers to additionally entrained plagioclase

Ol = olivine rich cumulates; Opx = orthopyroxene-rich cumulates, Cpx-pig = clinopyroxene-plagioclase-pigeonite-rich cumulates, Pl-pig-ol = plagioclase-pigeonite-olivine rich cumulates, IBC = ilmenite-bearing cumulates, KREEP = K-REE-P-rich rocks.

Acknowledgements

First, I would like to thank my supervisor Carsten Münker who has brought me into this research field and has raised my interest and passion in geochemistry and in particular mass spectrometry. I am really grateful to have had you as a supervisor and I really appreciate that your door was always open for me. I am also grateful for all the opportunities to participate in unforgettable field trips and conferences. Not to mention all the unforgettable numerous social events. There could not have been a better place than Cologne for my PhD! I am really looking forward to our future work together.

Special thanks goes to Jonas Tusch. Over the past years we have become a good team and we have pushed our limits several times. I am also greatly thankful for your rigorous collection of rare earth cuts that has saved me months of lab time. Without your support, the extent of Chapter II would have never been possible.

Mario Fischer-Gödde is thanked for his general support in the lab. I really appreciate that you always made time for me to discuss matters or fix things. Christiane Schnabel is thanked for introducing me to the Cerium isotope business. Analyzing Cerium has become a love-hate relationship ever since and I cannot say if it was a curse or a blessing. Thanks goes also to my former office mates Sebastian Kommescher and Maxwell Thiemens with whom working was always a pleasure. Sebastian, to this day I have benefited from your Excel skills. Thanks goes also to Mike Jansen who has a great organizational talent and made some unforgettable events and trips to the Eifel possible. Although I was unfortunately not able to participate in the two amazing Pilbara fieldtrips, I greatly thank Hugh Smithies and Martin Van Kranendonk for their field experience and for providing such a unique rock collection from the Pilbara Craton. Special thanks goes also to Frank Wombacher for his support on the Neptunes and for his help with the iCap. Thanks goes also to Daniela Hülle who organized an amazing and unforgettable India trip.

I would like to further thank Chris Marien, Peter Sprung, Erik Strub, Raúl Fonseca, Florian Kurzweil, Almut Katzemich, Alessandro Bragagni, Christina Obert, Meli Pfenning, Josua Pakulla, Julia van De Löcht and Ninja Braukmüller. Thank you all for some special years in the Black Box and hopefully some more!

Last but not least, I would like to thank my family and my soon-to-be wife Alina for their support over all those years. Thank you so much for always being there for me!

Financial support for this thesis has been provided by the European Commission by ERC grant 669666 'Infant Earth'.

Erklärung zu Chapter I

Chapter I baut auf meiner Masterarbeit “Radiogenic isotope and trace element characteristics of basalts and komatiites from the Pilbara Craton, NW Australia” auf. Im Rahmen dieser Masterarbeit wurde an 21 Archaischen Basalten aus dem Pilbara Kraton radiogene Hf-Nd-Ce Isotope untersucht. Chapter I baut auf diesen Grundlagen auf und im Rahmen dieser Dissertation werden Hf-Nd Isotopendaten für weitere 42 Proben sowie Ce Isotopendaten für weitere 19 Proben aus dem Pilbara Kraton berichtet. Da die Ce Isotopendaten der Masterarbeit noch von analytischen Artefakten beeinträchtigt waren, wurde das damals verwendete analytische Protokoll überarbeitet um diese Proben erneut aber mit besserer Präzession messen zu können. Zum Teil mussten diese Proben aufgrund von Materialmangel auch neu aufgeschlossen und separiert werden. Des Weiteren stammt der wesentliche Teil an Modellierungen aus dieser Dissertation, die als Grundlage genutzt wurden, um im Rahmen dieser Arbeit ein geodynamisches Modell zu erstellen. In die Publikation, die **Chapter I** darstellt, sind auch die Daten aus meiner Masterarbeit eingeflossen. Deshalb werden in dieser Dissertation sowohl der Datensatz der Masterarbeit als auch die hier gewonnenen Daten in ihrer Gesamtheit vorgestellt und neu interpretiert.

Erklärung

Ich versichere, dass ich die von mir vorgelegte Dissertation selbständig angefertigt, die benutzten Quellen und Hilfsmittel vollständig angegeben und die Stellen der Arbeit − einschließlich Tabellen, Karten und Abbildungen −, die anderen Werken im Wortlaut oder dem Sinn nach entnommen sind, in jedem Einzelfall als Entlehnung kenntlich gemacht habe; dass diese Dissertation noch keiner anderen Fakultät oder Universität zur Prüfung vorgelegen hat; dass sie − abgesehen von unten angegebenen Teilpublikationen − noch nicht veröffentlicht worden ist, sowie, dass ich eine solche Veröffentlichung vor Abschluss des Promotionsverfahrens nicht vornehmen werde. Die Bestimmungen der Promotionsordnung sind mir bekannt. Die von mir vorgelegte Dissertation ist von Prof. Dr. Carsten Münker betreut worden.

Nachfolgend genannte Teilpublikationen liegen vor:

E. Hasenstab., J. Tusch, C. Schnabel, C. S. Marien, M. J. Van Kranendonk, H. Smithies, H. Howard, W. D. Maier, and C. Münker (2021): Evolution of the early to late Archean mantle from Hf-Nd-Ce isotope systematics in basalts and komatiites from the Pilbara Craton. Earth and Planetary Science Letters 553: 116627.

Chapter I, Appendix A1

E. Hasenstab, C. Münker, J. Tusch, M.M. Thiemens, D. Garbe-Schönberg, E. Strub, P. Sprung (submitted): Cerium-Nd isotope evidence for an incompatible element depleted Moon.

Chapter III, Appendix A3

Datum: 17.02.2022 Unterschrift: